



DOCTORAL THESIS

**Mechanical properties of sound and of deteriorated softwood  
at different length scales:  
Poromicromechanical modeling and experimental investigations**

submitted in satisfaction of the requirements for the degree of  
Doctor of Science in Civil Engineering  
of the Vienna University of Technology, Faculty of Civil Engineering

---

DISSERTATION

**Mechanische Eigenschaften von fehlerfreiem und von  
abgebautem Nadelholz auf unterschiedlichen Längenskalen:  
Poromikromechanische Modellierung und  
experimentelle Untersuchungen**

ausgeführt zum Zwecke der Erlangung des akademischen Grades eines  
Doktors der technischen Wissenschaften  
eingereicht an der Technischen Universität Wien, Fakultät für Bauingenieurwesen

von

Dipl.-Ing. Thomas Karl Bader  
Matrikelnummer 0125636  
Tullnerbachstraße 9-11/3/71, A-3002 Purkersdorf, Österreich

Gutachter: Priv.-Doz. Dipl.-Ing. Dr. techn. Karin Hofstetter  
Institut für Mechanik der Werkstoffe und Strukturen  
Technische Universität Wien  
Karlsplatz 13/202, A-1040 Wien, Österreich

Gutachter: Prof. Kristofer Gamstedt, MSc., Ph.D.  
Institute for Applied Mechanics  
Uppsala University  
Lägerhyddsv. 1, Box 534, 751 21 Uppsala, Schweden

Wien, im Juni 2011

.....

# Acknowledgments

This thesis is based on the work done during my employment as a research assistant at the Institute for Mechanics of Materials and Structures at the Vienna University of Technology. It would not have been possible without the generous help of numerous people who contributed to the scientific results and provided the essential boundary conditions for this work.

I especially thank my advisor Priv.-Doz. Dr. Karin Hofstetter (Institute for Mechanics of Materials and Structures) for her guidance, encouragement, patience, and her continuous support throughout the last years. It was a pleasure to work with her at the Institute for Mechanics of Materials and Structures, particularly within the wood research group she is leading. Many thanks to Prof. Kristofer Gamstedt (Uppsala University, Sweden), who served as co-examiner of this thesis, also for the fruitful and inspiring discussions during the COST Action FP0802 (Experimental and Computational Micro-Characterization Techniques in Wood Mechanics) workshops.

Prof. Josef Eberhardsteiner, the dean of the Faculty of Civil Engineering and head of the Institute for Mechanics of Materials and Structures, is thanked for his personal support throughout this work. I sincerely thank Prof. Christian Hellmich for his assistance in the theoretical fundamentals of my work and its application to wood.

I am indebted to Dr. Gry Alfredsen (Norwegian Forest and Landscape Institute, Norway) and to Dr. Susanne Bollmus (Georg-August-University Göttingen, Germany) for their collaboration within the WoodWisdom Net project "WoodExter". The project coordinator Jöran Jermer (SP Träteknik, Sweden) is gratefully acknowledged for his support. I thank Dr. Daniel Keunecke (ETH Zürich, Switzerland) for his cooperation and his generous assistance in the mechanical characterization of yew wood.

It was a pleasure to visit Susan Braovac at the Museum of Cultural History in Oslo, Norway. I owe her my gratitude for many fruitful and inspiring discussions and I am very much looking forward to this ongoing collaboration on archaeological wood. Dr. Karin Fackler (Institute of Chemical Engineering, Vienna University of Technology) is gratefully acknowledged for her support and for her interest in the characterization of deteriorated and of archaeological wood.

I am very thankful to present and former colleagues at the Institute for Mechanics of Materials and Structures, Dipl.-Ing. Michael Dorn, Dipl.-Ing. Johannes Eitelberger, Dr. Andreas Fritsch, Dr. Josef Füssl, Dipl.-Ing. Stefan Gloimüller, Dr. Christoph Hackspiel, Dipl.-Ing. Georg Hochreiner, Dr. Andreas Jäger, Dr. Christoph Kohlhauser, Dipl.-Ing. Markus Lukacevic, Dr. Reinhard Stürzenbecher, and Dipl.-Ing. Leopold Wagner. Special thanks to Christoph Wikete for his assistance in the experimental work that to a great part contributed to the success of this thesis. I would like to thank Mag.(FH) Martina Pöll, Astrid Schuh, and Gabriele Ostrowski for their support in administrative issues.

This thesis would not have been possible unless the support of my family. Above all, I want to express my sincere gratitude to my wife Martina Bader-Rehak for her restless support. My sons Maximilian and Konstantin are a source of energy and inspiration. To them I dedicate this thesis.

# Kurzfassung

Mechanische Eigenschaften von Holz sind stark richtungsabhängig und breit gestreut aufgrund seines natürlichen Ursprungs und heterogenen Aufbaus. Ähnlich wie bei anderen biologischen Materialien ist auch die Holzmikrostruktur streng hierarchisch gegliedert, beginnend bei den mit freiem Auge ersichtlichen Jahrringen bis hin zu den Holzpolymeren Zellulose, Hemizellulose und Lignin auf der Nanometer-Ebene. Ziel der vorliegenden Dissertation ist die Gewinnung eines tieferen Verständnisses des Einflusses unterschiedlicher hierarchischer Ebenen und deren physikalischen und chemischen Eigenschaften auf das mechanische Verhalten von fehlerfreiem Holz und abgebautem Holz durch die Anwendung mikromechanischer Modellierung und experimenteller Methoden.

Diese Arbeit beinhaltet die Neuformulierung eines bestehenden Mikromechanikmodells für das elastische Verhalten und elastische Grenzzustände von Holz im Rahmen der Poromechanik. Das entwickelte poromikromechanische Mehrskalmodell erlaubt die Untersuchung der mechanischen Funktion von Zellwandwasser auf unterschiedlichen hierarchischen Ebenen. Im weiteren Sinne lässt sich mit diesem Modell die Übertragung von Eigenspannungen in der Zellwand bis zur makroskopischen Ebene untersuchen. Darüber hinaus werden mit Hilfe dieses Modells Versagensspannungen von Nadelholz von einem mikroskopischen Versagenskriterium für Lignin abgeleitet. Die Eignung dieses Modellierungsansatzes wird durch die zufriedenstellende Übereinstimmung zwischen vorhergesagten Versagensspannungen mit experimentellen Werten aus biaxialen Festigkeitsversuchen an Fichtenholz unterstrichen.

Eibenholz besitzt im Vergleich zu anderen Nadelhölzern außergewöhnliche mechanische Eigenschaften, die sich aus teilweise stark abweichenden mikrostrukturellen Eigenschaften der Eibe ergeben. Die Beziehung zwischen Mikrostruktur und Steifigkeiten der Eibe und deren Vergleich zur Fichte werden mit Hilfe des poromikromechanischen Modells und mechanischen Versuchen auf unterschiedlichen Längenskalen erforscht, womit sich auch eine erweiterte Modellvalidierung ergibt. Es stellt sich heraus, dass die Unterschiede im Mikrofibrillenwinkel der S2 Zellwandschicht und in der Dichte zwischen den beiden Holzarten einen größeren Einfluss haben als die Unterschiede in der Jahrringstruktur.

Außerdem wird die Eignung des poromikromechanischen Modells zur Beschreibung von Änderungen im mechanischen Verhalten von pilzabgebautem Holz aufgezeigt. Als Basis für die Modellierung werden Beziehungen zwischen der Mikrostruktur und mechanischen Eigenschaften von abgebautem Holz experimentell untersucht. Es werden Änderungen im mechanischen Verhalten und in der Mikrostruktur vorgestellt, die an Kieferproben aus genormten Dauerhaftigkeitsversuchen mit einem Braunfäulepilz (*Gloeophyllum trabeum*) und einem Weißfäulepilz (*Trametes versicolor*) gemessen wurden. Es stellt sich heraus, dass die transversalen Steifigkeiten sensibler auf den Abbau reagieren als die longitudinale Steifigkeit, vor allem durch den erheblichen Abbau von Hemizellulosen. Darüber hinaus zeigt sich, dass Anisotropiefaktoren aus den mit Hilfe von Ultraschall bestimmten Steifigkeiten einen Rückschluss auf Abbaumechanismen der beiden verwendeten Pilze erlauben. Letztlich werden die mechanischen Versuche durch mikromechanische Modellierung vervollständigt, wobei das Mikromechanikmodell erweitert wird, um abbauspezifische Mikrostruktureigenschaften berücksichtigen zu können.

# Abstract

Due to its natural origin and its inherent heterogeneities, mechanical properties of wood are highly anisotropic and show a broad variability, not only between different wood species, but also within a tree. Similar to other biological materials, the wood microstructure is well organized and hierarchically structured from the annual rings visible to the naked eye down to the wood polymers cellulose, hemicellulose, and lignin at the nanometer-scale. This thesis aims at a deeper understanding of the role of different hierarchical levels and their corresponding physical and chemical characteristics in relation to mechanical properties of sound wood and of deteriorated wood. This is achieved by means of micromechanical modeling and experimental analyses.

This thesis starts with the re-formulation of an existing micromechanical model for the elastic behavior and elastic limit states of wood in the framework of poromechanics. The mechanical role of cell wall water at different hierarchical levels is investigated by means of this model. In a broader sense, the developed model allows to investigate the transition of eigenstresses from the cell wall to the softwood level. Moreover, this poromicromechanical model forms the basis for subsequent consideration of a microscopic failure criterion for lignin for the derivation of softwood failure stresses. The suitability of the modeling approach is underlined by a satisfactory agreement of the model-predicted failure stresses with experimental results of biaxial strength tests on Norway spruce.

As a result of partly considerably different microstructural characteristics, Common yew exhibits exceptional mechanical properties compared to other softwood species. The relationship between microstructure and stiffness properties of Common yew and Norway spruce is investigated by means of the poromicromechanical model and mechanical tests across various length scales. Moreover, this offers the opportunity of a broader model validation. The influence of differences in microfibril angle of the S2 cell wall layer and in mass density between yew and spruce is found to be more dominant than the influence of differences in the annual ring characteristics.

The suitability of the poromicromechanical model to predict changes in mechanical properties upon fungal decay is demonstrated. For this purpose, relationships between microstructure and mechanical properties of deteriorated wood are experimentally explored. Changes in mechanical properties and in the microstructure, measured at pine wood samples after standard wood durability tests using one brown rot fungus (*Gloeophyllum trabeum*) and one white rot fungus (*Trametes versicolor*), are presented. Transverse stiffnesses are revealed to be more sensitive to degradation than longitudinal stiffness, particularly as a result of pronounced degradation of hemicelluloses. Moreover, ultrasonically derived anisotropy ratios of elastic stiffnesses allow to identify certain degradation mechanisms of the two considered fungi. The experimental campaign is complemented by micromechanical modeling. For this purpose, the micromechanical model is extended to take into account degradation-specific microstructural characteristics.

# Contents

<b>Introductory remarks</b>	<b>1</b>
Wood - a natural, hierarchically structured material . . . . .	1
Wood - inherent mechanical anisotropy and its relation to the microstructure .	3
Research objectives and synopsis of the thesis . . . . .	4
Main findings . . . . .	7
Perspectives and future research studies . . . . .	8
<b>1 The poroelastic role of water in cell walls of the hierarchical composite "softwood" (Bader et al., 2011a)</b>	<b>11</b>
1.1 Introduction . . . . .	13
1.2 Fundamentals of homogenization theory – representative volume element – micromechanical representation of wood . . . . .	14
1.2.1 Homogenization theory for materials with random microstructures – continuum micromechanics . . . . .	14
1.2.2 Hierarchy of wood – multiscale homogenization . . . . .	16
1.2.3 Homogenization theory for materials with periodic microstructures - unit cell method . . . . .	16
1.3 Poro-microelasticity of polymer network . . . . .	16
1.3.1 RVE, stress and strain averages . . . . .	16
1.3.2 Constitutive behavior of the material phases . . . . .	18
1.3.3 Homogenized poroelasticity of polymer network . . . . .	19
1.4 Microelasticity of cellulose . . . . .	22
1.5 Poro-microelasticity of cell wall material . . . . .	23
1.5.1 RVE, stress and strain averages . . . . .	23
1.5.2 Constitutive behavior of material phases . . . . .	24
1.5.3 Homogenized poroelasticity of cell wall material . . . . .	25
1.6 Poro-microelasticity of softwood . . . . .	27

---

1.6.1	RVE, stress and strain averages . . . . .	27
1.6.2	Constitutive behavior of material phases . . . . .	28
1.6.3	Homogenized poroelasticity of softwood . . . . .	28
1.7	Structure-property relationships . . . . .	32
1.8	Concluding remarks . . . . .	40
1.9	Appendix . . . . .	41
1.9.1	Hill tensor for spherical inclusion in isotropic matrix . . . . .	41
1.9.2	Hill tensor for cylindrical inclusions in isotropic matrix . . . . .	41
1.9.3	Unit cell model for softwood . . . . .	42
<b>2</b>	<b>Poromechanical scale transitions of failure stresses in wood: from lignin to the spruce level (Bader et al., 2010)</b>	<b>45</b>
2.1	Introduction . . . . .	48
2.2	Representative volume element, stress and strain averages, Hill's lemma . . . . .	50
2.3	Poroelasticity of softwood . . . . .	51
2.4	Effective (higher-order) strains at lignin level . . . . .	54
2.5	Upscaling failure criterion from lignin to softwood scale - identification of lignin strength . . . . .	59
2.6	Experimental validation - spruce under direction-variant biaxial loading . . . . .	61
2.7	Conclusions . . . . .	66
<b>3</b>	<b>Microstructure-stiffness relationships of Common yew and Norway spruce (Bader et al., 2011b)</b>	<b>71</b>
3.1	Introduction . . . . .	72
3.2	Materials and Methods . . . . .	73
3.2.1	Tensile tests . . . . .	73
3.2.2	Ultrasonic tests . . . . .	74
3.2.3	Nanoindentation (NI) . . . . .	74
3.2.4	Thermogravimetric analysis . . . . .	75
3.2.5	Microfibril angle (MFA) . . . . .	75
3.2.6	Micromechanical modeling . . . . .	75
3.3	Results . . . . .	76
3.3.1	Mechanical properties . . . . .	76
3.3.2	Physical and chemical properties . . . . .	78
3.4	Discussion . . . . .	79

---

3.4.1	Cell wall stiffness . . . . .	80
3.4.2	Macroscopic longitudinal stiffness . . . . .	81
3.4.3	Macroscopic transverse and shear stiffness . . . . .	82
3.5	Conclusions . . . . .	86
3.6	Appendix A . . . . .	87
<b>4</b>	<b>Changes in microstructure and stiffness of Scots pine (<i>Pinus sylvestris</i>) sapwood degraded by <i>Gloeophyllum trabeum</i> and <i>Trametes versicolor</i> - Part I: Physicochemical alterations (Bader et al., 2011c)</b>	<b>90</b>
4.1	Introduction . . . . .	91
4.2	Materials and Methods . . . . .	93
4.2.1	Thermogravimetric analysis . . . . .	93
4.2.2	Wet chemical analysis . . . . .	94
4.3	Results and Discussion . . . . .	95
4.3.1	Physical and chemical properties of sound samples . . . . .	95
4.3.2	Physical and chemical properties of degraded samples . . . . .	95
4.4	Conclusions . . . . .	102
<b>5</b>	<b>Changes in microstructure and stiffness of Scots pine (<i>Pinus sylvestris</i>) sapwood degraded by <i>Gloeophyllum trabeum</i> and <i>Trametes versicolor</i> - Part II: Anisotropic stiffness (Bader et al., 2011d)</b>	<b>104</b>
5.1	Introduction . . . . .	105
5.2	Materials and methods . . . . .	106
5.2.1	Tensile tests . . . . .	107
5.2.2	Ultrasonic tests . . . . .	107
5.3	Results and discussion . . . . .	109
5.3.1	Mechanical properties of sound samples . . . . .	109
5.3.2	Mechanical properties of degraded samples . . . . .	110
5.4	Concluding remarks . . . . .	118
<b>6</b>	<b>Decrease of stiffness properties of degraded wood predicted by means of micromechanical modeling (Bader et al., 2011e)</b>	<b>120</b>
6.1	Introduction . . . . .	121
6.2	Hierarchical organization of wood and fundamentals of homogenization theory . . . . .	122
6.2.1	Hierarchical organization of wood and alterations due to fungal decay	122
6.2.2	Fundamentals of homogenization theory . . . . .	123

---

6.2.2.1	Continuum micromechanics – random homogenization theory . . . . .	123
6.2.2.2	Unit cell method – periodic homogenization theory . . . . .	124
6.3	Micromechanical model for softwood stiffness . . . . .	124
6.4	Experimental program and results . . . . .	126
6.4.1	Materials and Methods . . . . .	126
6.4.2	Results and Discussion . . . . .	127
6.5	Experimental validation of micromechanical model . . . . .	129
6.5.1	Modeling of unaffected initial condition . . . . .	130
6.5.2	Modeling of brown rot ( <i>G. trabeum</i> ) and white rot ( <i>T. versicolor</i> ) degraded samples . . . . .	130
6.6	Conclusions and Perspectives . . . . .	134
	<b>Bibliography</b>	<b>136</b>
	<b>Publications and conference presentations</b>	<b>147</b>
	<b>Curriculum Vitae</b>	<b>149</b>



# Introductory remarks

Due to the natural diversity in microstructural characteristics of wood, its mechanical properties show a broad variability, not only between different wood species, but also within a tree. Variability and diversity are even increased, when mechanical properties of deteriorated wood are examined. This thesis aims at a deeper understanding of the role of different hierarchical levels and their corresponding physical and chemical characteristics on relationships between microstructure and mechanical properties of sound and deteriorated softwood. For this purpose, in addition to experimental techniques for mechanical characterization at various length scales, micromechanical modeling techniques are applied.

## Wood - a natural, hierarchically structured material

Nature provides many resources that can be used as materials for structural applications, whereby wood has been the most important construction material for centuries. In its natural condition the wood material is produced in a living tree system, where its main function, among other requirements such as water and nutrient transport, is to provide mechanical resistance. Continuous growing and, consequently, adjustments in the material according to the actual requirements, enables the tree to optimize its response to external influences. The material wood is hierarchically well structured, which enables the tree to very efficiently adapt its structure (see e.g. Fengel and Wegener (1984); Burgert (2006); Fratzl and Weinkamer (2007) and references therein).

### Hierarchical structure

Starting at the level of clear wood (without growth irregularities such as knots) the microstructure of softwood from gymnosperms can be described by four levels of hierarchy (see e.g. Fengel and Wegener (1984); Kollmann and Côté (1968); Côté (1965) among many others):

#### *Macrostructure – Softwood:*

At the level of softwood, i.e. at a piece of solid wood with some mm length, annual rings are clearly visible in the stem cross-section (radial-tangential plane). This structure arises from the continuous transition of bright earlywood (with high porosity) to dark latewood (with lower porosity) during each growth season. Depending on the course of

transition (smooth or abrupt), additionally, the assignment of a transition wood region can be suitable for certain wood species.

#### *Early- / Latewood:*

Taking a closer look at earlywood and latewood reveals their typical cellular structure of hollow cells (mainly tracheids) running in stem direction. Earlywood cells are thin walled with large lumina, whereas latewood cells have thick walls and small lumina. The cell wall thickness is strongly related to earlywood and latewood mass density and, thus, to the overall softwood mass density. Typical cell dimensions are diameters of 20–50  $\mu\text{m}$ , lengths of 2–10 mm, and wall thicknesses of 2–20  $\mu\text{m}$ . The cross-sectional shape of the tracheids can, in good approximation, be considered hexagonally with a continuously decreasing radial lumen diameter from earlywood (about 40–50  $\mu\text{m}$ ) to latewood (about 20–30  $\mu\text{m}$ ).

#### *Cell wall structure:*

Cell walls of softwood tracheids are composed of different layers: the primary wall (P) and the secondary walls (S1, S2, and S3). Two adjacent cells are bonded together by the middle lamella. The layers comprise different chemical and morphological characteristics. The so-called S2 layer (a sublayer of the secondary wall) is the dominant layer by volume, comprising about 80–90% by volume of the entire cell wall (Kollmann and Côté, 1968; Fengel and Wegener, 1984). Therein, cellulose fibrils are parallel and highly aligned, but inclined to the cell axis by the so-called microfibril angle (MFA).

#### *Ultrastructure – Polymer network and cellulose:*

The cell wall material of the cell wall layers of tracheids is composed of cellulose fibrils that are embedded into a polymer matrix composed of hemicelluloses, lignin, and extractives. Cellulose fibers, with about 30 nm side length, themselves are composed of crystalline microfibrils and amorphous parts (Salmén and Burgert, 2009). The term hemicelluloses refers to partly branched non-cellulosic polysaccharides. Some of them are associated with cellulose. Lignin is a polyphenolic, branched polymer with a complex three-dimensional structure. Typical dimensions of hemicellulose and lignin structures are 1–5 nm. In moist conditions, water is incorporated in temporary pores in the amorphous part of the cell wall.

As a consequence of the above described microstructure of wood that is continuously adapted according to the needs of a tree, compositional and morphological variations within a single tree (juvenile – adult wood, or earlywood – latewood), as well as between different wood species are observed. This is expressed in different tracheid cross-sectional shapes, cell wall thicknesses, chemical compositions, or in different orientations of cellulose microfibrils (Eder, 2007; Burgert, 2006).

## **Biodegradation**

The natural origin of wood comprises a considerable economic benefit. However, it requires also careful application of the material, since it is susceptible to biological degradation by microorganisms. While being desired in nature, it can considerably reduce the load bearing capacity of timber structures. Destroying of wood and degradation of

wood components can be caused by animals, such as insects, by fungi, or by bacteria. Basidiomycete fungi are among the most efficient wood degrading organisms. Related to their strategy to degrade wood, there are two main types: brown rot and white rot. Fungi related to brown rot degrade and mineralize wood polysaccharides, leaving behind a modified lignin that gives the decayed wood its characteristic color. On the contrary, white rot fungi are able to degrade and mineralize all major wood constituents, using ligninolytic and cellulytic/hemicellulytic enzymatic systems (Côté, 1965; Fengel and Wegener, 1984; Schwarze, 2007). There are white rot fungi that simultaneously degrade wood constituents (simultaneous rot), as well as white rot fungi that selectively degrade lignin (selective delignification) before the other components are degraded.

## Wood - inherent mechanical anisotropy and its relation to the microstructure

Due to the in general complex build up of natural, biological materials, such as wood or bone, their macroscopic mechanical properties are highly anisotropic (Fratzl and Weinkamer, 2007). This means, their mechanical properties are direction dependent. As regards wood, in good approximation, the generally curved shape of the growth rings is neglected by consideration of parallel aligned layers. Hence, the material behavior can be considered orthotropic, i.e. symmetry about three mutually perpendicular planes. Consequently, the principal material directions are the longitudinal (in stem direction), radial (from the pith to the bark), and tangential (circumferential and perpendicular to the other two) directions. The constitutive description (stress-strain relationship) requires nine independent elastic parameters. Additionally to the direction, failure stresses of wood are dependent on the mode of the loading (compression or tension), resulting in nine failure stresses related to the principal material directions. For instance, the tensile strength in longitudinal direction is about ten times higher than in radial and tangential direction (Bodig and Jayne, 1982). Furthermore, the failure mode (brittle or ductile) depends on the loading condition (Eberhardsteiner, 2002).

This clearly points out the extensive experimental efforts necessary for the mechanical characterization of wood. Moreover, material parameters vary according to different physical and chemical properties, not only between wood species, but also within a tree. Hence, macroscopic experimental testing delivers only limited insight into relationships between microstructure and mechanical properties. Universal relations are difficult to derive, since experiments give only single data points for specific material characteristics and testing conditions.

Recent experimental efforts focused on smaller length scales, where the material behavior is less understood. Also less variability in mechanical properties is expected at lower hierarchical levels. Particularly, small-sized tissue tests and single fiber tests (see e.g. Eder (2007) and references therein), as well as nanoindentation tests (see e.g. Wimmer et al. (1997); Gindl et al. (2004); Gindl and Schöberl (2004); Konnerth et al. (2010)) were performed. They gave considerable insight into structure-function relationships on lower length scales of wood.

A strategy to overcome the limitations of experimental testing and, consequently, to gain enhanced insight into effects of specific microstructural characteristics on macroscopic mechanical properties is micromechanical modeling. Corresponding methods are based on the idea of homogenization, i.e. the derivation of effective mechanical properties of a quasi-homogeneous material that yields the same average mechanical response than the actual micro-heterogeneous material. Homogenization methods are mainly based either on representative volume elements (RVEs), where the microstructure is described in a statistical manner by average properties of homogeneous subdomains (so-called phases), or repetitive unit cells (RUCs), where the microstructure is mapped in a periodic phase arrangement (Hofstetter and Gamstedt, 2009). By means of homogenization methods, effective mechanical properties are predicted, based on compositional (components and their amount), morphological (shape, orientation, and distribution), and mechanical (stiffness and interaction of components) information. Use of micromechanical modeling at different material length scales yields multiscale models that represent a hierarchical structure.

Hierarchical models for elastic properties of wood were based on rules of mixture approach, the unit cell theory, and the laminate theory (see Hofstetter and Gamstedt (2009) and references therein). Particularly the investigation of representative unit cells with the Finite Element method lead to a deeper understanding of the elastic and hygroexpansion behavior of wood (see e.g. Persson (2000)). A comprehensive review of homogenization methods and micromechanical models for wood is given in Hofstetter and Gamstedt (2009). Recent developments of a continuum micromechanics-based hierarchical model for softwood stiffness (Hofstetter et al., 2005, 2006, 2007) and strength (Hofstetter et al., 2008) form the basis of this thesis.

## Research objectives and synopsis of the thesis

Research in the field of wood mechanics is mainly driven by the aim to optimize timber structures by more accurately describing the mechanical properties of clear wood, of timber (including growth irregularities), and also of wood based products. A better constitutive description of the material leads to a more reliable design and enables an optimized, application-tailored use. On the other side, natural materials are a source of inspiration to mimic nature in biomimetic materials. Particularly at small length scales, nature's strategies for optimal design in terms of efficient application of materials are of specific interest.

The work presented in this thesis aims at developing mathematical models in the framework of micromechanics that suitably relate microstructural characteristics of clear wood to its mechanical properties. This fundamental link forms the basis for subsequent studies extending to mechanical properties of timber and, thus, to a more efficient design of timber structures. The suitability of the modeling approach needs to be assessed by comparing model predictions for sample-specific characteristics with corresponding experimental results. Since the hierarchical structure of wood is taken into account, model verification not only after the last homogenization step, but also at intermediate steps is possible and desired. Application of a micromechanical model to modified or degraded wood can

further verify the modeling approach, since it tests the model for other and often more extreme settings of microstructural characteristics. Thus, this work aims at assessing if alterations in the microstructure due to wood decay by fungi and corresponding changes in mechanical properties are suitably represented by the micromechanical model.

**Publication 1** is dedicated to the extension of the existing micromechanical model for softwood stiffness to the prediction of poromechanical quantities. The re-formulation of the homogenization procedure in a poro-micromechanical framework allows to take into account water-specific characteristics, such as a minimal capability to carry tensile loads and the possibility to enter or leave the pore spaces of wood at an arbitrary pressure. This work strives for a better understanding of the mechanical role of the cell wall water at different hierarchical levels. Particularly, effects of its pressurization state on the mechanical deformation of wood is investigated. The softwood microstructure is represented in four homogenization steps, namely polymer network, cellulose, cell wall material, and softwood. The poromechanical extension of the applied continuum micromechanical methods and of the unit cell method yields an effective drained stiffness, an effective Biot tensor, and an effective Biot modulus for each homogenization level. The drained stiffness relates to the material with empty nano-pores. The Biot tensor expresses the relation between a pore pressure in the nano pores and the resulting macroscopic eigenstresses under deformation-free conditions. The Biot modulus, finally, describes the corresponding change of nano-porosity in consequence of a pore pressure. Combination of the methods results in a multiscale poromicromechanical model for softwood and, consequently, in effective poroelastic properties of softwood that are dependent on the microstructural characteristics. Finally, effects of the amount of cell wall water and of lumen porosity on the effective poroelastic properties of the cell wall material and of softwood are illustrated and discussed.

**Publication 2** describes the derivation of softwood failure stresses, based on the consideration of a microscopic failure criterion for lignin, within the multiscale poromicromechanical model presented before. The poroelastic approach allows to take into account the mechanical state of water. Local stress and strain peaks associated with material failure are not directly accessible through mean values derived from continuum micromechanical approaches based on mean field theory. Thus, quadratic averages of the deviatoric strain of lignin, as a function of the loading parameters, are estimated using elastic energy considerations. Based on a *von Mises* criterion for lignin, a softwood failure criterion is derived. Due to a lack of experimental data related to lignin strength, the developed failure criterion is applied to identify a lignin shear strength from a macroscopic pure shear experiment on spruce. The micromechanical model is validated with experimental data for biaxial strength of spruce. Additionally, the relation between lignin failure-induced stresses and macroscopic limit stresses (ultimate strength and yield limit) is studied for typical loading conditions and corresponding stress-strain relationships. Finally, the influence of cell wall water and lumen porosity on lignin failure-induced macroscopic failure stresses is illustrated and discussed.

In **Publication 3**, the poromicromechanical model for softwood stiffness is applied to investigate microstructure-stiffness relationships of Common yew and Norway spruce, in addition to experimental data derived by means of tensile tests, ultrasound, and nanoindentation. Compared to other softwood species, yew exhibits exceptional mechanical properties. Norway spruce is taken as a reference. Recent experimental research works highlighted the microstructural origin of the different mechanical properties of these species. Among other peculiarities, particularly a higher microfibril angle (MFA) and a higher mass density of yew, compared to spruce, are observed. However, the contribution of each of these microstructural characteristics to the macroscopic stiffness was not so clear. Thus, microstructural investigations (MFA, chemical composition, mass density) and mechanical tests (uniaxial tension, ultrasound, and nanoindentation) are performed on Common yew and Norway spruce specimens. Together with earlier data from mechanical and microstructural characterization efforts, a consistent set of physical, chemical, and mechanical data is compiled. Subsequently, microstructure-stiffness relationships are explored, starting at the cell wall level, where particularly the cellulose content and the orientation of the cellulose fibrils (expressed by the MFA) affect stiffness properties. Already at this level, considerably different properties of yew and spruce are observed. Additionally, we apply the well verified poromicromechanical model for wood stiffness, which allows to predict the influence of certain microstructural features in addition to the single experimental data points. At the macroscopic level, highly anisotropic stiffness properties are observed, as a result of overlaid effects of the microstructure. The specific influences of MFA, mass density, density ratio of latewood to earlywood density, and latewood content are detached by means of the micromechanical model.

Publication 4 and 5 present experimental results from wood degraded by basidiomycete fungi. These publications form the basis for subsequent micromechanical modeling of deteriorated softwood in Publication 6.

In **Publication 4**, changes in physical and chemical properties of wood due to fungal degradation are experimentally investigated. In particular, pine sapwood samples are measured in the sound state, as well as after degradation by one brown rot fungus (*Gloeophyllum trabeum*) and one white rot fungus (*Trametes versicolor*). Standardly, loss in oven-dry mass is measured in durability tests according to EN 113 (1996). Also alterations of chemical components upon fungal degradation are well understood. On the contrary, less data is available on changes in mass density and equilibrium moisture content (EMC) at specific ambient conditions. Moreover, the relation between these technological properties (mass, mass density, chemical composition, EMC) is not so clear. Hence, the aim of this contribution is to establish a consistent set of physical data (mass, mass density, EMC) and chemical data (relative amount of chemical constituents) for subsequent determination of correlations between changes in the microstructure. Except for the oven-dry mass, the tests are performed under constant climatic conditions of 20 °C and 65 % relative humidity. For verification of the thermogravimetric approach for chemical wood decay characterization, chemical compositions are also measured by wet chemical analysis techniques. Having at hand the consistent data set, relations between the earlier described parameters are explored.

In **Publication 5**, changes in stiffness properties of wood due to fungal degradation are experimentally investigated on the same samples as analyzed in Publication 4. So far, mechanical tests on degraded wood have mainly focused on properties related to the longitudinal direction, while limited data related to the transverse directions is available. Due to the degradation of hemicelluloses, which form a part of the cell wall matrix material, by wood destroying fungi, transverse stiffness is expected to be more strongly reduced than the longitudinal one. Aiming, finally, at derivation of microstructure-stiffness relationships of degraded wood, the microstructural and technological experimental data described in Publication 4, are herein complemented by results from uniaxial tension tests in longitudinal direction and from ultrasonic tests in the longitudinal, radial, and tangential direction. The tests are performed under constant climatic conditions of 20 °C and 65 % relative humidity. The finally assembled data set allows to relate microstructural alterations to changes in macroscopic stiffness properties.

In **Publication 6**, the suitability of the micromechanical modeling approach to predict stiffness properties of degraded wood is assessed. The poromicromechanical model developed in Publication 1 is applied. In order to take into account the degradation-specific changes of the microstructure, the model is adapted. Particularly, a pore space resulting from degradation of cell wall constituents is added as phase in homogenization step Ia (polymer network). Based on sample-specific mass densities, equilibrium moisture contents, and chemical compositions, together with average microfibril angles and morphological parameters related to the cellular softwood structure, model predicted sound wood stiffness properties are compared to experimental results. Thereon, model predicted stiffness properties of the degraded state are calculated with sample-specific mass densities and equilibrium moisture contents of degraded samples. The comparison of model predicted changes in longitudinal elastic modulus and in radial and tangential stiffness with corresponding experimental results underlines the predictive capability of the model.

## Main findings

This thesis aims at assessing the suitability and potential of a poromicromechanical model for prediction of softwood stiffness and strength, across various softwood species in sound and degraded state. The re-formulation of the micromechanical model for softwood stiffness in a poromechanical framework, gave considerable insight into the effect of cell wall water on stiffness. In a broader sense, as a novel issue, the established method allows to relate eigenstresses arising within the cell wall microstructure to macroscopic eigenstresses in softwood. Influences of the cell wall water content and lumen porosity on the drained stiffness tensor components, the Biot tensor components, and on Biot moduli of the cell wall material as well as of softwood were quantified for microstructural characteristics typical for spruce.

Based on this model, consideration of microscale higher-order strains, derived from energy consideration, in a failure criterion for lignin, suitably predicted biaxial strength of spruce. Except for loading conditions with predominantly longitudinal tension, model

predictions agree well with corresponding experimental data. The so verified micromechanical model allows to assess influences of specific microstructural characteristics on lignin-failure induced softwood failure stresses and, thus, contributes to a deeper understanding of microstructure-strength relationships in spruce and – in a broader sense – in wood.

Application of the poromicromechanical model with sample-specific data to Common yew and Norway spruce, allowed quantifying the contribution of a change in the microfibril angle (MFA), cellulose content, mass density, density ratio of latewood to earlywood, and latewood content to their macrosopic stiffness. It could be shown that most of the difference in anisotropic stiffnesses of yew and spruce is a consequence of the differences in MFA and mass density, while their macroscopic stiffness is only slightly affected by growth ring characteristics. Mechanical characterization of the S2 cell wall layer of yew and spruce by means of nanoindentation allowed to verify model predictions even on a lower length scale. Moreover, application of the model at the cell wall level allowed to show the influence of the MFA on cell wall stiffness, while on the softwood level, its influence is overlaid with influences of growth ring characteristics.

The micromechanical modeling approach was also found to suitably describe changes in the mechanical properties of softwood upon fungal decay. The experimental work related to the physicochemical and mechanical characterization of the degraded pine sapwood samples provided valuable data for subsequent micromechanical modeling. Furthermore, the experiments revealed that transverse stiffness properties are more sensitive to degradation by fungi than longitudinal stiffness, particularly due to the hemicellulose degradation. Longitudinal stiffness is more strongly related to cellulose, which was found to be more stable under biodegradation in these tests. The experiments even delivered enhanced insight into degradation strategies of the two different types of fungi. Particularly, anisotropy ratios of elastic stiffnesses derived from ultrasonic tests revealed the different effects of the brown rot and the white rot fungi on mechanical properties of pine sapwood. Since the mechanical properties reflect structural alterations, it could be concluded that the brown rot fungus *G. trabeum* more strongly affects earlywood than latewood, while the white rot fungus *T. versicolor* more strongly affects latewood than earlywood. This demonstrates the capability of micromechanical models to verify or falsify hypothesis on certain microstructural arrangements.

## Perspectives and future research studies

The developed poromicromechanical model will serve as the basis for further investigations of the hygro-mechanical behavior of wood. On the one hand, further comparisons of model predictions with mechanical properties from experiments on different and in the future even lower length scales of the hierarchical structure of softwood will further enhance the current understanding of microstructure-mechanics relationships. On the other hand, model extensions and adaptations can increase the applicability of the model to a broader range of sound wood species (e.g. hardwood), as well as to ancient wood or to on purpose modified wood (e.g. thermally modified wood).



A subsequent study, which has already been started, concerns stiffness properties of **hardwood** at different length-scales. Cell wall stiffness will be measured by means of nanoindentation. At this scale, cellulose content and orientation will be related to the indentation moduli. Together with mechanical properties measured at hardwood scale, influences of vessel contents and distribution, as well as ray cell contents, as typical features of hardwood, will be explored. In a similar manner as done for yew and spruce, their influence will also be studied by means of the poromicromechanical model. For this purpose, an additional homogenization step accounting for vessels and ray cells will be formulated using a continuum micromechanical approach.

Related to moisture dependent mechanical properties, the poromechanical multiscale model offers itself for further investigations of **moisture-stiffness relationships**, even at lower length scales. Recent nanoindentation tests under various climatic conditions (Yu et al., 2011) could be used for comparison with model predictions. Moreover, the currently employed simplified morphology of the cell wall ultrastructure could be refined by adapting the model. Particularly, glucomannan, which is associated with cellulose, and xylan, which is associated with lignin, could be considered as separate (hemicellulose) phases. Their spatial orientation in cellulose fiber direction was recently revealed by means of Fourier transform infrared (FTIR) microscopy (Stevanic and Salmén, 2009). Moreover, different hypotheses on the spatial distribution and orientation of water, or more precisely of sorption sites, within the cell wall could be tested. However, a problem often associated with such refinements is a lack of mechanical properties of the constituents, particularly under in-situ conditions. This will be one future challenge for experimental micro-characterization techniques.

Furthermore, the poromechanical approach forms the basis for subsequent studies of the **hygroexpansion** behavior of wood. In this case, additionally to the currently considered pressure that arises from mechanical loading, a swelling pressure arising from moisture adsorption or desorption needs to be taken into account. Having at hand the relationship between a swelling pressure in the water phase within the cell wall and the macroscopic stresses and strains, either eigenstresses in case of restrained boundary conditions, or free deformations in case of unrestrained boundary conditions at the level of softwood, can be predicted. It is expected that the layered assembly of the cell wall considerably affects the anisotropic hygroexpansion behavior of softwood, due to their distinctly different chemical composition and microfibril angles. This will require extension of the unit cell model, which is possible in a straightforward manner.

Finally, there is the broad field of **degraded, altered, or modified wood**, where microstructure-mechanics relationships are poorly understood or entirely missing. One ongoing study is dealing with ancient oak wood from a Viking ship (Oseberg ship, Museum of Cultural History, Oslo, Norway), which is about 1,200 years old. Particularly, the small size of specimens required for nanoindentation and the non-destructive nature of ultrasonic testing comprise advantages in material characterization of museum objects. In addition, the micromechanical modeling approach is expected to deliver more insight into effects of degradation and modification methods, even on smaller length scales.

The work presented in this thesis and the future work outlined before is clearly assigned to the field of basic research. Thus, application of the results gained herein to practical applications in timber engineering requires translation of the clear wood properties to mechanical properties of timber. For linking these length scales, it is necessary to include growth irregularities, such as knots [see e.g. Hackspiel (2010)]. Nevertheless, use of the poromicromechanical model predicted mechanical properties, e.g. as input parameters for Finite Element analysis of timber structures, allows to take into account differences in macroscopic mechanical properties based on the clear physical basis of different microstructural characteristics, such as different mass densities or variations in moisture content.

# The poroelastic role of water in cell walls of the hierarchical composite "softwood" (Bader et al., 2011a)

Authored by Thomas K. Bader, Karin Hofstetter, Christian Hellmich, and Josef Eberhardsteiner

Published in *Acta Mechanica*, 217:75–100, 2011

Wood is an anisotropic, hierarchically organized material, and the question how the hierarchical organization governs the anisotropy of its mechanical properties (such as stiffness and strength) has kept researchers busy for decades. While the honeycomb structure of softwood or the chemical composition of the cell wall have been fairly well established, the mechanical role of the cell wall water is less understood. The question arises how its capability to carry compressive loads (but not tensile loads) and its pressurization state affect mechanical deformations of the hierarchical composite "wood". By extending the framework of poro-micromechanics to more than two material phases, we here provide corresponding answers from a novel hierarchical set of matrix-inclusion problems with eigenstresses: (i) Biot tensors, expressing how much of the cell wall water-induced pore pressure is transferred to the boundary of an overall deformation-free representative volume element (RVE), and (ii) Biot moduli, expressing the porosity changes invoked by a pore pressure within such an RVE, are reported as functions of the material's composition, in particular of its water content and its lumen space. At the level of softwood, where we transform a periodic homogenization scheme into an equivalent matrix-inclusion problem, all Biot tensor components are found to increase with decreasing lumen volume fraction. A further research finding concerns the strong anisotropy of the Biot tensor with

respect to the water content: Transverse components increase with increasing water content, while the relationship "longitudinal Biot tensor component versus volume fraction of water within the wood cell wall" exhibits a maximum, representing a trade-off between pore pressure increase (increasing the longitudinal Biot tensor component, dominantly at low water content) and softening of the cell wall (reducing this component, dominantly at high water contents). Soft cell wall matrices reinforced with very stiff cellulose fibers may even result in negative longitudinal Biot tensor components. The aforementioned maximum effect is also noted for the Biot modulus.

### Nomenclature

$\mathbb{A}_r$	Concentration tensor of phase $r$
$\mathbf{a}_r$	Pore pressure-related influence tensor of phase $r$
<i>amocel</i>	Amorphous cellulose
$\mathbf{b}^{hom}$	Homogenized ('macroscopic') Biot tensor $r$
$\mathbf{b}_r$	Biot tensor of phase $r$
$\mathbb{C}^{hom}$	Homogenized ('macroscopic') stiffness tensor
$\mathbb{C}_r$	Stiffness tensor of phase $r$
$C_{r,ijkl}$	Components of the stiffness tensor of phase $r$
<i>cel</i>	Cellulose
<i>crycel</i>	Crystalline cellulose
<i>cwm</i>	Cell wall material
$\mathbf{E}$	Homogenized ('macroscopic') strain tensor
$\mathbf{E}^\infty$	Fictitious strain tensor at infinity
<i>ext</i>	Extractives
$\tilde{f}_r, \bar{f}_r, f_r, \hat{f}_r$	Volume fraction of phase $r$ in a representative volume element (RVE) of polymer network, cellulose, cell wall material, or softwood, respectively
$H_2O$	Water
<i>hemcel</i>	Hemicellulose
$k_r$	Bulk modulus of phase $r$
$\mathbf{1}$	Second-order unity tensor
$\mathbb{1}$	Fourth-order unity tensor
$\mathbb{J}$	Volumetric part of $\mathbb{1}$
$\mathbb{K}$	Deviatoric part of $\mathbb{1}$
$L$	Longitudinal direction
$l_R$	Mean radial lumen diameter of softwood unit cell
$l_T$	Mean tangential lumen diameter of softwood unit cell
$l_I, l_{II}, l_{III}$	Lengths of the cell wall axes
$l_{I,r}, l_{II,r}, l_{III,r}$	Free lengths of the cell walls
<i>lig</i>	Lignin
<i>lum</i>	Lumen
$N^{hom}$	Homogenized ('macroscopic') Biot modulus
$N_r$	Biot modulus of phase $r$
$p$	Pore pressure within cell wall
$\overset{\circ}{p}$	Eigenstress, eigenstrain (superscript)

**Nomenclature cont'd**

$polynet$	Polymer network
$\mathbb{P}_r^s$	Hill tensor of inclusion or phase $r$ embedded in a matrix material $s$
$R$	Radial direction
$\mathbb{S}_r^{Esh,s}$	Eshelby tensor of inclusion or phase $r$ embedded in a matrix material $s$
$SW$	Softwood
$T$	Tangential direction
$t$	Cell wall thickness
$V_{RVE}$	Volume of representative volume element (RVE)
$V_r$	Volume inside representative volume element (RVE), occupied by phase $r$
$\mathbf{x}$	Position vector inside a representative volume element
$\alpha$	Inclination angle of the radial cell walls
$\delta_{ij}$	Kronecker delta
$\boldsymbol{\varepsilon}_r$	Average ('microscopic') strain tensor of phase $r$
$\phi$	Lagrangian porosity, i.e. volume of pores over volume of RVE of porous material in the (undeformed) reference condition
$\phi_0$	Initial porosity
$\theta, \varphi$	Latitudinal and longitudinal angles (spherical coordinates)
$\bar{\theta}$	Microfibril angle
$\lambda$	Cross-sectional aspect ratio of softwood unit cell
$\mu_r$	Shear modulus of phase $r$
$\boldsymbol{\xi}$	Microscopic displacement vector
$\boldsymbol{\Sigma}$	Homogenized ('macroscopic') stress tensor
$\boldsymbol{\sigma}_r$	Average ('microscopic') stress tensor of phase $r$
$\langle(\cdot)\rangle$	Volume average of quantity $(\cdot)$
$\langle(\cdot)\rangle_{V_r}$	Volume average over phase $r$ , of quantity $(\cdot)$
$\cdot$	First-order tensor contraction (inner product)
$:$	Second-order tensor contraction

**1.1 Introduction**

Wood is an anisotropic, hierarchically organized material, and the question how the hierarchical organization governs the anisotropy of its mechanical properties (such as stiffness and strength) has kept researchers busy for decades. In this context, emphasis has been laid on the fact that the periodic honeycomb microstructure seen at an observation scale of hundreds of microns strongly influences the overall mechanical properties (Gillis, 1972; Easterling et al., 1982; Kahle et al., 1994; Gibson and Ashby, 1997; Holmberg et al., 1999). However, when building mathematical models for related honeycombs, key input parameters concern the mechanical properties of the cell wall material building up these honeycombs. These quantities, however, are again anisotropic and tissue-specific – being governed by other microstructures at yet lower scales. This was the motivation to further resolve the micro- and nanostructures of wood, considering the mechanical interaction of the material's elementary constituents: crystalline and amorphous cellulose, hemicellulose, lignin, and water. Given the more random nature of these components' distribution, homogenization based on Eshelby-Laws-type matrix-inclusion problems (Eshelby, 1957;

Laws, 1977), which is also referred to as mean-field homogenization (Pedersen, 1983; Friebel et al., 2006) or continuum micromechanics (Hill, 1963; Suquet, 1997; Zaoui, 2002), has turned out as very suitable tool for predicting wood's mechanical properties from its microstructure and composition. This prediction was based on 'universal' mechanical properties of cellulose, hemicellulose, lignin, and water (Hofstetter et al., 2005, 2006, 2007, 2008). In all these approaches, the latter component was considered as incompressible solid (with finite bulk and zero shear modulus), which quite often constitutes a reasonable approximation (Hellmich and Ulm, 2005).

This approximation, however, cannot account for two main characteristics of the component "water":

- (i) as compared to the compression regime, its capability to carry tensile loads is minimal,
- (ii) it may enter or leave the pore spaces of wood at an arbitrary pressure.

This calls for a careful extension and re-formulation of multiscale homogenization techniques for wood in the framework of poro-micromechanics (Dormieux and Ulm, 2004; Dormieux et al., 2006). The corresponding first step concerns the realm of poroelasticity, i.e. the study of elastic deformations induced by pore pressure exerted through the cell wall water onto all the solid microstructures building up softwood across different hierarchical levels. This is, in short, the focus of the present paper. It is organized as follows: A short review of fundamentals of continuum micromechanics [such as the representative volume element (RVE)] and our vision of a multiscale micromechanical representation of wood, encompassing four RVEs at different observation scales, will be given in Section 1.2. Subsequently, techniques for upscaling poroelastic properties over the aforementioned RVEs will be given in Sections 1.3 to 1.6. The resulting (micro)structure – (poroelastic) property relationships are discussed in Section 1.7, before the paper is concluded in Section 1.8.

## 1.2 Fundamentals of homogenization theory – representative volume element – micromechanical representation of wood

### 1.2.1 Homogenization theory for materials with random microstructures – continuum micromechanics

In continuum micromechanics (Hill, 1963; Suquet, 1997; Zaoui, 2002), a material is understood as a macro-homogeneous, but micro-heterogeneous body filling a representative volume element (RVE) with characteristic length  $\ell$ ,  $\ell \gg d$ ,  $d$  standing for the characteristic length of inhomogeneities within the RVE (see Figure 1.1), and  $\ell \ll \mathcal{L}$ ,  $\mathcal{L}$  standing for the characteristic lengths of geometry or loading of a structure built up by the material defined on the RVE. In general, the microstructure within one RVE is so complicated

that it cannot be described in complete detail. Therefore, quasi-homogeneous subdomains with known physical quantities (such as volume fractions, elastic properties, and eigenstresses) are reasonably chosen. They are called material phases. The 'homogenized' mechanical behavior of the overall material, i.e., the relation between homogeneous deformations acting on the boundary of the RVE and resulting (average) stresses, or the relation between an internal pore pressure and stresses acting on the boundary of the RVE, can then be estimated from the mechanical behavior of the aforementioned homogeneous phases (representing the inhomogeneities within the RVE), their dosages within the RVE, their characteristic shapes, and their interactions. The homogenized material behavior can be derived either from a set of Finite Element models directly reflecting the randomness within the material (Ostoja-Starzewski, 2006; Kaminski, 2005; Kanit et al., 2003), or from suitably chosen Eshelby-Laws-type matrix-inclusion problems (Dormieux et al., 2006). Throughout this paper, we adopt the second choice, motivated by successful experimental validation of our previous multiscale models for wood elasticity (Hofstetter et al., 2005, 2006, 2007). If a single phase exhibits a heterogeneous microstructure itself, its mechanical behavior can be estimated by introduction of an RVE within the phase, with dimensions  $\ell_2 \leq d$ , comprising again smaller phases with characteristic length  $d_2 \ll \ell_2$ , and so on, leading to a multistep homogenization scheme (see Figure 1.1).

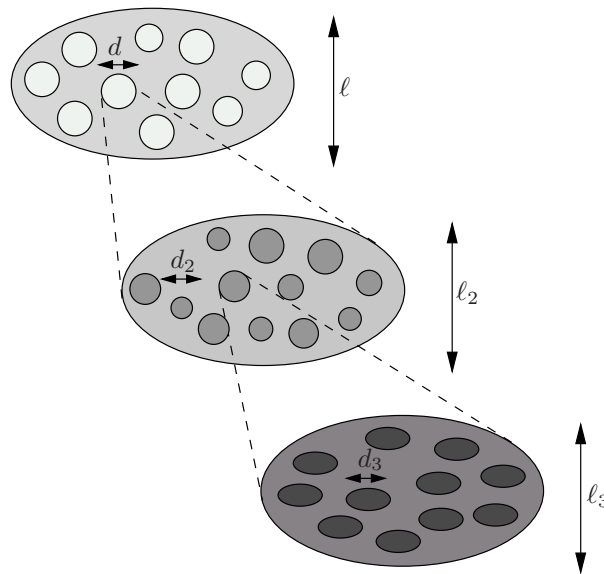


**Figure 1.1:** Multistep homogenization: properties of phases (with characteristic lengths of  $d$ ,  $d_2$ , and  $d_3$ , respectively) inside RVEs with characteristic lengths of  $l$ ,  $l_2$ , or  $l_3$ , respectively, are determined from homogenization over smaller RVEs with characteristic lengths of  $l_2 \leq d$  and  $l_3 \leq d_2$ , respectively.

## 1.2.2 Hierarchy of wood – multiscale homogenization

As regards wood, we employ a multistep homogenization scheme encompassing four RVEs at different observation scales (see Figure 1.2):

- (i) an RVE of polymer network consisting of hemicellulose, water, and lignin;
- (ii) an RVE of cellulose consisting of crystalline cellulose fibrils surrounded by amorphous cellulose;
- (iii) an RVE of cell wall material consisting of cellulose fibers embedded into the aforementioned polymer matrix; and
- (iv) an RVE of softwood as porous honeycomb made of cell wall material, where the pores are referred to as "lumens".

The last homogenization step, however, comprises elements of the periodic homogenization theory, described next.

## 1.2.3 Homogenization theory for materials with periodic microstructures - unit cell method

The unit cell method (Suquet, 1987; Michel et al., 1999; Böhm, 2004) proposes to approximate the real (micro-)heterogeneous material through a periodic (repetitive) microstructure, by means of defining a basic repetitive unit (the 'unit cell'), such that the spatial variations of a physical quantity can be represented as a combination of local fluctuations at the level of the elementary (unit) cell and a drift at the level of the macroscopic structure (Dormieux et al., 2006). Subjecting the unit cell to periodic deformations at its boundaries (whose average is equal to the macroscopic strain) allows for determination of the resulting inhomogeneous microstress and microstrain fields in the microstructure. Depending on the complexity of the microstructure, these fields are determined either analytically (Cecchi and Sab, 2002; Hofstetter et al., 2007) or numerically, e.g. by means of the Finite Element method (Böhm et al., 2004; Kaminski, 2005). The homogenized mechanical behavior is estimated from evaluating the average value of the periodic microstress field in the unit cell in relation to the macroscopic strains acting on the boundary of the unit cell.

## 1.3 Poro-microelasticity of polymer network

### 1.3.1 RVE, stress and strain averages

Within an RVE of *polymer network* with 20 nm characteristic length, we distinguish the material phases "lignin", "hemicellulose", and "nanoporous space filled with water and solvated extractives" [see step I(a) in Figure 1.2]. These phases occupy the volume



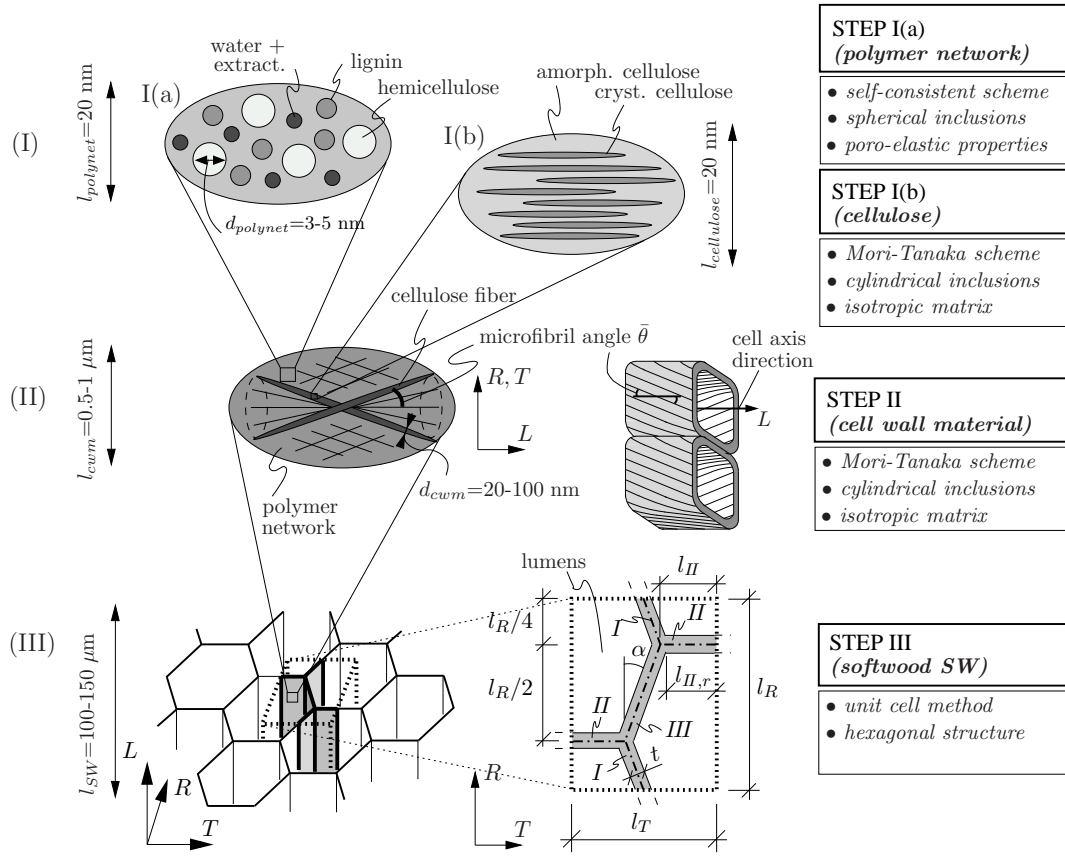


**Figure 1.2:** Four-step homogenization scheme on three hierarchical levels, with base frame for definition of stiffness tensors:  $L$  (longitudinal) marks direction parallel to grain, and all directions in the plane spanned by  $R$  (radial) and  $T$  (tangential) are perpendicular to the grain.

fractions  $\tilde{f}_{lig}$ ,  $\tilde{f}_{hemcel}$ , and  $\tilde{f}_{H_2Oext} = 1 - \tilde{f}_{lig} - \tilde{f}_{hemcel}$ . Subscript  $H_2Oext$  indicates that wood extractives (Fengel and Wegener, 1984) are considered to be solved in water. Homogeneous strains  $\mathbf{E}_{polynet}$  are imposed at the boundary of the RVE  $V_{polynet}$  in terms of displacements  $\boldsymbol{\xi}$  on  $\partial V_{polynet}$  (Hashin and Rosen, 1964):

$$\boldsymbol{\xi}(\mathbf{x}) = \mathbf{E}_{polynet} \cdot \mathbf{x}, \quad (1.1)$$

with  $\mathbf{x}$  as the position vector inside the RVE. Consequently (Hashin and Rosen, 1964; Zaoui, 2002), the spatial average of kinematically admissible (micro-)strains  $\boldsymbol{\varepsilon}(\mathbf{x})$  within the RVE is identical to the homogeneous strains  $\mathbf{E}_{polynet}$ ,

$$\begin{aligned} \mathbf{E}_{polynet} &= \langle \boldsymbol{\varepsilon} \rangle_{V_{polynet}} \\ &= \tilde{f}_{lig} \langle \boldsymbol{\varepsilon} \rangle_{V_{lig}} + \tilde{f}_{hemcel} \langle \boldsymbol{\varepsilon} \rangle_{V_{hemcel}} + \tilde{f}_{H_2Oext} \langle \boldsymbol{\varepsilon} \rangle_{V_{H_2Oext}}, \end{aligned} \quad (1.2)$$

**Table 1.1:** 'Universal' (tissue-independent) phase properties

Phase	Material behavior	Bulk modulus $k$ [GPa]	Shear modulus $\mu$ [GPa]	Experimental sources
Amorphous cellulose	Isotropic	$k_{amocel} = 5.56$	$\mu_{amocel} = 1.85$	Eichhorn and Young (2001)
Hemicellulose	Isotropic	$k_{hemcel} = 8.89$	$\mu_{hemcel} = 2.20$	Cousins (1978)
Lignin	Isotropic	$k_{lig} = 5.00$	$\mu_{lig} = 2.20$	Cousins (1976)
Water + extractives	Isotropic	$k_{H_2Oext} = 2.30$	$\mu_{H_2Oext} = 0$	
Stiffness tensor components $c_{ijkl}$ [GPa]				
Crystalline cellulose	Transversely Isotropic	$c_{crycel,1111} = 34.86$	$c_{crycel,1122} = 0$	Tashiro and Kobayashi (1991)
		$c_{crycel,3333} = 167.79$	$c_{crycel,2233} = 0$	
		$c_{crycel,1313} = 5.81$		

with  $\langle(\cdot)\rangle_V$  denoting the spatial average of quantity  $(\cdot)$  over the volume  $V$

$$\langle(\cdot)\rangle_V = \frac{1}{V} \int_V (\cdot)(\mathbf{x}) dV \quad (1.3)$$

and  $V_{lig}$ ,  $V_{hemcel}$ ,  $V_{H_2Oext}$  being the subvolumes of the phases inside the RVE with volume

$$V_{polymet} = V_{lig} + V_{hemcel} + V_{H_2Oext}. \quad (1.4)$$

Consistently, the homogeneous stresses  $\Sigma_{polymet}$  are equal to the spatial average of equilibrated (micro-) stresses  $\boldsymbol{\sigma}(\mathbf{x})$  within the RVE (Hashin and Rosen, 1964)

$$\begin{aligned} \Sigma_{polymet} &= \langle \boldsymbol{\sigma} \rangle_{V_{polymet}} \\ &= \tilde{f}_{lig} \langle \boldsymbol{\sigma} \rangle_{V_{lig}} + \tilde{f}_{hemcel} \langle \boldsymbol{\sigma} \rangle_{V_{hemcel}} + \tilde{f}_{H_2Oext} \langle \boldsymbol{\sigma} \rangle_{V_{H_2Oext}}. \end{aligned} \quad (1.5)$$

### 1.3.2 Constitutive behavior of the material phases

Hemicellulose behaves linear elastically and isotropically

$$\forall \mathbf{x} \in V_{hemcel} : \boldsymbol{\sigma}(\mathbf{x}) = \mathfrak{C}_{hemcel} : \boldsymbol{\varepsilon}(\mathbf{x}), \quad \mathfrak{C}_{hemcel} = 3k_{hemcel}\mathbb{J} + 2\mu_{hemcel}\mathbb{K}, \quad (1.6)$$

with  $k_{hemcel}$  and  $\mu_{hemcel}$  as the bulk modulus and the shear modulus of hemicellulose (which are experimentally accessible through indentation tests of Cousins (1978), see Tab. 1.1 and Hofstetter et al. (2005) for further details); with  $\mathbb{J} = \frac{1}{3}\mathbf{1} \otimes \mathbf{1}$  and  $\mathbb{K} = \mathbb{I} - \mathbb{J}$  as the volumetric and the deviatoric part of the fourth-order unity tensor  $\mathbb{I}$  with components  $I_{ijkl} = 1/2(\delta_{ik}\delta_{jl} + \delta_{il}\delta_{kj})$ ; the second order unity tensor  $\mathbf{1}$  has components  $\delta_{ij}$ , with Kronecker delta  $\delta_{ij}$  being 1 for  $i = j$  and 0 otherwise.

Lignin behaves linear elastically and isotropically

$$\forall \mathbf{x} \in V_{lig} : \boldsymbol{\sigma}(\mathbf{x}) = \mathbb{c}_{lig} : \boldsymbol{\varepsilon}(\mathbf{x}), \quad \mathbb{c}_{lig} = 3k_{lig}\mathbb{J} + 2\mu_{lig}\mathbb{K}, \quad (1.7)$$

whereby the bulk and shear moduli,  $k_{lig}$  and  $\mu_{lig}$ , are experimentally accessible through tension, torsion, and indentation tests of Cousins et al. (1975) and Cousins (1976), see Tab. 1.1 and Hofstetter et al. (2005) for further details.

The nanoporous space is characterized by a water-exerted uniform pressure  $p$ ,

$$\forall \mathbf{x} \in V_{H_2O_{ext}} : \boldsymbol{\sigma}(\mathbf{x}) = -p \mathbf{1}. \quad (1.8)$$

### 1.3.3 Homogenized poroelasticity of polymer network

Linear elastic behavior of the solid material phases "hemicellulose" and "lignin" implies that the homogenized material behavior of the polymer network takes the multi-linear form (Dormieux et al., 2006)

$$\boldsymbol{\Sigma}_{polynet} = \mathbb{C}_{polynet}^{hom} : \mathbf{E}_{polynet} - \mathbf{b}_{polynet}^{hom} p, \quad (1.9)$$

with the drained elasticity tensor of the polymer network,  $\mathbb{C}_{polynet}^{hom}$ , and the polymer network-related Biot tensor  $\mathbf{b}_{polynet}^{hom}$ . For the same reason, also the change of the nanoporous space (with Lagrangian porosity  $\phi = \tilde{f}_{H_2O_{ext}}$ ) follows a bilinear form, namely

$$(\phi - \phi_0)_{polynet} = \mathbf{b}_{polynet}^{hom} : \mathbf{E}_{polynet} + \frac{p}{N_{polynet}^{hom}}, \quad (1.10)$$

where the repeated occurrence of  $\mathbf{b}_{polynet}^{hom}$  in (1.9) and (1.10) follows from the thermodynamic requirement of  $(\partial \boldsymbol{\Sigma}_{polynet} / \partial p) = (-\partial \phi / \partial \mathbf{E}_{polynet})$  [see e.g. Coussy (2004), page 72], and  $N_{polynet}$  is the so-called Biot modulus related to the solid material phases. While Biot tensor  $\mathbf{b}_{polynet}^{hom}$  expresses how much of the cell wall water-induced pore pressure is transferred to the boundary of an overall deformation-free representative volume element (RVE), Biot modulus  $N_{polynet}^{hom}$  expresses the porosity changes invoked by the aforementioned pore pressure within such an RVE; and to our knowledge, the derivation of these central poroelastic quantities for the material "softwood" constitutes an original contribution. In order to estimate the homogenized properties  $\mathbb{C}_{polynet}^{hom}$ ,  $\mathbf{b}_{polynet}^{hom}$ , and  $N_{polynet}^{hom}$ , we recall the disordered arrangement of all mentioned phases, and consider, accordingly, a self-consistent homogenization scheme based on the following three matrix-inclusion problems involving eigenstresses:

- a spherical inclusion of hemicellulose (with stiffness  $\mathbb{c}_{hemcel}$ ) is embedded into an infinite matrix of the homogenized material with elasticity  $\mathbb{C}_{polynet}^{hom}$  and eigenstresses  $\boldsymbol{\Sigma}_{polynet}^p = -\mathbf{b}_{polynet}^{hom} p$ , subjected at infinity to fictitious strains  $\mathbf{E}^\infty$ . The corresponding (homogeneous) strains in the hemicellulose inclusion follow to be (Zaoui, 2002)

$$\begin{aligned} \boldsymbol{\varepsilon}_{hemcel} &= \left[ \mathbb{I} + \mathbb{P}_{sph}^{polynet} : (\mathbb{c}_{hemcel} - \mathbb{C}_{polynet}^{hom}) \right]^{-1} : \\ &\left[ \mathbf{E}^\infty - \mathbb{P}_{sph}^{polynet} : \mathbf{b}_{polynet}^{hom} p \right]. \end{aligned} \quad (1.11)$$

In (1.11),  $\mathbb{P}_{sph}^{polynet}$  is the Hill tensor accounting for the spherical shape of the inclusion embedded in a material with stiffness  $\mathbb{C}_{polynet}^{hom}$ , see the Appendix 1.9.1 for its components.

- a spherical inclusion of lignin (with stiffness  $\mathbb{C}_{lig}$ ) is embedded into an infinite matrix of the homogenized material with elasticity  $\mathbb{C}_{polynet}^{hom}$  and eigenstresses  $\Sigma_{polynet}^p = -\mathbf{b}_{polynet}^{hom} p$ , subjected at infinity to fictitious strains  $\mathbf{E}^\infty$ . The corresponding (homogeneous) strains in the lignin inclusion follow to be (Zaoui, 2002)

$$\begin{aligned} \boldsymbol{\varepsilon}_{lig} &= \left[ \mathbb{I} + \mathbb{P}_{sph}^{polynet} : (\mathbb{C}_{lig} - \mathbb{C}_{polynet}^{hom}) \right]^{-1} : \\ &\left[ \mathbf{E}^\infty - \mathbb{P}_{sph}^{polynet} : \mathbf{b}_{polynet}^{hom} p \right]. \end{aligned} \quad (1.12)$$

- a spherical nanoporous inclusion (without any stiffness, but with prestress  $\boldsymbol{\sigma}_{H_2Oext}^p = -\mathbf{1} p$ ) is embedded into an infinite matrix of the homogenized material with elasticity  $\mathbb{C}_{polynet}^{hom}$  and eigenstresses  $\Sigma_{polynet}^p = -\mathbf{b}_{polynet}^{hom} p$ , subjected at infinity to fictitious strains  $\mathbf{E}^\infty$ . The corresponding (homogeneous) strains in the nanoporous inclusion follow to be (Zaoui, 2002)

$$\begin{aligned} \boldsymbol{\varepsilon}_{H_2Oext} &= \left[ \mathbb{I} - \mathbb{P}_{sph}^{polynet} : \mathbb{C}_{polynet}^{hom} \right]^{-1} : \\ &\left[ \mathbf{E}^\infty + \mathbb{P}_{sph}^{polynet} : (\mathbf{1} p - \mathbf{b}_{polynet}^{hom} p) \right]. \end{aligned} \quad (1.13)$$

The homogeneous strains in the inclusions, (1.11) – (1.13), are used to approximate the phase averages in Eq. (1.2). Correspondingly, substitution in Eq. (1.2), of  $\langle \boldsymbol{\varepsilon} \rangle_{V_{hemcel}}$ ,  $\langle \boldsymbol{\varepsilon} \rangle_{V_{lig}}$ , and  $\langle \boldsymbol{\varepsilon} \rangle_{V_{H_2Oext}}$ , by  $\boldsymbol{\varepsilon}_{hemcel}$ ,  $\boldsymbol{\varepsilon}_{lig}$ , and  $\boldsymbol{\varepsilon}_{H_2Oext}$  according to (1.11) – (1.13), results in a relation between the RVE-related strains  $\mathbf{E}_{polynet}$  and the fictitious strains  $\mathbf{E}^\infty$ . Use of this relation in (1.11) to (1.13) yields so-called concentration and influence relations (Dvorak and Benveniste, 1992; Fritsch et al., 2009) between the independent "loading variables"  $\mathbf{E}_{polynet}$  and  $p$ , and the strains in the three material phases:

$$\boldsymbol{\varepsilon}_{hemcel} = \mathbb{A}_{hemcel}^{polynet} : \mathbf{E}_{polynet} + \mathbf{a}_{hemcel}^{polynet} p, \quad (1.14)$$

$$\boldsymbol{\varepsilon}_{lig} = \mathbb{A}_{lig}^{polynet} : \mathbf{E}_{polynet} + \mathbf{a}_{lig}^{polynet} p, \quad (1.15)$$

$$\boldsymbol{\varepsilon}_{H_2Oext} = \mathbb{A}_{H_2Oext}^{polynet} : \mathbf{E}_{polynet} + \mathbf{a}_{H_2Oext}^{polynet} p, \quad (1.16)$$

with the concentration tensors reading as

$$\begin{aligned}
\mathbb{A}_{hemcel}^{polynet} &= \left[ \mathbb{I} + \mathbb{P}_{sph}^{polynet} : (\mathbb{C}_{hemcel} - \mathbb{C}_{polynet}^{hom}) \right]^{-1} \\
&: \left\{ \tilde{f}_{hemcel} \left[ \mathbb{I} + \mathbb{P}_{sph}^{polynet} : (\mathbb{C}_{hemcel} - \mathbb{C}_{polynet}^{hom}) \right]^{-1} \right. \\
&\quad + \tilde{f}_{lig} \left[ \mathbb{I} + \mathbb{P}_{sph}^{polynet} : (\mathbb{C}_{lig} - \mathbb{C}_{polynet}^{hom}) \right]^{-1} \\
&\quad \left. + \tilde{f}_{H_2OExt} \left[ \mathbb{I} - \mathbb{P}_{sph}^{polynet} : \mathbb{C}_{polynet}^{hom} \right]^{-1} \right\}^{-1}, \tag{1.17}
\end{aligned}$$

$$\begin{aligned}
\mathbb{A}_{lig}^{polynet} &= \left[ \mathbb{I} + \mathbb{P}_{sph}^{polynet} : (\mathbb{C}_{lig} - \mathbb{C}_{polynet}^{hom}) \right]^{-1} \\
&: \left\{ \tilde{f}_{hemcel} \left[ \mathbb{I} + \mathbb{P}_{sph}^{polynet} : (\mathbb{C}_{hemcel} - \mathbb{C}_{polynet}^{hom}) \right]^{-1} \right. \\
&\quad + \tilde{f}_{lig} \left[ \mathbb{I} + \mathbb{P}_{sph}^{polynet} : (\mathbb{C}_{lig} - \mathbb{C}_{polynet}^{hom}) \right]^{-1} \\
&\quad \left. + \tilde{f}_{H_2OExt} \left[ \mathbb{I} - \mathbb{P}_{sph}^{polynet} : \mathbb{C}_{polynet}^{hom} \right]^{-1} \right\}^{-1}, \tag{1.18}
\end{aligned}$$

$$\begin{aligned}
\mathbb{A}_{H_2Oext}^{polynet} &= \left[ \mathbb{I} - \mathbb{P}_{sph}^{polynet} : \mathbb{C}_{polynet}^{hom} \right]^{-1} \\
&: \left\{ \tilde{f}_{hemcel} \left[ \mathbb{I} + \mathbb{P}_{sph}^{polynet} : (\mathbb{C}_{hemcel} - \mathbb{C}_{polynet}^{hom}) \right]^{-1} \right. \\
&\quad + \tilde{f}_{lig} \left[ \mathbb{I} + \mathbb{P}_{sph}^{polynet} : (\mathbb{C}_{lig} - \mathbb{C}_{polynet}^{hom}) \right]^{-1} \\
&\quad \left. + \tilde{f}_{H_2OExt} \left[ \mathbb{I} - \mathbb{P}_{sph}^{polynet} : \mathbb{C}_{polynet}^{hom} \right]^{-1} \right\}^{-1}, \tag{1.19}
\end{aligned}$$

and the influence tensors reading as

$$\mathbf{a}_{hemcel}^{polynet} = -\tilde{f}_{H_2Oext} \mathbb{A}_{hemcel}^{polynet} : \left[ \mathbb{I} - \mathbb{P}_{sph}^{polynet} : \mathbb{C}_{polynet}^{hom} \right]^{-1} : \mathbb{P}_{sph}^{polynet} : \mathbf{1}, \tag{1.20}$$

$$\mathbf{a}_{lig}^{polynet} = -\tilde{f}_{H_2Oext} \mathbb{A}_{lig}^{polynet} : \left[ \mathbb{I} - \mathbb{P}_{sph}^{polynet} : \mathbb{C}_{polynet}^{hom} \right]^{-1} : \mathbb{P}_{sph}^{polynet} : \mathbf{1}, \tag{1.21}$$

$$\mathbf{a}_{H_2Oext}^{polynet} = \left[ \mathbb{I} - \tilde{f}_{H_2Oext} \mathbb{A}_{H_2Oext}^{polynet} \right] : \left[ \mathbb{I} - \mathbb{P}_{sph}^{polynet} : \mathbb{C}_{polynet}^{hom} \right]^{-1} : \mathbb{P}_{sph}^{polynet} : \mathbf{1}. \tag{1.22}$$

Interestingly, none of these tensors depends on the matrix prestress  $\Sigma_{polynet}^p$ , which is due to the identical shape of all material phases. Use of concentration/influence relations (1.17), (1.18), and (1.19) in phase elasticity laws (1.6), (1.7), and (1.8), and insertion of the corresponding results into the stress average rule (1.5), yields a relation which allows

for identification of the drained stiffness  $\mathbb{C}_{polynet}^{hom}$  and of the Biot tensor  $\mathbf{b}_{polynet}^{hom}$ ,

$$\mathbb{C}_{polynet}^{hom} = \tilde{f}_{hemcel} \mathbb{C}_{hemcel} : \mathbb{A}_{hemcel}^{polynet} + \tilde{f}_{lig} \mathbb{C}_{lig} : \mathbb{A}_{lig}^{polynet}, \quad (1.23)$$

$$\mathbf{b}_{polynet}^{hom} = -\tilde{f}_{hemcel} \mathbb{C}_{hemcel} : \mathbf{a}_{hemcel}^{polynet} - \tilde{f}_{lig} \mathbb{C}_{lig} : \mathbf{a}_{lig}^{polynet} + \tilde{f}_{H_2Oext} \mathbf{1}, \quad (1.24)$$

where  $\mathbb{A}_{hemcel}^{polynet}$  and  $\mathbb{A}_{lig}^{polynet}$  still follow (1.17) and (1.18), and where  $\mathbf{a}_{hemcel}^{polynet}$  and  $\mathbf{a}_{lig}^{polynet}$  still follow (1.20) and (1.21). Finally, recalling that

$$(\phi - \phi_0)_{polynet} = \tilde{f}_{H_2Oext} \mathbf{1} : \boldsymbol{\varepsilon}_{H_2Oext}, \quad (1.25)$$

together with use of (1.16), allows for identification of the Biot tensor  $\mathbf{b}_{polynet}^{hom}$  and of the solid Biot modulus  $N_{polynet}^{hom}$ ,

$$\mathbf{b}_{polynet}^{hom} = \tilde{f}_{H_2Oext} \mathbf{1} : \mathbb{A}_{H_2Oext}^{polynet}, \quad (1.26)$$

$$\frac{1}{N_{polynet}^{hom}} = \tilde{f}_{H_2Oext} \mathbf{1} : \mathbf{a}_{H_2Oext}^{polynet}, \quad (1.27)$$

where  $\mathbb{A}_{H_2Oext}^{polynet}$  still follows (1.19), and where  $\mathbf{a}_{H_2Oext}^{polynet}$  still follows (1.22). As expected, the right-hand expressions of (1.24) and (1.26) are identical.

## 1.4 Microelasticity of cellulose

Experiments (Fengel and Wegener, 1984; O’Sullivan, 1997; Salmén and Burgert, 2009) suggest crystalline cellulose fibrils to be surrounded by amorphous cellulose. Accordingly, an RVE of cellulose consists of an amorphous cellulose matrix in which parallel crystalline cellulose fibrils are embedded (see step I(b) in Figure 1.2). Such an RVE of cellulose exhibits 20 nm characteristic length and encompasses material phases ”crystalline cellulose” (with volume fraction  $\bar{f}_{crycel}$  and stiffness  $\mathbb{C}_{crycel}$ ) and ”amorphous cellulose” (with volume fraction  $\bar{f}_{amocel} = 1 - \bar{f}_{crycel}$  and stiffness  $\mathbb{C}_{amocel}$ ). The stiffness of crystalline cellulose is accessible from lattice-dynamical computations of Tashiro and Kobayashi (1991), and given the similarities of the molecular structures of glassy polymers and amorphous cellulose (Eichhorn and Young, 2001), the stiffness of the latter can be approximated by that of the former, as given in Young and Lovell (1991), see Tab. 1.1 and Hofstetter et al. (2005) for further details. As was the case for the polymer network, linear elastic behavior in the small strain regime implies the average phase strains  $\boldsymbol{\varepsilon}_{amocel}$  and  $\boldsymbol{\varepsilon}_{crycel}$  to be linearly related to homogeneous strains  $\mathbf{E}_{cel}$  applied at the boundary of the RVE (Hill, 1963),

$$\boldsymbol{\varepsilon}_{amocel} = \mathbb{A}_{amocel}^{cel} : \mathbf{E}_{cel}, \quad (1.28)$$

$$\boldsymbol{\varepsilon}_{crycel} = \mathbb{A}_{crycel}^{cel} : \mathbf{E}_{cel}, \quad (1.29)$$

with the concentration tensors  $\mathbb{A}_{amocel}^{cel}$  and  $\mathbb{A}_{crycel}^{cel}$ . The corresponding elastic behavior is suitably represented by a Mori-Tanaka homogenization scheme (Mori and Tanaka, 1973;

Benveniste, 1987), which is characterized by the concentration tensors in (1.28) and (1.29) reading as

$$\mathbb{A}_{amocel}^{cel} = \left\{ \bar{f}_{amocel} \mathbb{I} + \bar{f}_{crycel} \left[ \mathbb{I} + \mathbb{P}_{cyl}^{amocel} : (\mathbb{C}_{crycel} - \mathbb{C}_{amocel}) \right]^{-1} \right\}^{-1}, \quad (1.30)$$

$$\begin{aligned} \mathbb{A}_{crycel}^{cel} &= \left[ \mathbb{I} + \mathbb{P}_{cyl}^{amocel} : (\mathbb{C}_{crycel} - \mathbb{C}_{amocel}) \right]^{-1} \\ &: \left\{ \bar{f}_{amocel} \mathbb{I} + \bar{f}_{crycel} \left[ \mathbb{I} + \mathbb{P}_{cyl}^{amocel} : (\mathbb{C}_{crycel} - \mathbb{C}_{amocel}) \right]^{-1} \right\}^{-1}, \end{aligned} \quad (1.31)$$

where  $\mathbb{P}_{cyl}^{amocel}$  is the Hill tensor accounting for the cylindrical shape of a crystalline cellulose inclusion embedded in an infinite matrix of amorphous cellulose with stiffness  $\mathbb{C}_{amocel}$ , see the Appendix 1.9.2 for its components. Finally, the homogenized stiffness of cellulose reads as

$$\mathbb{C}_{cel}^{hom} = \bar{f}_{amocel} \mathbb{C}_{amocel} : \mathbb{A}_{amocel}^{cel} + \bar{f}_{crycel} \mathbb{C}_{crycel} : \mathbb{A}_{crycel}^{cel}, \quad (1.32)$$

where  $\mathbb{A}_{amocel}^{cel}$  and  $\mathbb{A}_{crycel}^{cel}$  still follow (1.30) and (1.31).

## 1.5 Poro-microelasticity of cell wall material

### 1.5.1 RVE, stress and strain averages

Microscopic observations (Kollmann and Côté, 1968; Fengel and Wegener, 1984) suggest the cell wall material to be a composite where the hemicellulose-lignin-water network of homogenization step I(a) of Figure 1.2 (Section 1.3) is reinforced by strong fibers with 20-100 nm diameter, which are made of cellulose (following homogenization step I(b) of Figure 1.2, Section 1.4). A corresponding RVE of cell wall material exhibits 0.5 to 1  $\mu\text{m}$  characteristic length, and comprises the material phases "cellulose" [with volume fraction  $f_{cel}$  and stiffness  $\mathbb{C}_{cel} = \mathbb{C}_{cel}^{hom}$ , see Section 1.4] and "polymer network" [with volume fraction  $f_{polynet} = 1 - f_{cel}$ ; and with poroelastic behavior (1.9) and (1.10), characterized by drained stiffness  $\mathbb{C}_{polynet} = \mathbb{C}_{polynet}^{hom}$ , by Biot tensor  $\mathbf{b}_{polynet} = \mathbf{b}_{polynet}^{hom}$ , and by solid Biot modulus  $N_{polynet} = N_{polynet}^{hom}$ , see Section 1.3.3]. However, since the cellulose fibers are helically wound, the cellulose phase needs to be divided into an infinite amount of subphases, which are all characterized by the same latitudinal deviation angle  $\bar{\theta}$  [which is identical to the so-called average microfibril angle (see Figs. 1.2 and 1.3)], but by different longitudinal angles  $\varphi$  (see Figure 1.3), so that the analogue to strain average (1.2) now reads as

$$\mathbf{E}_{cwm} = f_{polynet} \langle \boldsymbol{\varepsilon} \rangle_{V_{polynet}} + f_{cel} \frac{1}{2\pi} \int_{\varphi=0}^{2\pi} \langle \boldsymbol{\varepsilon} \rangle_{V_{cel, \varphi \bar{\theta}}}(\varphi, \bar{\theta}) d\varphi, \quad (1.33)$$

where the volume of the cell wall material consists of cellulose and polymer network volumes,

$$V_{cwm} = V_{cel} + V_{polynet}, \quad (1.34)$$

and where  $\langle \boldsymbol{\varepsilon} \rangle_{V_{cel, \varphi \bar{\theta}}}$  are the average strains in cellulose fibers oriented in direction  $(\varphi, \bar{\theta})$ . Consistently, the stresses at the level of the cell wall material  $\boldsymbol{\Sigma}_{cwm}$ , being homogeneous with respect to  $RVE_{cwm}$ , follow to be

$$\boldsymbol{\Sigma}_{cwm} = f_{polymer} \langle \boldsymbol{\sigma} \rangle_{V_{polymer}} + f_{cel} \frac{1}{2\pi} \int_{\varphi=0}^{2\pi} \langle \boldsymbol{\sigma} \rangle_{V_{cel, \varphi \bar{\theta}}}(\varphi, \bar{\theta}) d\varphi, \quad (1.35)$$

where  $\langle \boldsymbol{\sigma} \rangle_{V_{cel, \varphi \bar{\theta}}}$  are the average (micro-)stresses in cellulose fibers oriented in direction  $(\varphi, \bar{\theta})$ , see Figs. 1.2 and 1.3.

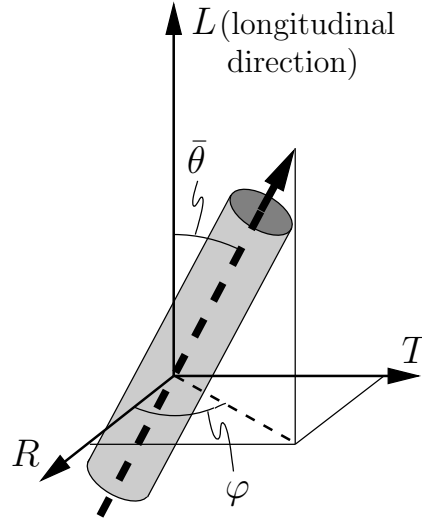


**Figure 1.3:** Orientation of a microfibril defined by two Euler angles  $\theta$  and  $\varphi$  in a Cartesian base frame  $\mathbf{e}_R, \mathbf{e}_T, \mathbf{e}_L$ .

### 1.5.2 Constitutive behavior of material phases

Cellulose behaves linear elastically and transversely isotropically [with the anisotropy direction being colinear to the cellulose fiber direction  $(\varphi, \bar{\theta})$ ],

$$\forall \mathbf{x} \in V_{cel, \varphi \bar{\theta}} : \boldsymbol{\sigma}(\mathbf{x}) = \mathbb{c}_{cel}(\varphi, \bar{\theta}) : \boldsymbol{\varepsilon}(\mathbf{x}), \quad (1.36)$$

with  $\mathbb{c}_{cel}(\varphi, \bar{\theta}) = \mathbb{C}_{cel}^{hom}$  according to (1.30) to (1.32), provided that the length direction of the cylindrical inclusions of cellulose is colinear with the cellulose fiber direction  $(\varphi, \bar{\theta})$ . Direct testing methods, such as polarization microscopy, staining, or examination of the direction of iodine crystals, indicate a mean microfibril angle of  $20^\circ$  averaged over the cell wall thickness and holding across various softwood species (Harada, 1965; Mark, 1967; Tang, 1973).

The polymer network behaves linear poroelastically and isotropically,

$$\forall \mathbf{x} \in V_{polymer} : \boldsymbol{\sigma}(\mathbf{x}) = \mathbb{c}_{polymer} : \boldsymbol{\varepsilon}(\mathbf{x}) - \mathbf{b}_{polymer} p(\mathbf{x}), \quad (1.37)$$

$$(\phi - \phi_0) = \mathbf{b}_{polymer} : \boldsymbol{\varepsilon}(\mathbf{x}) + \frac{p(\mathbf{x})}{N_{polymer}}, \quad (1.38)$$



with  $\mathbb{C}_{polynet} = \mathbb{C}_{polynet}^{hom}$  according to (1.23), together with (1.17) and (1.18); with  $\mathbf{b}_{polynet} = \mathbf{b}_{polynet}^{hom}$  according to (1.24), together with (1.20) and (1.21); and with  $N_{polynet} = N_{polynet}^{hom}$  according to (1.27), together with (1.22).

### 1.5.3 Homogenized poroelasticity of cell wall material

Linear elastic behavior of the material phases "cellulose" [according to (1.32), together with (1.30) and (1.31)] and linear poroelastic behavior of the material phase "polymer network" [according to (1.9) and (1.10), together with (1.17) to (1.27)] imply that the homogenized material behavior of the cell wall material takes the multi-linear form (Dormieux et al., 2006)

$$\Sigma_{cwm} = \mathbb{C}_{cwm}^{hom} : \mathbf{E}_{cwm} - \mathbf{b}_{cwm}^{hom} p, \quad (1.39)$$

with the drained elasticity tensor of the cell wall material,  $\mathbb{C}_{cwm}^{hom}$ , and the cell wall material-related Biot tensor  $\mathbf{b}_{cwm}^{hom}$ . As was the case in Section 1.3.3, Eq. (1.10), the aforementioned linear constitutive behavior of the material phases also implies a bilinear form for the nano-porosity change (now measured at the scale of the cell wall material), namely

$$(\phi - \phi_0)_{cwm} = \mathbf{b}_{cwm}^{hom} : \mathbf{E}_{cwm} + \frac{p}{N_{cwm}^{hom}}, \quad (1.40)$$

with the solid Biot modulus  $N_{cwm}^{hom}$  now relating to the cell wall material. In order to estimate the homogenized properties  $\mathbb{C}_{cwm}^{hom}$ ,  $\mathbf{b}_{cwm}^{hom}$ , and  $N_{cwm}^{hom}$ , we recall the deviation of the cellulose fibers by an average angle of  $\bar{\theta}$  (microfibril angle given in Figure 1.3), and consider, accordingly, a Mori-Tanaka-type homogenization scheme based on the following (strictly speaking, infinitely many) matrix-inclusion problems:

- Cylindrical cellulose inclusions of identical shape, oriented at identical latitudinal angle  $\bar{\theta}$ , but at varying longitudinal angles  $\varphi$  (see Figure 1.3), are embedded into infinite matrices of polymer network (with elasticity  $\mathbb{C}_{polynet}$  and eigenstresses  $\boldsymbol{\sigma}_{polynet}^p = -\mathbf{b}_{polynet} p$ ). All these infinite matrices are subjected to the same fictitious strains  $\mathbf{E}^\infty$  at infinity. The corresponding (homogeneous) strains in the cellulose fiber inclusions follow to be (Zaoui, 2002)

$$\begin{aligned} \boldsymbol{\varepsilon}_{cel}(\varphi) &= \left\{ \mathbb{I} + \mathbb{P}_{cyl}^{polynet}(\varphi, \bar{\theta}) : [\mathbb{C}_{cel}(\varphi, \bar{\theta}) - \mathbb{C}_{polynet}] \right\}^{-1} \\ &: \left[ \mathbf{E}^\infty - \mathbb{P}_{cyl}^{polynet}(\varphi, \bar{\theta}) : \mathbf{b}_{polynet} p \right]. \end{aligned} \quad (1.41)$$

- The polymer network acts as matrix phase, the corresponding "inclusion" strains read as

$$\boldsymbol{\varepsilon}_{polynet} = \mathbf{E}^\infty. \quad (1.42)$$

The homogeneous strains in the inclusions, (1.41) and (1.42), are used to approximate the phase averages occurring in (1.33). Accordingly, substitution in (1.33) of  $\langle \boldsymbol{\varepsilon} \rangle_{V_{cel, \varphi \bar{\theta}}}$  and  $\langle \boldsymbol{\varepsilon} \rangle_{V_{polynet}}$ , by  $\boldsymbol{\varepsilon}_{cel}(\varphi)$  and  $\boldsymbol{\varepsilon}_{polynet}$  according to (1.41) and (1.42), yields a relation between the RVE-related strains  $\mathbf{E}_{cwm}$  and the fictitious strains  $\mathbf{E}^\infty$ . Similar to the procedure described in Section 1.3.3, we use this relation in (1.41) and (1.42) for getting access to the concentration and influence relations between the "loading variables"  $\mathbf{E}_{cwm}$  and  $p$ , and the strains in the material phases

$$\boldsymbol{\varepsilon}_{cel}(\varphi) = \mathbb{A}_{cel}^{cwm}(\varphi) : \mathbf{E}_{cwm} + \mathbf{a}_{cel}^{cwm}(\varphi) p, \quad (1.43)$$

$$\boldsymbol{\varepsilon}_{polynet} = \mathbb{A}_{polynet}^{cwm} : \mathbf{E}_{cwm} + \mathbf{a}_{polynet}^{cwm} p, \quad (1.44)$$

with the concentration tensors reading as

$$\begin{aligned} \mathbb{A}_{cel}^{cwm}(\varphi) &= \left[ \mathbb{I} + \mathbb{P}_{cyl}^{polynet}(\varphi, \bar{\theta}) : (\mathbb{C}_{cel}(\varphi, \bar{\theta}) - \mathbb{C}_{polynet}) \right]^{-1} \\ &: \left\{ f_{polynet} \mathbb{I} + f_{cel} \frac{1}{2\pi} \int_{\varphi=0}^{2\pi} \left[ \mathbb{I} + \mathbb{P}_{cyl}^{polynet}(\varphi, \bar{\theta}) \right. \right. \\ &: \left. \left. (\mathbb{C}_{cel}(\varphi, \bar{\theta}) - \mathbb{C}_{polynet}) \right]^{-1} d\varphi \right\}^{-1}, \end{aligned} \quad (1.45)$$

$$\begin{aligned} \mathbb{A}_{polynet}^{cwm} &= \left\{ f_{polynet} \mathbb{I} + f_{cel} \frac{1}{2\pi} \int_{\varphi=0}^{2\pi} \left[ \mathbb{I} + \mathbb{P}_{cyl}^{polynet}(\varphi, \bar{\theta}) \right. \right. \\ &: \left. \left. (\mathbb{C}_{cel}(\varphi, \bar{\theta}) - \mathbb{C}_{polynet}) \right]^{-1} d\varphi \right\}^{-1}, \end{aligned} \quad (1.46)$$

and the influence tensors reading as

$$\begin{aligned} \mathbf{a}_{cel}^{cwm}(\varphi) &= f_{cel} \mathbb{A}_{cel}^{cwm}(\varphi) : \frac{1}{2\pi} \int_{\varphi=0}^{2\pi} \left[ \mathbb{I} + \mathbb{P}_{cyl}^{polynet}(\varphi, \bar{\theta}) : (\mathbb{C}_{cel}(\varphi, \bar{\theta}) - \mathbb{C}_{polynet}) \right]^{-1} \\ &: \mathbb{P}_{cyl}^{polynet}(\varphi, \bar{\theta}) : \mathbf{b}_{polynet} d\varphi \\ &- \left[ \mathbb{I} + \mathbb{P}_{cyl}^{polynet}(\varphi, \bar{\theta}) : (\mathbb{C}_{cel}(\varphi, \bar{\theta}) - \mathbb{C}_{polynet}) \right]^{-1} \\ &: \mathbb{P}_{cyl}^{polynet}(\varphi, \bar{\theta}) : \mathbf{b}_{polynet}, \end{aligned} \quad (1.47)$$

$$\begin{aligned} \mathbf{a}_{polynet}^{cwm} &= f_{cel} \mathbb{A}_{polynet}^{cwm} : \frac{1}{2\pi} \int_{\varphi=0}^{2\pi} \left[ \mathbb{I} + \mathbb{P}_{cyl}^{polynet}(\varphi, \bar{\theta}) : (\mathbb{C}_{cel}(\varphi, \bar{\theta}) - \mathbb{C}_{polynet}) \right]^{-1} \\ &: \mathbb{P}_{cyl}^{polynet}(\varphi, \bar{\theta}) : \mathbf{b}_{polynet} d\varphi. \end{aligned} \quad (1.48)$$

Use of concentration and influence relations (1.43) and (1.44) in phase (poro)elasticity laws (1.36) and (1.37), and insertion of the corresponding results into (1.39), yields a relation which allows for identification of the drained stiffness of cell wall material,  $\mathbb{C}_{cwm}^{hom}$ , and of the corresponding Biot tensor  $\mathbf{b}_{cwm}^{hom}$ ,

$$\mathbb{C}_{cwm}^{hom} = f_{polymer} \mathbb{C}_{polymer} : \mathbb{A}_{polymer}^{cwm} + f_{cel} \frac{1}{2\pi} \int_{\varphi=0}^{2\pi} \mathbb{C}_{cel}(\varphi, \bar{\theta}) : \mathbb{A}_{cel}^{cwm}(\varphi) d\varphi, \quad (1.49)$$

$$\begin{aligned} \mathbf{b}_{cwm}^{hom} = & -f_{polymer} \mathbb{C}_{polymer} : \mathbf{a}_{polymer}^{cwm} + f_{polymer} \mathbf{b}_{polymer} \\ & -f_{cel} \frac{1}{2\pi} \int_{\varphi=0}^{2\pi} \mathbb{C}_{cel}(\varphi, \bar{\theta}) : \mathbf{a}_{cel}^{cwm}(\varphi) d\varphi, \end{aligned} \quad (1.50)$$

where  $\mathbb{A}_{cel}^{cwm}(\varphi)$  and  $\mathbb{A}_{polymer}^{cwm}$  still follow (1.45) and (1.46), and where  $\mathbf{a}_{cel}^{cwm}(\varphi)$  and  $\mathbf{a}_{polymer}^{cwm}$  still follow (1.47) and (1.48). Finally, we upscale the nano-porosity from the polymer level to that of the cell wall material,

$$(\phi - \phi_0)_{cwm} = f_{polymer}(\phi - \phi_0)_{polymer}, \quad (1.51)$$

so that combination of (1.51) with (1.10) and (1.44), while considering  $\mathbf{E}_{polymer} = \boldsymbol{\varepsilon}_{polymer}$ , yields a relation which allows for identification of  $\mathbf{b}_{cwm}^{hom}$  and  $N_{cwm}^{hom}$  in (1.40), in the form

$$\mathbf{b}_{cwm}^{hom} = f_{polymer} \mathbf{b}_{polymer} : \mathbb{A}_{polymer}^{cwm}, \quad (1.52)$$

$$\frac{1}{N_{cwm}^{hom}} = f_{polymer} \mathbf{b}_{polymer} : \mathbf{a}_{polymer}^{cwm} + f_{polymer} \frac{1}{N_{polymer}}. \quad (1.53)$$

In (1.52) and (1.53),  $\mathbb{A}_{polymer}^{cwm}$  and  $\mathbf{a}_{polymer}^{cwm}$ , respectively, still follow (1.46) and (1.48), respectively.

## 1.6 Poro-microelasticity of softwood

### 1.6.1 RVE, stress and strain averages

Softwood exhibits a honeycomb-type, periodic microstructure, being oriented in stem direction, see homogenization step III in Figure 1.2. Consideration of softwood as honeycomb-type structure is well accepted in the wood mechanics community, see e.g. Papka and Kyriakides (1999); Da Silva and Kyriakides (2007). Consequently, from a micromechanical viewpoint, softwood can be considered as consisting of a large number of identical unit cells, where the spatial strain average across individual unit cells equals the macroscopic strains at the scale of softwood,

$$\mathbf{E}_{SW} = \hat{f}_{cwm} \langle \boldsymbol{\varepsilon} \rangle_{V_{cwm}} + \hat{f}_{lum} \langle \boldsymbol{\varepsilon} \rangle_{V_{lum}}, \quad (1.54)$$

with the volume of softwood hosting cell wall material and lumen pores,

$$V_{SW} = V_{cwm} + V_{lum}. \quad (1.55)$$

Consistently, the stresses at the level of softwood  $\Sigma_{SW}$  read as

$$\Sigma_{SW} = \hat{f}_{cwm} \langle \boldsymbol{\sigma} \rangle_{V_{cwm}} + (1 - \hat{f}_{cwm}) \langle \boldsymbol{\sigma} \rangle_{V_{lum}}. \quad (1.56)$$

### 1.6.2 Constitutive behavior of material phases

The cell wall material behaves linear poroelastically and transversely isotropically (with the anisotropy direction being colinear to stem direction  $L$ ),

$$\forall \mathbf{x} \in V_{cwm} : \quad \boldsymbol{\sigma}(\mathbf{x}) = \mathbb{c}_{cwm} : \boldsymbol{\varepsilon}(\mathbf{x}) - \mathbf{b}_{cwm} p(\mathbf{x}), \quad (1.57)$$

$$(\phi - \phi_0) = \mathbf{b}_{cwm} : \boldsymbol{\varepsilon}(\mathbf{x}) + \frac{p(\mathbf{x})}{N_{cwm}}, \quad (1.58)$$

with  $\mathbb{c}_{cwm} = \mathbb{C}_{cwm}^{hom}$  according to (1.49), together with (1.45) and (1.46); with  $\mathbf{b}_{cwm} = \mathbf{b}_{cwm}^{hom}$  according to (1.50), together with (1.47) and (1.48); and with  $N_{cwm} = N_{cwm}^{hom}$  according to (1.53), together with (1.48). The lumen pores are regarded as empty,

$$\forall \mathbf{x} \in V_{lum} : \quad \boldsymbol{\sigma}(\mathbf{x}) = 0, \quad (1.59)$$

see e.g. (Dormieux et al., 2002, 2006) for the definition of an empty pore space. Accordingly, the right-hand term in Eq. (1.56) vanishes.

### 1.6.3 Homogenized poroelasticity of softwood

Linear poroelastic behavior of the material phase "cell wall material" [according to (1.39) and (1.40), together with (1.45) to (1.53)] implies that the homogenized material behavior of softwood takes the multi-linear form (Dormieux et al., 2006)

$$\Sigma_{SW} = \mathbb{C}_{SW}^{hom} : \mathbf{E}_{SW} - \mathbf{b}_{SW}^{hom} p, \quad (1.60)$$

with the drained elasticity tensor of softwood,  $\mathbb{C}_{SW}^{hom}$ , and the softwood-related Biot tensor  $\mathbf{b}_{SW}^{hom}$ . When choosing  $p = 0$ , we observe that the drained elasticity tensor is identical to the elasticity tensor for empty nanopores so that all relations depicted in Figure 1.4 are independent of any water properties. This is a well-known feature of poroelasticity, which has been repeatedly described [Auriault and Sanchez-Palencia (1977), p. 591; Thompson and Willis (1991), Figure 1; Chateau and Dormieux (1998, 2002), p. 834; Hellmich and Ulm (2005), p. 246]. As was the case in Section 1.3.3, Eq. (1.10), linear constitutive behavior of the material phases according to Eq. (1.60) also implies a bilinear form for the nano-porosity change (now measured at the scale of softwood), namely

$$(\phi - \phi_0)_{SW} = \mathbf{b}_{SW}^{hom} : \mathbf{E}_{SW} + \frac{p}{N_{SW}^{hom}}, \quad (1.61)$$

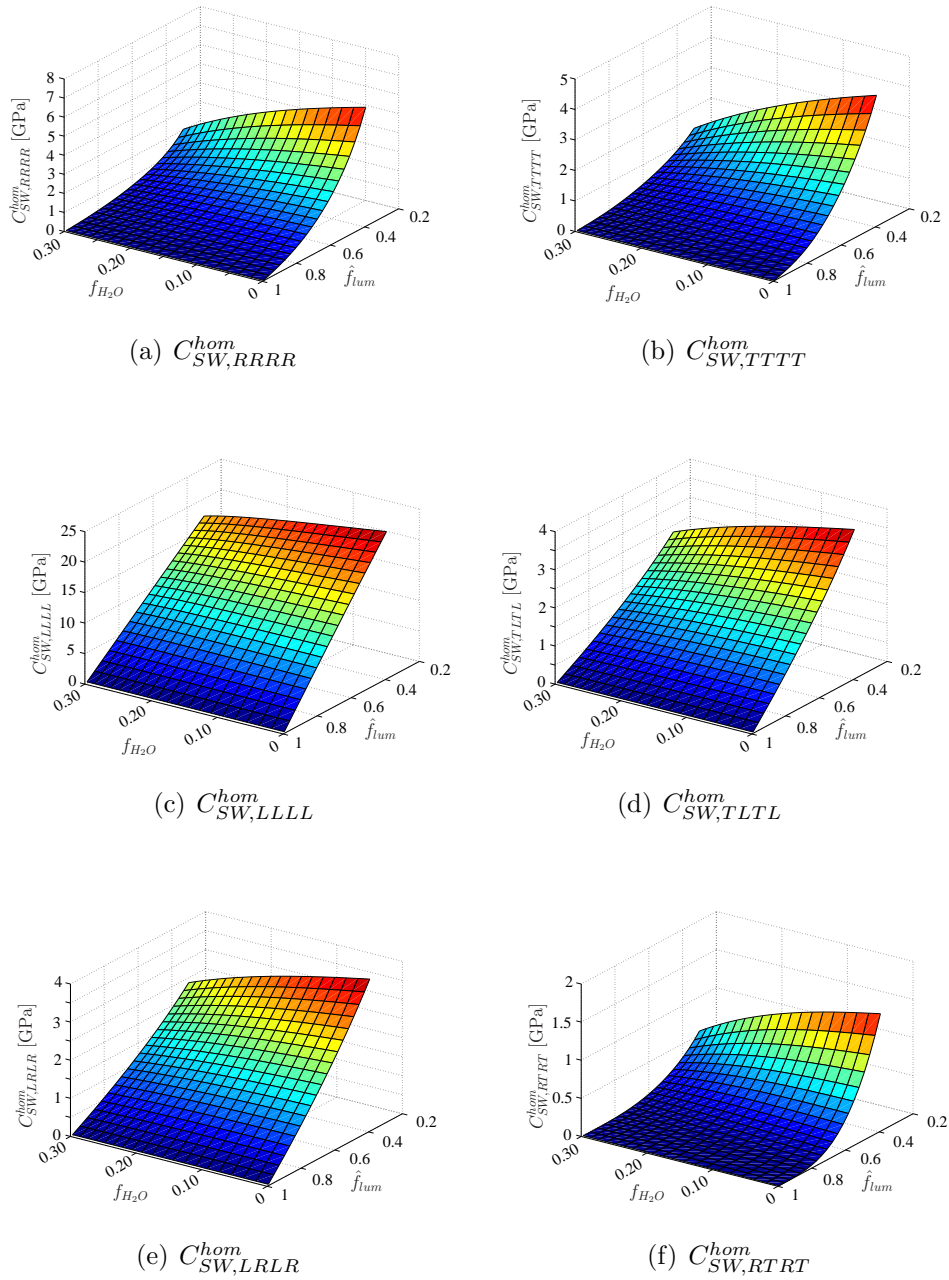


**Figure 1.4:** Characteristics of the poromechanical model for wood: Components of the softwood-related drained stiffness tensor as functions of the lumen volume fraction  $\hat{f}_{lum}$ , and of the cell wall-related volume fraction of water,  $f_{H_2O}$ , for a fixed ratio of volume fractions of crystalline cellulose, amorphous cellulose, hemicellulose, lignin, and extractives (0.26:0.13:0.27:0.29:0.05), typical for spruce. Indices after a comma refer to tensor components, and not to partial differentiation.

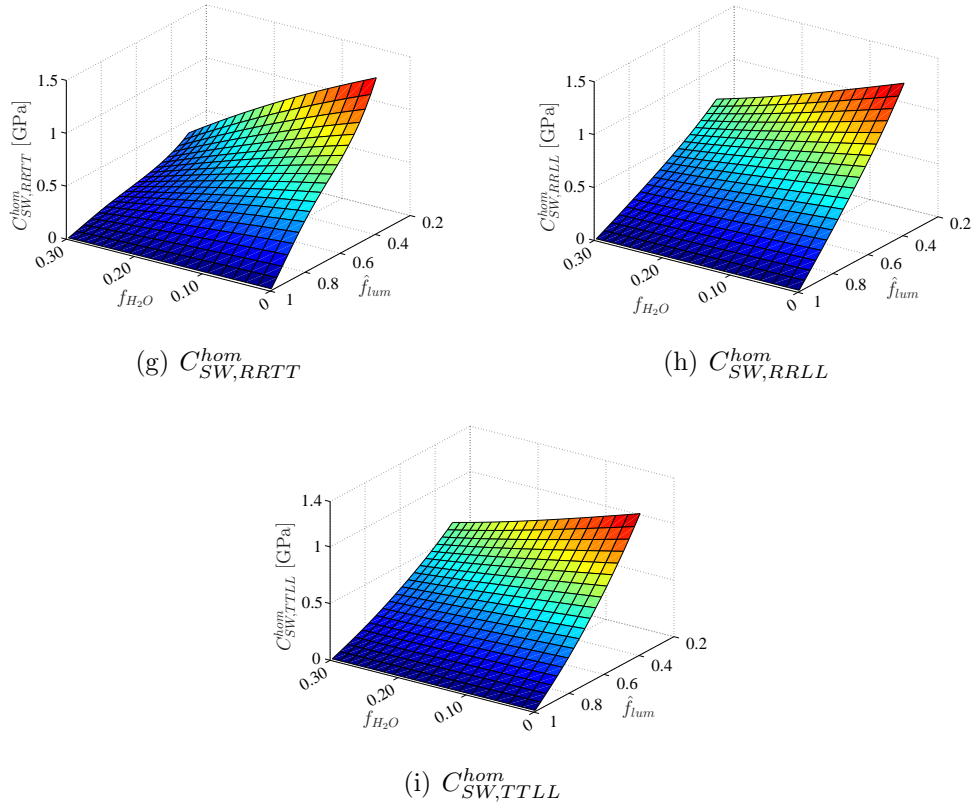


**Figure 1.4** continued: Characteristics of the poromechanical model for wood: Components of the softwood-related drained stiffness tensor as functions of the lumen volume fraction  $\hat{f}_{lum}$ , and of the cell wall-related volume fraction of water,  $f_{H_2O}$ , for a fixed ratio of volume fractions of crystalline cellulose, amorphous cellulose, hemicellulose, lignin, and extractives (0.26:0.13:0.27:0.29:0.05), typical for spruce. Indices after a comma refer to tensor components, and not to partial differentiation.

with the solid Biot modulus  $N_{SW}^{hom}$  now relating to softwood.

In order to estimate the drained stiffness tensor  $\mathbb{C}_{SW}^{hom}$ , we consider periodic plate-like bending and out-of-plane shear deformations at the boundary of the unit cell, see Hofstetter et al. (2007) and the Appendix 1.9.3 for details. To extend this drained elasticity results to the poroelastic case, we adopt, as an original methodical feature of this paper, the formalism of matrix-inclusion problem-based continuum micromechanics employed throughout Sections 1.3 to 1.5, to the case of softwood: The analogon of (1.23) for softwood reads as

$$\mathbb{C}_{SW}^{hom} = \hat{f}_{cwm} \mathbb{C}_{cwm} : \mathbb{A}_{cwm}^{SW}, \quad (1.62)$$

which gives access to concentration tensor  $\mathbb{A}_{cwm}^{SW}$  as

$$\mathbb{A}_{cwm}^{SW} = \frac{1}{\hat{f}_{cwm}} \mathbb{C}_{cwm}^{-1} : \mathbb{C}_{SW}^{hom}. \quad (1.63)$$

Relating  $\mathbb{A}_{cwm}^{SW}$  to a (formal) Mori-Tanaka type homogenization scheme analogous to (1.30), where the cell wall material takes the role of a solid matrix and the lumens take the role of empty inclusions, delivers a (formal) Hill tensor  $\mathbb{P}_{hex}^{cwm}$  reading as

$$\mathbb{P}_{hex}^{cwm} = \left[ \mathbb{I} - (1 - \hat{f}_{cwm}) \left( \mathbb{A}_{cwm}^{SW,-1} - \hat{f}_{cwm} \mathbb{I} \right)^{-1} \right] : \mathbb{C}_{cwm}^{-1}. \quad (1.64)$$

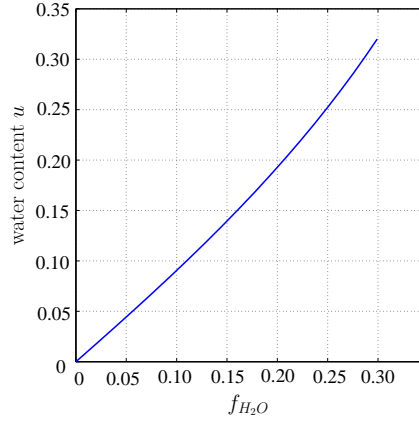


**Figure 1.5:** Water content (standardly defined in wood mechanics as the mass of water over the entire dry piece of wood), as function of the cell wall-related volume fraction of water  $f_{H_2O}$ , for a fixed ratio of volume fractions of crystalline cellulose, amorphous cellulose, hemicellulose, lignin, and extractives (0.26:0.13:0.27:0.29:0.05), typical for spruce.

Based on this tensor, the (formal) matrix-inclusion problem can be extended from the purely elastic case to that of a poroelastic matrix [see Zaoui (2002) and consider replacement in (1.41) of the cellulose inclusions by a single lumen inclusion in the present case]

$$\boldsymbol{\varepsilon}_{lum} = [\mathbb{I} - \mathbb{P}_{hex}^{cwm} : \mathbb{C}_{cwm}]^{-1} : [\mathbf{E}^\infty - \mathbb{P}_{hex}^{cwm} : \mathbf{b}_{cwm} p]. \quad (1.65)$$

In (1.65),  $\mathbf{E}^\infty$  are the fictitious strains at the remote boundary of the (formal) matrix-inclusion problem. Considering

$$\boldsymbol{\varepsilon}_{cwm} = \mathbf{E}^\infty \quad (1.66)$$

in the cell wall material matrix, and using (1.65) and (1.66) in order to estimate the strain averages in (1.54), we arrive at a relation between  $\mathbf{E}_{SW}$  and  $\mathbf{E}^\infty$ . Use of this relation in (1.66) yields a concentration/influence relation between the "loading variables"  $\mathbf{E}_{SW}$  and  $p$ , and the strains in the cell wall material phase

$$\boldsymbol{\varepsilon}_{cwm} = \mathbb{A}_{cwm}^{SW} : \mathbf{E}_{SW} + \mathbf{a}_{cwm}^{SW} p, \quad (1.67)$$

with  $\mathbb{A}_{cwm}^{SW}$  still following (1.63) and the influence tensor  $\mathbf{a}_{cwm}^{SW}$  reading as

$$\mathbf{a}_{cwm}^{SW} = \hat{f}_{lum} \mathbb{A}_{cwm}^{SW} : [\mathbb{I} - \mathbb{P}_{hex}^{cwm} : \mathbb{C}_{cwm}]^{-1} : \mathbb{P}_{hex}^{cwm} : \mathbf{b}_{cwm}. \quad (1.68)$$

Finally, we upscale the nano-porosity from the cell wall level to that of softwood

$$(\phi - \phi_0)_{SW} = \hat{f}_{cwm}(\phi - \phi_0)_{cwm}, \quad (1.69)$$

so that combination of (1.69) with (1.40) and (1.67), while considering  $\mathbf{E}_{cwm} = \boldsymbol{\varepsilon}_{cwm}$ , yields a relation which allows for identification of  $\mathbf{b}_{SW}^{hom}$  and  $N_{SW}^{hom}$ , in the form

$$\mathbf{b}_{SW}^{hom} = \hat{f}_{cwm} \mathbf{b}_{cwm} : \mathbb{A}_{cwm}^{SW}, \quad (1.70)$$

$$\frac{1}{N_{SW}^{hom}} = \hat{f}_{cwm} \mathbf{b}_{cwm} \mathbf{a}_{cwm}^{SW} + \hat{f}_{cwm} \frac{1}{N_{cwm}}. \quad (1.71)$$

## 1.7 Structure-property relationships

Sections 1.3 to 1.6 have given access to relationships between composition and porosities at different length scales, and the resulting poroelastic properties. These relationships account for the micro-morphological features characterizing the hierarchical biological material "wood". Out of the quantities concerning composition and porosity, the water content in the cell wall and the lumen volume fraction (often expressed as the apparent mass density of softwood) are known to undergo the largest changes when considering all the variability of softwood from earlywood to latewood, as well as from the totally water-saturated to the totally dried state. This motivates us to illustrate, for a typical softwood, such as spruce, the elastic properties  $\mathbb{C}_{SW}^{hom}$ , the Biot tensors  $\mathbf{b}_{SW}^{hom}$ , and the Biot moduli  $N_{SW}^{hom}$ , as functions of the cell wall-related volume fraction of water,  $f_{H_2O}$ , and of lumen volume fraction  $\hat{f}_{lum}$ .  $f_{H_2O}$  is uniquely and monotonously related to the water content, see Figure 1.5. According to Kollmann (1982), the water content is defined as the mass of water over the mass of the entire dry piece of softwood.  $f_{H_2O}$  typically varies between 0 and 0.3, see Hofstetter et al. (2005) and references therein for further details. On the other hand,  $\hat{f}_{lum}$  typically varies between 0.4 and almost 1, see Hofstetter et al. (2005) for further details. Spruce is characterized by typical ratios between the (non-liquid) chemical constituents of the cell wall, namely  $f_{crycel} : f_{amocel} : f_{hemcel} : f_{lig} : f_{ext} = 0.26 : 0.13 : 0.27 : 0.29 : 0.05$  irrespective of the drying state of the considered sample. Except for  $f_{ext}$ , all these volume fractions refer to solid material phases, while  $f_{ext}$  itself, together with water, makes up a liquid phase filling the nanoporous phase, since the extractives are assumed to be solved in water, as was already stated in Section 1.3.1, see also Hofstetter et al. (2005) and references therein for further details. Hence, the cell wall-related volume fractions for such softwood samples read as:

$$f_{crycel} = 0.26(1 - f_{H_2O}), \quad (1.72)$$

$$f_{amocel} = 0.13(1 - f_{H_2O}), \quad (1.73)$$

$$f_{hemcel} = 0.27(1 - f_{H_2O}), \quad (1.74)$$

$$f_{lig} = 0.29(1 - f_{H_2O}), \quad (1.75)$$

$$f_{H_2Oext} = f_{H_2O} + 0.05(1 - f_{H_2O}). \quad (1.76)$$



Within an RVE of polymer network, the volume fractions of hemicellulose, of lignin, and of water and extractives, read as

$$\tilde{f}_r = f_r / (1 - f_{crycel} - f_{amocel}), \quad r \in [hemcel, lig, H_2Oext]. \quad (1.77)$$

Analogously, within an RVE of cellulose, the volume fractions of crystalline cellulose and amorphous cellulose read as

$$\bar{f}_r = f_r / (1 - f_{hemcel} - f_{lig} - f_{H_2O} - f_{ext}), \quad r \in [crycel, amocel]. \quad (1.78)$$

Use of these volume fractions in Eq. (1.23) [with (1.17), (1.18), and (1.79)-(1.82)], in Eq. (1.32) [with (1.30), (1.31), and (1.83)-(1.87)], in Eq. (1.49) [with (1.45), (1.46), and (1.83)-(1.87)], and in Eq. (1.88)-(1.106), yields the components of the elasticity tensor of softwood,  $\mathbb{C}_{SW}^{hom}$ , as function of the and the lumen volume fraction  $\hat{f}_{lum}$  [see Figure 1.4, where we consider the "universal" elastic components of amorphous and crystalline cellulose, hemicellulose, lignin, and water of Table 1.1, as detailed in Hofstetter et al. (2005)]. Axial ("L"-) direction-related components are characterized by a linear (decreasing) dependence of (increasing) porosity, while transverse ("R" (radial) and "T" (tangential), see Figure 1.2) directions-related components are characterized by an overlinear increase, when considered as function of decreasing porosity (see Figure 1.4a,b,e,f,g). In all cases, increase of water content, expressed through the related volume fraction of water,  $f_{H_2O}$ , leads to a moderate reduction of stiffness [see Figure 1.4(a-i)].

These elastic model responses were carefully verified through experiments, as detailed in Hofstetter et al. (2007). From these validations, we gain confidence in the relevant representation of the elastic interactions in the hierarchy of wood, through the multistep homogenization scheme of Figure 1.2, i.e. in the type of load transfers through the microstructures. Virtually the same load transfer types are evoked when the microstructures are not loaded through overall strains (and zero pore pressure), but through non-zero pore pressures (and vanishing overall strains). Hence, we can be quite confident in the relevance of deriving poroelastic properties from the homogenization scheme of Figure 1.2 (although, to the knowledge of the authors, direct poroelastic tests on wood have not been performed so far). The characteristics of the corresponding Biot tensors and moduli are derived along the following lines.

Use of the volume fractions (1.77) and (1.78) in Eq. (1.24) [with (1.20), (1.21), and (1.79)-(1.82)], in Eq. (1.50) [with (1.47), (1.48), and (1.83)-(1.87)], and in Eq. (1.70) [with (1.63) and (1.88)-(1.106)] yields the components of the Biot tensor of softwood,  $\mathbf{b}_{SW}^{hom}$ , as function of the volume fraction of water within the cell wall,  $f_{H_2O}$ , and of the lumen volume fraction  $\hat{f}_{lum}$  (see Figure 1.6, where we consider the "universal" elastic components of amorphous and crystalline cellulose, hemicellulose, lignin, and water of Table 1.1, as detailed in Hofstetter et al. (2005)).

Transverse ("R" (radial) and "T" (tangential)) direction-related components are characterized by an strongly overlinear increase, when considered as function of both increasing volume fraction of water within the cell wall, and decreasing lumen volume fraction [Figure 1.6(a,b)]. In other words, the higher the water content and the lower the lumen volume fraction, the more the pore pressure inside the polymer network is transferred, in

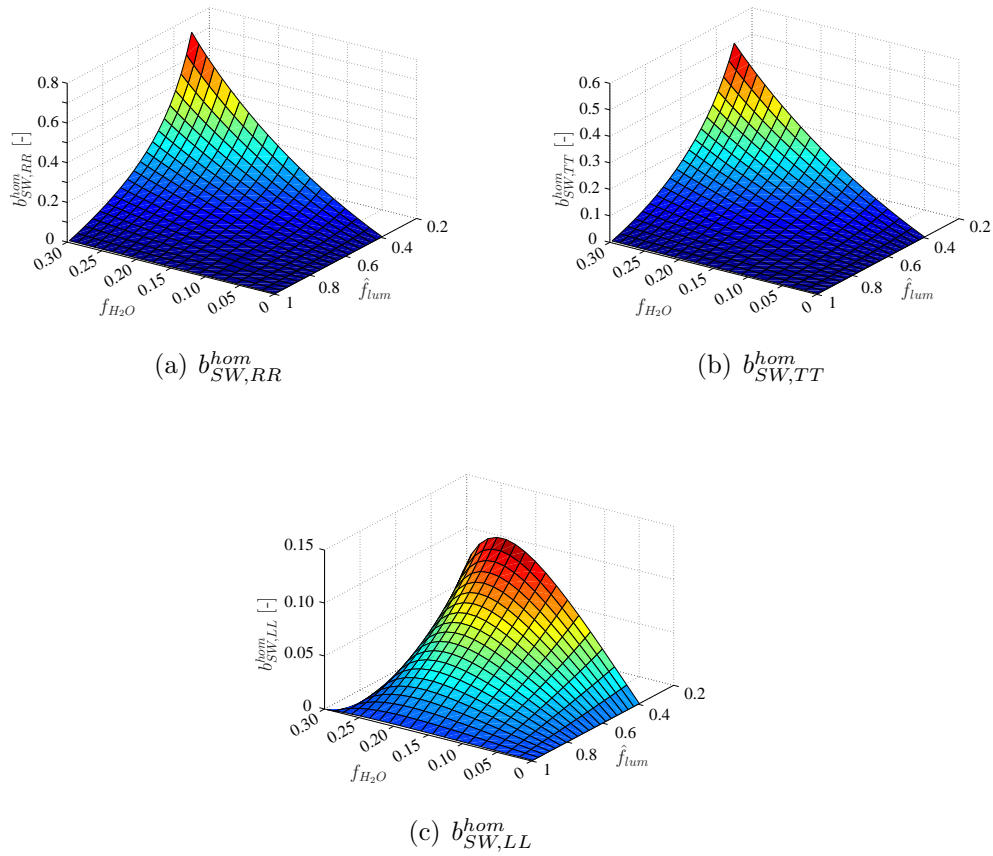


**Figure 1.6:** Characteristics of the poromechanical model for wood: Components of the softwood-related Biot tensor as functions of the lumen volume fraction  $\hat{f}_{lum}$ , and of the cell wall-related volume fraction of water,  $f_{H_2O}$ , for a fixed ratio of volume fractions of crystalline cellulose, amorphous cellulose, hemicellulose, lignin, and extractives (0.26:0.13:0.27:0.29:0.05), typical for spruce. Indices after a comma refer to tensor components, and not to partial differentiation.

terms of transverse normal stresses, onto the boundaries of an RVE of softwood, which is restrained, at these boundaries, from any overall deformation. The longitudinal ("L"-) direction-related non-zero components of the Biot tensor of softwood is characterized by a slightly overlinear increase when considered as a function of decreasing lumen volume fraction [see Figure 1.6(c)]. In other words, pore pressure within the polymer network provokes the more longitudinal normal stresses acting on an overall deformation-free RVE of softwood, the less lumen volume fraction the latter exhibits. Most remarkably, the influence of the water content on the longitudinal component of softwood's Biot tensor is fundamentally different from that of the lumen volume fraction: the function  $b_{SW,33}^{hom}(f_{H_2O})$  exhibits a maximum at  $f_{H_2O} \approx 0.20$  [Figure 1.6(c)]. In other words, starting from the totally dried case ( $f_{H_2O} = 0$ ), any additional pore pressure in the polymer network resulting from additionally available (pressurized) water leads to an increase of longitudinal stresses acting on an overall deformation-free RVE of softwood. However, increasing volume fractions of water inside the cell wall material reduces this material's stiffness, being less and

less able to transfer the pore pressure, from the low level of the polymer network to the high level of softwood. At  $f_{H_2O} \approx 0.20$ , this second effect (reduced pore pressure "transfer capacity") becomes dominant with regard to the first effect ("more pressurized water available"), and from there on,  $b_{SW,33}^{hom}$ , decreases with increasing  $f_{H_2O}$ .

Inserting the relation for the volume fractions (1.77) and (1.78) into Eq. (1.27) [with (1.22)], and into Eq. (1.26) [with (1.19)]; and inserting the corresponding results into Eq. (1.53) [with (1.48)], into Eq. (1.50) [with (1.47) and (1.48)], and finally into Eq. (1.71) [with (1.68)], yields the Biot modulus of softwood  $N_{SW}^{hom}$ , as function of the volume fraction of water within the cell wall  $f_{H_2O}$ , and of the lumen volume fraction  $\hat{f}_{lum}$  (see Figure 1.7, where we consider the "universal" elastic components of amorphous and crystalline cellulose, hemicellulose, lignin, and water of Table 1.1, as detailed in Hofstetter et al. (2005)). For lower water contents ( $f_{H_2O} < 0.15$ ), the Biot compliance of softwood,  $1/N_{SW}^{hom}$ , increases monotonously with decreasing lumen volume fraction (Figure 1.7b), while for higher water contents ( $f_{H_2O} > 0.15$ ),  $1/N_{SW}^{hom}$ , when considered as function of lumen volume fraction  $\hat{f}_{lum}$ , exhibits a maximum at  $\hat{f}_{lum} \approx 0.35 - 0.53$ . In other words, for lower water contents (and in an iso-deformation condition at the softwood level), the pore pressure expands its own pore space the more, the less lumen volume fraction is available for accommodating the pore pressure through deformations at higher scales. For higher water contents, however, reduction of the lumen volume fraction reduces the overall microstructural compliance so significantly, that a further expansion at the polymer network pore space becomes impossible.

At the length scale of the polymer network [homogenization step I(a) in Figure (1.2)], the poroelastic interactions are expectedly much easier to be understood: the more pressurized water to be found in the polymer network, the more of this pressure is felt at the boundary of an undeformed RVE of polymer network [quantified in terms of the Biot tensor components, as shown in Figure 1.8(a), based on Eq. (1.24), together with

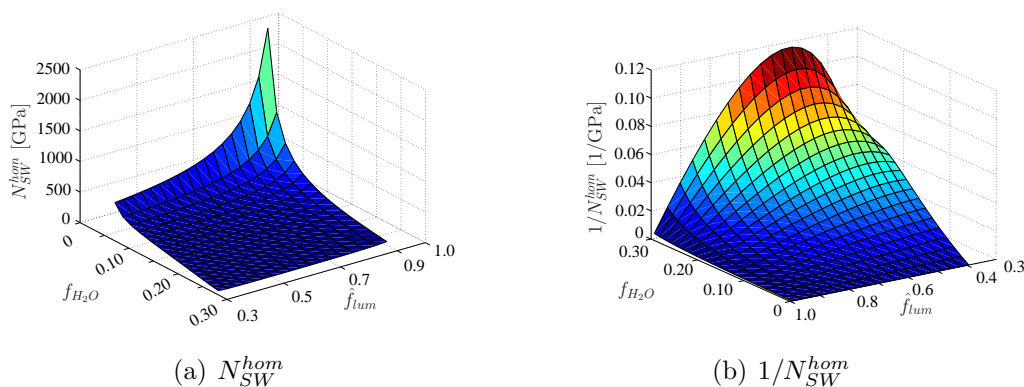


**Figure 1.7:** Characteristics of the poromechanical model for wood: Softwood-related Biot modulus (a) and its inverse (b) as functions of the lumen volume fraction  $\hat{f}_{lum}$ , and of the cell wall-related volume fraction of water,  $f_{H_2O}$ , for a fixed ratio of volume fractions of crystalline cellulose, amorphous cellulose, hemicellulose, lignin, and extractives (0.26:0.13:0.27:0.29:0.05), typical for spruce.

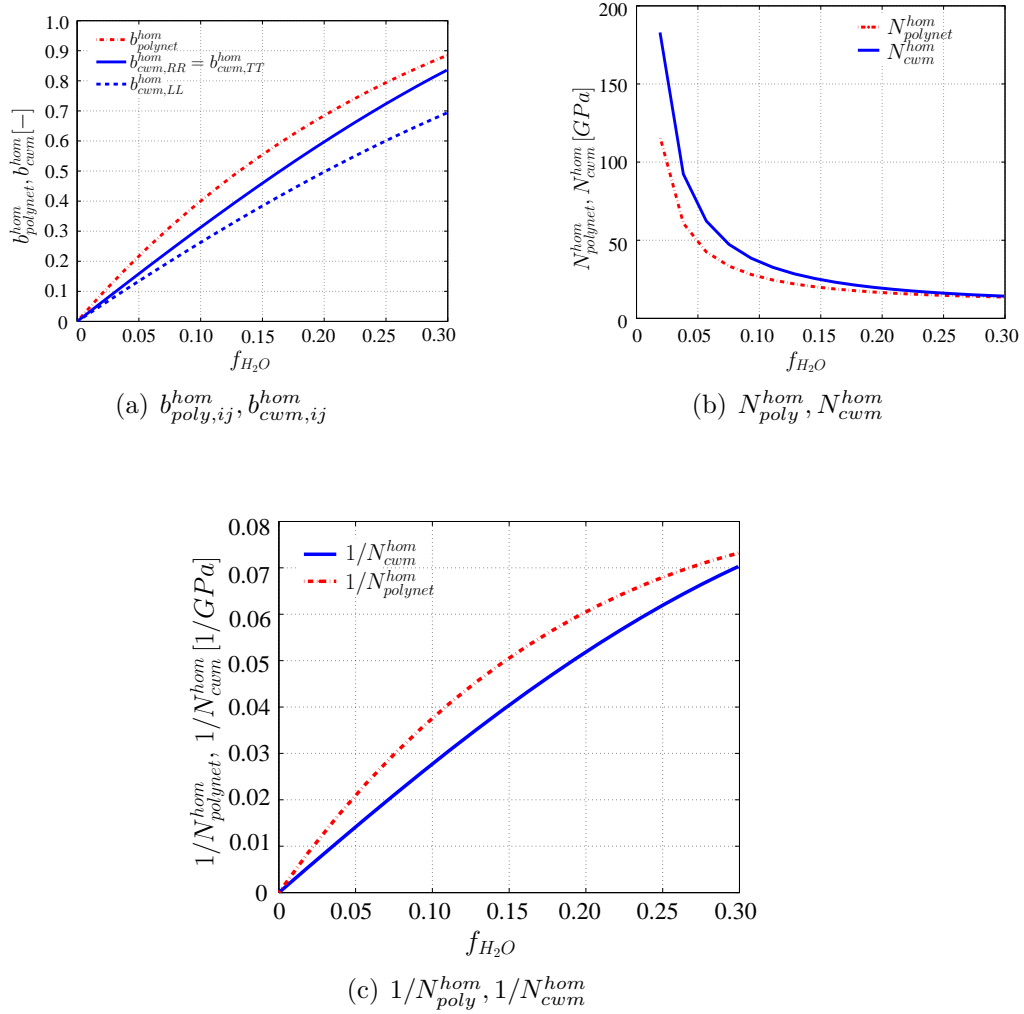


**Figure 1.8:** Characteristics of the poromechanical model for wood: (a) Components of the Biot tensor of the polymer network (*polynet*) and of the cell wall material (*cwm*); and the Biot modulus (b) and its inverse (c) of the polymer network (*polynet*) and of the cell wall material (*cwm*); as functions of the cell wall-related volume fraction of water,  $f_{H_2O}$ , for a fixed ratio of volume fractions of crystalline cellulose, amorphous cellulose, hemicellulose, lignin, and extractives (0.26:0.13:0.27:0.29:0.05), typical for spruce. Indices after a comma refer to tensor components, and not to partial differentiation.

**Table 1.2:** Chemical composition of cell walls of different softwoods

Wood species	$f_{crycel}$	$f_{amocel}$	$f_{hemcel}$	$f_{lig}$	$f_{ext}$	Source
Spruce	0.26	0.13	0.27	0.29	0.05	Hofstetter et al. (2005)
Douglasie	0.23	0.12	0.26	0.31	0.08	Hofstetter et al. (2005)
Cedar	0.27	0.14	0.20	0.31	0.08	Hofstetter et al. (2005)

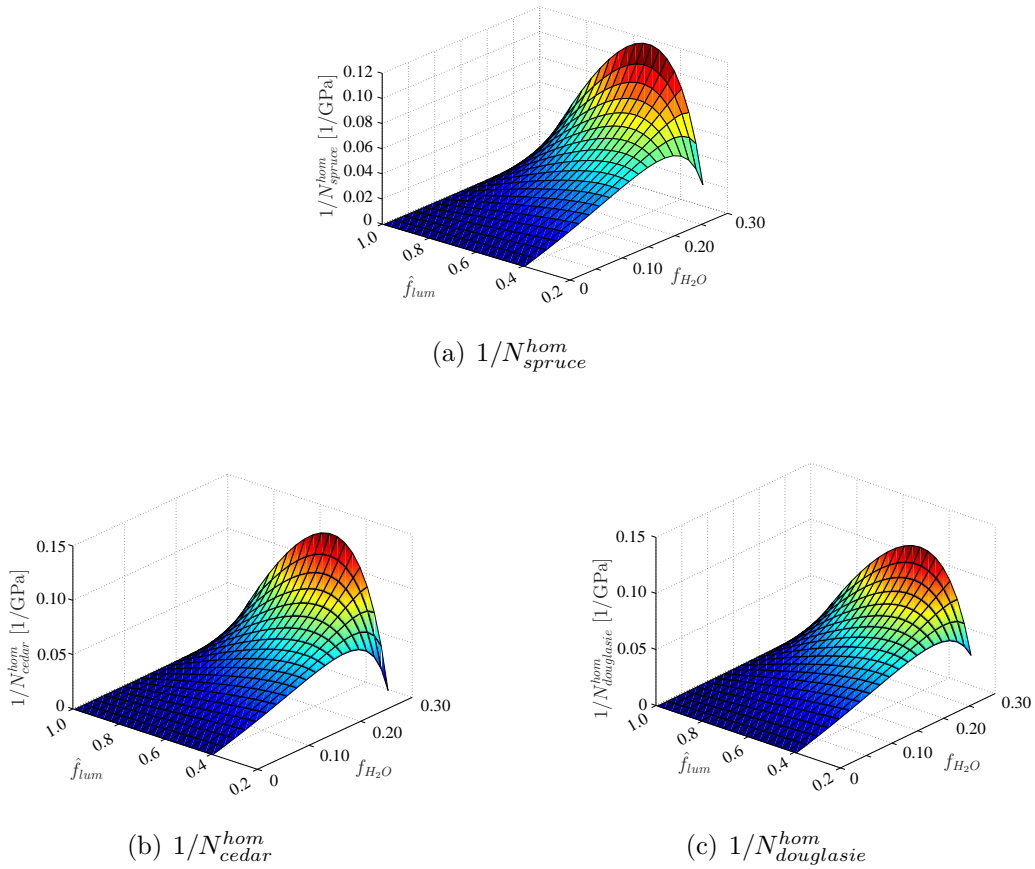


**Figure 1.9:** Characteristics of the promechanical model for wood: Softwood-related Biot modulus (a) and its inverse (b) as functions of the volume fraction of lumen pores  $\hat{f}_{lum}$ , and of the cell wall-related volume fraction of water,  $f_{H_2O}$ , for three different, fixed ratios of volume fractions of crystalline cellulose, amorphous cellulose, hemicellulose, lignin, and extractives (see Tab. 1.2), typical for three different softwoods.

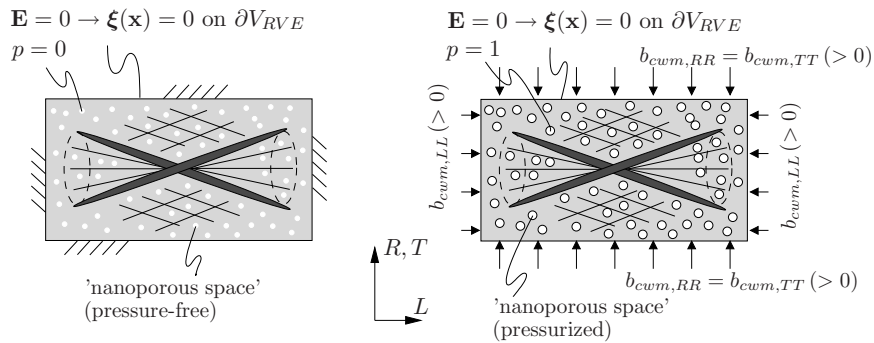


**Figure 1.10:** Illustration of Biot tensor components of cell wall material.

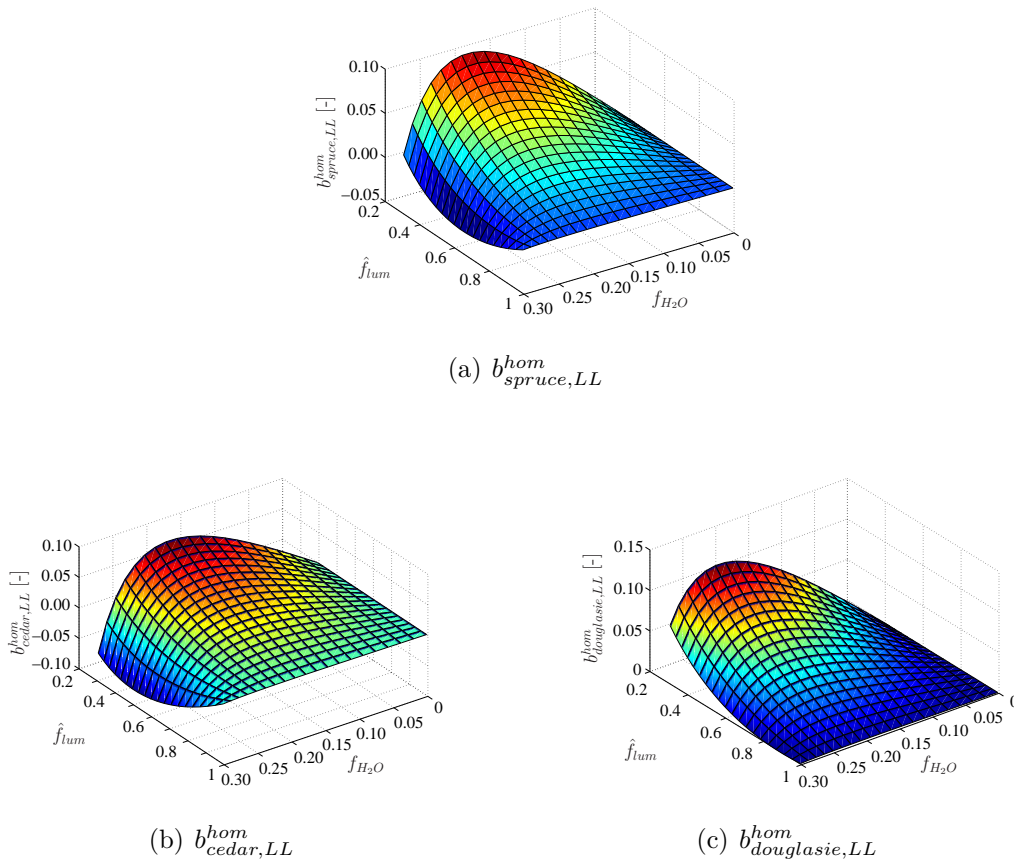


**Figure 1.11:** Characteristics of the poromechanical model for wood: Components of the softwood-related Biot tensor as functions of the lumen volume fraction  $\hat{f}_{lum}$ , and of the cell wall-related volume fraction of water,  $f_{H_2O}$ , for three different, fixed ratios of volume fractions of crystalline cellulose, amorphous cellulose, hemicellulose, lignin, and extractives (see Tab. 1.2), typical for three different softwoods. Indices after a comma refer to tensor components, and not to partial differentiation.

(1.17)-(1.22) and (1.79)-(1.82)]; and at the same time, the more this pressure expands the pore space occupied by the cell wall water [quantified in terms of the Biot modulus, as shown in Figs. 1.8(b) and 1.8(c), based on Eq. (1.27), together with (1.19), (1.22), and (1.79)-(1.82)]. The same holds for the cell wall level (see Figure 1.8).

It is also interesting to study the influence of different chemical compositions of the cell walls of different softwoods (see Tab. 1.2 for spruce, douglasie, and cedar), on the overall poroelastic properties. The Biot tensor coefficients and moduli at the polymer network level, related to different cell wall compositions, vary by up to 5.1 %. Slightly higher variations of up to 5.3 % are encountered with the Biot tensor components and the Biot moduli at the cell wall level. The by far largest influence is observed at the softwood level: As a function of the cell wall composition, softwood Biot moduli change by as much as 24.3 % (see Figure 1.9), and drained softwood elastic components change by up to 17 %. Moreover, Biot tensor components change even qualitatively: While the Biot tensor com-

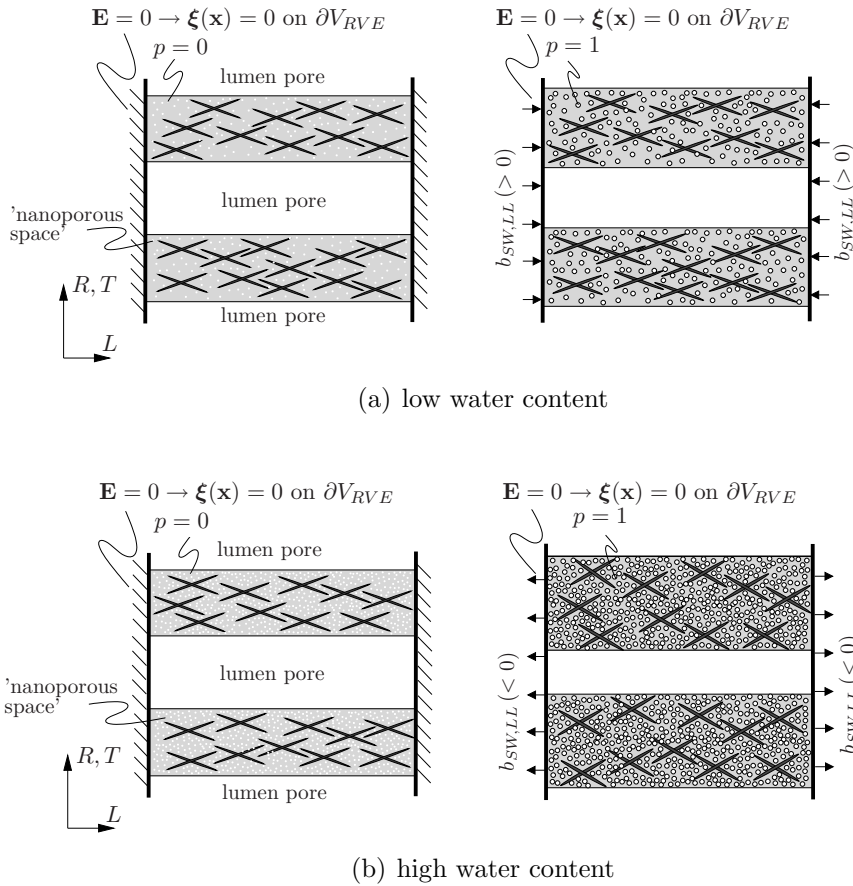


**Figure 1.12:** Illustration of Biot tensor components of softwood material for (a) low water contents and for (b) high water contents, where large lateral expansion leads to re-orientation of cellulose fibers towards the transverse direction, which finally provokes longitudinal tension in the cell walls of the softwood honeycomb.

ponents at the lower material levels are always positive (pore pressure leads to compressive traction forces at the fixed boundary of an RVE, see Figure 1.10), the axial longitudinal Biot tensor component  $b_{SW,LL}$  may even change its sign, depending on the water content of the considered piece of softwood. For lower water contents, the same (positive) sign is encountered as in the hierarchical levels below that of "softwood", regardless of the lumen volume fraction, see Figure 1.11. For high water contents, however, the polymer network matrix becomes extremely soft (with respect to the quite stiff, inclined crystalline cellulose fibers embedded into it), so that nanoporous pressure results in significant extension of the polymer network matrix. At the level of an unconstrained piece of cell wall material, this extension of the matrix would lead to lateral expansion, but to longitudinal contraction, because of the inclined configuration of the stiff fibers of crystalline cellulose. In a piece of softwood, however, the longitudinal deformations are restrained (much more than the lateral deformations of the cell wall material, which is virtually free to expand into the lumen pores), so that nanoporous pressure finally provokes tensile tractions in the longitudinal direction, as indicated in Figure 1.12(b).



## 1.8 Concluding remarks

By extending the framework of poro-micromechanics to more than two material phases, we here elucidated the poroelastic role of water in the cell walls of softwood. All Biot tensor components, expressing how much of the cell wall water-induced pore pressure is transferred to the boundary of an overall deformation-free representative volume element (RVE), were found to increase with increasing water content. On the other hand, the relationship "longitudinal Biot tensor component versus volume fraction of water within the wood cell wall" exhibits a maximum, representing a trade-off between pore pressure increase (increasing the longitudinal Biot tensor component, dominant at low water content) and softening of the cell wall (reducing this component, dominantly at high volume fractions of water). Soft cell wall matrices reinforced with very stiff cellulose fibers may result in even negative longitudinal Biot tensor components. To the authors knowledge, this is the first time a negative Biot tensor component has been reported, and it should be emphasized that this negativity stems from the combination of very soft porous matrices reinforced by very stiff, inclined fibers, forming, at a much higher scale, a relatively thin wall in a periodic plate-type microstructure. One could expect a similar phenomenon concerning the pores between wax grains forming cell walls reinforced by silk fibers, within honeybee combs (Zhang et al., 2010). The aforementioned maximum effect is also noted for the Biot modulus. This quantity expresses the porosity changes invoked by a pore pressure within such an RVE.

All the aforementioned relationships are expected to be a valuable source when it comes to quantifying the failure risk induced in drying processes of wood (when the present model will help to quantify the stress states in the solid portions of wood evoked by water pore pressure changes due to water loss), but also when modeling the multiscale failure behavior of wood in general, since the present approach allows in a direct way to account for the capability of water to carry hydrostatic compressive loads [leading to a non-zero, positive pressure  $p$  as introduced in Eq. (1.8)], rather than tensile loads [suggesting negative values for  $p$  as inadmissible]. These issues are the topic of ongoing research work.

Thereby, in case of large variations in water content (due to drying or water uptake), attention has to be paid to the fact that the volume of the water-saturated pore space within the cell wall is a function of the water content itself (Stamm, 1964; Kollmann, 1982). Corresponding micromechanical models for materials with changing volume fractions have been recently proposed for creep of aging concrete (Scheiner and Hellmich, 2009). In case of drying, micromechanics modeling of capillary effects (Chateau and Dormieux, 1998, 2002) might play an important role when the focus is on removal of water from the lumen pores (after cutting a living tree). However, the present contribution was focused on already empty lumen pores, and further drying would be rather related to removal of water which is bound by means of hydrogen bonds (Fengel and Wegener, 1984) to the surfaces of the lignin-hemicellulose "skeleton" of homogenization step I in Figure 1.2. This removal is accompanied by a merging of skeleton surfaces through new hydrogen bonds, leading to a significant reduction of what we here introduced as "nanoporous space".



## 1.9 Appendix

### 1.9.1 Hill tensor for spherical inclusion in isotropic matrix

This Hill tensor is employed for the spherically shaped phases embedded in the polymer network matrix of homogenization step I(a), see Figure 1.2 and Section 1.3. Accordingly,  $\mathbb{P}_{sph}^{polynet}$  reads as (Eshelby, 1957; Zaoui, 2002)

$$\mathbb{P}_{sph}^{polynet} = \mathbb{S}^{Esh,polynet} : \mathbb{C}_{polynet}^{hom,-1}, \quad (1.79)$$

$$\mathbb{S}^{Esh,polynet} = \alpha_{polynet} \mathbb{J} + \beta_{polynet} \mathbb{K}, \quad (1.80)$$

with

$$\alpha_{polynet} = \frac{3k_{polynet}^{hom}}{3k_{polynet}^{hom} + 4\mu_{polynet}^{hom}}, \quad (1.81)$$

$$\beta_{polynet} = \frac{6(k_{polynet}^{hom} + 2\mu_{polynet}^{hom})}{5(3k_{polynet}^{hom} + 4\mu_{polynet}^{hom})}, \quad (1.82)$$

where  $k_{polynet}$  and  $\mu_{polynet}$  are the bulk and shear moduli of the homogenized polymer network with stiffness  $\mathbb{C}_{polynet}^{hom}$ ;  $\mathbb{J} = \frac{1}{3}\mathbf{1} \otimes \mathbf{1}$  and  $\mathbb{K} = \mathbb{I} - \mathbb{J}$  are the volumetric and the deviatoric part of the fourth-order unity tensor  $\mathbb{I}$  with components  $I_{ijkl} = 1/2(\delta_{ik}\delta_{jl} + \delta_{il}\delta_{kj})$ .

### 1.9.2 Hill tensor for cylindrical inclusions in isotropic matrix

This Hill tensor is employed for the cylindrically shaped phases embedded in the amorphous cellulose matrix of homogenization step I(b), see Figure 1.2 and Section 1.4, and in the polymer network matrix of homogenization step II, see Figure 1.2 and Section 1.5. Accordingly, the non-zero components of the symmetric Hill tensor  $\mathbb{P}_{cyl}^{amocel}$  read as (Hellmich et al., 2004a; Hofstetter et al., 2005)

$$P_{cyl,1111}^{amocel} = P_{cyl,2222}^{amocel} = 1/8(5c_{amocel,1111} - 3c_{amocel,1122})/c_{amocel,1111}/\mathcal{D}, \quad (1.83)$$

$$P_{cyl,1122}^{amocel} = P_{cyl,2211}^{amocel} = -1/8(c_{amocel,1111} + c_{amocel,1122})/c_{amocel,1111}/\mathcal{D}, \quad (1.84)$$

$$P_{cyl,2323}^{amocel} = P_{cyl,1313}^{amocel} = 1/(8c_{amocel,2323}), \quad (1.85)$$

$$P_{cyl,1212}^{amocel} = 1/8(3c_{amocel,1111} - c_{amocel,1122})/c_{amocel,1111}/\mathcal{D}, \quad (1.86)$$

whereby

$$\mathcal{D} = c_{amocel,1111} - c_{amocel,1122} \quad (1.87)$$

and  $c_{amocel,2323} = 1/2(c_{amocel,1111} - c_{amocel,1122})$ , since the matrix material is isotropic. When replacing, (1.83)-(1.87), "amocel" by "polynet", the non-zero components of  $\mathbb{P}_{cyl}^{polynet}$  are given.

### 1.9.3 Unit cell model for softwood

The stiffness tensor components of softwood read as Hofstetter et al. (2007)

$$C_{SW,RRRR}^{hom} = \frac{1}{4\lambda}A, \quad (1.88)$$

$$C_{SW,TTTT}^{hom} = \lambda B, \quad (1.89)$$

$$\begin{aligned} C_{SW,LLLL}^{hom} = & (1 - \hat{f}_{lum}) \left( c_{LLLL} - \frac{c_{RRLL}^2}{c_{RRRR}} \right) - \frac{t}{l_R} \frac{t}{l_T} \left\{ \frac{c_{RRLL}^2}{c_{RRRR}} \left[ 1 - \left( \frac{c_{RRTT}}{c_{RRRR}} \right)^2 \right]^{-1} \right. \\ & \cdot \left( 1 - \frac{c_{RRTT}}{c_{RRRR}} \right)^2 \left( 4 \frac{l_{I,r}}{t} + 2 \frac{l_{II,r}}{t} \right) - 4 \left( \frac{l_{I,r}}{t} \right)^2 \bar{\Delta}_{E,I} \cos^2 \alpha \\ & (\bar{\Delta}_{Q,I} \sin^2 \alpha + \bar{\Delta}_{N,I} \cos^2 \alpha)^{-1} - 4C \frac{l_{I,r}}{t} \bar{\Delta}_{E,I} \cos^2 \alpha \\ & (\bar{\Delta}_{Q,I} \sin^2 \alpha + \bar{\Delta}_{N,I} \cos^2 \alpha)^{-1} \left[ \sin \alpha + \cos^2 \alpha \sin \alpha (\bar{\Delta}_{Q,I} - \bar{\Delta}_{N,I}) \right. \\ & \left. (\bar{\Delta}_{Q,I} \sin^2 \alpha + \bar{\Delta}_{N,I} \cos^2 \alpha)^{-1} \right] - 4C \frac{l_{II,r}}{t} \left. \right\}, \quad (1.90) \end{aligned}$$

$$C_{SW,RRTT}^{hom} = \frac{1}{2} \sin \alpha \cos \alpha (\bar{\Delta}_{Q,I} - \bar{\Delta}_{N,I}) (\sin^2 \alpha \bar{\Delta}_{Q,I} + \cos^2 \alpha \bar{\Delta}_{N,I})^{-1} B, \quad (1.91)$$

$$\begin{aligned} C_{SW,RRLL}^{hom} = & \frac{t}{l_T} \left[ \cos \alpha \sin \alpha (\bar{\Delta}_{Q,I} - \bar{\Delta}_{N,I}) C + \frac{l_{I,r}}{t} \bar{\Delta}_{E,I} \cos \alpha \right] \cdot \\ & \cdot (\bar{\Delta}_{Q,I} \sin^2 \alpha + \bar{\Delta}_{N,I} \cos^2 \alpha)^{-1}, \quad (1.92) \end{aligned}$$

$$C_{SW,TTLL}^{hom} = 2 \frac{t}{l_R} C, \quad (1.93)$$

$$C_{SW,LTLT}^{hom} = c_{LTLT} \lambda \frac{2t}{4l_{II} + l_{III}}, \quad (1.94)$$

$$C_{SW,LRLR}^{hom} = c_{LRLR} \frac{1}{\lambda} \frac{t}{2l_I + l_{III}}, \quad (1.95)$$

$$\begin{aligned} C_{SW,RTRT}^{hom} = & \frac{1}{l_R} \left\{ \left[ \bar{\Delta}_{Q,I} (-\sin \alpha \cos \alpha + 2\lambda \cos^2 \alpha) + \bar{\Delta}_{N,I} (\sin \alpha \cos \alpha + 2\lambda \sin^2 \alpha) \right. \right. \\ & \left. \left. \left( l_I + \frac{l_{III}}{2} \right)^{-1} \cos^{-1} \alpha \right] + \frac{\bar{\Delta}_{Q,II}}{l_{II}} \right\}^{-1}, \quad (1.96) \end{aligned}$$

with

$$A = \left[ (\bar{\Delta}_{Q,I} \sin^2 \alpha + \bar{\Delta}_{N,I} \cos^2 \alpha) - \sin^2 \alpha \cos^2 \alpha (-\bar{\Delta}_{Q,I} + \bar{\Delta}_{N,I})^2 \cdot \right. \\ \left. \cdot (\bar{\Delta}_{Q,I} \cos^2 \alpha + \bar{\Delta}_{N,I} \sin^2 \alpha + 2 \bar{\Delta}_{N,II})^{-1} \right]^{-1}, \quad (1.97)$$

$$B = \left[ (\cos^2 \alpha \bar{\Delta}_{Q,I} + \sin^2 \alpha \bar{\Delta}_{N,I} + 2 \bar{\Delta}_{N,II}) - \sin^2 \alpha \cos^2 \alpha (-\bar{\Delta}_{Q,I} + \bar{\Delta}_{N,I})^2 \cdot \right. \\ \left. \cdot (\sin^2 \alpha \bar{\Delta}_{Q,I} + \cos^2 \alpha \bar{\Delta}_{N,I})^{-1} \right]^{-1}, \quad (1.98)$$

$$C = \left[ \left( \frac{l_{I,r}}{t} \bar{\Delta}_{E,I} \sin \alpha + \frac{l_{II,r}}{t} \bar{\Delta}_{E,II} \right) - \sin \alpha \cos^2 \alpha (-\bar{\Delta}_{Q,I} + \bar{\Delta}_{N,I}) \frac{l_{I,r}}{t} \bar{\Delta}_{E,I} \cdot \right. \\ \left. \cdot (\bar{\Delta}_{Q,I} \sin^2 \alpha + \bar{\Delta}_{N,I} \cos^2 \alpha)^{-1} \right] \left[ (\bar{\Delta}_{Q,I} \cos^2 \alpha + \bar{\Delta}_{N,I} \sin^2 \alpha + 2 \bar{\Delta}_{N,II}) - \right. \\ \left. - \sin^2 \alpha \cos^2 \alpha (-\bar{\Delta}_{Q,I} + \bar{\Delta}_{N,I})^2 (\bar{\Delta}_{Q,I} \sin^2 \alpha + \bar{\Delta}_{N,I} \cos^2 \alpha)^{-1} \right]^{-1}, \quad (1.99)$$

$$\bar{\Delta}_{N,I/II} = \frac{l_{I/II,r}}{t c_{RRRR}} \left[ 1 - \left( \frac{c_{RRTT}}{c_{RRRR}} \right)^2 \right]^{-1}, \quad (1.100)$$

$$\bar{\Delta}_{E,I/II} = \frac{c_{RRLL}}{c_{RRRR}} \left[ 1 - \left( \frac{c_{RRTT}}{c_{RRRR}} \right)^2 \right]^{-1} \left( 1 - \frac{c_{RRTT}}{c_{RRRR}} \right), \quad (1.101)$$

$$\bar{\Delta}_{Q,I/II} = \left( \frac{l_{I/II,r}}{t} \right)^3 \frac{4}{c_{RRRR}} \left[ 1 - \left( \frac{c_{RRTT}}{c_{RRRR}} \right)^2 \right]^{-1} + \frac{l_{I/II,r}}{t} \frac{1.2}{c_{RTT}}, \quad (1.102)$$

$$\frac{t}{l_R} = \left\{ 1 + \frac{1}{\lambda \cos \alpha} \left( 1 - \frac{1}{2} \sin \alpha \right) - \right. \\ \left. - \sqrt{\left[ 1 + \frac{1}{\lambda \cos \alpha} \left( 1 - \frac{1}{2} \sin \alpha \right) \right]^2} - \right. \\ \left. \frac{4}{\lambda} \left[ \frac{3(1 - \sin \alpha)}{\cos \alpha} + \frac{1}{2} 2 \cos \alpha (\sin \alpha - 1) + \frac{1}{2} (1 - 2 \sin \alpha)^2 \tan \alpha \right] (1 - \hat{f}_{lum}) \right\} \cdot \\ \cdot \left\{ \frac{2}{\lambda} \left[ \frac{3(1 - \sin \alpha)}{\cos \alpha} + \frac{1}{2} 2 \cos \alpha (\sin \alpha - 1) + \frac{1}{2} (1 - 2 \sin \alpha)^2 \tan \alpha \right] \right\}^{-1}, \quad (1.103)$$

$$\frac{t}{l_I} = 4 \cos \alpha \frac{t}{l_R}, \quad (1.104)$$

$$\frac{t}{l_{II}} = \frac{4}{2\lambda - \tan \alpha} \frac{t}{l_R}, \quad (1.105)$$

$$\frac{t}{l_{III}} = 2 \cos \alpha \frac{t}{l_R} = \frac{1}{2} \frac{t}{l_I}. \quad (1.106)$$

In (1.88), (1.89), (1.94), (1.95), (1.96), (1.103), and (1.105),  $\lambda = l_T/l_R$  is the cross-sectional aspect ratio of the hexagonally shaped softwood unit cell, i.e. lambda is the ratio of the mean tangential lumen diameter  $l_T$  to the mean radial lumen diameter  $l_R$ .  $\alpha$  is the inclination angle of the radial cell walls.

# Poromechanical scale transitions of failure stresses in wood: from lignin to the spruce level (Bader et al., 2010)

Authored by Thomas K. Bader, Karin Hofstetter, Christian Hellmich, and Josef Eberhardsteiner

Published in *Zeitschrift für Angewandte Mathematik und Mechanik, ZAMM*, 90:750–767, 2010

Wood strength is highly anisotropic, due to the inherent structural hierarchy of the material. In the framework of a combined random-periodic multiscale poro-micromechanics model, we here translate compositional information throughout this hierarchy into the resulting anisotropic strength at the softwood level, based on "universal" elastic properties of cellulose, hemicellulose, and lignin, and on the shear strength of the latter elementary constituent. Relating, through elastic energy-derived higher-order strains in a poromechanical representative volume element, the (quasi-)brittle failure of lignin to overall softwood failure, results in a macroscopic microstructure-dependent failure criterion for softwood. The latter satisfactorily predicts the biaxial strength of spruce at various loading angles with respect to the grain direction. The model also predicts the experimentally well-established fact that uniaxial tensile and compressive strengths, as well as the shear strength of softwood, depend quasi-linearly on the cell water content, but highly nonlinearly on the lumen porosity.

## Nomenclature

$amocel$	amorphous cellulose
$\mathbf{b}^{hom}$	homogenized ('macroscopic') Biot tensor $r$
$\mathbf{b}_r$	Biot tensor of phase $r$
$\mathbf{B}_S^{hom}$	homogenized Skempton tensor
$\mathbb{C}^{hom}$	homogenized ('macroscopic') stiffness tensor
$\mathbb{c}_r$	stiffness tensor of phase $r$
$C_{r,ijkl}$	components of the stiffness tensor of phase $r$
$c$	compression (subscript)
$cel$	cellulose
$crycel$	crystalline cellulose
$cwm$	cell wall material
$d$	characteristic length of inhomogeneity
$\mathcal{E}$	elastic energy density
$\mathbf{E}$	homogenized ('macroscopic') strain tensor
$\bar{E}$	mean of absolute errors
$\mathbf{e}$	base vector
$e$	mean of relative errors
$ext$	extractives
$exp$	experimental value
$\mathcal{F}$	failure function
$f_r$	volume fraction of phase $r$
$\tilde{f}_r, \bar{f}_r, f_r, \hat{f}_r$	volume fraction of phase $r$ in a representative volume element (RVE) of polymer network, cellulose, cell wall material, or softwood, respectively
$H_2O$	water
$hemcel$	hemicellulose
$k_r$	bulk modulus of phase $r$
$\mathbf{1}$	second-order unity tensor
$\mathbb{1}$	fourth-order unity tensor
$\mathbb{J}$	volumetric part of $\mathbb{1}$
$\mathbb{K}$	deviatoric part of $\mathbb{1}$
$l$	characteristic length of RVE
$\mathcal{L}$	material or loading length
$lig$	lignin
$lum$	lumen
$M^{hom}$	homogenized overall Biot modulus
$\mathbf{n}$	unit normal vector
$N^{hom}$	homogenized ('macroscopic') Biot modulus

**Nomenclature cont'd**

$N_r$	Biot modulus of phase $r$
$p$	pore pressure within cell wall
$p$	eigenstress, eigenstrain (superscript)
<i>polynet</i>	polymer network
<i>pred</i>	predicted by poroelastic multiscale model
$\mathbf{R}_\alpha$	second-order rotation tensor related to rotation angle $\alpha$
RVE	representative volume element
$\bar{S}$	standard deviation of absolute errors
$s$	standard deviation of relative errors
<i>SW</i>	softwood
$t$	tension (subscript)
$\mathbf{T}$	(microscopic) traction force
$tr(\cdot)$	trace of tensorial quantity ( $\cdot$ )
<i>ult</i>	ultimate strength
<i>undr</i>	undrained conditions
$V_r$	volume inside representative volume element (RVE), occupied by phase $r$
$w$	weakest compound in composite material (subscript)
$\mathbf{x}$	position vector inside a representative volume element
$\alpha$	loading angle = grain angle = fiber angle
$\delta_{ij}$	Kronecker delta
$\bar{\bar{\epsilon}}_{n,d}$	quadratic average of norm of deviatoric strain of phase $n$
$\epsilon_{n,d}$	norm of deviatoric strain
$\boldsymbol{\epsilon}_d$	deviatoric strain tensor
$\varphi$	inclination angle of the radial cell walls
$\phi$	nano-porosity within cell wall, related to softwood volume
$\phi_0$	initial nano-porosity
$\gamma$	biaxiality ratio
$\bar{\theta}$	microfibril angle
$\lambda$	loading parameter
$\rho$	apparent mass density
$\mu_r$	shear modulus of phase $r$
$\boldsymbol{\xi}$	microscopic displacement vector
$\boldsymbol{\Sigma}$	homogenized ('macroscopic') stress tensor
$\boldsymbol{\Sigma}^0$	normalized direction in stress space
$\boldsymbol{\sigma}_r$	(average 'microscopic') stress tensor of phase $r$
$\sigma_{d,r}^{ult}$	shear strength of phase $r$

**Nomenclature cont'd**

$\Omega$	volume of a representative volume element (RVE)
$\partial\Omega$	surface of a representative volume element (RVE)
$\omega_p$	volume occupied by the nanoporous space
1, 2, 3	principal material directions
$I, II, III$	principal loading directions
$R, T, L$	radial, tangential, and longitudinal material directions
$\langle \cdot \rangle$	volume average
$\langle \cdot \rangle_{V_r}$	volume average over phase $r$
$\cdot$	first-order tensor contraction (inner product)
$:$	second-order tensor contraction
$\ \cdot\ $	tensor norm

**2.1 Introduction**

Wood strength is highly anisotropic: The material resistance in stem direction is about one order of magnitude higher than that orthogonal to the stem (Bodig and Jayne, 1982; Kollmann, 1982; Eberhardsteiner, 2002). Obviously, this anisotropy stems from the intrinsic structural hierarchy of the material (Fengel and Wegener, 1984; Kollmann and Côté, 1968). Wood is composed of prismatic wood cells with hard walls and hollow cores making up the so-called lumen porosity. The wood cells exhibit a quasi-hexagonal cross-sectional shape (of one to a few hundreds of microns characteristic length), which allows them to be assembled in form of a honeycomb structure, which is oriented in stem direction. The cell wall is built up by stiff cellulose fibrils with crystalline cores and amorphous surfaces, deviating from the stem direction by an average angle (*microfibril angle*  $\bar{\theta}$ ) of typically 20 ° (Harada, 1965; Mark, 1967; Tang, 1973) from stem direction. These fibrils are embedded in a soft polymer matrix composed of hemicellulose, lignin, extractives, and water. Consequently, it is well accepted that changes in lumen porosity, as well as such in cell wall composition are the key factors governing wood strength magnitude and anisotropy. However, what remains a matter of discussion is how wood strength is functionally dependent on the aforementioned key factors. In this context, correlations between respective experimental data are often expressed in terms of empirical relations (Hankinson, 1921; Ashkenazi, 1966; Tsai and Wu, 1971). However, such relations are, as a rule, restricted in applicability and reliability, since they do not explicitly consider the mechanical behavior of the complex hierarchical microstructure of wood, which underlies the aforementioned correlations.

As a remedy, we here aim at predicting relationships between porosity/composition and strength (i.e. brittle ultimate strength and yield limit in case of ductile behavior) in a micromechanical framework. Therefore, we do not go so far as to perform any inelastic macromechanical stress-strain analysis based on some micromechanical input. Still, the developments described in the sequel of this paper go clearly beyond purely elastic macromechanical stress-strain relationships: we investigate poroelastic macroscopic rela-



**Table 2.1:** Experimental set I: 'Universal' (tissue-independent) phase properties [experimental sources: C76... Cousins (1976), C78... Cousins (1978), EY01... Eichhorn and Young (2001), TK91... Tashiro and Kobayashi (1991)]

Phase	Material behavior	Bulk modulus $k$ [GPa]	Shear modulus $\mu$ [GPa]	Source
Amorphous cellulose	isotropic	$k_{amocel} = 5.56$	$\mu_{amocel} = 1.85$	EY01
Hemicellulose	isotropic	$k_{hemcel} = 8.89$	$\mu_{hemcel} = 2.20$	C78
Lignin	isotropic	$k_{lig} = 5.00$	$\mu_{lig} = 2.30$	C76
Water+ extractives	isotropic	$k_{H_2Oext} = 2.30$	$\mu_{H_2Oext} = 0$	
Stiffness tensor components $c_{ijkl}$ [GPa]				
Crystalline cellulose	transversely isotropic	$c_{crycel,1111} = 34.86$	$c_{crycel,1122} = 0$	TK91
		$c_{crycel,3333} = 167.79$	$c_{crycel,2233} = 0$	
		$c_{crycel,1313} = 5.81$		

tionships (with explicit consideration of the pore pressure in the polymer network), and our focus is on concentration and influence relations linking stresses in the lignin phase to the macroscopic stresses and the pore pressure. Thereby, the challenge lies in finding a measure for the stresses in the lignin phase, which is relevant for lignin strength. This challenge concerns two aspects: (i) how to represent the stress heterogeneities throughout the lignin phase?, and (ii) which characteristic of the stress state is relevant for failure? Accounting for the fact that shear failure is a probable failure mode in lignin (Zimmermann et al., 1994; Hepworth and Vincent, 1998; Hofstetter et al., 2008), we investigate the relevance of a *von Mises* criterion, setting a strength limit to the norm of the deviatoric stresses. On the other hand, since the spatial average of (micro-)stresses over a material phase is typically not suitable for reflecting stress peaks leading to local failure (Pichler et al., 2009), we evaluate quadratic stress averages which avoid potential canceling out of positive and negative stress tensor components in the course of the spatial averaging process. Due to the selection of the *von Mises* criterion, however, the aforementioned quadratic stress averages need not to be known for all stress tensor components, but just for the norm of the deviatoric stress. Before discussing these aspects in detail, we will shortly recall basic fundamentals of micromechanics (in Section 2.2), and we will then rely on a recently proposed multiscale microporoelastic model for softwood (Hofstetter et al., 2007; Bader et al., 2010), in which random homogenization techniques (Zaoui, 2002) at the cell wall level (see Figure 2.1, steps I and II) are combined with the periodic homogenization technique (Suquet, 1987) at the softwood level (see Figure 2.1, step III). On the basis of tissue-independent ("universal") elastic properties of the elementary building blocks "lignin", "water", "cellulose", and "hemicellulose", the aforementioned model predicts

the drained stiffness tensor of a specific softwood, as well as its Biot tensor and modulus, as functions of its volume fractions of cellulose, hemicellulose, lignin, (intracellular) water (filling the nanoporous space within the cell walls), and lumens. Respective state equations are reviewed in Section 2.3, covering also the cases of drained and undrained conditions in the nanoporous space within the wood cell walls. Subsequently, in Section 2.4, we focus on how the aforementioned volume fractions and poroelastic properties govern the microstress and microstrain states within a representative material volume of softwood, in the form of higher-order stress/strain averages in the lignin phase. The latter are derived from energy considerations both at the softwood ("macro") level and at the ("micro") level of the elementary components (Dormieux et al., 2002). Relating such higher-order "effective" stresses, representing stress peaks within the lignin phase, to the (quasi-brittle) strength of lignin, yields composition/porosity-dependent elastic limit criteria at the level of softwood, given in Section 2.5. If reaching the lignin strength coincides with overall softwood failure, then the aforementioned elastic limit criteria are identical composition/porosity-dependent failure criteria for softwood. Their practical relevance is studied for the case of spruce, in Section 2.6, on the basis of the biaxial strength testing campaign of Eberhardsteiner (2002). The paper is concluded by micromechanics-based structure-property relationships concerning softwood strength, in Section 2.7.

## 2.2 Representative volume element, stress and strain averages, Hill's lemma

In continuum micromechanics (Hill, 1963, 1965; Zaoui, 2002; Dormieux et al., 2006), a material is understood as matter filling a representative volume element, whereby the following separation-of-scales requirement needs to be fulfilled: the characteristic length of the RVE,  $l$ , needs to be considerably smaller than the length of the structure built up by the material or the loading length of this structure,  $\mathcal{L}$ , - then differential calculus may be used in continuum mechanics applied to the structure. On the other hand,  $l$  needs to be considerably larger than the characteristic length of the inhomogeneities,  $d$ , being statistically representatively dispersed throughout the RVE, - then, material properties (such as elasticity or strength) can be reasonably defined on the RVE. Mathematically, we have

$$d \ll l \ll \mathcal{L}. \quad (2.1)$$

Let the positions within the RVE be labeled by position vector  $\mathbf{x}$ , and let the RVE have volume  $\Omega$  and surface  $\partial\Omega$  with unit normal vectors  $\mathbf{n}(\mathbf{x})$ . If such an RVE is subjected, at its boundary, to traction forces  $\mathbf{T}(\mathbf{x})$  corresponding to homogeneous stresses  $\Sigma$ ,

$$\forall \mathbf{x} \in \partial\Omega : \quad \mathbf{T}(\mathbf{x}) = \Sigma \cdot \mathbf{n}(\mathbf{x}), \quad (2.2)$$

then these homogeneous stresses are equal to the spatial average of the (equilibrated) microstresses within the RVE,

$$\Sigma = \frac{1}{\Omega} \int_{\Omega} \boldsymbol{\sigma}(\mathbf{x}) dV = \langle \boldsymbol{\sigma}(\mathbf{x}) \rangle_{\Omega}, \quad (2.3)$$

**Table 2.2:** Characteristics of the cell wall and of the hexagonally shaped unit cell of spruce wood as tested by Eberhardsteiner (2002)

RVE (see Figure 2.1)	characteristics
Step I(a): polymer network	$\tilde{f}_{hemcel} = 0.40, \tilde{f}_{lig} = 0.40, \tilde{f}_{H_2Oext} = 0.20$
Step I(b): cellulose	$\bar{f}_{crycel} = 0.66, \bar{f}_{amocel} = 0.34$
Step II: cell wall material	$f_{polymet} = 0.66, f_{cel} = 0.34, \bar{\theta} = 20^\circ$
Step III: softwood	$\hat{f}_{lum} = 1 - \rho_{SW}/\rho_{cwm}, \rho_{cwm} = 1.445 \text{ g/cm}^3,$ $\varphi = 20^\circ, l_T/l_R = 1.00$

which is standardly referred to as the "stress average rule". On the other hand, if the RVE is subjected, at its boundary, to displacements  $\boldsymbol{\xi}(\mathbf{x})$  corresponding to homogeneous strains  $\mathbf{E}$ ,

$$\forall \mathbf{x} \in \partial\Omega : \quad \boldsymbol{\xi}(\mathbf{x}) = \mathbf{E} \cdot \mathbf{x}, \quad (2.4)$$

then these homogeneous strains are equal to the spatial average of the (kinematically compatible) microstrains within the RVE,

$$\mathbf{E} = \frac{1}{\Omega} \int_{\Omega} \boldsymbol{\varepsilon}(\mathbf{x}) dV = \langle \boldsymbol{\varepsilon}(\mathbf{x}) \rangle_{\Omega}, \quad (2.5)$$

which is standardly referred to as the "strain average rule". Finally, the average of work done by any equilibrated microstresses (stemming from a traction field related to homogeneous macro-stresses, according to Eq. (2.2)), on any kinematically compatible microstrains (stemming from a displacement field related to homogeneous macro-strains, according to Eq. (2.4)), is equal to the work done by the average microstresses on the average microstrains,

$$\langle \boldsymbol{\sigma}(\mathbf{x}) : \boldsymbol{\varepsilon}(\mathbf{x}) \rangle_{\Omega} = \langle \boldsymbol{\sigma}(\mathbf{x}) \rangle_{\Omega} : \langle \boldsymbol{\varepsilon}(\mathbf{x}) \rangle_{\Omega} = \boldsymbol{\Sigma} : \mathbf{E} \quad (2.6)$$

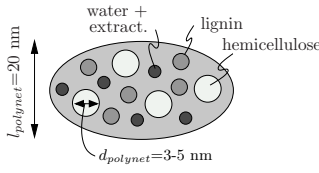
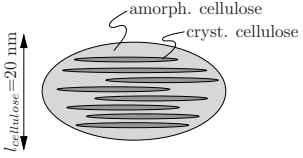
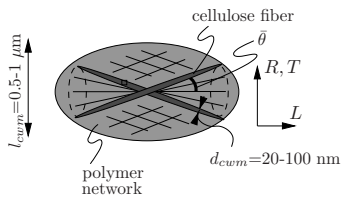
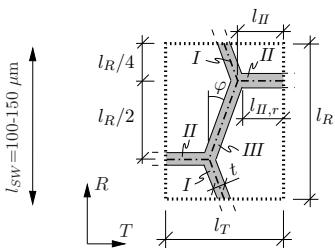
which is standardly referred to as Hill's lemma.

## 2.3 Poroelasticity of softwood

The poroelastic state of an RVE of softwood is characterized by the following state equations,

$$\boldsymbol{\Sigma}_{SW} = \mathbb{C}_{SW}^{hom} : \mathbf{E}_{SW} - \mathbf{b}_{SW}^{hom} p, \quad (2.7)$$

$$(\phi - \phi_0)_{SW} = \mathbf{b}_{SW}^{hom} : \mathbf{E}_{SW} + \frac{p}{N_{SW}^{hom}}, \quad (2.8)$$

RVE	phase	volume fraction	constitutive behavior
<b>Step I(a): polymer network</b>			
self-consistent scheme with spherical inclusions			
	hemicellulose	$\tilde{f}_{hemcel}$	linear elastic, isotropic, $\mathbb{C}_{hemcel}$
	lignin	$\tilde{f}_{lig}$	linear elastic, isotropic, $\mathbb{C}_{lig}$
	water	$\tilde{f}_{H_2O_{ext}}$	water exerted pressure $p$
<b>Step I(b): cellulose</b>			
Mori-Tanaka scheme with cylindrical inclusions			
	amorph. cellulose	$\bar{f}_{amocel}$	linear elastic, isotropic, $\mathbb{C}_{amocel}$
	cryst. cellulose	$\bar{f}_{crycel}$	linear elastic, transv. isotropic, $\mathbb{C}_{crycel}$
<b>Step II: cell wall material</b>			
Mori-Tanaka scheme with cylindrical inclusions			
	polymer network [step I(a)]	$f_{polymet}$	linear poroelastic, isotropic, $\mathbb{C}_{polymet}$ , $\mathbf{b}_{polymet}$ , $1/N_{polymet}$
	cellulose [step I(b)]	$f_{cel}$	linear elastic, transv. isotropic, $\mathbb{C}_{cel}$
<b>Step III: softwood</b>			
Unit cell method with hexagonal lumens			
	cell wall material [step II]	$\hat{f}_{cwm}$	linear poroelastic, transv. isotropic, $\mathbb{C}_{cwm}$ , $\mathbf{b}_{cwm}$ , $1/N_{cwm}$
	lumens	$\hat{f}_{lum}$	empty pores, $\mathbb{C}_{lum} = \mathbb{0}$

**Figure 2.1:** Four-step homogenization scheme on three hierarchical levels, with base frame for definition of stiffness tensors:  $L$  (longitudinal) marks direction parallel to grain, and all directions in the plane spanned by  $R$  (radial) and  $T$  (tangential) are perpendicular to the grain (see also Tab. 2.2).

where  $\boldsymbol{\Sigma}_{SW}$  is the (macroscopic) softwood stress, i.e. the average over the stresses prevailing in the periodically strained honeycomb-type softwood microstructure of Figure 2.1, step III,  $\mathbf{E}_{SW}$  is the (macroscopic) softwood strain, i.e. the average over the strains within the aforementioned honeycomb-type microstructure, and  $\mathbb{C}_{SW}^{hom}$  is the drained homogenized stiffness tensor, linking the two former quantities in absence of a pore pressure  $p$ . As in Bader et al. (2010), we here consider the "nano"-pore pressure  $p$ , exerted by the water within the cell walls, onto the cellulose-lignin network around this cell wall water. In absence of overall softwood strains,  $\mathbf{E}_{SW} = \mathbf{0}$ , this nanopore pressure provokes macroscopic stresses, which are quantified through the second-order tensor of Biot coefficients  $\mathbf{b}_{SW}^{hom}$ , see Eq. (2.7). For thermodynamic reasons [see e.g. Coussy (2004), page 72], the same tensor quantifies the change in (intramural) nanoporosity,  $(\phi - \phi_0)_{SW}$ , resulting from overall softwood strains in absence of any pore pressure, see Eq. (2.8); and in case of overall isodeformation conditions ( $\mathbf{E}_{SW} = \mathbf{0}$ ), the Biot modulus  $N_{SW}^{hom}$  quantifies the nanoporosity change provoked by pressure  $p$ . The poroelastic quantities  $\mathbb{C}_{SW}^{hom}$ ,  $\mathbf{b}_{SW}^{hom}$ , and  $N_{SW}^{hom}$  reflect the complex hierarchical organization of wood, and through a multiscale poroelastic homogenization scheme (Bader et al., 2010), they can all be given as functions of the volume fractions and of the stiffnesses of the elementary components of wood, i.e. of cellulose, hemicellulose, and lignin (see Tab. 2.1). These relationships, documented elsewhere (Hofstetter et al., 2007; Bader et al., 2010), will be the basis for the subsequent developments.

Therefore, it is useful to recall the definitions of drained and undrained conditions (Coussy, 1995, 2004): Under drained conditions, the pore fluid is free to leave or enter the softwood material, and pore pressure  $p$  is controlled by fluid flow and chemo-physical forces. Under undrained conditions, no fluid mass can escape the pore space it fills, which, in case of a linear elastic fluid with bulk modulus  $k_f$ , leads to the following porosity–pore pressure relation (Dormieux et al., 2006; Hellmich and Ulm, 2005; Hellmich et al., 2009):

$$p = -k_{H_2O_{ext}} \frac{(\phi - \phi_0)_{SW}}{\phi_{0,SW}} \quad \text{for } \frac{(\phi - \phi_0)_{SW}}{\phi_{0,SW}} < 0, \quad (2.9)$$

$$p = 0 \quad \text{otherwise.}$$

Eq. (2.9) accounts for the fact that the load bearing capacity of water in tension is negligible when compared to that in compression. Use of Eq. (2.9) in Eq. (2.8) allows for deriving a relationship between macroscopic, softwood-related strain  $\mathbf{E}_{SW}$  and pore pressure  $p$ , in the form

$$p = -M_{SW}^{hom} \mathbf{b}_{SW}^{hom} : \mathbf{E}_{SW} \quad \text{for } \mathbf{b}_{SW}^{hom} : \mathbf{E}_{SW} < 0, \quad (2.10)$$

$$p = 0 \quad \text{otherwise,}$$

with

$$\frac{1}{M_{SW}^{hom}} = \frac{1}{N_{SW}^{hom}} + \frac{\phi_0}{k_{H_2O_{ext}}}. \quad (2.11)$$

Use of Eq. (2.11) in state equation (2.7) yields, upon elimination of  $p$ , the undrained stress-strain relation

$$\boldsymbol{\Sigma}_{SW} = \mathbb{C}_{SW}^{hom,undr} : \mathbf{E}_{SW}, \quad (2.12)$$

with the undrained stiffness tensor

$$\begin{aligned}\mathbb{C}_{SW}^{hom,undr} &= \mathbb{C}_{SW}^{hom} + M_{SW}^{hom} \mathbf{b}_{SW}^{hom} \otimes \mathbf{b}_{SW}^{hom} \quad \text{for } \mathbf{b}_{SW}^{hom} : \mathbf{E}_{SW} < 0, \\ \mathbb{C}_{SW}^{hom,undr} &= \mathbb{C}_{SW}^{hom} \quad \text{otherwise.}\end{aligned}\quad (2.13)$$

On the other hand, upon elimination of  $\mathbf{E}_{SW}$ , combination of Eq. (2.7) and Eq. (2.11) yields the stress-undrained pressure relationship

$$\begin{aligned}p &= -\mathbf{B}_{S,SW}^{hom} : \boldsymbol{\Sigma}_{SW} \quad \text{for } \mathbf{b}_{SW}^{hom} : \mathbf{E}_{SW} < 0, \\ p &= 0 \quad \text{otherwise,}\end{aligned}\quad (2.14)$$

with the Skempton tensor

$$\mathbf{B}_{S,SW}^{hom} = M_{SW}^{hom} \mathbf{b}_{SW}^{hom} : \mathbb{C}_{SW}^{hom,undr,-1}. \quad (2.15)$$

## 2.4 Effective (higher-order) strains at lignin level

While Eq. (2.7) and (2.8) quantify the relationships between the pore pressure residing within the cell wall and the stresses and strains defined at the softwood level, it does not give access to stresses and strains occurring at a finer level, i.e. within the micro and nanostructures making up the cell wall. However, when it comes to material failure and material strength, the interest lies exactly in such finer-scale stresses and strains, more precisely in related local stress and strain peaks where the weakest compound of the composite material would fail. It has been shown (Dormieux et al., 2002; Lemarchand et al., 2002) that such ("microscopic") stress and strain peaks can be estimated through quadratic averages of corresponding deviatoric quantities, reading as

$$\bar{\bar{\varepsilon}}_{w,d} = \sqrt{\frac{1}{2} \frac{1}{V_w} \int_{V_w} \boldsymbol{\varepsilon}_d(\mathbf{x}) : \boldsymbol{\varepsilon}_d(\mathbf{x}) dV} = \sqrt{\frac{1}{2} \langle \boldsymbol{\varepsilon}_d(\mathbf{x}) : \boldsymbol{\varepsilon}_d(\mathbf{x}) \rangle_{V_w}}, \quad (2.16)$$

where  $\boldsymbol{\varepsilon}_d(\mathbf{x})$  is the deviatoric part of the strain tensor  $\boldsymbol{\varepsilon}$

$$\boldsymbol{\varepsilon}_d(\mathbf{x}) = \boldsymbol{\varepsilon}(\mathbf{x}) - \frac{1}{3} \text{tr} \boldsymbol{\varepsilon}(\mathbf{x}). \quad (2.17)$$

In Eq. (2.16)  $V_w$  denotes the subvolume of  $\Omega$ , which is filled by the weakest compound of the composite material, referred to by index  $w$ . In order to derive, from Eqs. (2.7) and (2.8), "effective" higher-order strains according to Eq. (2.16), we follow the line of Dormieux et al. (2002), and consider the elastic energy within an RVE of softwood (with volume  $\Omega$ ). Thereby, we are interested in the average elastic energy in the subvolume  $V$ , which is the overall volume minus the volume  $\omega_p$  occupied by the nanoporous space,

$$V = \Omega - \omega_p. \quad (2.18)$$

The aforementioned elastic energy density  $\mathcal{E}$  (per unit volume of softwood) can be expressed in terms of kinematically compatible (microscopic) strains  $\boldsymbol{\varepsilon}$  within the RVE, in the form

$$\begin{aligned}\mathcal{E} &= (1 - \phi_{SW}) \frac{1}{2} \langle \boldsymbol{\varepsilon}(\mathbf{x}) : \mathbf{c}(\mathbf{x}) : \boldsymbol{\varepsilon}(\mathbf{x}) \rangle_V = \\ &= (1 - \phi_{SW}) \frac{1}{2} \sum_i \langle \boldsymbol{\varepsilon}(\mathbf{x}) : \mathbf{c}_i : \boldsymbol{\varepsilon}(\mathbf{x}) \rangle_{V_i},\end{aligned}\quad (2.19)$$

where  $V_i$ ,  $i = \text{hemcel}, \text{cel}, \text{lig}, \text{lum}$  are the subvolumes of the softwood material volume, which are occupied by hemicellulose, cellulose, lignin, and lumens, respectively. According to (2.19), we separate the softwood volume into subvolumes related to the elementary material components, rather than such related to all intermediate hierarchical structures of Figure 2.1; thereby following the strategy proposed by Pichler et al. (2008, 2009) in the context of cement and concrete materials. Furthermore, in Eq. (2.19),  $\mathbf{x}$  labels the positions within the RVE of softwood, and  $\mathbf{c}(\mathbf{x})$  relates to the inhomogeneous (micro)elasticity distribution, being approximately uniform in the subvolumes  $V_i$ . When considering the nanoporous space as having zero (solid) stiffness,

$$\forall \mathbf{x} \in \omega_p : \quad \mathbf{c}(\mathbf{x}) = \mathbf{0}, \quad (2.20)$$

and (micro)eigenstresses

$$\forall \mathbf{x} \in \omega_p : \quad \boldsymbol{\sigma}^p = -\mathbf{1}p, \quad (2.21)$$

Eq. (2.19) can be recast in the form Dormieux et al. (2002)

$$\mathcal{E} = \frac{1}{2} \langle \boldsymbol{\varepsilon}(\mathbf{x}) : \mathbf{c}(\mathbf{x}) : \boldsymbol{\varepsilon}(\mathbf{x}) \rangle_\Omega = \frac{1}{2} \langle \boldsymbol{\sigma}(\mathbf{x}) : \boldsymbol{\varepsilon}(\mathbf{x}) \rangle_\Omega - \frac{1}{2} \phi_{0,SW} \langle (-p) \text{tr} \boldsymbol{\varepsilon}(\mathbf{x}) \rangle_{\omega_p}, \quad (2.22)$$

whereby small volume changes  $\text{tr} \boldsymbol{\varepsilon}$  in the nanoporous space fulfill (Dormieux et al., 2002)

$$\forall \mathbf{x} \in \omega_p : \quad \langle \text{tr} \boldsymbol{\varepsilon}(\mathbf{x}) \rangle_{\omega_p} = [\phi - \phi_0]_{SW} / \phi_{0,SW} \approx [\phi - \phi_0]_{SW} / \phi. \quad (2.23)$$

Applying Hill's lemma (2.6) to the first term of the right-hand expression in Eq. (2.22), and combining the result with Eq. (2.7) yields

$$\frac{1}{2} \langle \boldsymbol{\sigma}(\mathbf{x}) : \boldsymbol{\varepsilon}(\mathbf{x}) \rangle_\Omega = \frac{1}{2} \mathbf{E}_{SW} : \mathbb{C}_{SW}^{hom} : \mathbf{E}_{SW} - \frac{1}{2} p \mathbf{b}_{SW}^{hom} : \mathbf{E}_{SW}. \quad (2.24)$$

Applying Hill's lemma (2.6) to the last term of the right-hand expression in Eq. (2.22), and combining the result with Eq. (2.23) and Eq. (2.8) yields

$$\frac{1}{2} \phi_{SW} \langle (-p) \text{tr} \boldsymbol{\varepsilon}(\mathbf{x}) \rangle_{\omega_p} = -\frac{1}{2} p \mathbf{b}_{SW}^{hom} : \mathbf{E}_{SW} - \frac{1}{2} p^2 \frac{1}{N_{SW}^{hom}}. \quad (2.25)$$

Subsequent insertion of Eq. (2.24) and Eq. (2.25) into the right-hand expression of Eq. (2.22) yields a "macroscopic" representation of the energy density  $\mathcal{E}$ , in the form (Dormieux et al., 2002),

$$\mathcal{E} = \frac{1}{2} \mathbf{E}_{SW} : \mathbb{C}_{SW}^{hom} : \mathbf{E}_{SW} + \frac{1}{2} p^2 \frac{1}{N_{SW}^{hom}}. \quad (2.26)$$

In order to quantify, from energy expressions Eq. (2.19) and Eq. (2.26), the higher-order strains (2.16), we consider the isotropy of the weakest phase, lignin, with stiffness  $\mathfrak{C}_{lig} = 3k_{lig}\mathbb{J} + 2\mu_{lig}\mathbb{K}$ , with bulk modulus  $k_{lig}$  and shear modulus  $\mu_{lig}$ , and with  $\mathbb{J}$ ,  $J_{ijkl} = 1/3\delta_{ij}\delta_{kl}$  and  $\mathbb{K} = \mathbb{I} - \mathbb{J}$  being the volumetric and deviatoric parts of the fourth-order unity tensor  $\mathbb{I}$ ,  $I_{ijkl} = 1/2(\delta_{ik}\delta_{jl} + \delta_{il}\delta_{kj})$ , and we then derive the aforementioned energy expressions with respect to the lignin shear modulus  $\mu_{lig}$ , considering corresponding changes in  $\mathfrak{C}_{lig}$ ,  $\boldsymbol{\varepsilon}(\mathbf{x})$ ,  $\mathfrak{C}_{hom}^{SW}$ , and  $N_{SW}^{hom}$ . This yields (with  $\partial\mathfrak{C}_{lig}/\partial\mu_{lig} = 2\mathbb{K}$ )

$$\begin{aligned} \frac{\partial\mathcal{E}}{\partial\mu_{lig}} &= 2\hat{f}_{lig}\bar{\bar{\varepsilon}}_{w,d}^2 + (1 - \phi_{SW}) \left\langle \boldsymbol{\sigma}(\mathbf{x}) : \frac{\partial\boldsymbol{\varepsilon}(\mathbf{x})}{\partial\mu_{lig}} \right\rangle_V = \\ &\frac{1}{2}\mathbf{E}_{SW} : \frac{\partial\mathfrak{C}_{SW}^{hom}}{\partial\mu_{lig}} : \mathbf{E}_{SW} + \frac{1}{2}p^2 \frac{\partial}{\partial\mu_{lig}} \left( \frac{1}{N_{SW}^{hom}} \right), \end{aligned} \quad (2.27)$$

where  $\hat{f}_{lig}$  is the volume fraction of lignin at the softwood level. When considering Eq. (2.20) and (2.21), the average expression in Eq. (2.27) can be recast in the form (Dormieux et al., 2002)

$$(1 - \phi_{SW}) \left\langle \boldsymbol{\sigma}(\mathbf{x}) : \frac{\partial\boldsymbol{\varepsilon}(\mathbf{x})}{\partial\mu_{lig}} \right\rangle_V = \left\langle \boldsymbol{\sigma}(\mathbf{x}) : \frac{\partial\boldsymbol{\varepsilon}(\mathbf{x})}{\partial\mu_{lig}} \right\rangle_{\Omega} + \phi_{SW}p \left\langle \frac{\partial(tr\boldsymbol{\varepsilon})}{\partial\mu_{lig}} \right\rangle_{\omega_p}. \quad (2.28)$$

Applying strain average rule (2.5) and Hill's lemma (2.6) to the first term of the right-hand expression in (2.28) yields

$$\left\langle \boldsymbol{\sigma}(\mathbf{x}) : \frac{\partial\boldsymbol{\varepsilon}(\mathbf{x})}{\partial\mu_{lig}} \right\rangle_{\Omega} = \boldsymbol{\Sigma} : \frac{\partial\mathbf{E}_{SW}}{\partial\mu_{lig}} = 0, \quad (2.29)$$

since the homogeneous strains at the boundary of  $\Omega$  are prescribed: they are therefore independent of  $\mu_{lig}$ . Considering Eq. (2.29) when combining Eq. (2.28) with Eq. (2.23) and Eq. (2.8) yields

$$\phi_{SW}p \left\langle \frac{\partial(tr\boldsymbol{\varepsilon})}{\partial\mu_{lig}} \right\rangle_{\omega_p} = p \frac{\partial\mathbf{b}_{SW}}{\partial\mu_{lig}} : \mathbf{E}_{SW} + p^2 \frac{\partial}{\partial\mu_{lig}} \left( \frac{1}{N_{SW}^{hom}} \right). \quad (2.30)$$

Finally, re-insertion of Eq. (2.30) into (2.27) delivers the sought estimate for the higher-order deviatoric strains in the lignin phase, as

$$\begin{aligned} \bar{\bar{\varepsilon}}_{lig,d} &= \frac{1}{2\sqrt{\hat{f}_{lig}}} \left\{ \mathbf{E}_{SW} : \frac{\partial\mathfrak{C}_{SW}^{hom}}{\partial\mu_{lig}} : \mathbf{E}_{SW} - p^2 \frac{\partial}{\partial\mu_{lig}} \left( \frac{1}{N_{SW}^{hom}} \right) - \right. \\ &\left. 2p \frac{\partial\mathbf{b}_{SW}^{hom}}{\partial\mu_{lig}} : \mathbf{E}_{SW} \right\}^{1/2}. \end{aligned} \quad (2.31)$$

The derivatives of the drained softwood stiffness, of the softwood Biot tensor, and of the softwood Biot modulus with respect to the lignin shear stiffness,  $\partial\mathfrak{C}_{SW}^{hom}/\partial\mu_{lig}$ ,  $\partial\mathbf{b}_{SW}^{hom}/\partial\mu_{lig}$ , and  $\partial(1/N_{SW}^{hom})/\partial\mu_{lig}$ , are accessible through the aforementioned poroelastic multistep random-periodic homogenization scheme of Bader et al. (2010); Hofstetter et al. (2007).



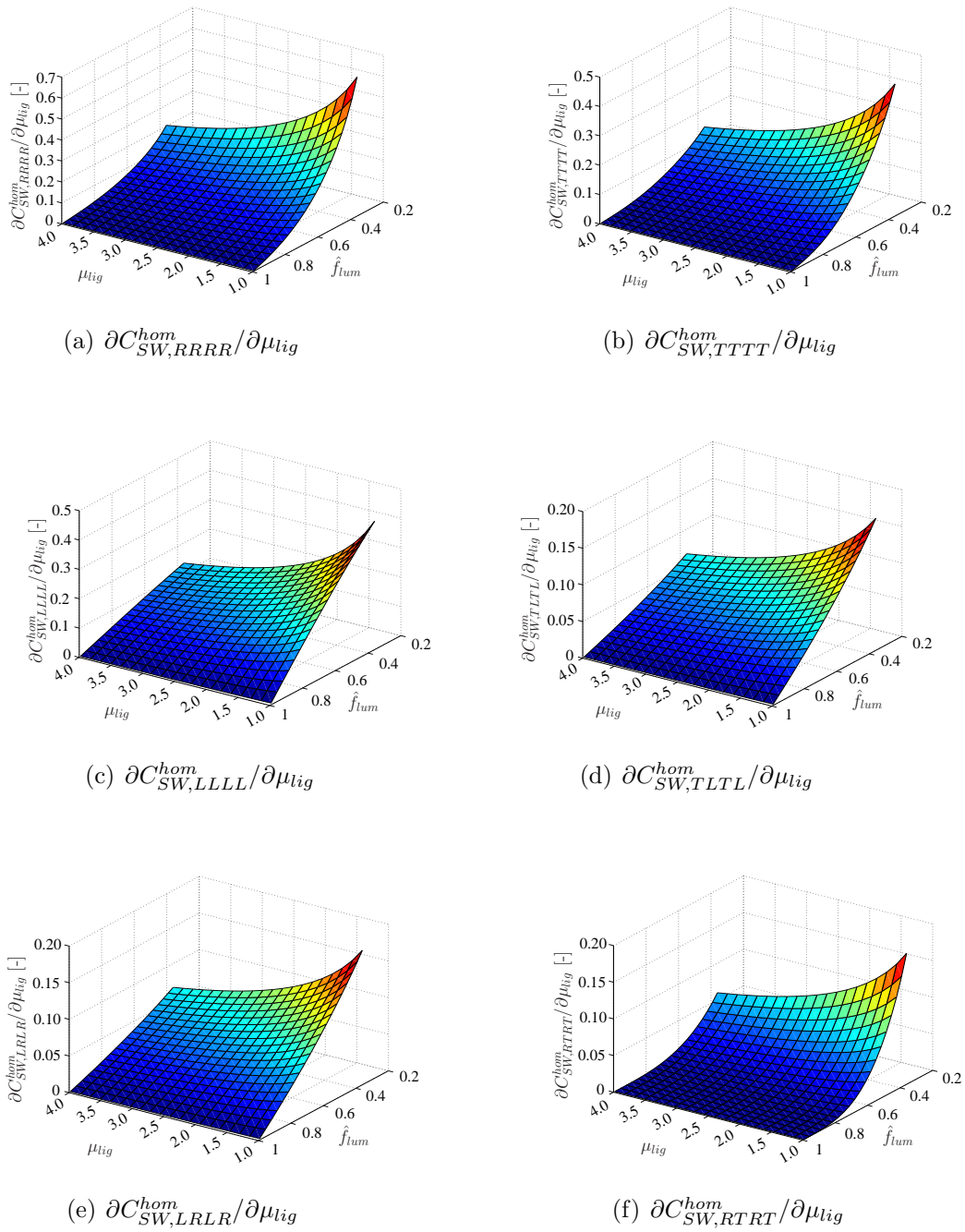


**Figure 2.2:** Characteristics of the poromechanical model for wood strength: Components of the derivative of the softwood-related drained stiffness tensor as functions of the volume fraction of lumen pores  $\hat{f}_{lum}$ , and of the shear modulus of lignin,  $\mu_{lig}$ , for the cell wall characteristics of spruce as tested by Eberhardsteiner (2002) (see Tab. 2.2).

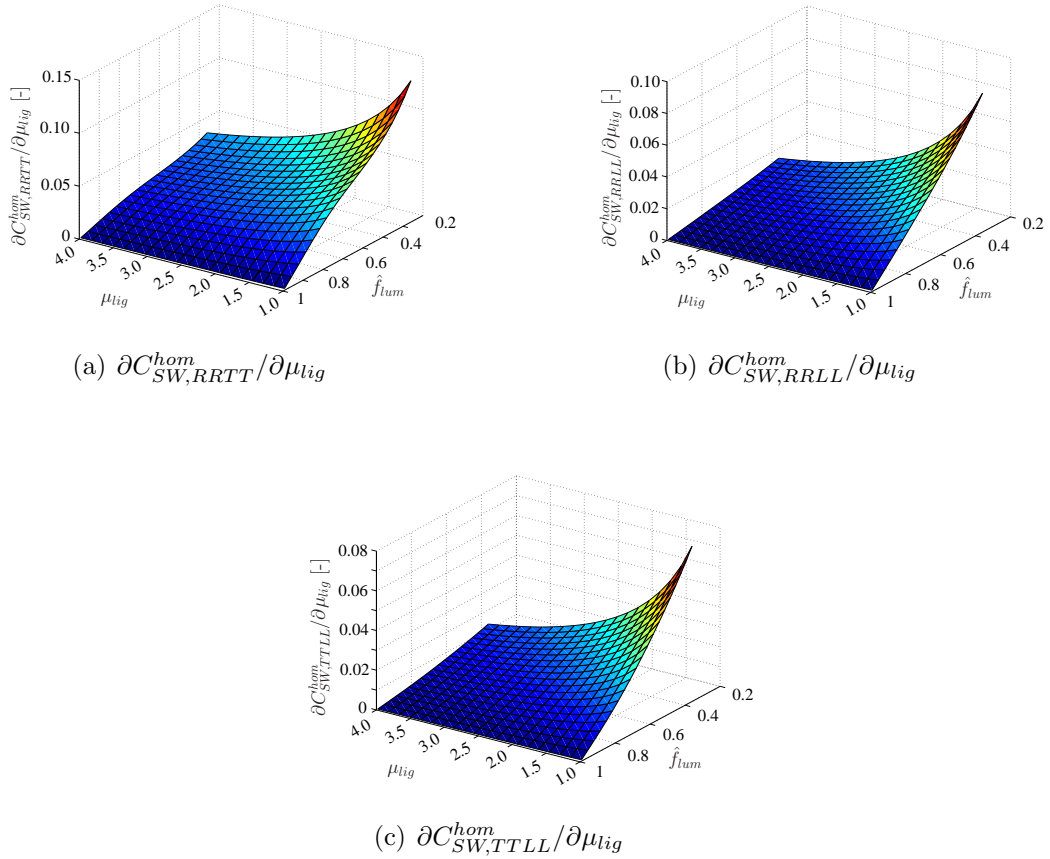


**Figure 2.3:** Characteristics of the poromechanical model for wood strength: Components of the derivative of the softwood-related drained stiffness tensor as functions of the volume fraction of lumen pores  $\hat{f}_{lum}$ , and of the shear modulus of lignin,  $\mu_{lig}$ , for the cell wall characteristics of spruce as tested by Eberhardsteiner (2002) (see Tab. 2.2).

More precisely, this scheme gives the softwood stiffness as a function of the stiffness and volume fraction of the cell wall material (see step III in Figure 2.1), the cell wall stiffness as function of the volume fractions and stiffnesses of cellulose and of a polymeric matrix (see step II in Figure 2.1), the stiffness of the polymeric matrix as function of the stiffnesses and volume fractions of hemicellulose and lignin (see step I(a) in Figure 2.1). Accordingly, the derivation of the softwood stiffness with respect to the lignin shear modulus follows from the chain rule

$$\frac{\partial C_{SW,ijkl}^{hom}}{\partial\mu_{lig}} = \frac{\partial C_{SW,mnpq}^{hom}}{\partial C_{cwm,rstu}^{hom}} \frac{\partial C_{cwm,rstu}^{hom}}{\partial C_{polymet,vwxy}^{hom}} \frac{\partial C_{polymet,vwxy}^{hom}}{\partial\mu_{lig}}, \quad (2.32)$$

in a similar fashion as it was presented by Pichler et al. (2008) in the context of multiscale modeling of concrete. Corresponding results are illustrated in Figs. 2.2 to 2.5, on the basis of the cell wall characteristics of spruce as tested by Eberhardsteiner (2002) (see Tab. 2.2).

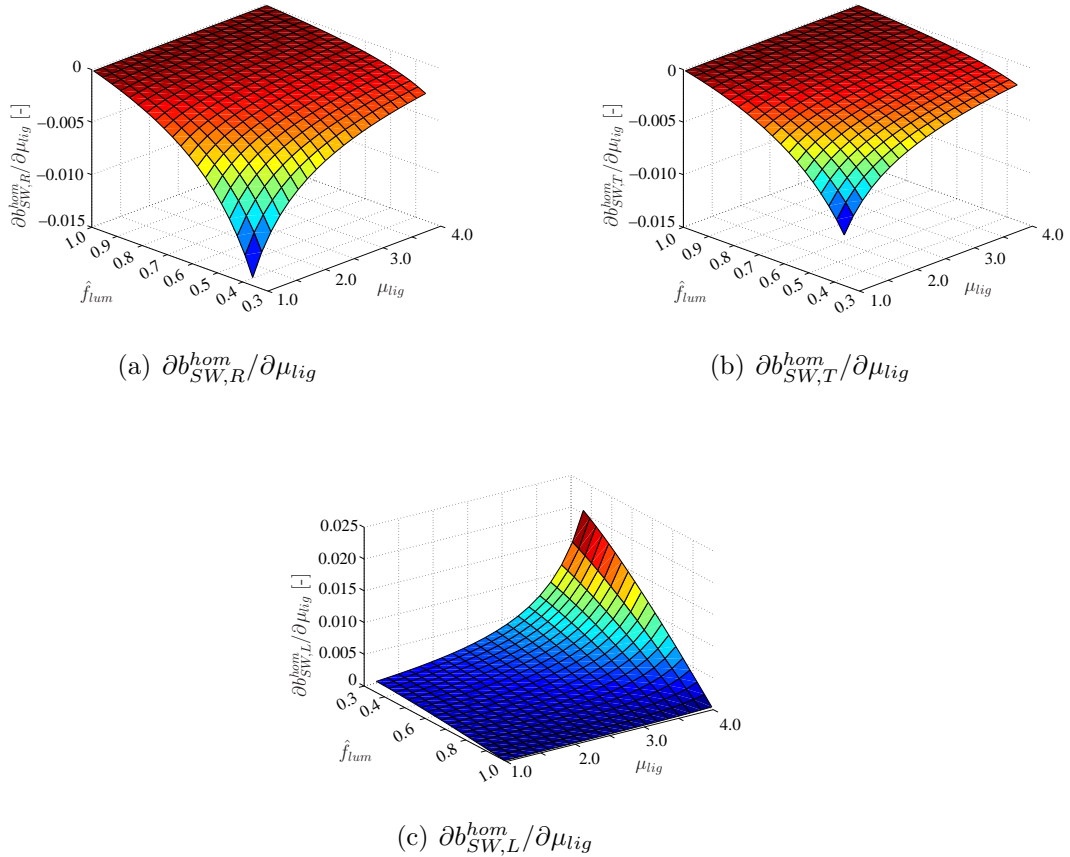


**Figure 2.4:** Characteristics of the poromechanical model for wood strength: Components of the derivative of the softwood-related Biot tensor as functions of the volume fraction of lumen pores  $\hat{f}_{lum}$ , and of the shear modulus of lignin,  $\mu_{lig}$ , for the cell wall characteristics of spruce as tested by Eberhardsteiner (2002) (see Tab. 2.2).

## 2.5 Upscaling failure criterion from lignin to softwood scale - identification of lignin strength

Lignin is known for failing in shear once a threshold is surpassed (Zimmermann et al., 1994; Hepworth and Vincent, 1998). Accordingly, all admissible strain states in the lignin phase are given by

$$\forall \mathbf{x} \in V_{lig} : \mathcal{F}(\varepsilon_d(\mathbf{x})) = \max \left[ 2 \mu_{lig} \varepsilon_d(\mathbf{x}) \right] - \sigma_{d,lig}^{ult} \leq 0, \quad (2.33)$$

where the equal sign in Eq. (2.33) relates to lignin failure, while the lower-than sign relates to linear elastic behavior of lignin. In Eq. (2.33),  $\varepsilon_d$  is the norm of the deviatoric strains  $\varepsilon_d$ ,

$$\varepsilon_d(\mathbf{x}) = \sqrt{\frac{1}{2} \varepsilon_d(\mathbf{x}) : \varepsilon_d(\mathbf{x})}, \quad (2.34)$$

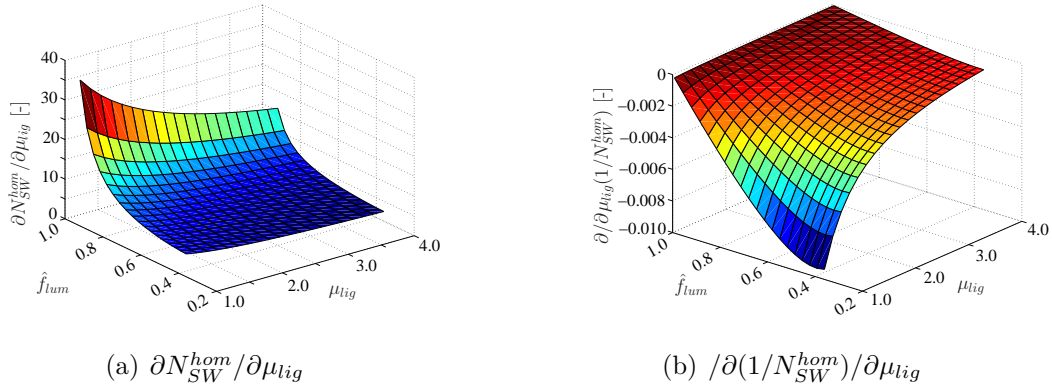


**Figure 2.5:** Characteristics of the poromechanical model for wood strength: Derivative of the softwood-related Biot modulus (a) and its inverse (b) as functions of the volume fraction of lumen pores  $\hat{f}_{lum}$ , and of the shear modulus of lignin,  $\mu_{lig}$ , for the cell wall characteristics of spruce as tested by Eberhardsteiner (2002) (see Tab. 2.2).

and  $\sigma_{d,lig}^{ult}$  is the shear strength of lignin. Eq. (2.33) represents a *von Mises* strength criterion for lignin. In general, the yield behavior of amorphous polymers depends on the hydrostatic pressure because of its influence on molecular mobility (Quinson et al., 1997). This influence is particularly strong at temperatures close to the glass transition region and for polymers exhibiting pronounced molecular relaxation mechanisms (Quinson et al., 1997; Kameda et al., 2007). However, restriction to moderate temperatures in the current context, as well as the strongly cross-linked structure of lignin justify the use of a pressure-independent microscopic failure criterion [Eq. (2.33)] herein.

Strength is governed by (stress or) strain peaks in the corresponding phase (here the lignin phase), as indicated by the max operator in Eq. (2.33). This maximum will be estimated through the higher-order deviatoric strain average Eq. (2.31). Accordingly, micro-strain-related criterion (2.33) can be recast in a macroscopic form, reading as

$$\forall \mathbf{x} \in V_{lig} : \mathcal{F}(\mathbf{E}_{SW}) = \left[ \mu_{lig} \frac{1}{\sqrt{\hat{f}_{lig}}} \left\{ \mathbf{E}_{SW} : \frac{\partial \mathbb{C}_{SW}^{hom}}{\partial \mu_{lig}} : \mathbf{E}_{SW} - p^2 \frac{\partial}{\partial \mu_{lig}} \left( \frac{1}{N_{SW}^{hom}} \right) - 2p \frac{\partial \mathbf{b}_{SW}^{hom}}{\partial \mu_{lig}} : \mathbf{E}_{SW} \right\}^{1/2} \right] - \sigma_{d,lig}^{ult} \leq 0. \quad (2.35)$$

In the following, we consider the particular case of proportional macroscopic loading under undrained conditions. In this case, a scalar loading parameter  $\lambda$  can be determined, by which the macroscopic loading has to be scaled to result in failure. In particular, for a given (undrained) macroscopic loading path  $\Sigma_{SW} = \lambda \Sigma_{SW}^0$ ,  $p = -\lambda \mathbf{B}_{S,SW}^{hom} : \Sigma_{SW}^0$  [see Eq. (2.14)], defined by normalized tensors

$\Sigma_{SW}^0 = \{\Sigma_{SW,ij}^0\}$ ,  $\|\Sigma_{SW}^0\| = \sqrt{1/2 \Sigma_{SW,ij}^0 : \Sigma_{SW,ij}^0} = 1$  marking the direction of the loading in the stress space, the macroscopic strain  $\mathbf{E}_{SW}$  reads as

$$\mathbf{E}_{SW} = \lambda \mathbb{C}_{SW}^{hom,undr,-1} : \Sigma_{SW}^0. \quad (2.36)$$

Use of these specifications in Eq. (2.35) gives a macroscopic failure criterion with  $\Sigma_{SW}^0$  and  $\lambda$  as arguments,

$$\begin{aligned} \forall \mathbf{x} \in V_{lig} : \mathcal{F}(\Sigma_{SW}) = & \left[ \mu_{lig} \frac{\lambda}{\sqrt{\hat{f}_{lig}}} \left\{ \mathbb{C}_{SW}^{hom, undr, -1} : \Sigma_{SW}^0 : \frac{\partial \mathbb{C}_{SW}^{hom}}{\partial \mu_{lig}} : \mathbb{C}_{SW}^{hom, undr, -1} : \Sigma_{SW}^0 - \right. \right. \\ & - (\mathbf{B}_{S, SW}^{hom} : \Sigma_{SW}^0)^2 \frac{\partial}{\partial \mu_{lig}} \left( \frac{1}{N_{SW}^{hom}} \right) + \\ & \left. \left. + 2 \mathbf{B}_{S, SW}^{hom} : \Sigma_{SW}^0 \frac{\partial \mathbf{b}_{SW}^{hom}}{\partial \mu_{lig}} : \mathbb{C}_{SW}^{hom, undr, -1} : \Sigma_{SW}^0 \right\}^{1/2} \right] - \sigma_{d, lig}^{ult} \leq 0. \end{aligned} \quad (2.37)$$

When considering the equal sign in Eq. (2.37), this equation gives for each loading direction  $\Sigma_{SW}^0$ , the corresponding macroscopic loading parameter  $\lambda$  indicating when the elastic limit of lignin is reached. Still, this requires quantification of the lignin strength  $\sigma_{d, lig}^{ult}$ , which, to the best knowledge of the authors, cannot be determined from direct experiments (yet). Hence, we consider a pure shear loading condition  $\Sigma_{SW}^0 = \mathbf{e}_I \otimes \mathbf{e}_I + \mathbf{e}_{III} \otimes \mathbf{e}_{III}$ , where direction  $\mathbf{e}_{III}$  deviates by  $\pi/4$  from the longitudinal stem direction (see Figure 2.7). For spruce, the corresponding loading parameter  $\lambda$  was measured as  $\lambda = 6.045$  MPa Eberhardsteiner (2002), so that insertion of this pair  $(\Sigma_{SW}^0, \lambda)$  into Eq. (2.37) allows for identification of the lignin shear strength as  $\sigma_{d, lig}^{ult} = 14.3$  MPa.

## 2.6 Experimental validation - spruce under direction-variant biaxial loading

Eberhardsteiner (2002) performed biaxial mechanical tests on spruce, see Figure 2.6 and Mackenzie-Helnwein et al. (2003) for the test setup and test procedure. Only clear wood without any growth irregularities and with linear, parallel and approximately equidistant growth rings was used for the specimens in order to assure approximate material homogeneity. In addition, a special device for displacement-controlled loading of the specimens (see Figure 2.6) ensured that the loading states within the samples stayed homogeneous, even for deviations of the principal loading direction from the principal material directions. Otherwise, shear loading would be encountered as well. This is fundamental for validity of Eq. (2.38).

In a large number of tests, brittle failure is observed. Then, the maximum load is directly related to the strength of the test specimen in terms of an elastic limit state. However, at predominantly compressive loading, especially perpendicular to the grain or lumen axis, a rather ductile failure is observed, resulting in pronounced inelastic deformations. Then, strength in the sense of an elastic limit is defined as the stress where the slope of the experimental stress-strain curve starts to decrease.

Corresponding stresses at the limit states are expressed in pairs of principal stresses,  $[\Sigma_I^{exp}, \Sigma_{III}^{exp}]$ , acting in perpendicular loading directions  $\mathbf{e}_I$  and  $\mathbf{e}_{III}$ ,

$$\Sigma_{biax}^{exp} = \Sigma_I^{exp} \mathbf{e}_I(\alpha) \otimes \mathbf{e}_I(\alpha) + \Sigma_{III}^{exp} \mathbf{e}_{III}(\alpha) \otimes \mathbf{e}_{III}(\alpha), \quad (2.38)$$

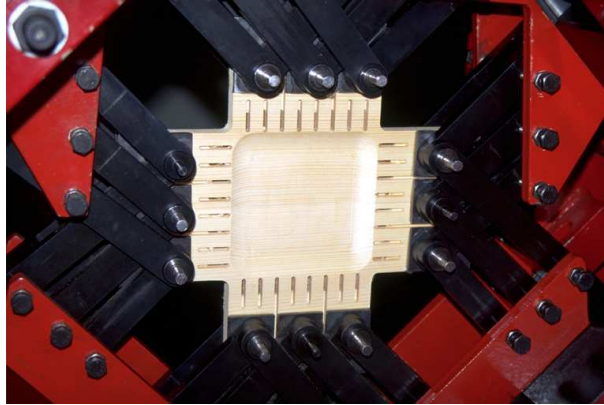


**Figure 2.6:** Cruciform test specimen for biaxial strength tests (Eberhardsteiner, 2002)

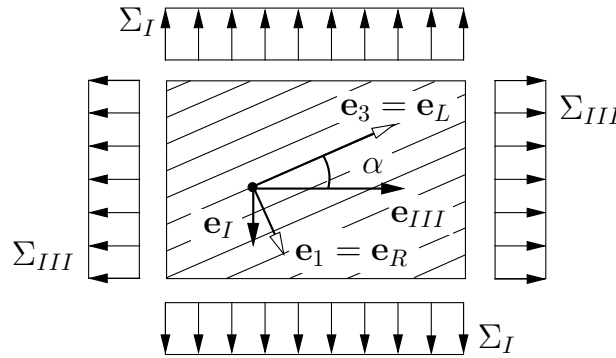


**Figure 2.7:** Biaxial tests at loading or grain angle  $\alpha$  between the principal loading directions  $\mathbf{e}_I, \mathbf{e}_{III}$  and the principal material directions  $\mathbf{e}_L = \mathbf{e}_3$  (parallel to grain),  $\mathbf{e}_R = \mathbf{e}_1$  (perpendicular to grain and to growth rings)

see also Figure 2.7. Loading directions  $\mathbf{e}_I$  and  $\mathbf{e}_{III}$  deviate from the principal material directions  $\mathbf{e}_3 = \mathbf{e}_L$  (oriented parallel to the grain or lumen axis, i.e. in the longitudinal direction  $L$ ) and  $\mathbf{e}_1 = \mathbf{e}_R$  (oriented perpendicular to the growth rings, i.e. in the radial direction  $R$ ) by the loading or grain angle  $\alpha$  (Figure 2.7). This can be expressed by a second-order rotation tensor  $\mathbf{R}_\alpha$ ,

$$\mathbf{R}_\alpha = \mathbf{e}_1 \otimes \mathbf{e}_1 + \cos \alpha \mathbf{e}_2 \otimes \mathbf{e}_2 + \sin \alpha \mathbf{e}_2 \otimes \mathbf{e}_3 - \sin \alpha \mathbf{e}_3 \otimes \mathbf{e}_2 + \cos \alpha \mathbf{e}_3 \otimes \mathbf{e}_3, \quad (2.39)$$

through

$$\mathbf{e}_I(\alpha) = \mathbf{R}_\alpha \cdot \mathbf{e}_1, \quad \mathbf{e}_{III}(\alpha) = \mathbf{R}_\alpha \cdot \mathbf{e}_3. \quad (2.40)$$

Test results are documented for the grain angles  $\alpha \in [0^\circ, 7.5^\circ, 15^\circ, 30^\circ, 45^\circ]$  and for a variety of biaxiality ratios  $\gamma = \Sigma_{III}^{exp} / \Sigma_I^{exp}$ , covering biaxial tension, biaxial compression as well as combined tension / compression in the principal loading directions, respectively (see Eberhardsteiner (2002)).

In the following, we check whether these (ultimate strength or yield) limit values can be predicted by the micromechanical model of Eq. (2.37). Therefore, we feed this model with spruce-specific volume fractions of the cell wall constituents (see Tab. 2.2), with the

strength of lignin amounting to  $\sigma_{d,lign}^{ult} = 14.3$  MPa (see Section 2.5 for details), and with sample-specific values for the lumen porosity, which directly follows from the apparent mass density of softwood given in Eberhardsteiner (2002), through

$$\hat{f}_{lum} = 1 - \frac{\rho_{SW}}{\rho_{cwm}}, \quad (2.41)$$

and the mass density of the cell wall material of softwood amounting to  $\rho_{cwm} = 1.445$  g/cm<sup>3</sup> Hofstetter et al. (2005). More precisely, we evaluate Eq. (2.37) for normalized stress directions  $\Sigma_{SW}^0 = \Sigma_{SW,\gamma\alpha}^0$ ,

$$\Sigma_{SW,\gamma\alpha}^0 = \frac{1}{\sqrt{1+\gamma^2}} [\mathbf{e}_I(\alpha) \otimes \mathbf{e}_I(\alpha) + \gamma \mathbf{e}_{III}(\alpha) \otimes \mathbf{e}_{III}(\alpha)], \quad (2.42)$$

with the aforementioned grain angles and biaxiality ratios of model predictions  $\gamma = \Sigma_{III}^{pred}/\Sigma_I^{pred} \in [-10000, 10000]$ . The aforementioned evaluation yields a specimen- and load-specific loading parameter  $\lambda = \lambda^{ult}(\alpha, \gamma)$ , giving access to estimates for biaxial macroscopic stress states related to the elastic limit of lignin, through

$$\Sigma_{biax}^{ult,pred} = \lambda^{ult}(\alpha, \gamma) \Sigma_{SW,\gamma\alpha}^0 = \Sigma_I^{ult,pred}(\alpha, \gamma) \mathbf{e}_I(\alpha) \otimes \mathbf{e}_I(\alpha) + \Sigma_{III}^{ult,pred}(\alpha, \gamma) \mathbf{e}_{III}(\alpha) \otimes \mathbf{e}_{III}(\alpha) \quad (2.43)$$

with

$$\Sigma_I^{ult,pred}(\alpha, \gamma) = \frac{\lambda^{ult}(\alpha, \gamma)}{\sqrt{1+\gamma^2}}, \quad \Sigma_{III}^{ult,pred}(\alpha, \gamma) = \gamma \Sigma_I^{ult,pred}(\alpha, \gamma). \quad (2.44)$$

For model validation purposes, model-predicted strength estimates for biaxial loading states are depicted in the  $(\Sigma_I, \Sigma_{III})$ -plane, together with experimental results (Figure 2.8). The failure surface, predicted for the mean density of all experimental samples (solid lines in Figure 2.8), gives a good approximation of the mean experimental response (Figure 2.8, test results marked by crosses). Evaluating the model for the minimum and maximum density of all samples results in failure surfaces (dashed lines in Figure 2.8) enclosing most of the experimental elastic limit data. This underlines the suitability of the model and, hence, the central role of lignin as strength-governing component in wood. However, still a remarkable number of experimental points lies outside the predicted failure surfaces related to lignin failure at particular loading states. These points refer to situations where lignin failure does not directly cause overall composite material failure. In fact, at tensile loading in the fiber direction, the cellulose fibrils may keep carrying the load as separated strands, beyond the failure of the polymers. Experimental evidence of intact fibrils after matrix failure under tensile load parallel to the fiber axis was provided by, e.g., Vincent (2003). He presents a photo of the wood microstructure after matrix failure [Figure 5 in Vincent (2003)], which clearly shows that the matrix fractures between the inclined cellulose fibrils, leaving the fibrils largely undamaged. The extra load carrying capacity of the cellulose fibrils shows a large variability, causing a wide spreading of corresponding experimental results (cf. Figure 2.8). The higher the loading angle  $\alpha$ , the lower the additional bearing capacity of wood beyond lignin failure due to the cellulose fibrils, and the lower the number of experimental points outside the largest of the predicted failure surfaces (surfaces of elastic limits). This extra load carrying capacity in tension is also

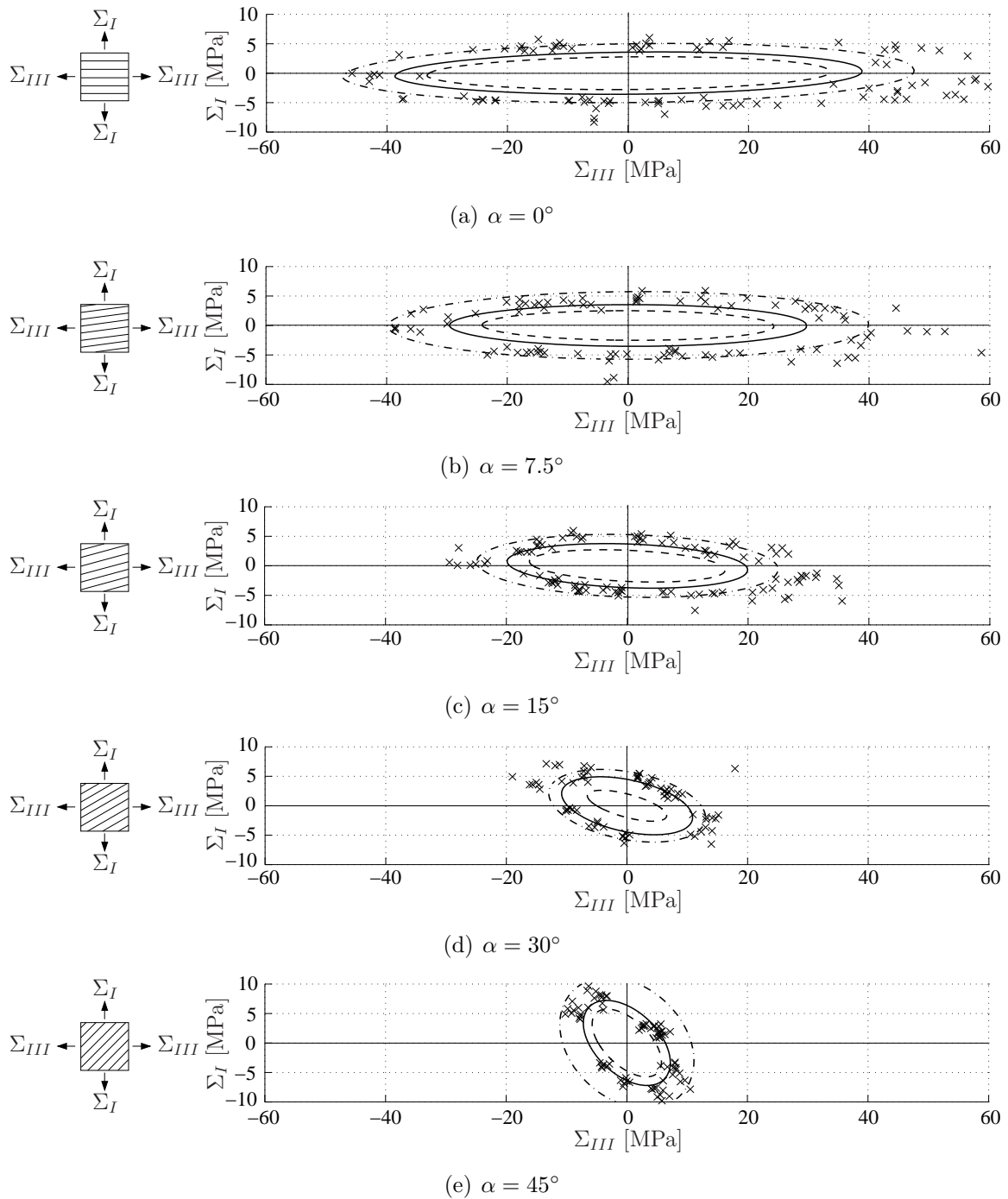


**Figure 2.8:** Results of biaxial experiments and corresponding microporomechanical predictions of plane failure surfaces at different angles  $\alpha$  between principal loading and material directions; model predictions with mean mass density (—) and with maximum and minimum mass density (---) of all test specimens



underlined by the comparison of model predictions for norms of macroscopic stress states related to the elastic limit of lignin,

$$\left\| \underline{\underline{\Sigma}}_{biax}^{ult,pred} \right\| = \sqrt{\frac{1}{2} \underline{\underline{\Sigma}}_{biax}^{ult,pred} : \underline{\underline{\Sigma}}_{biax}^{ult,pred}} = \sqrt{\frac{1}{2} (\Sigma_I^{ult,pred,2} + \Sigma_{III}^{ult,pred,2})}, \quad (2.45)$$

with corresponding experimental results

$$\left\| \underline{\underline{\Sigma}}_{biax}^{ult,exp} \right\| = \sqrt{\frac{1}{2} \underline{\underline{\Sigma}}_{biax}^{ult,exp} : \underline{\underline{\Sigma}}_{biax}^{ult,exp}} = \sqrt{\frac{1}{2} (\Sigma_I^{ult,exp,2} + \Sigma_{III}^{ult,exp,2})}, \quad (2.46)$$

see Figure 2.9. In tension (Figure 2.9(b)), the mean of the absolute errors between model predictions and experiments,

$$\bar{E} = \frac{1}{n} \sum \left( \left\| \underline{\underline{\Sigma}}_{biax}^{ult,pred} \right\| - \left\| \underline{\underline{\Sigma}}_{biax}^{ult,exp} \right\| \right), \quad (2.47)$$

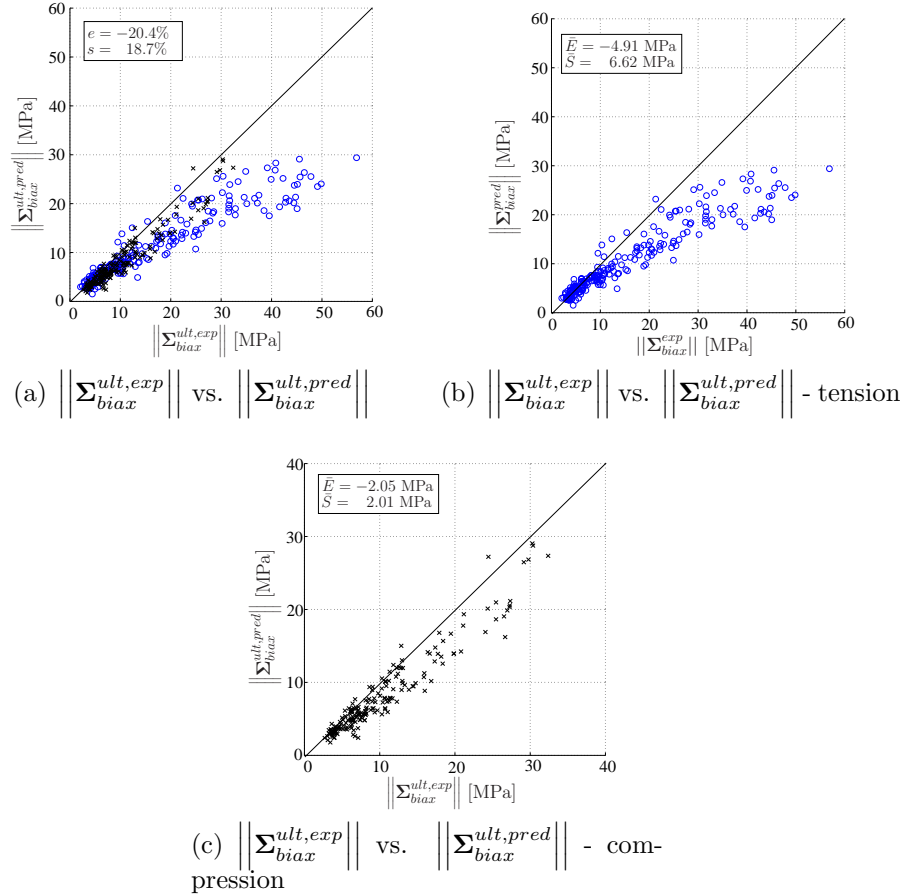


**Figure 2.9:** Comparison of model predicted and measured biaxial strength values expressed by the norm of the corresponding stress tensor for conditions with predominantly tension  $[\circ]$ ,  $sgn[\max(|\Sigma_{III}^{ult,exp}|, |\Sigma_I^{ult,exp}|)] = +1$ , and predominantly compression  $[\times]$ ,  $sgn[\max(|\Sigma_{III}^{ult,exp}|, |\Sigma_I^{ult,exp}|)] = -1$ ; under consideration of sample-specific mass densities.

is by far larger than in compression (Figure 2.9(c)). Still, the latter is also negative, indicating that, also in compression, there may exist a certain load carrying capacity beyond the elastic limit point of lignin. Also the standard deviation of the absolute errors between model predictions and experiments differs significantly in tension and compression (compare Figs. 2.9(b) and 2.9(c)). The by far larger value in tension indicates a larger variety of cellulose load carrying mechanism in tension (where the fiber angles indicated in Figure 2.1, step II are expected to play a central role), when compared to compression.

## 2.7 Conclusions

By combining a recently developed poroelastic multiscale model for softwood Bader et al. (2010); Hofstetter et al. (2007) with a *von Mises*-type failure criterion for lignin, we developed a species and specimen-specific multiscale model for lignin-related elastic limits in softwood. This model was shown to very satisfactorily predict compression-dominated biaxial strength data for spruce (where lignin failure at the nanolevel closely indicates overall failure at the softwood level), and it gives a reliable lower bound for tension-dominated biaxial strength data of spruce (where significant loads may be carried even after lignin has reached its elastic limit). Given these overall satisfactory predictive capabilities of the model (see e.g. Figure 2.9), the model offers itself for studies related to the influence of lumen porosity and loading angle on the uniaxial tensile strength [following from evaluation of Eq. (2.37) for  $\Sigma_{SW}^0 = \Sigma_{SW,\gamma\alpha}^0$  with  $\gamma \rightarrow \infty$ , resulting in  $\lambda_{SW,t}^{ult}(\alpha) = \Sigma_{SW,t\alpha}^{ult,pred}$ ], see Figure 2.10. Corresponding predictions of uniaxial strength show a quasi-linear dependence of strength on porosity and a highly non-linear dependence on

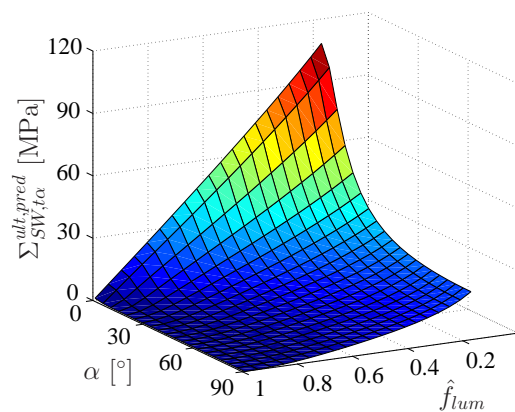


**Figure 2.10:** Model estimates for the tensile elastic limit of softwood,  $\Sigma_{SW,t\alpha}^{ult,pred}$ , as a function of the volume fraction of lumen pores,  $\hat{f}_{lum}$ , and of the loading or grain angle  $\alpha$  between principal loading and material directions, for volume fractions typical for softwood (see Tab. 2.2).

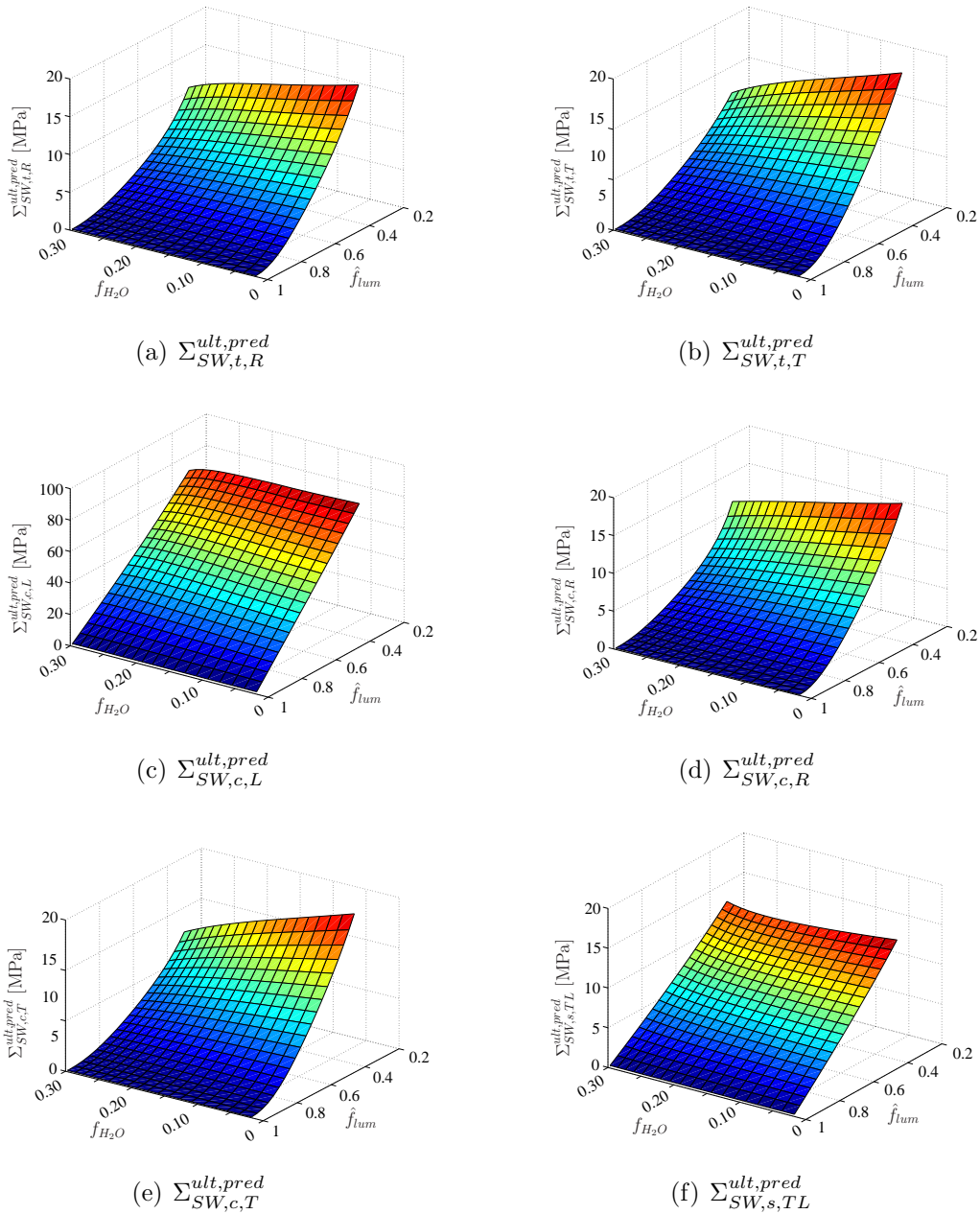


**Figure 2.11:** Characteristics of the poromechanical model for wood strength: Macroscopic stress states related to the elastic limit of lignin, for uniform loading conditions as function of lumen pores  $\hat{f}_{lum}$  and of the cell wall-related volume fraction of water,  $f_{H_2O}$ , for volume fractions typical for softwood (see Tab. 2.2): uniaxial tension in (a) radial and (b) tangential direction, uniaxial compression in (c) longitudinal, (d) radial, and (e) tangential direction; shear in (f) tangential-longitudinal, (g) longitudinal-radial, and (h) radial-tangential planes.

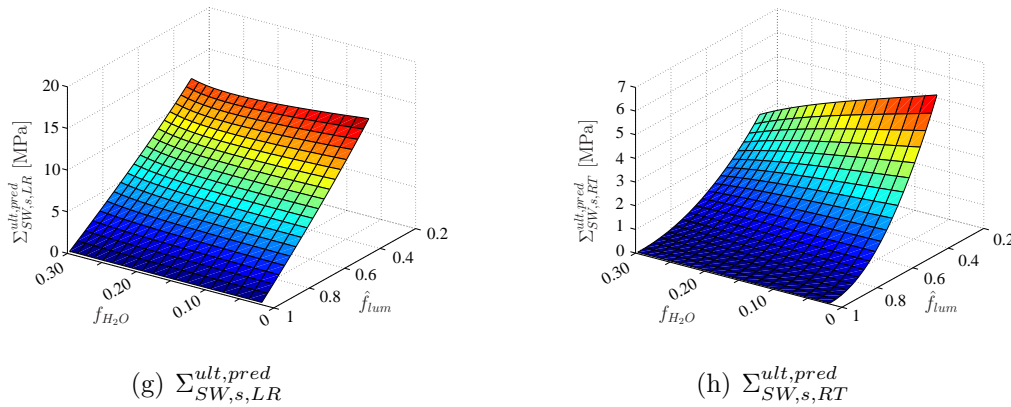


**Figure 2.11** continued: Characteristics of the poromechanical model for wood strength: Macroscopic stress states related to the elastic limit of lignin, for uniform loading conditions as function of lumen pores  $\hat{f}_{lum}$  and of the cell wall-related volume fraction of water,  $f_{H_2O}$ , for volume fractions typical for softwood (see Tab. 2.2): uniaxial tension in (a) radial and (b) tangential direction, uniaxial compression in (c) longitudinal, (d) radial, and (e) tangential direction; shear in (f) tangential-longitudinal, (g) longitudinal-radial, and (h) radial-tangential planes.

the grain angle. These general characteristics agree well with experimental observations gained over decades, which so far were frequently expressed only in terms of empirical relationships (Kollmann, 1934, 1982; Hankinson, 1921). The model also gives access to how strength (or more precisely, lignin-related elastic limits being lower bounds for the former) are governed by the water content in the cell wall, see Figure 2.11 for tensile (t), compressive (c), and shear (s) strength values in the radial (R), tangential (T), and longitudinal (L) directions of spruce, respectively.

It is also interesting to discuss our modeling approach, which is based on poroelastic concentration and influence relations employed to relate lignin failure stresses to stresses at the macroscopic level of spruce, in view of possible nonlinearities in the macroscopic stress-strain relations prior to reaching the ultimate strength of spruce. In this context, it is beneficial to refer to four basic mechanisms in spruce behavior as discussed by Mackenzie-Helnwein et al. (2003): Upon dominant tensile loading in fiber direction, a linear elastic stress-strain regime is bounded by perfectly brittle failure (see Figure 2.12(a)). Under these conditions, the micromechanics-predicted, lignin-failure related limit state of macroscopic stress is identical to the ultimate strength of spruce (unless additional load carrying capacity is provided by the cellulose fibers once the lignin has failed, as is reflected by the experimental points lying outside the model-predicted surfaces in Figure 2.8(a)). The same situation is encountered upon dominant tensile loading in radial direction, see Figure 2.12(b). Upon dominant compressive loading in fiber direction, an elastic regime pertains up to about 75% of the ultimate stress level, followed by a regime of reduced stiffness, before the sample experiences brittle failure (see Figure 2.12(c)). Also under these conditions, the micromechanics-predicted, lignin failure-related limit state of macroscopic

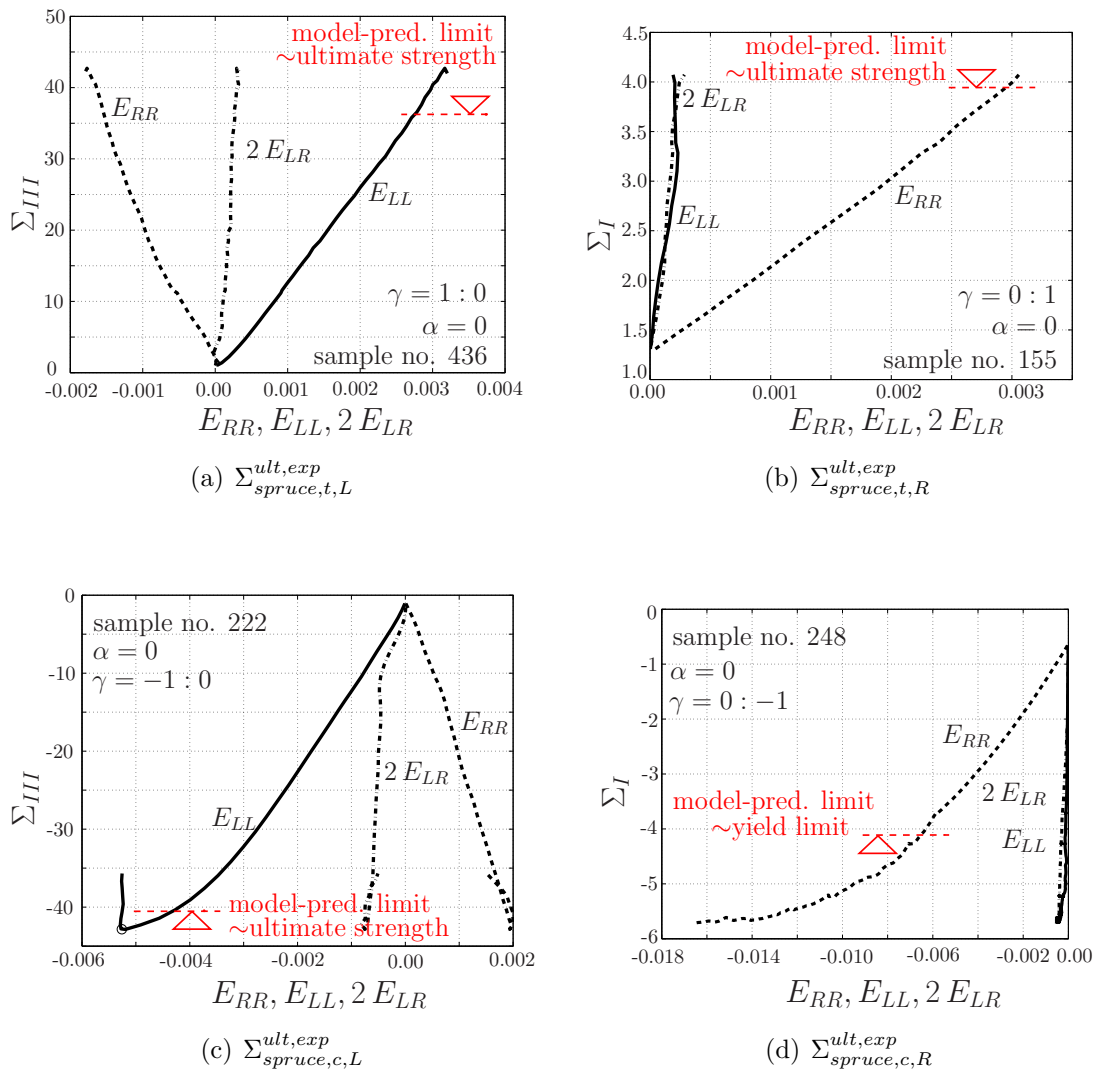


**Figure 2.12:** Typical stress-strain relationships in experiments of Eberhardsteiner (2002), and corresponding model-predicted lignin failure-induced strength limits, see also Figure 2.8(a): (a) uniaxial tension in longitudinal direction, (b) uniaxial tension in radial direction, (c) uniaxial compression in longitudinal direction, (d) uniaxial compression in radial direction.

stress is identical to the ultimate strength of spruce. Hence, in comparison to the purely elastic case, damaging processes leading to the reduced stiffnesses prior to reaching the ultimate load level do not alter the relations between microscopic failure stresses in lignin and corresponding macroscopic stress in spruce. This strongly suggests that the aforementioned damage processes are not related to lignin failure, but rather occur in terms of microcracks at the lignin-cellulose interface. Also upon dominant compressive loading in radial direction, the macroscopic stress-strain curve exhibits a nonlinear portion (see

Figure 2.12(d)). However, under these loading conditions, the micromechanics-predicted, lignin failure-related limit states of macroscopic stress relate to the elastic limit (yield limit) of the material. Hence, inelastic processes in lignin, potentially related to compaction of the polymer matrix, are key to the nonlinear regime which finally encompasses ductile material failure.

While the authors believe that the present model is the very first multiscale poromechanics model related to wood strength, the theoretical restriction to lignin-related elastic limits may be regarded as limitation worth to be overcome in the future: This could be done in the newly emerging field of random homogenization-based multiscale elastoplasticity Fritsch et al. (2009); Pichler and Hellmich (2009).

# Microstructure-stiffness relationships of Common yew and Norway spruce (Bader et al., 2011b)

Authored by Thomas K. Bader, Karin Hofstetter, Josef Eberhardsteiner, and Daniel Keunecke

Accepted for publication in *Strain*, 2011

Yew (*Taxus baccata* L.) exhibits among conifers a unique macroscopic elastic behavior. For example, it shows a comparatively low longitudinal elastic modulus related to its comparatively high density. We herein explore the microstructural origin of these peculiarities, aiming at the derivation of microstructure-stiffness relationships. We measure stiffness properties of yew at different hierarchical levels and compare them to corresponding stiffnesses of Norway spruce (*Picea abies* [L.] Karsten). Cell wall stiffness is investigated experimentally by means of nanoindentation in combination with microscopy and thermogravimetric analysis. On the macroscopic level, we perform uniaxial tension and ultrasonic tests. Having at hand, together with previously reported stiffnesses, a consistent data set of mechanical, chemical, and physical properties across hierarchical levels of wood, we discuss influences of microstructural characteristics at different scales of observation. Moreover, a micromechanical model is applied to predict trends of effects of the microstructure on the investigated stiffness properties. On the cell wall level, particularly, the amount of cellulose and its orientation - which was earlier reported to be distinctly different for yew and spruce - result in differences between the two considered species. On the macroscopic scale, model predicted effects of the annual ring structure on transversal

stiffness and shear stiffness are found to be smaller than effects of the microfibril angle and mass density

### 3.1 Introduction

Already in the Stone Age, Common yew (*Taxus baccata* L.) was known for its superior characteristics for the manufacturing of bows (Oeggel, 2009). The name "taxus", which in Greek means bow, clearly reflects this usage. In medieval times, yew was extensively used for this purpose (Gamstedt et al., 2010). However, the origin of its superior mechanical properties was not so clear up to recent times. Particularly due to developments in experimental characterization techniques that allow resolving material properties down to very small length-scales, these issues concerned recent research efforts (Garab et al., 2010; Keunecke et al., 2007, 2008a,b, 2009).

As other biological materials, wood exhibits a well hierarchically organized microstructure. Starting at the macroscopic level, the growth ring structure is visible to the naked eye and evolves from the alternating formation of bright earlywood and dark latewood during each growth season. Considering the principal material directions in an orthogonal coordinate system, the axis in stem direction is referred to as *longitudinal*, the axis from the pith to the bark as *radial*, and the axis in circumferential direction and perpendicular to the other two as *tangential*. Under the microscope, the cellular structure of wood, with hexagonally shaped wood cells running in stem direction, becomes evident. Their cell walls are composed of different layers, whereby the S2 layer is the dominant one by volume. The cell wall material itself is a typical fiber composite, composed of partially crystalline cellulose fibrils embedded in a polymer matrix of hemicelluloses, lignin, and extractives. In the S2 layer, the cellulose fibrils are highly orientated and inclined to the cell axis by the so-called microfibril angle (MFA). In moist conditions, water is incorporated in the amorphous part of the cell wall.

In contrast to Norway spruce (*Picea abies* [L.] Karsten), which is most commonly taken as a reference in wood science, yew exhibits a lower longitudinal elastic modulus, although it has a considerably higher mass density. This was shown to be a result of a considerably higher MFA in yew cell walls than in spruce cell walls (Keunecke et al., 2008b, 2009). As a further peculiarity compared to other softwood species, yew has a low density ratio from latewood to earlywood, which is also assumed to affect its mechanical properties (Keunecke et al., 2008a).

Aside these singular observations, the particular contribution of each of the microstructural characteristics to the macroscopic stiffness of yew wood is not so clear yet. This motivates to follow up these research activities herein and, as an original contribution, to compile a consistent set of data (mechanical, chemical, and physical properties) across length scales, in order to explore structure-stiffness relations of yew and spruce. This allows to systematically explore specialties of these quite different species and, in a broader context, to deliver a better understanding of wood micromechanics.



Making use of state-of-the-art test methods allows stepping down to still smaller length scales when measuring stiffness properties than previously done. Particularly, we apply nanoindentation to study stiffness properties of Common yew and Norway spruce S2 cell wall layers. Furthermore, we experimentally investigate corresponding cellulose contents and microfibril angles of the S2 layers. Related to the macroscopic scale, we present results from the same samples characterized by means of uniaxial tensile tests and ultrasonic tests. This data is completed by previously reported mechanical (transversal elastic moduli and shear moduli), chemical (extractive content), and physical properties (related to the annual ring structure) of yew and spruce (Garab et al., 2010; Keunecke et al., 2007, 2008a, 2009). The finally assembled consistent data set allows us to bridge the length-scales and to identify the sought microstructure-stiffness relations.

The experimental campaign is complemented by modeling activities. The applied micromechanical model for wood (Bader et al., 2010, 2011a; Hofstetter et al., 2005, 2007) allows to predict stiffness properties at different length scales based on chemical and physical characteristics of the wood microstructure. It is employed to elucidate trends of microstructural influences on stiffness properties in addition to the single experimental data points. This is done at cell wall scale where the influences of cellulose content and orientation on indentation modulus are studied. At the macroscopic scale, effects of the MFA, mass density, and the annual ring structure on the orthotropic stiffness properties are further investigated by means of the model.

## 3.2 Materials and Methods

Five specimens each from the outer heartwood region of Common yew (*Taxus baccata* L.) and Norway spruce (*Picea abies* [L.] Karsten) with dimensions of 20 x 20 x 210 mm<sup>3</sup> (radial  $l_R$  x tangential  $l_T$  x longitudinal  $l_L$ ) were equilibrated to constant climatic conditions of 20 °C and 40 % relative humidity (RH). The longitudinal elastic modulus in tension was measured, before three cubes with dimensions of 20 x 15 x 20 mm<sup>3</sup> ( $l_R$  x  $l_T$  x  $l_L$ ) were cut out of each bar. They served for measurements of stiffnesses in the three principal material directions by means of ultrasound. Thereon, two nanoindentation samples were prepared out of one cube of each species. All mechanical tests are described in more detail below. From the same ultrasound sample, on which the nanoindentation tests had been performed, thermogravimetric analysis was performed to determine the chemical composition. Additionally, microscopy techniques were used to measure microfibril angles of the S2 layer.

### 3.2.1 Tensile tests

Tensile tests were performed on a MTS 858 MiniBionix (MTS Systems corporation, Eden Prairie, MN, USA) with a 15 kN load cell. Longitudinal strain was measured by HBM DD1 clamp-on strain transducers (Hottinger Baldwin Messtechnik GmbH, Wien, Austria) with a zero span of 25 mm. To ensure elastic conditions during the measurement, tensile specimens were loaded with a cross head speed of 0.3 mm min<sup>-1</sup> up to a maximum

displacement of 0.3 mm, which resulted in a maximum stress between 5 and 10 MPa. The elastic modulus  $E_L$  was calculated by fitting regression to the linear part of the recorded curve (10 - 80 % of maximum applied stress).

### 3.2.2 Ultrasonic tests

Ultrasonic (US) tests were performed using a pulser-receiver PR 5077 (Panametrics Inc., Waltham, MA, USA), a digital oscilloscope (WaveRunner 62Xi, Lecroy Corporation, Chestnut Ridge, NY, USA), a pair of ultrasonic transducers for longitudinal pulses with a frequency of 100 kHz (Panametrics Inc., Waltham, MA, USA), honey as coupling medium, and an auxiliary testing device to hold the transducers. In addition, a delay line cylinder made of aluminum alloy 5083 with a height of 20 mm, referring to a time delay of 3.77  $\mu\text{s}$ , was used to re-locate the receiver signal out of the time range of receiver disturbances. A cellophane film was used to prevent the coupling medium honey from infiltrating the wood microstructure and, thus, influencing its stiffness properties. All tests were performed in transmission-through mode in all three principal material directions of wood, namely longitudinal, radial, and tangential direction (see Kohlhauser et al. (2009) for details on the test setup and the equipment). The oscilloscope yields the time of flight of the ultrasonic wave through the specimen  $t_i$ , which provides, in combination with the travel distance through the specimen,  $l_i$ , the phase velocity in a specific material direction  $i = [L, R, T]$  of the wave according to  $v_{ii} = l_i/t_i$ . Elastic stiffnesses, or more precisely, in case of bulk waves, components of the elasticity tensor,  $C_{iii}$ , related to the corresponding direction are then obtained from

$$C_{iii} = \rho v_{ii}^2, \quad (3.1)$$

with sample-specific mass densities  $\rho$  (Bucur, 2006; Kohlhauser et al., 2009).

### 3.2.3 Nanoindentation (NI)

Nanoindentation tests were performed using a Hysitron TriboIndenter system (Hysitron Inc., Eden Prairie, MN, USA), equipped with a three-sided pyramid diamond indenter tip (Berkovich type). The indents per specimen were placed at earlywood and latewood regions, respectively. Experiments were performed in the load-controlled mode using a five segment load ramp: load application within 5 s, holding time 5 s, and unloading time 1 s for each segment. Intermediate segment loads were set to 6, 45, 110, and 195  $\mu\text{N}$  and the peak load to 300  $\mu\text{N}$  for all indents. After every intermediate segment, the sample was unloaded to half of the corresponding load, namely 3, 22.5, 55, and 97.5  $\mu\text{N}$ . Load-indentation depth curves recorded during the NI experiments were evaluated according to Oliver and Pharr (1992) for each load segment. This yields a reduced modulus of elasticity (indentation modulus) from the initial slope of the unloading curve, which is a function of the elastic properties of the cell wall material (Jäger et al., 2011). For each wood species, average indentation moduli of earlywood,  $M_{EW,S2}$ , and of latewood,  $M_{LW,S2}$ , were derived by means of the arithmetic mean of the corresponding indent-specific moduli, whereby a minimum of 20 indents at each region were performed.

### 3.2.4 Thermogravimetric analysis

Thermogravimetric analysis (TGA) measures the amount and rate of change of the weight of a material as a function of temperature and time in a controlled atmosphere. In the present study, TGA was performed according to a method described in Grønli et al. (2002). The tests delivered weight fractions of hemicelluloses, cellulose, lignin, and extractives.

### 3.2.5 Microfibril angle (MFA)

Harsh drying of water-saturated samples at 100 °C induces cracks in the cell wall oriented parallel to the microfibrils in the S2 layer. They were visualized by staining of 20 μm thin radial slices of Norway spruce specimens, according to the method described in Senft and Bendtsen (1985). For Common yew, MFA was measured by investigating the orientation of ray/tracheid cross field pit-apparatus. This method goes back to Cockrell (1974) and was already earlier applied to measure MFA of Common yew (see Keunecke et al. (2008b)).

### 3.2.6 Micromechanical modeling

To elucidate effects of microstructural characteristics on stiffness properties of wood at different length-scales, we apply a well verified multiscale micromechanical model (Bader et al., 2010, 2011a; Hofstetter et al., 2005, 2007), which represents the softwood microstructure in five homogenization steps, see Figure 3.1. Homogenization methods allow to predict the effective mechanical behavior of a micro-heterogeneous material from com-

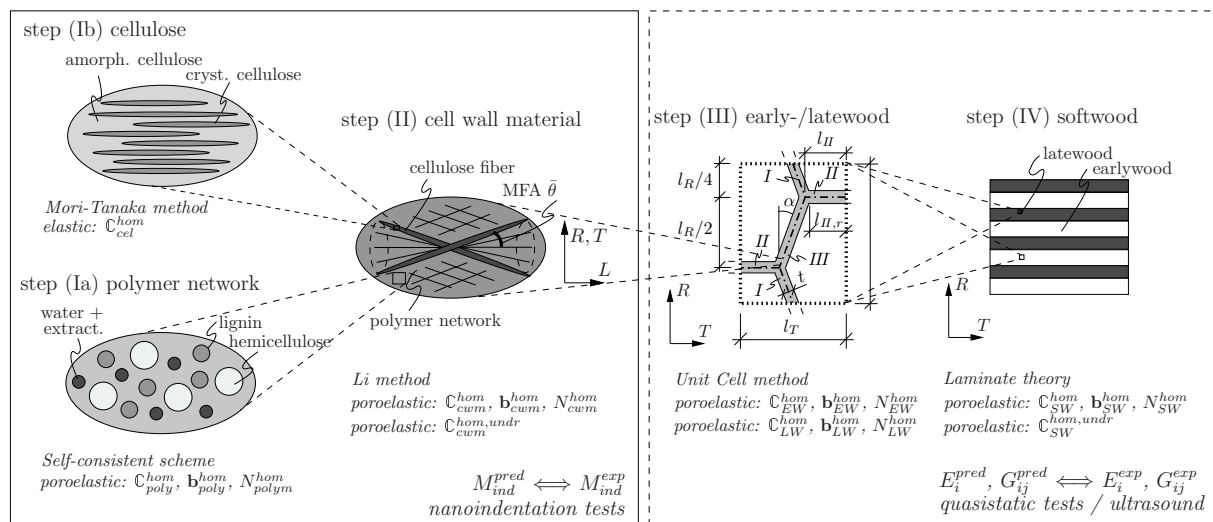


**Figure 3.1:** Micromechanical model for softwood stiffness and evaluation strategy for prediction of microstructural effects at cell wall level, comparable to results of nanoindentation tests (solid box on the left) and on macroscopic stiffness, comparable to results of quasistatic and ultrasonic tests (dashed box on the right).

positional (components and their amount), morphological (shape, orientation and distribution), and mechanical information (stiffness and interaction of components). In the micromechanical model for softwood, effective stiffness properties of the polymer-network [step (Ia)], of cellulose [step (Ib)], and of the cell wall material [step (II)] are predicted by means of continuum micromechanics, whereas that of earlywood and latewood [step (III)] are predicted by means of the unit cell method. Compared to the previous models, herein, the unit cell is numerically analyzed using the commercial Finite Element code ABAQUS. For the investigation of effects of the annual ring structure on softwood stiffness, we extend the micromechanical model documented in Bader et al. (2011a) by an additional homogenization step [step (IV) in Figure 3.1]. This homogenization step is consistently formulated in a poromechanical manner by using laminate theory according to El Omri et al. (2000). A detailed description of this step is given in Appendix A, see Section 3.6.

For comparison of the model with the nanoindentation tests, we determine reduced indentation moduli from the predicted cell wall stiffnesses by following a strategy presented by Jäger et al. (2011).

### 3.3 Results

#### 3.3.1 Mechanical properties

On the macroscopic scale, mean longitudinal elastic moduli in tension of 9.09 GPa ( $\pm 1.34$  GPa) and 14.06 GPa ( $\pm 1.61$  GPa) were measured for yew and spruce, respectively (see Table 3.1). Values in parenthesis refer to corresponding standard deviations. Consistently, we found longitudinal ultrasonic stiffnesses of 12.82 GPa ( $\pm 0.77$  GPa) and 15.74 GPa ( $\pm 1.53$  GPa). Thus, not only the stiffnesses themselves, but also the ratios of longitudinal stiffness to longitudinal elastic modulus are considerably different between yew (mean 1.41) and spruce (mean 1.12). The results are in good agreement with earlier experiments on yew and spruce (Keunecke et al., 2007, 2008a). In addition, ultrasonic tests revealed clearly higher radial and tangential stiffnesses for yew compared to spruce, see Table 3.1. Measured anisotropy ratios of longitudinal to tangential, longitudinal to

**Table 3.1:** Mass density,  $\rho$ , elastic modulus in tension,  $E_L$ , and US-determined stiffnesses in longitudinal,  $C_{LLLL}$ , radial,  $C_{RRRR}$ , and tangential,  $C_{TTTT}$ , direction. Values in parenthesis refer to corresponding standard deviations.

Species	$\rho$ (g/cm <sup>3</sup> )	$E_L$ (GPa)	$C_{LLLL}$ (GPa)	$C_{RRRR}$ (GPa)	$C_{TTTT}$ (GPa)
Yew ( <i>Taxus baccata</i> L.)	0.611 (0.013)	9.09 (1.34)	12.82 (0.77)	4.11 (0.07)	2.91 (0.24)
Spruce ( <i>Picea abies</i> [L.] Karsten)	0.448 (0.009)	14.06 (1.61)	15.74 (1.53)	1.73 (0.09)	1.37 (0.08)

**Table 3.2:** Average nanoindentation moduli of earlywood,  $M_{EW,S2}$ , and of latewood  $M_{LW,S2}$ , S2 cell wall layers, together with corresponding microfibril angles of earlywood,  $MFA_{EW,S2}$ , and latewood,  $MFA_{LW,S2}$ , for yew and spruce, respectively. Values in parenthesis refer to corresponding standard deviations.

Species	$M_{EW,S2}$ (GPa)	$M_{LW,S2}$ (GPa)	$MFA_{EW,S2}$ (°)	$MFA_{LW,S2}$ (°)
Yew ( <i>Taxus baccata</i> L.)	12.86 (1.31)	14.12 (1.71)	38 (6)	27 (6)
Spruce ( <i>Picea abies</i> [L.] Karsten)	18.91 (1.16)	21.16 (1.32)	14 (5)	9 (5)

radial, and radial to tangential stiffness are well in line with earlier test results (Keunecke et al., 2007). However, due to the ultrasound testing technique, the obtained stiffnesses are frequency dependent and known to be considerably higher than corresponding elastic moduli (Bucur, 2006; Keunecke et al., 2007, 2008a; Kohlhauser et al., 2009).

On the cell wall level, clearly higher indentation moduli were measured in spruce than in yew, not only in earlywood but also in latewood (see Table 3.2). Earlywood indentation moduli amounted to 12.86 GPa ( $\pm 1.31$  GPa) and to 18.91 GPa ( $\pm 1.16$  GPa) for yew and spruce, respectively. For both wood species, higher latewood than earlywood indentation moduli were measured. They amounted to 14.12 GPa ( $\pm 1.71$  GPa) and to 21.16 GPa ( $\pm 1.32$  GPa) for yew and spruce, respectively. Figures 3.2b,e show the cellular structure and a cell wall image after nanoindentation tests for both wood species.

Finally, the mechanical data set is completed by transversal elastic moduli and shear moduli previously reported for yew and spruce (Keunecke et al., 2008a), see Table 3.3.

**Table 3.3:** Transversal elastic moduli and shear moduli of yew and spruce reported by Keunecke et al. (2007, 2008a).

Species	$\rho$ (g/cm <sup>3</sup> )	$E_R$ (GPa)	$E_T$ (GPa)	$G_{LR}$ (GPa)	$G_{TL}$ (GPa)	$G_{RT}$ (GPa)
Yew	0.620 (0.039)	0.927 (0.228)	0.627 (0.110)			
( <i>Taxus baccata</i> L.)	0.650 (0.073)			1.740 (0.226)	1.650 (0.226)	0.368 (0.044)
Spruce	0.470 (0.032)	0.625 (0.128)	0.397 (0.041)			
<i>Picea abies</i> [L.] Karsten)	0.400 (0.039)			0.617 (0.075)	0.587 (0.060)	0.053 (0.006)

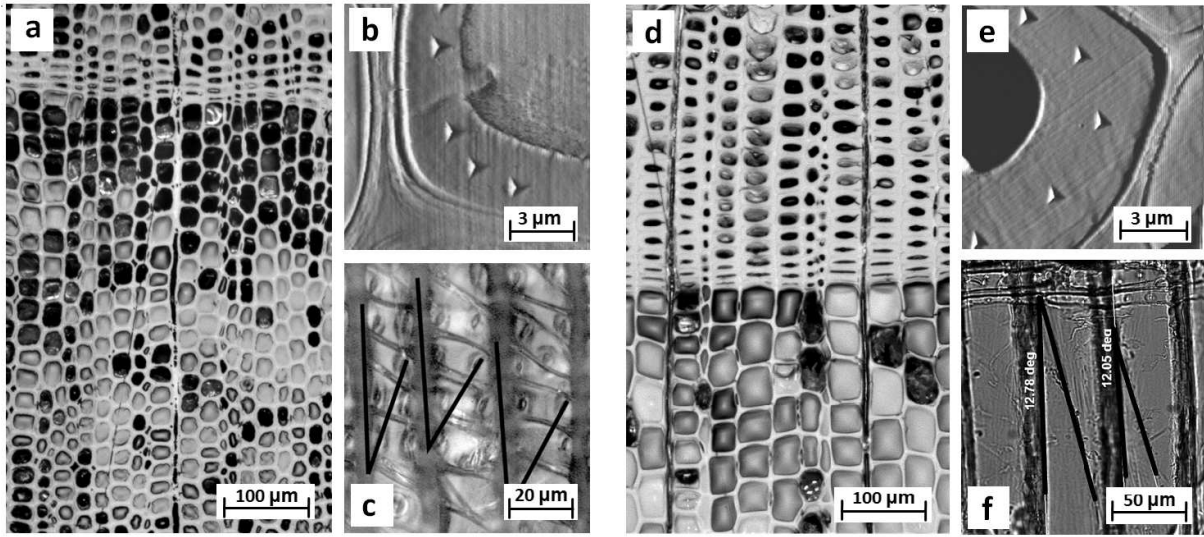


**Figure 3.2:** Microscopy images of cross sections of earlywood and latewood transition regions (a and d), microscopy images of cell walls after nanoindentation (b and e) and a radial view of the cells, where the orientation of cellulose microfibrils in the S2 layer is marked (c and f), for yew (a,b,c) and spruce (d,e,f), respectively.

### 3.3.2 Physical and chemical properties

Mass densities at ambient conditions (20 °C and 40 %RH) amounted to 0.611 g/cm<sup>3</sup> ( $\pm 0.013$  g/cm<sup>3</sup>) and 0.448 g/cm<sup>3</sup> ( $\pm 0.009$  g/cm<sup>3</sup>) for yew and spruce, respectively, see Table 3.1. The cellular structure of both wood species is shown in cross-sectional light microscopy images in Figures 3.2a,d together with cell wall details showing the indents (Figures 3.2b,e) and radial views of the cells, where the directions of the cellulose microfibrils in the S2 layer are marked (Figures 3.2c,f). Our measurements yielded a considerably higher MFA in yew than in spruce, not only in earlywood but also in latewood, see Table 3.2 and Figure 3.2, which is in line with earlier reports (Keunecke et al., 2008b, 2009).

**Table 3.4:** Chemical composition of wood species: weight fractions of cellulose,  $WF_{cel}$ , hemicellulose,  $WF_{hemcel}$ , lignin,  $WF_{lig}$ , extractives,  $WF_{extr}$ , determined by means of thermogravimetric analysis (average) and computed for the S2 layer according to Fengel (1970) (S2 layer).

Species		$WF_{cel}$	$WF_{hemcel}$	$WF_{lig}$	$WF_{extr}$
		(%)	(%)	(%)	(%)
Yew ( <i>Taxus baccata</i> L.)	average	44.7	22.8	29.9	2.6
	S2 layer	53.6	17.6	25.9	2.9
Spruce ( <i>Picea abies</i> [L.] Karsten)	average	49.1	24.4	23.7	2.8
	S2 layer	58.1	18.6	20.2	3.1

**Table 3.5:** Input parameters for micromechanical model for comparison with experimental results from Keunecke et al. (2007, 2008a); chemical composition ... [cellulose, hemicellulose, lignin, extractives].

Wood species	yew ( <i>Taxus baccata</i> L.)		spruce ( <i>Picea abies</i> [L.] Karsten)	
chemical composition	[0.447 0.208 0.239 0.106]		[0.491 0.244 0.237 0.028]	
mass density $\rho$ (g/cm <sup>3</sup> )	0.620		0.470	
moisture content $u$ (-)	0.12 (20 C and 65 %RH)		0.12 (20 C and 65 %RH)	
	earlywood	latewood	earlywood	latewood
density $\rho$ (g/cm <sup>3</sup> )	0.551	0.827	0.379	0.985
microfibril angle ( $^{\circ}$ )	30 $^{\circ}$		12 $^{\circ}$	
volume fraction (-)	0.75	0.25	0.85	0.15
aspect ratio $\lambda$ (-)	0.85	0.95	0.75	1.00
inclination angle $\alpha$ ( $^{\circ}$ )	20 $^{\circ}$	10 $^{\circ}$	20 $^{\circ}$	10 $^{\circ}$

Earlywood MFAs of 38 $^{\circ}$  ( $\pm 6^{\circ}$ ) and 14 $^{\circ}$  ( $\pm 5^{\circ}$ ), and latewood MFAs of 27 $^{\circ}$  ( $\pm 6^{\circ}$ ) and 9 $^{\circ}$  ( $\pm 5^{\circ}$ ) were measured for yew and spruce, respectively. As regards the pit-apparatus method that was used for measuring MFA of yew, the earlywood MFA of yew might be slightly overestimated (see e.g. Huang et al. (1997)).

The chemical composition measured by means of TGA of yew and spruce is summarized in Table 3.4 (average). The cellulose content of yew was found to be slightly lower than that of spruce. Surprisingly, the extractives content of yew was very low, particularly compared to earlier reports (see e.g. references in Keunecke et al. (2007)).

Additionally, microstructural characteristics of the previously investigated yew and spruce samples as documented in Keunecke et al. (2008b) (related to data of transversal and shear moduli summarized in Table 3.3) are specified in Table 3.5. This data is based on X-ray densitometry, X-ray diffraction, and optical microscopy measurements of yew and spruce derived by means of a Silviscan device as documented in Keunecke et al. (2009). The measurements indicate that the latewood to earlywood density ratio is lower for yew ( $\approx 1.5$ ) than for spruce ( $\approx 2.6$ ), see also Kollmann (1982), which is also visible in Figures 3.2a,d in terms of a smaller difference in change of cell wall thickness at the growth ring border in yew than in spruce (see also Fig. 4 in Keunecke et al. (2008a)). Additionally, when considering the reported radial and tangential tracheid diameters, the average ratio of tangential to radial tracheid diameter (aspect ratio  $\lambda$  in Table 3.5) is smaller in yew than in spruce.

### 3.4 Discussion

Starting from the cell wall level up to the macroscopic level, we discuss the experimental results with the specific aim to identify microstructure-stiffness relationships of yew and

spruce and – in a broader and generalizing sense – of wood.

### 3.4.1 Cell wall stiffness

Nanoindentation moduli were found to be distinctly different for Common yew and Norway spruce S2 cell wall layers in earlywood as well as in latewood. This reveals that the different macroscopic mechanical properties of these species are already manifested at the cell wall level. These indentation results are in good agreement with results of micro-tensile tests on yew and spruce wood (see Keunecke et al. (2008b)), where axial cell wall stiffness of yew was found to be considerably smaller than that of spruce. According to the fiber-reinforced composite structure of the cell wall, its axial stiffness and its indentation modulus are considerably affected by the amount and the orientation of the stiff cellulose fibrils (see e.g. Cave (1968); Jäger et al. (2011) among many others). The latter is expressed by the microfibril angle (MFA). The MFA measurements underline differences between spruce and yew with a higher MFA of yew. Moreover, cellulose content of yew was slightly lower than that of spruce (see Table 3.4). Experimentally determined differences in earlywood and latewood indentation moduli can be explained by the lower MFA in latewood than in earlywood, as it was e.g. also shown by Keunecke et al. (2009). The trend of the influences of cellulose content and orientation on the cell wall stiffness is further also elucidated by means of the micromechanical model. For model predictions of stiffness of the S2 layer, we translate the overall chemical compositions of the particular wood species to S2 layer-specific ones according to Fengel (1970), see Table 3.4. Due to

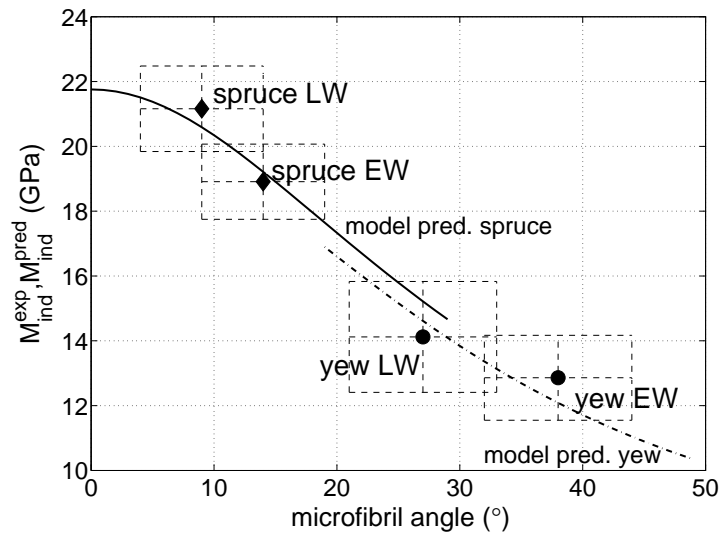


**Figure 3.3:** Influence of MFA at cell wall scale: experimental results (mean: markers, standard deviation: dashed lines) and micromechanical model predictions for the earlywood and latewood indentation moduli,  $M_{EW,S2}$  and  $M_{LW,S2}$ , of spruce (solid line) and yew (dot and dash line) (at 8% moisture content and S2 layer-specific chemical compositions according to Table 3.4).



the low cellulose content of the middle lamella and the primary wall, the cellulose weight fraction of the S2 layer is higher than the overall one. Based on this microstructure data, the effect of changing MFA on the indentation modulus is shown in Figure 3.3. The slight shift of the model predictions for spruce and yew, respectively, results from the lower cellulose content of yew. The markers show the experimental results, and the dashed boxes indicate the experimentally determined variation of indentation modulus and MFA. The almost diagonal crossing of the boxes by the trend line confirms that most of the variation in the indentation modulus can be explained by a corresponding variation in MFA. As discussed earlier, the indentation modulus changes non-linearly with MFA (see Figure 3.3).

### 3.4.2 Macroscopic longitudinal stiffness

Longitudinal elastic moduli obtained in the uniaxial tension tests were found to be distinctly different for Common yew and Norway spruce. As regards longitudinal stiffness, the governing microstructural characteristic between cell wall and solid wood level is mass density, which is strongly related to the cell wall thickness (see e.g. Keunecke et al. (2009) for yew and spruce). Due to the parallel arrangement of earlywood and latewood layers with different densities is negligible in the longitudinal direction. Thus, the longitudinal stiffness is affected by density and – through its dominant effect on the cell wall stiffness – by MFA to the most part. Micromechanical model predicted influences of these two characteristics on the longitudinal elastic modulus are depicted in Figure 3.4. Species-specific

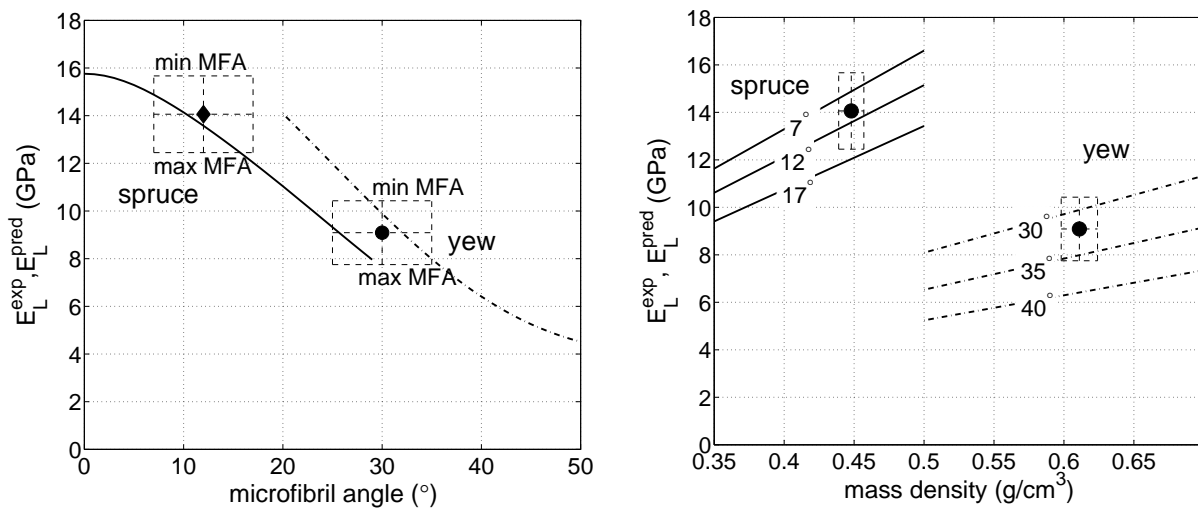


**Figure 3.4:** Influence of MFA (left) and mass density (right) at scale of softwood: experimental results (mean: markers, standard deviation: dashed lines) and micromechanical model predictions for the longitudinal elastic modulus  $E_L$  of yew and spruce (at 8% moisture content, average chemical compositions according to Table 3.4, and mass densities according to Table 3.1).

average chemical compositions according to Table 3.4 and mass densities according to Table 3.1 were used therein. The markers in Figure 3.4 show the experimental results, and the dashed boxes indicate the experimentally determined variation of longitudinal elastic modulus, of MFA, and of mass density. As regards MFA, based on the experimental data of earlywood and latewood MFAs, average values of  $30^\circ (\pm 5^\circ)$  and  $12^\circ (\pm 5^\circ)$  were considered for yew and spruce, respectively, in Figure 3.4a. Similar to the cell wall stiffness, the almost diagonal crossing of the boxes by the trend line in Figure 3.4a confirms that also at macroscopic level most of the variation in the elastic modulus can be explained by a corresponding variation in MFA. Consistently, a non-linear influence of the MFA on the longitudinal elastic modulus is observed. However, the higher mass density of yew has an inverse effect and results in a higher elastic modulus of yew compared to spruce. Figure 3.4b shows the effect of changing mass density for three MFAs for yew and spruce, where a linear relation between longitudinal elastic modulus and mass density becomes evident.

The ultrasonic tests are in line with the quasistatic tension tests and revealed a higher longitudinal elastic stiffness of yew than of spruce. In addition, the ratio of elastic stiffness to elastic modulus was found to be considerably higher in yew than in spruce. Since the ultrasonically determined stiffnesses relate to laterally constrained conditions (Kohlhauser et al., 2009), it can be concluded that yew exhibits a larger lateral contraction than spruce when longitudinal stresses are applied. This is again ascribed to the different MFAs.

### 3.4.3 Macroscopic transverse and shear stiffness

Transversal stiffnesses and shear stiffnesses are found to be distinctly different for Common yew and Norway spruce, see Table 3.3. However, in contrast to longitudinal stiffnesses, transversal stiffnesses and shear stiffnesses of yew are considerably higher than that of spruce. This can be ascribed to various microstructural characteristics, since at this scale of observation, stiffness properties are a function of the entire heterogeneous microstructure of softwood.

On the cell wall level, MFA and cellulose content are the governing characteristics, as described before. While increasing MFA results in decreasing longitudinal stiffness, it causes transversal stiffnesses to increase. Experimental results and model predicted influences of MFA on transversal elastic moduli (based on microstructure properties according to Table 3.5) are depicted in Figure 3.5. As clearly visible in Figure 3.5, low MFAs typical for spruce have a minor effect on transversal moduli; however shear stiffnesses  $G_{LR}$  and  $G_{TL}$  increase with increasing MFA. On the contrary, higher MFAs typical for yew considerably raise radial and tangential moduli as well as shear moduli compared to spruce.

Additionally, macroscopic stiffness properties depend on the thickness of the cell walls, which govern mass density. Figure 3.6 illustrates the influence of changing mass density on transversal and shear stiffnesses for yew and spruce. The markers in Figure 3.6 show the experimental results, and the dashed boxes indicate the experimentally determined variation of elastic moduli, shear moduli, and mass density (see Keunecke et al. (2007, 2008a)). All elastic moduli increase with increased mass density. When considering the

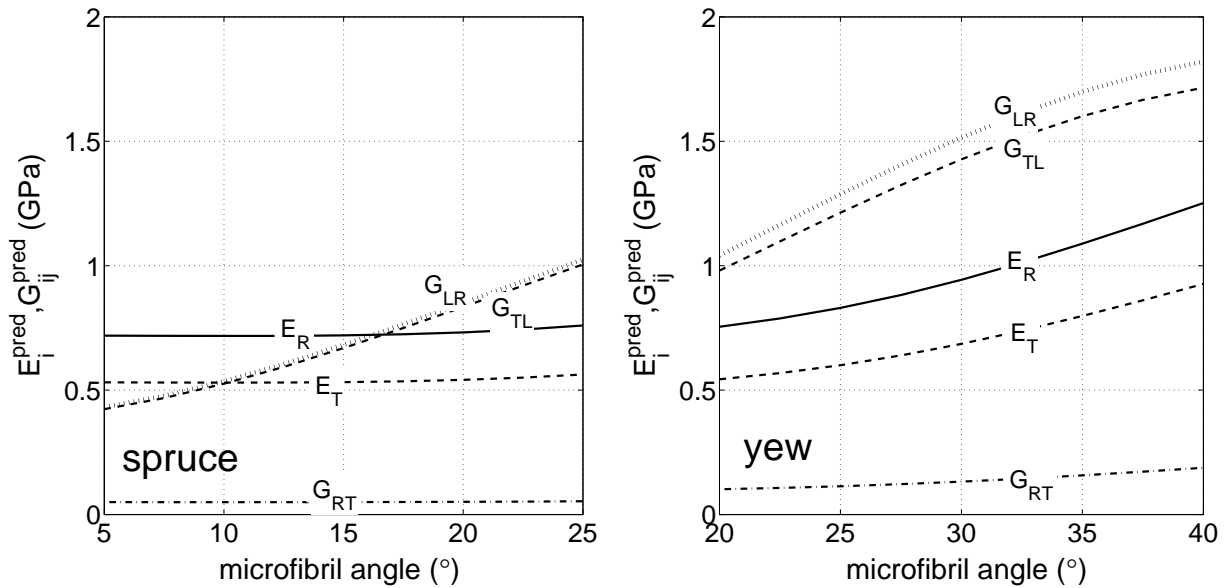


**Figure 3.5:** Influence of MFA at scale of softwood: micromechanical model predictions for the transversal elastic moduli and shear moduli of spruce (left) and yew (right), see Table 3.5 for the species-specific microstructural characteristics.

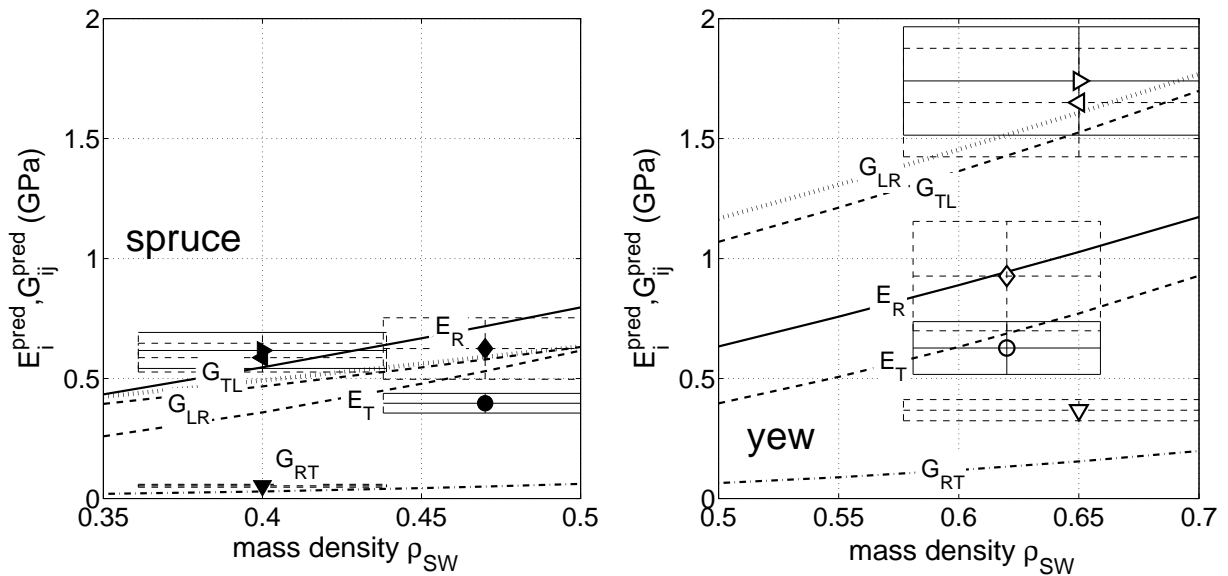
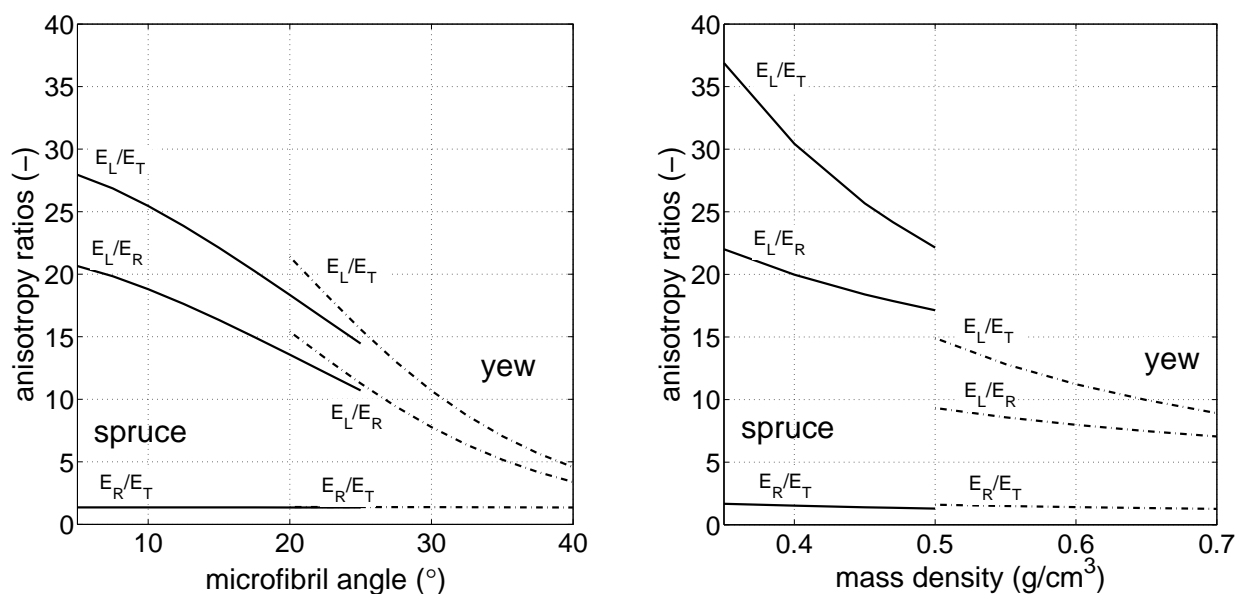


**Figure 3.6:** Influence of mass density at scale of softwood: experimental results documented in (Keunecke et al., 2007, 2008a) (mean:  $\diamond E_R$ ,  $\circ E_T$ ,  $\triangleright G_{LR}$ ,  $\triangleleft G_{TL}$ ,  $\nabla G_{RT}$ , standard deviation: dashed lines, see Table 3.3 for the values) and micromechanical model predictions for the transversal elastic moduli and shear moduli of spruce (left) and yew (right), see Table 3.5 for the species-specific microstructural characteristics.

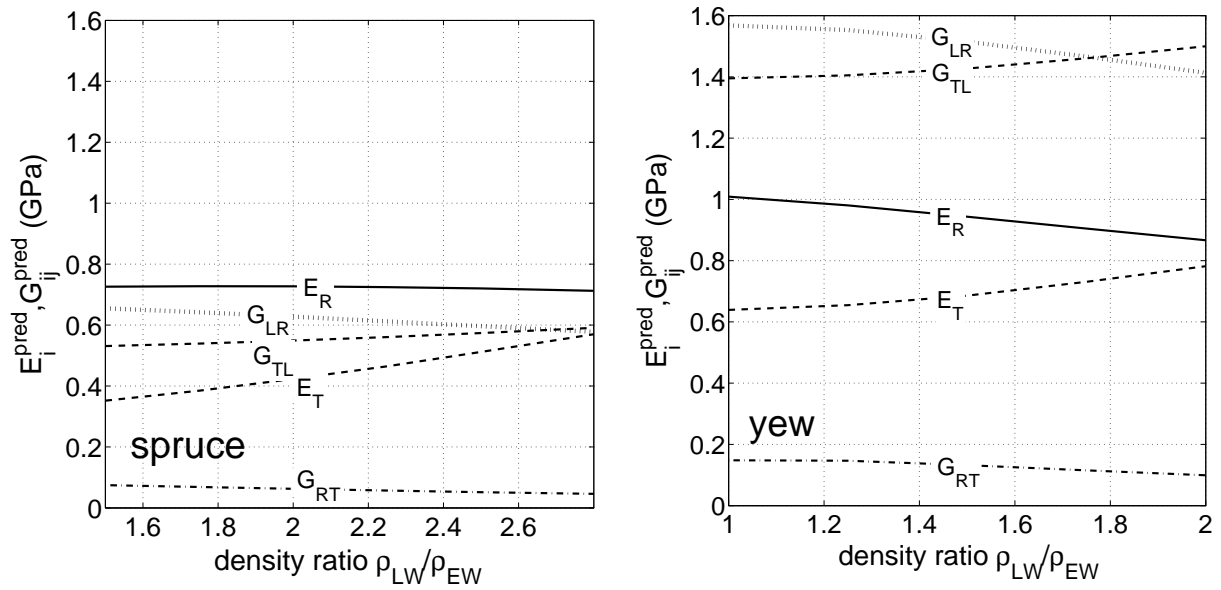
elastic moduli for a density of  $0.500 \text{ g/cm}^3$  for both wood species, it becomes evident that the density-related relative transversal stiffnesses  $E_R$  and  $E_T$  of yew are smaller than that of spruce. This is concluded to result from the different chemical compositions of yew and spruce (see Table 3.5). Elastic moduli  $E_R$  and  $E_T$  of spruce are more strongly dependent on mass density than on MFA. Shear stiffnesses  $G_{LR}$  and  $G_{TL}$  are considerably higher in yew than in spruce, not only due to a high mass density, but also due to the higher MFA and the tracheid shape expressed by the aspect ratio (cf. Figure 3.5).

Figure 3.7 confirms that anisotropy ratios  $E_L/E_T$  and  $E_L/E_R$  of elastic moduli, as discussed earlier and also reported in Keunecke et al. (2007), are strongly dependent on the MFA and mass density. Thus, they are very sensitive to corresponding variations. As regards MFA, strong influence results from the contrary effect of MFA on longitudinal and transversal stiffnesses (cf. Figure 3.4 and Figure 3.5). For the ratio  $E_R/E_T$ , the similar effect of MFA on both of these transversal elastic moduli results in an almost constant course over MFA. As regards mass density, an increase more strongly increases stiffness in the transversal directions than in the longitudinal one (cf. Figure 3.4 and Figure 3.6). This results in a decrease of the anisotropy ratios  $E_L/E_T$  and  $E_L/E_R$  with increasing density.

Macroscopic transverse and shear stiffnesses are also affected by the annual ring structure of alternating earlywood and latewood layers with different densities [step (IV)]. Particularly the latewood to earlywood density ratio and the latewood content are relevant. Due to the lack of specific experimental data, their influence is only studied by means of the micromechanical model. As discussed before, the density ratio is small in yew, whereas it is considerably higher in spruce. Its effect is depicted in Figure 3.8, with con-



**Figure 3.7:** Influence of MFA (left) and mass density (right) at scale of softwood: micromechanical model predictions for anisotropy ratios of elastic moduli of yew and spruce, see Table 3.5 for the species-specific microstructural characteristics.



**Figure 3.8:** Influence of density ratio of latewood to earlywood density at scale of softwood: micromechanical model predictions for the transversal elastic moduli and shear moduli of spruce (left) and yew (right), see Table 5 for the species-specific microstructural characteristics.

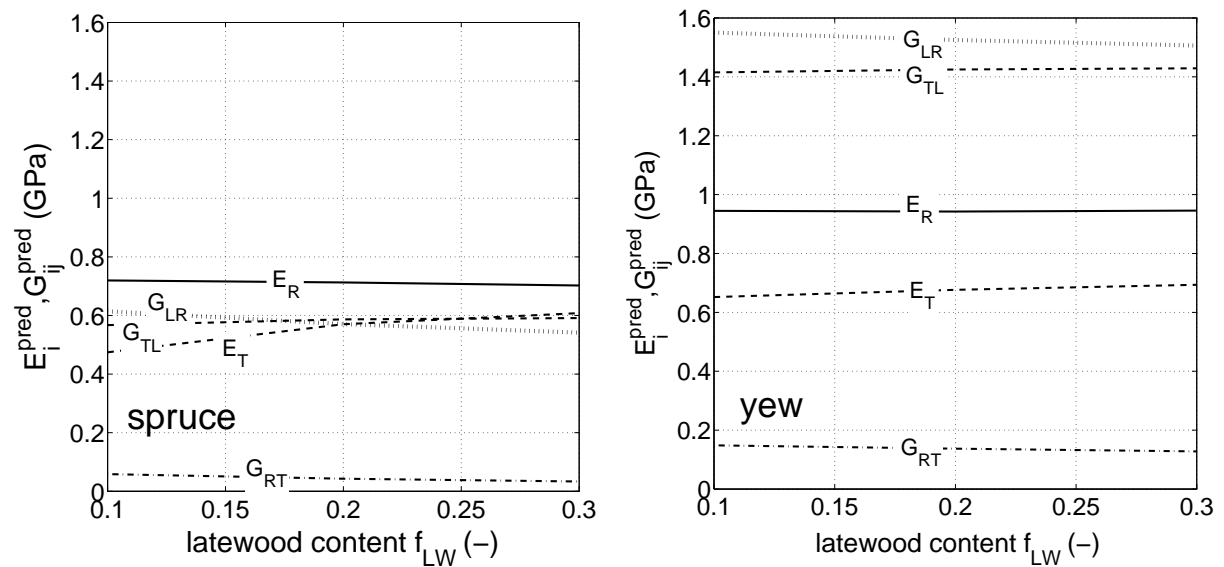


**Figure 3.9:** Influence of latewood content at scale of softwood: micromechanical model predictions for the transversal elastic moduli and shear moduli of spruce (left) and yew (right), see Table 3.5 for the species-specific microstructural characteristics.

stant earlywood and latewood volume fractions according to Table 3.5. Radial modulus  $E_R$  and shear stiffnesses  $G_{RT}$  and  $G_{LR}$  decrease with increasing density ratio, whereas the tangential modulus  $E_T$  and the shear stiffness  $G_{TL}$  increase, see Figure 3.8. Considering a realistic variation for each of the wood species, the effect is in relative terms most pronounced for  $G_{RT}$ , whereas the other elastic parameters only slightly change up by at most 10 %. Effects of the latewood volume fraction  $f_{LW}$  are illustrated in Figure 3.9, where constant density ratios of 1.50 and 2.80 are assumed for yew and spruce, respectively. Consequently, latewood and earlywood densities are reduced with increasing latewood content. Accordingly, radial stiffness  $E_R$  and shear stiffnesses  $G_{RT}$  and  $G_{LR}$  decrease, whereas tangential stiffness  $E_T$  and shear stiffness  $G_{TL}$  increase for both wood species. Both studies related to the annual ring structure reveal that the tangential elastic modulus  $E_T$  increases with increasing latewood density, while the radial elastic modulus  $E_R$  increases with increasing earlywood density. However, the effect of the annual ring structure on the distinct differences in the stiffness of the two considered wood species is by far less pronounced than that of microfibril angle and of overall mass density.

### 3.5 Conclusions

Considerably different macroscopic stiffness properties and microstructural characteristics of Common yew and Norway spruce motivated to investigate microstructure-stiffness relationships for these two wood species. Mechanical tests were carried out at different length scales, and, as a novel issue, micromechanical modeling was performed in order to reveal trends of the influences of particular microstructural characteristics on the material stiffness.

We found distinctly different stiffness properties of these two species in the S2 layers of earlywood and latewood tracheids by means of the nanoindentation technique. Microfibril angle (MFA) and cellulose content are the main influencing characteristics on this hierarchical level. Micromechanical model predictions for the indentation modulus underline and allow to quantify the dominant (non-linear) effect of the MFA on the cell wall stiffness. This effect is also observed at the macroscopic scale for the longitudinal elastic modulus, where it is overlaid by the influence of mass density. Moreover, the model reveals that a variation of the typically high MFA of yew considerably affects transversal stiffnesses and shear stiffnesses at this scale. On the contrary a variation of MFAs typical for spruce only significantly affects the shear stiffnesses  $G_{LR}$  and  $G_{TL}$ , but not transversal elastic moduli  $E_R$  and  $E_T$ . Model predicted effects of the annual ring structure on transversal stiffness and shear stiffness are found to be smaller than effects of the microfibril angle and mass density. Anisotropy ratios of elastic moduli are shown to nonlinearly depend on the MFA and on mass density.

In a similar manner, future research efforts could concern the influence of moisture content on cell wall stiffness of yew and spruce by means of nanoindentation (as e.g. recently shown by Yu et al. (2011) for Masson pine). Based on this data, micromechanical modeling could be applied to study the effect of moisture on the cell wall stiffness to gain a deeper understanding of moisture-stiffness relationships.

### 3.6 Appendix A

For investigating effects of the annual ring structure in a micromechanical framework, we apply the laminate theory, according to El Omri et al. (2000), in a poromechanical formulation following the procedure documented in Bader et al. (2011a). We distinguish between the material phases "earlywood" [homogenization step (III), see Bader et al. (2011a)] and "latewood" (homogenization step (III), see Bader et al. (2011a)] that occupy volume fractions  $f_{EW}$  and  $f_{LW} = 1 - f_{EW}$ , and exhibit poroelastic properties  $\mathbb{C}_{EW}^{hom}$ ,  $\mathbf{b}_{EW}^{hom}$ ,  $N_{EW}^{hom}$  and  $\mathbb{C}_{LW}^{hom}$ ,  $\mathbf{b}_{LW}^{hom}$ ,  $N_{LW}^{hom}$ , respectively, see Figure 3.1. Linear poroelastic behavior of the phases (according to Bader et al. (2011a)) implies that the homogenized material behavior of "softwood" takes the multilinear form

$$\boldsymbol{\Sigma}_{SW} = \mathbb{C}_{SW}^{hom} : \mathbf{E}_{SW} - \mathbf{b}_{SW}^{hom} p, \quad (3.A.1)$$

with the drained elasticity tensor of softwood,  $\mathbb{C}_{SW}^{hom}$ , and the softwood-related Biot tensor,  $\mathbf{b}_{SW}^{hom}$ . Consistently, this implies a bilinear form for the nanoporosity change (measured at the scale of softwood), namely

$$(\phi - \phi_0)_{SW} = \mathbf{b}_{SW}^{hom} : \mathbf{E}_{SW} + \frac{p}{N_{SW}^{hom}}, \quad (3.A.2)$$

with the solid Biot modulus  $N_{SW}^{hom}$  related to softwood. In order to estimate homogenized properties of softwood, we consider the laminate theory by using a tensorial decomposition in plane and antiplane components of the stresses and the strains according to El Omri et al. (2000)

$$\begin{bmatrix} \sigma_P \\ \sigma_A \end{bmatrix} = \begin{bmatrix} \mathbf{c}_{PP,i} & \mathbf{c}_{PA,i} \\ \mathbf{c}_{AP,i} & \mathbf{c}_{AA,i} \end{bmatrix} : \begin{bmatrix} \varepsilon_P \\ \varepsilon_A \end{bmatrix} - \begin{bmatrix} b_{P,i} \\ b_{A,i} \end{bmatrix} p, \quad (3.A.3)$$

with plane and antiplane components of the stress tensor, exemplarily reading in compressed matrix notation as

$$\sigma_P = \begin{bmatrix} \sigma_{RR} & \sigma_{LL} & \sqrt{2}\sigma_{LR} \end{bmatrix}, \quad (3.A.4)$$

$$\sigma_A = \begin{bmatrix} \sigma_{TT} & \sqrt{2}\sigma_{TL} & \sqrt{2}\sigma_{RT} \end{bmatrix}. \quad (3.A.5)$$

Within an RVE of softwood composed of earlywood and latewood layers in perfectly parallel arrangement, antiplane stress components and plane strain components are uniform

$$\varepsilon_{P,EW} = \varepsilon_{P,LW} = E_{P,SW}, \quad (3.A.6)$$

$$\sigma_{A,EW} = \sigma_{A,LW} = \Sigma_{A,SW}. \quad (3.A.7)$$

Analogously, poroelastic properties of the two phases can be decomposed in these components. Partial inversion of the poroelastic constitutive law yields a form, where only constant stress and strain components stand on the left hand side of the equation, reading as

$$\begin{bmatrix} \sigma_P \\ \varepsilon_A \end{bmatrix} = \begin{bmatrix} \mathbf{c}_{PP,i} - \mathbf{c}_{PA,i} : \mathbf{c}_{AA,i}^{-1} : \mathbf{c}_{AP,i} & \mathbf{c}_{PA,i} \mathbf{c}_{AA,i}^{-1} \\ -\mathbf{c}_{AA,i}^{-1} : \mathbf{c}_{AP,i} & \mathbf{c}_{AA,i}^{-1} \end{bmatrix} : \begin{bmatrix} E_P \\ \Sigma_A \end{bmatrix} - \begin{bmatrix} \mathbf{b}_{P,i} - \mathbf{c}_{PA,i} \mathbf{c}_{AA,i}^{-1} \mathbf{b}_{A,i} \\ -\mathbf{c}_{AA,i}^{-1} \mathbf{b}_{A,i} \end{bmatrix} p. \quad (3.A.8)$$

Consequently, terms on the right hand side can be averaged over the constituents of the laminate. Reassembling the equation to the form of Eq. (3.A.1), yields the components of the homogenized drained elasticity tensor of softwood as

$$\begin{aligned} \mathbf{C}_{PP,SW}^{hom} &= \langle \mathbf{c}_{PP,i} - \mathbf{c}_{PA,i} : \mathbf{c}_{AA,i}^{-1} : \mathbf{c}_{AP,i} \rangle_V - \\ &\quad \langle \mathbf{c}_{PA,i} : \mathbf{c}_{AA,i}^{-1} \rangle_V : \langle \mathbf{c}_{AA,i}^{-1} \rangle_V^{-1} : \langle \mathbf{c}_{AA,i}^{-1} : \mathbf{c}_{AP,i} \rangle_V, \end{aligned} \quad (3.A.9)$$

$$\mathbf{C}_{PA,SW}^{hom} = \langle \mathbf{c}_{PA,i} : \mathbf{c}_{AA,i}^{-1} \rangle_V : \langle \mathbf{c}_{AA,i}^{-1} \rangle_V^{-1}, \quad (3.A.10)$$

$$\mathbf{C}_{AP,SW}^{hom} = -\langle \mathbf{c}_{AA,i}^{-1} \rangle_V^{-1} : \langle -\mathbf{c}_{AA,i}^{-1} : \mathbf{c}_{AP,i} \rangle_V, \quad (3.A.11)$$

$$\mathbf{C}_{AA,SW}^{hom} = \langle \mathbf{c}_{AA,i}^{-1} \rangle_V^{-1} \quad (3.A.12)$$

$$(3.A.13)$$

and the components of the softwood-related Biot tensor as

$$\begin{aligned} b_{P,SW}^{hom} &= \langle b_{P,i} - \mathbf{c}_{PA,i} : \mathbf{c}_{AA,i}^{-1} : b_{A,i} \rangle_V - \\ &\quad \langle \mathbf{c}_{PA,i} : \mathbf{c}_{AA,i}^{-1} \rangle_V : \langle \mathbf{c}_{AA,i}^{-1} \rangle_V^{-1} : \langle -\mathbf{c}_{AA,i}^{-1} : b_{A,i} \rangle_V, \end{aligned} \quad (3.A.14)$$

$$b_{A,SW}^{hom} = -\langle \mathbf{c}_{AA,i}^{-1} \rangle_V^{-1} : \langle -\mathbf{c}_{AA,i}^{-1} : b_{A,i} \rangle_V. \quad (3.A.15)$$

Therein,  $\langle (\cdot) \rangle$  denotes the average of quantity  $(\cdot)$  over the volume of an RVE of softwood, or in a discrete manner, the volume-weighted sum over the two layers

$$\langle (\cdot) \rangle = \sum_i f_i(\cdot), \quad (3.A.16)$$

with  $i=[EW, LW]$ , for earlywood and latewood layers, respectively.



Consistently, we upscale the nanoporosity from the earlywood and latewood level to that of softwood. For this purpose, the second poromechanical state equation of a lamella is expressed in terms of the uniform components of the stress and strain tensors. Thereon, by expressing the antiplane stress components out of the macroscopic constitutive law, an effective tensor of Biot coefficients (equal to the one derived earlier) and an effective skeleton Biot modulus are obtained by volume averaging over the RVE. Thus, the skeleton Biot modulus reads as

$$\frac{1}{N_{SW}^{hom}} = \langle -b_{A,i} : \mathbf{c}_{AA,i}^{-1} : b_{A,SW}^{hom} + b_{A,i} : \mathbf{c}_{AA,i}^{-1} : b_{A,i} + \frac{1}{N_i} \rangle_V. \quad (3.A.17)$$

In wood, undrained conditions are prevailing, characterized by constant fluid mass in the RVE under mechanical loading. This allows relating the pore pressure  $p$  to the macroscopic strain, which is then the only loading parameter (Bader et al., 2010). This yields the undrained stiffness according to Eq. (13) in Bader et al. (2010).

**Changes in microstructure and stiffness of Scots pine (*Pinus sylvestris*) sapwood degraded by *Gloeophyllum trabeum* and *Trametes versicolor* - Part I: Physicochemical alterations (Bader et al., 2011c)**

Authored by Thomas K. Bader, Karin Hofstetter, Gry Alfredsen, and  
Susanne Bollmus

Accepted for publication in *Holzforschung*, 2011

As a natural organic material, wood is susceptible to fungal degradation. This results in alterations of the microstructure, expressed in terms of changes in physical and chemical properties. While mass loss due to fungal degradation and alterations of the chemical composition of the cell wall are well investigated, loss in mass density and changes in equilibrium moisture content, as well as their relations to the former two, are not so clear. However, these physical and chemical alterations are crucial when linking microstructural characteristics to macroscopic mechanical properties. Thus, as an original contribution, we present a consistent set of physical, chemical, and mechanical characteristics measured on the same sample before and after fungal degradation. In the first part of this two-part contribution, elucidating microstructure/stiffness-relationships of degraded wood, we in-

investigate changes in physical and chemical properties of specimens of Scots pine (*Pinus sylvestris*) sapwood degraded by *Gloeophyllum trabeum* (brown rot) and *Trametes versicolor* (white rot), respectively, for up to 28 weeks. A comparison of mass loss with corresponding loss in mass density elucidates that mass loss comprises two effects: firstly, a decrease in sample size (more pronounced for *G. trabeum*) and secondly, a decrease of mass density within the sample (more pronounced for *T. versicolor*). These two concurrent effects result in dependence on sample size and shape of the relationship between mass loss and loss in mass density. Observed changes in chemical composition of the cell wall reveal hemicelluloses and cellulose decomposition due to *G. trabeum*, while *T. versicolor* additionally was able to degrade lignin. Particularly, due to the breakdown of hemicelluloses and cellulose, the equilibrium moisture content of degraded samples is lower than that of sound pine.

## 4.1 Introduction

As a natural, organic material, wood is susceptible to deteriorating organisms. In nature, biodegradation is beneficial and a desired effect, whereas in timber structures, degradation of wood can considerably decrease the load bearing capacity and, thus, in the worst case, can lead to structural failure. Due to a lack of scientifically based methods for relations between degradation and its effects on mechanical properties, knowledge of fundamental microstructure/mechanics-relationships is gaining in importance. From a mechanical point of view, wood shows a highly anisotropic mechanical behavior, which is governed by the composition and morphology of its hierarchically well organized microstructure (Kollmann and Côté, 1968). Fungal degradation alters this microstructure (Côté, 1965; Fengel and Wegener, 1984; Schwarze, 2007) and, thus, causes changes in mechanical properties (Winandy et al., 2000; Curling et al., 2001, 2002; Wilcox, 1978).

Wood deterioration by fungi is characterized by a breakdown or/and modification of chemical constituents to varying extents, depending on the fungal species, the wood species, and the growth conditions within the wood (Côté, 1965; Fengel and Wegener, 1984; Schwarze, 2007). Mainly the polysaccharides and lignin are affected. Related to the strategy of basidiomycetes to degrade wood, they can be classified as: brown rot and white rot (Côté, 1965; Fengel and Wegener, 1984; Schwarze, 2007). Fungi related to the brown rot degrade and mineralize wood polysaccharides, leaving behind a modified lignin that gives the decayed wood its characteristic color. On the contrary, white rot fungi are able to degrade and mineralize all major wood constituents using ligninolytic and cellulolytic/hemicellulytic enzymatic systems (Côté, 1965; Fengel and Wegener, 1984; Schwarze, 2007). *Trametes versicolor* is one of the most efficient wood-degrading white rot basidiomycetes and causes the simultaneous decay of lignin, cellulose, and hemicellulose (Crawford, 1981; Enoki et al., 1989).

The relation between microstructure and macroscopic mechanical properties was highlighted in several experimental approaches, for clear wood [see e.g. Keunecke et al. (2007, 2008a)], as well as for decayed wood [see. e.g. Winandy et al. (2000) and Curling et al.

(2001, 2002)], thermally modified wood [see e.g. Yildiz et al. (2006) and Windeisen et al. (2009)], and enzymatically treated wood [see e.g. Konnerth et al. (2010)]. However, in traditional wood durability testing, decreases in mechanical properties are related only to mass loss [see e.g. Hartley (1958) in Wilcox (1978)]. Changes in mass density are not determined, although this quantity is expected to be more strongly related to the remaining load bearing capacity of degraded wood due to its size independent character. Additionally, the change of the equilibrium moisture content upon degradation would have to be taken into account, since the moisture content considerably affects the mechanical properties of wood (Kollmann, 1982). This change results from breakdown or modification of chemical components of the cell wall. It is well known for thermally modified wood, where the decrease in hygroscopicity resulting from the induced chemical alterations is desired in order to increase dimensional stability (Tjeerdsma et al., 1998; Windeisen et al., 2009). From a mechanical point of view, wood can be considered as orthotropic material in good approximation, showing three axes of symmetry: longitudinal (in stem axis), radial (from pith to bark), and tangential (circumferential) direction. So far, effects of degradation by fungi on mechanical properties have mainly been investigated in the longitudinal direction only, although transversal properties are expected to be more sensitive to degradation than longitudinal ones (Przewloka et al., 2008).

All this motivates to experimentally investigate effects of fungal degradation on physical, chemical, and stiffness properties of wood and to relate them to each other. With the experiments performed herein, we want to consistently investigate the following alterations of wood properties due to fungal decay:

- (i) change of mass and of mass density,
- (ii) change of equilibrium moisture content (EMC),
- (iii) change of chemical composition of the dry cell wall,
- (iv) change of anisotropic stiffness properties [see Bader et al. (2011d)].

This contribution is organized in two parts: The following first part focuses on alterations in physical and chemical properties due to fungal decay and correlations between them. Particularly, we investigate

- how mass density changes with mass loss,
- how the chemical composition of Scots pine sapwood quantitatively changes due to brown rot and white rot, and
- if changes in the EMC can be related to changes in the chemical composition.

The second part (Bader et al., 2011d) focuses on effects of fungal decay on anisotropic stiffness properties and their relation to the microstructure alterations presented herein.

## 4.2 Materials and Methods

In the following, the experimental program (cf. Figure 4.1), including fungal decay tests and the applied experimental techniques for measuring physical, chemical, and mechanical properties (see also Bader et al. (2011d)), are presented in detail. 406 specimens of cuboidal shape were cut from sapwood boards of Scots pine (*Pinus sylvestris* L.) with dimensions of 20 x 15 x 130 mm<sup>3</sup> (radial  $l_R$  x tangential  $l_T$  x longitudinal  $l_L$ ). In a first step, the oven-dry mass and oven-dry dimensions of each sample were determined. Thereon, the initial unaffected physical condition of all specimens under constant climatic conditions of 20 °C and 65 % relative humidity was characterized by measuring mass density and equilibrium moisture content (EMC). In addition, tensile tests and ultrasonic tests were performed in longitudinal direction under the same climatic conditions, which are described in detail in the second part of this paper (Bader et al., 2011d). Out of the 406 specimens, 14 samples served as reference material. Three cubes with dimensions of 20 x 15 x 20 mm<sup>3</sup> ( $l_R$  x  $l_T$  x  $l_L$ ) were cut out of each specimen, and the normal stiffness tensor components in all three principal material directions of wood were measured by means of ultrasonic testing. The other specimens - 196 bars for each fungus - were exposed to *Gloeophyllum trabeum* [(Pers.) Murrill, strain CTB 863A] and to *Trametes versicolor* [(L.) Lloyd, strain FPRL 280], respectively, for up to 28 weeks. These decay tests were carried out adapted to EN113 (1996). After every second week 14 specimens were taken out as representatives of one degradation stage. For these samples, changes in oven-dry mass and changes in EMC were evaluated in comparison to the initial sound state. Additionally, 14 beech samples were used for the virulence test of *T. versicolor*. According to EN113 (1996) the mass loss was determined after 16 weeks degradation time.

After tensile testing of degraded samples, three cubes with corresponding cross-sections and 20 mm length  $l_L$  were cut out of each bar and served for ultrasonic testing in all three principal material directions - analogous to the testing procedure performed on the reference samples (Bader et al., 2011d). Finally, the chemical composition of reference samples and degraded samples was evaluated by thermogravimetric analysis (TGA). In order to check the applicability of TGA to degraded wood samples, corresponding results were verified by means of wet chemical analysis techniques [for details see Alfredsen et al. (2011)].

### 4.2.1 Thermogravimetric analysis

Thermogravimetric analysis (TGA) measures the amount and rate of change in the weight of a material as a function of temperature and time in a controlled atmosphere. In the present study, TGA was performed according to a method described in Grønli et al. (2002). The tests delivered weight fractions of the wood components hemicelluloses, cellulose, lignin, and extractives.

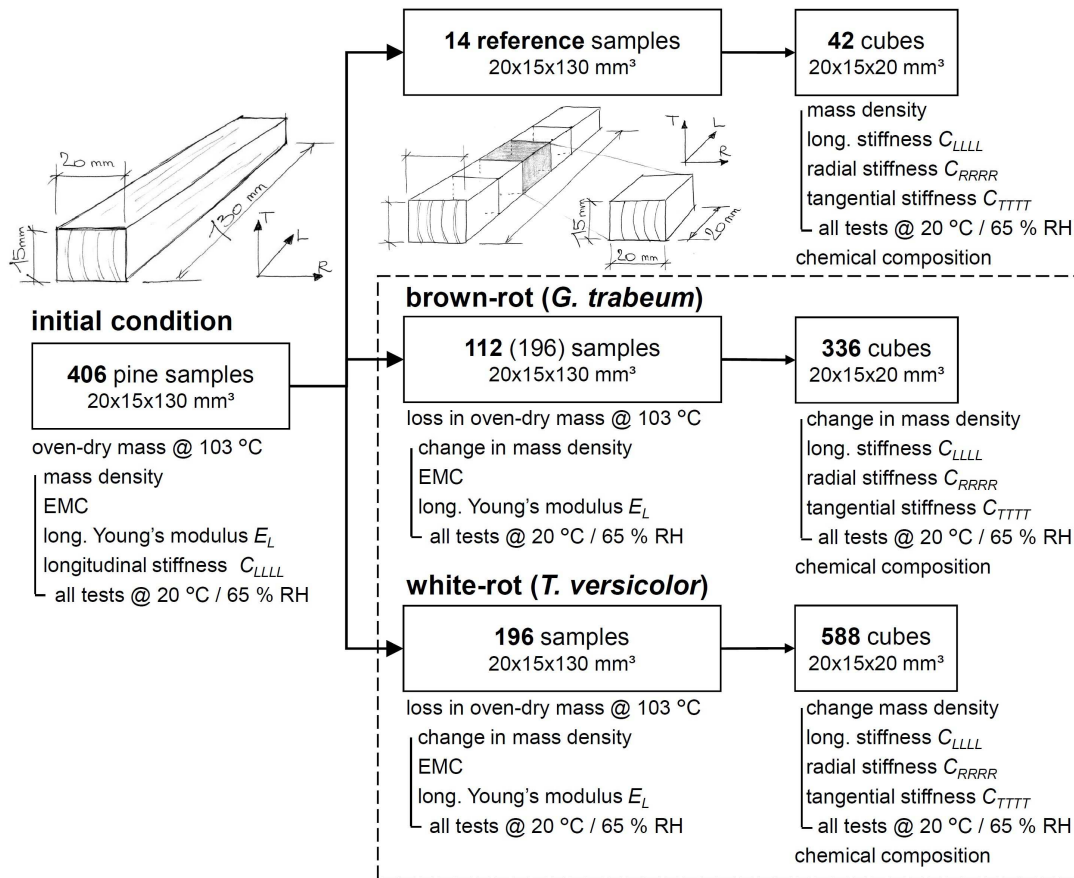


Figure 4.1: Test program, specifying shapes, dimensions, and numbers of test specimens.

### 4.2.2 Wet chemical analysis

Milled samples were extracted with a mixture of cyclohexane:acetone (9:1) in a Soxtec apparatus Tappi T 204 cm-07 (1998). The extract was evaporated and measured gravimetrically. Thereon, the extracted samples were hydrolyzed in an autoclave at 1 bar pressure, according to Tappi T 249 cm-00 (2000). The solubilized monosaccharides were quantified using Ion Chromatography with a pulse amperometric detector (IC-PAD). The insoluble residue (Klason lignin) was measured gravimetrically according to Tappi T 222 cm-00 (1983). The soluble acid lignin was determined by means of UV spectroscopy evaluating the absorption band at a wavelength of 205 nm, using an absorptivity coefficient of 128 l g<sup>-1</sup> cm<sup>-1</sup>. Again, weight fractions of hemicelluloses, cellulose, lignin, and extractives were determined within these tests.

## 4.3 Results and Discussion

### 4.3.1 Physical and chemical properties of sound samples

The oven-dry mass of the samples ranged from 16.40 to 20.92 g and the corresponding dry mass density from 0.436 to 0.575 g/cm<sup>3</sup>. By conditioning to 20 °C and 65 % RH, the mass of the pine sapwood samples increased and finally amounted to 18.20 - 23.31 g. Consistently, increased conditioned mass densities were observed, ranging between 0.474 and 0.622 g/cm<sup>3</sup>. The homogeneity of the set of specimens is indicated by a very good correlation between mass and mass density, both in dry state (coefficient of determination  $R^2=0.98$ ) as well as conditioned to the specified climate ( $R^2=0.97$ ). Specimens exhibited an average EMC of 11.0 % ( $\pm 0.3$  %, n=406). Values in parenthesis refer to corresponding standard deviations, followed by the number of test specimens n.

The average chemical composition of the 14 reference samples, expressed in terms of weight fractions of hemicelluloses, cellulose, lignin, and extractives, is given in Table 4.1. These results agree well with weight fractions specified in literature for pine sapwood, see e.g. Esteves et al. (2005).

**Table 4.1:** Chemical composition of 14 reference samples in terms of weight fractions of the dry cell wall.

	hemicellulose	cellulose	lignin	extractives
	(%)	(%)	(%)	(%)
average	24.39	47.41	24.58	3.62
std.dev.	1.34	1.60	0.90	0.52

### 4.3.2 Physical and chemical properties of degraded samples

As expected, both types of basidiomycete decay, namely brown rot and white rot, considerably affect physical and chemical properties of Scots pine sapwood.

Due to the highly irregular shape of the brown rotted samples after degradation, all specimens needed to be reshaped to a regular cuboidal form with well-specified volume and cross-sectional area in order to allow determination of the degraded mass density and of the mean stresses in the specimens in the tensile tests. As shown by Macchioni and Palanti (2007) and confirmed by own densitometry measurements, brown rot (*Coniophora puteana*) on Scots pine samples causes homogenous degradation inside the sample in addition to possibly pronounced surface degradation. Under this consideration, reshaping has no effect on the results. Only the waviness of the surface, as a results of the surface degradation, was removed and a maximum of 1 mm was cut off from each surface. Specimens degraded by *G. trabeum* tended to crack into cubes after 18 weeks. Since the samples no longer comprised any mechanical resistance, only mass loss was measured for the remaining weeks of degradation. On the contrary, white rotted samples still exhibited

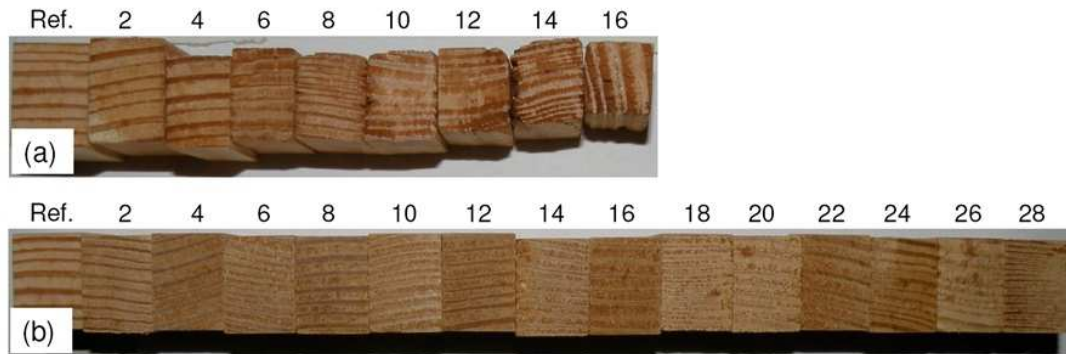


**Figure 4.2:** Exemplary cross-sections of reference and degraded specimens from 2 to 16 weeks degradation by (a) *G. trabeum* and from 2 to 28 weeks exposure to (b) *T. versicolor*.

the initial regular cuboidal shape after 28 weeks degradation without pronounced surface damage due to the less severe degradation by the white rot fungus.

Examining the cross-sections of degraded samples (Figure 4.2) clearly shows that brown rot degradation has a more severe impact on the physical condition of pine sapwood than white rot degradation. Consequently, mass loss due to *G. trabeum* is considerably higher than that due to *T. versicolor* in Scots pine sapwood. This is an expected results, since brown rot generally prefer conifers and white rot prefer hardwoods. As indicated earlier, the tested brown rot fungus results in loss of mechanical resistance of Scots pine specimens after 18 weeks degradation time, corresponding to a mass loss of 33.7 % ( $\pm 3.6$  %, n=14), see Table 6.3 and Figure 4.3a. This complies well with earlier findings (Winandy et al., 2000; Curling et al., 2001, 2002). On the contrary, mass loss after 28 weeks *T. versicolor* degradation amounted to only 16.7 % ( $\pm 3.2$  %, n=14), see Table 6.3 and Figure 4.3b. The mass loss of the virulence samples from beech was 27.10 % ( $\pm 3.58$  %) and met the requirements of the standard EN113 (1996). According changes in mass density amounted to 13.4 % ( $\pm 2.0$  %, n=14) after 16 weeks degradation by *G. trabeum* (see Figure 4.3a) and to 17.4 % ( $\pm 3.5$  %, n=14) after 28 weeks degradation by *T. versicolor* (see Figure 4.3b), and samples were still mechanically intact then. Comparing changes in mass density and corresponding mass loss supported two distinctly different degradation mechanisms. For samples degraded by *G. trabeum*, firstly, mass density decreases less than the overall mass. Thus, there is a high effect of the fungus on the surfaces of the samples, resulting in a decrease of sample size. The difference in the course of mass loss and density decrease is even more dominant after 6 weeks degradation time than in the beginning. It is also clearly visible as a continuous decrease in the corresponding cross-sectional size, as shown in Figure 4.2a. For *T. versicolor*, a good correlation between density change and mass loss is found. Here, changes in size are negligible, and degradation occurs dominantly within the sample (see Figure 4.3b). This corresponds to our visual observations of a constant cross-section size up to 28 weeks degradation time, clearly visible in Figure 4.2b. From a (micro)mechanical point of view, this is of particular interest, since the "remaining" load bearing capacity is strongly affected by the residual amount of cell wall material.



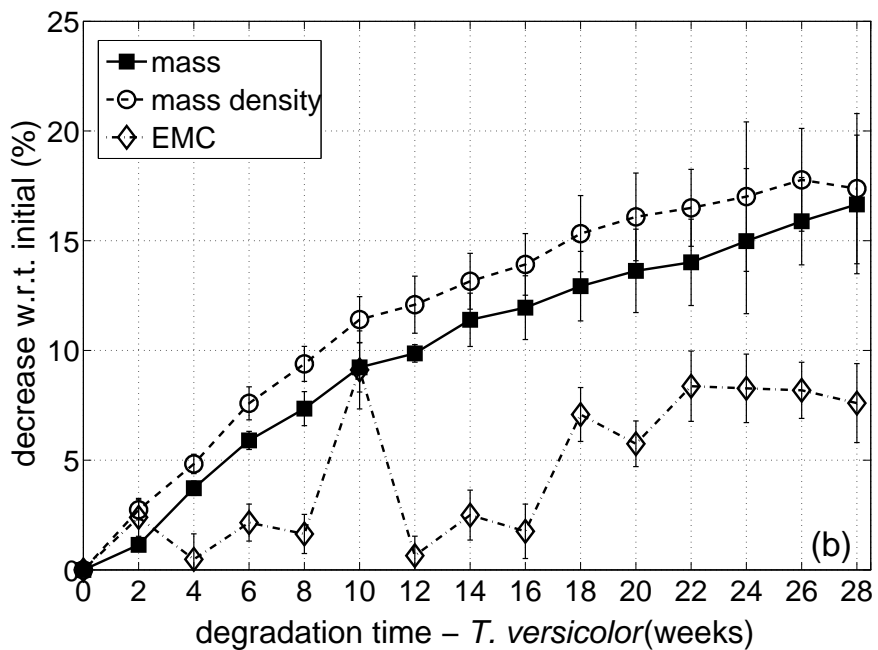
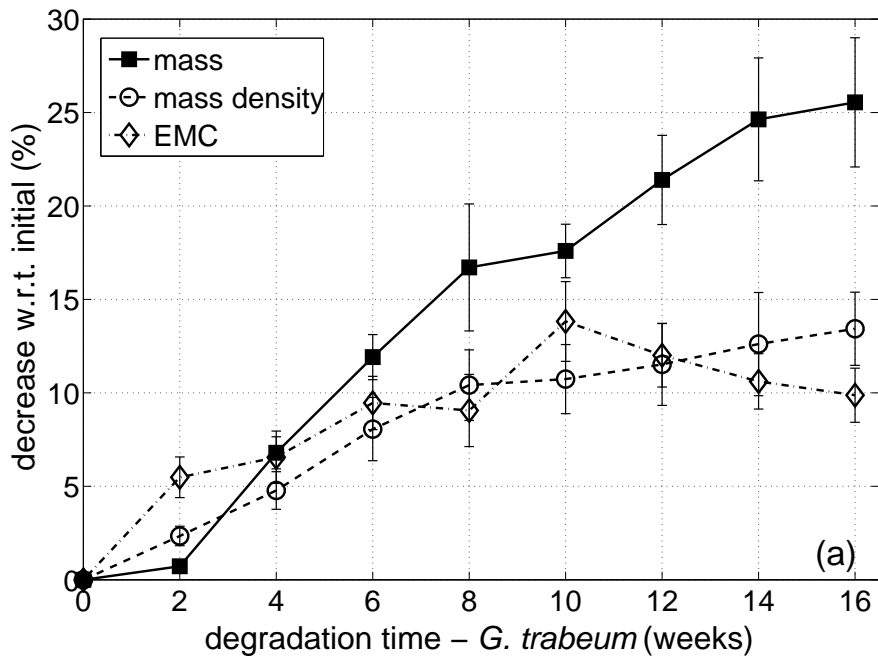


**Figure 4.3:** Decrease in mass, in density, and in EMC due to degradation by (a) *G. trabeum* and by (b) *T. versicolor* over degradation time. Error bars indicate corresponding standard deviations (n=14 for each degradation stage and fungus).

**Table 4.2:** Decrease of mass loss, mass density, and equilibrium moisture content (EMC) for degradation of Scots pine sapwood by *G. trabeum* and by *T. versicolor*, respectively, for 2 to 28 weeks.

weeks of exp.	mass loss		mass density loss		EMC loss	
	mean (%)	std. dev. (%)	mean (%)	std. dev. (%)	mean (%)	std. dev. (%)
<i>G. trabeum</i> (brown rot)						
2	0.7	0.3	2.3	0.5	5.5	1.1
4	6.8	0.9	4.8	1.0	6.6	1.4
6	11.9	1.2	8.1	1.7	9.5	1.4
8	16.7	3.4	10.4	1.9	9.1	1.9
10	17.6	1.4	10.7	1.8	13.8	2.1
12	21.4	2.4	11.5	2.2	12.0	1.7
14	24.6	3.3	12.6	2.8	10.6	1.5
16	25.5	3.5	13.4	2.0	9.9	1.4
18	33.7	3.6				
20	33.0	7.8				
22	40.2	6.3	no residual mechanical resistance, therefore no further testing			
24	47.5	4.7				
26	46.7	6.7				
28	52.9	4.9				
<i>T. versicolor</i> (white rot)						
2	1.1	0.2	2.8	0.4	2.4	0.9
4	3.7	0.3	4.8	0.4	0.5	1.2
6	5.9	0.4	7.6	0.8	2.2	0.8
8	7.3	0.8	9.4	0.8	1.6	0.9
10	9.2	1.1	11.4	1.0	9.1	1.8
12	9.9	0.4	12.1	1.3	0.6	0.9
14	11.4	1.2	13.2	1.3	2.5	1.1
16	11.9	1.5	13.9	1.4	1.8	1.2
18	12.9	1.6	14.6	3.4	7.1	1.2
20	13.6	1.9	16.1	2.0	5.7	1.0
22	14.0	2.0	16.5	1.8	8.4	1.6
24	15.0	3.3	17.0	3.4	8.3	1.6
26	15.9	2.0	17.8	2.4	8.2	1.3
28	16.7	3.2	17.4	3.5	7.6	1.8

The correlation between mass loss and change in mass density is nevertheless strong (Figure 4.4), expressed by coefficients of determination for brown rot of  $R^2=0.98$  ( $n=112$ ) and for white rot of  $R^2=0.99$  ( $n=196$ ). Such a strong correlation was also found by Macchioni and Palanti (2007) for Scots pine degraded by the brown rot fungus *Coniophora puteana*. However, it has to be noted that the concrete relationship depends on the fungus and the wood species. In addition, even sample size and shape affects them, since mass loss in general comprises both aforementioned degradation mechanisms. From these considerations we expect that surface degradation leading to high mass loss but low density decrease is the more dominant the larger the specimen is.

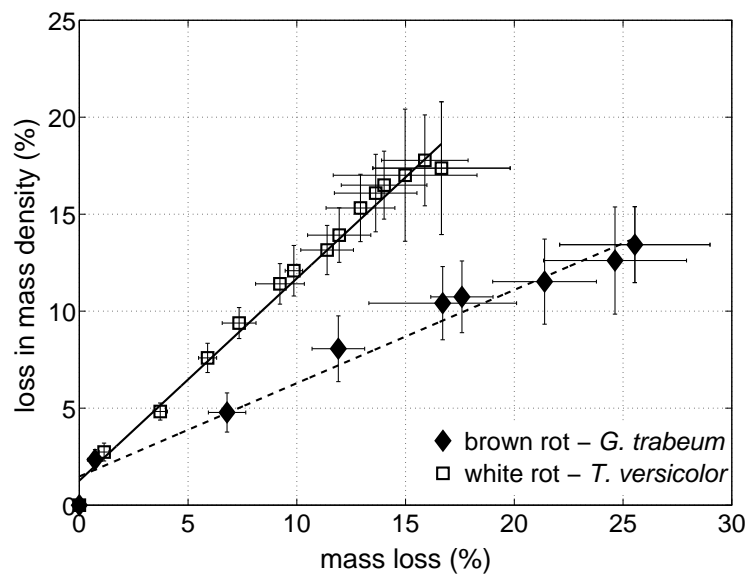


**Figure 4.4:** Relationship between mass loss and corresponding loss in mass density for samples degraded by *G. trabeum* and *T. versicolor*, respectively. Error bars indicate corresponding standard deviations ( $n=14$  for each degradation stage and fungus).

Four samples of each degradation stage were tested by means of TGA. Additionally, for verification of the TGA data, wet chemical analysis was performed for eight samples of the reference condition and for three specific degradation states for each fungus (brown rot: 2, 8, and 16 weeks; white rot: 2, 16, and 28 weeks), respectively. The good agreement of the results obtained with the two methods confirms that TGA is a suitable technique to be applied to pine sapwood in the initial unaffected state and also after degradation by *G. trabeum*. However, TGA cannot correctly detect lignin degradation by the white rot fungus *T. versicolor*, for details see Alfredsen et al. (2011). Therefore, data from wet chemical analysis was used for results in relation to white rotted samples.

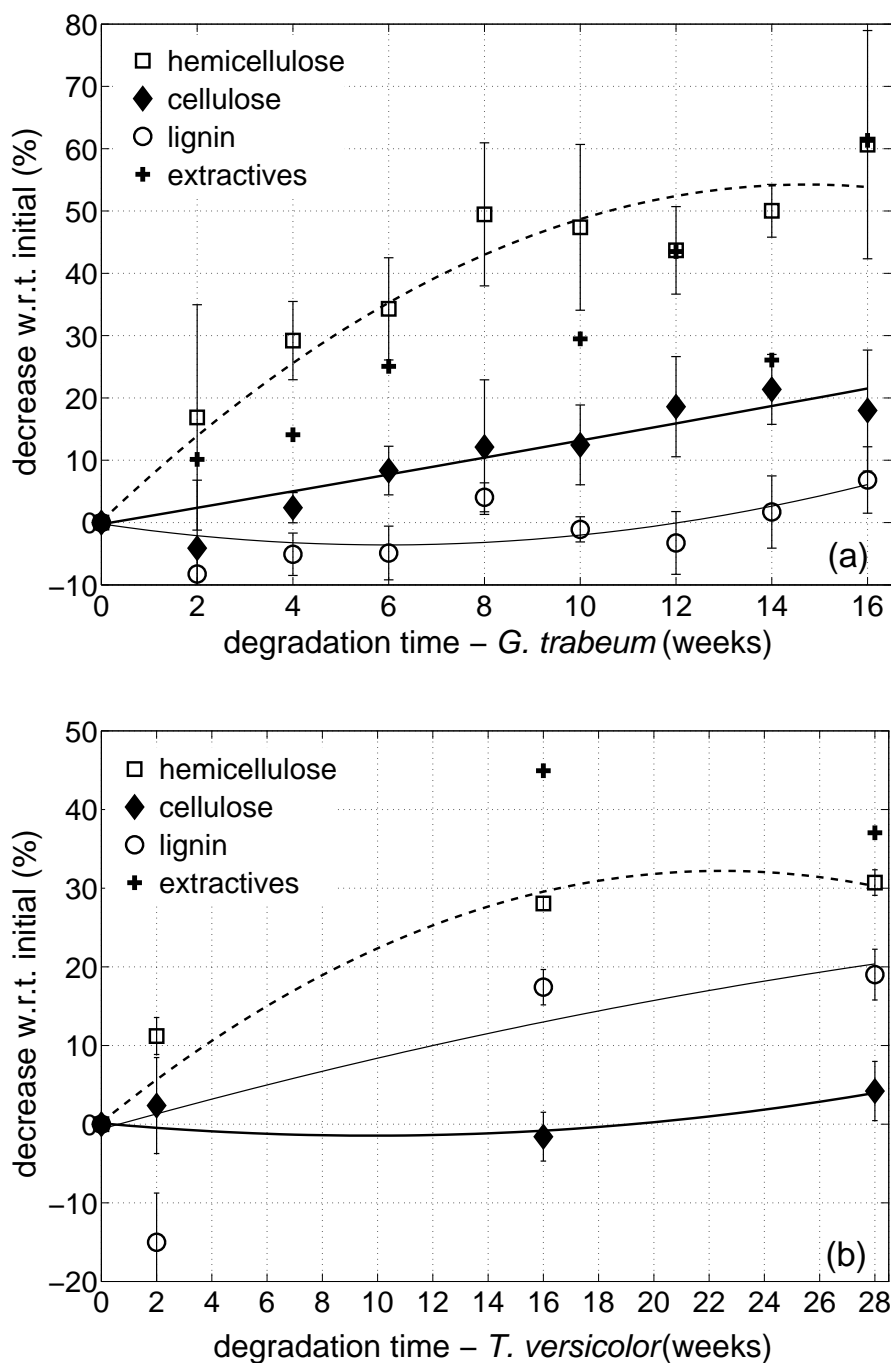


**Figure 4.5:** Decrease of weight fractions of chemical components, corrected with mass loss, with respect to the initial amount for samples degraded by (a) *G. trabeum* and (b) *T. versicolor*. Error bars indicate corresponding standard deviations [(a) n=4 and (b) n=3 for each degradation stage].

**Table 4.3:** Change in weight fractions of chemical components of Scots pine sapwood degraded by *G. trabeum* and by *T. versicolor*, respectively; Hc ... hemicelluloses; Cel ... cellulose; Lig ... lignin; Extr ... extractives.

week	weight fract. of dry cell wall				method	mass loss	weight fract. corrected with mass loss			
	Hc	Cel	Lig	Extr			Hc	Cel	Lig	Extr
brown rot by <i>G. trabeum</i>										
0	24.39	47.41	24.58	3.62	TGA	–	24.39	47.41	24.58	3.62
2	20.38	49.61	26.75	3.27	TGA	0.50	20.27	49.36	26.61	3.25
2	21.35	47.98	29.53	1.13	w.chem.	0.50	21.26	47.77	29.41	1.13
4	18.66	50.04	27.93	3.36	TGA	7.51	17.27	46.28	25.83	3.11
6	18.20	49.42	29.30	3.08	TGA	12.03	16.02	43.45	25.78	2.71
8	14.93	50.29	28.56	6.22	TGA	17.34	12.33	41.67	23.59	5.08
8	15.66	52.34	29.50	2.50	w.chem.	17.34	12.76	42.53	23.95	2.01
10	15.69	50.79	30.41	3.12	TGA	18.26	12.83	41.50	24.85	2.55
12	17.24	48.32	31.88	2.55	TGA	20.24	13.73	38.59	25.39	2.04
14	15.96	48.82	31.69	3.53	TGA	23.69	12.19	37.28	24.17	2.68
16	13.19	53.36	31.51	1.94	TGA	27.22	9.60	38.88	22.90	1.40
16	15.92	51.58	30.97	1.53	w.chem.	27.22	11.60	37.54	22.53	1.11
white rot by <i>T. versicolor</i>										
0	24.39	47.41	24.58	3.62	TGA	–	24.39	47.41	24.58	3.62
2	21.93	46.87	28.63	2.56	w.chem.	1.25	21.66	46.29	28.27	2.53
16	19.94	54.72	23.07	2.27	w.chem.	11.99	17.55	48.17	20.30	1.99
28	20.00	53.73	23.57	2.70	w.chem.	15.50	16.90	45.41	19.91	2.28

As expected, degradation of specific chemical components depends on the fungal species and thus, on the type of rot, see Table 4.3 and Figure 4.5. The change of the chemical composition across different degradation stages is given in Table 4.3, firstly, in terms of weight fractions  $wf$  of the dry cell wall, as a direct result of the tests, and secondly, corrected with the sample-specific mass loss by using the relation

$$wf_{corr} = wf \left( 1 - \frac{mass\ loss[\%]}{100} \right) \quad (4.1)$$

The latter specifies the component-specific decrease with respect to the initial reference composition, illustrated in Figure 4.5. For brown rot caused by *G. trabeum*, there is a strong degradation of polysaccharides, whereas lignin is hardly affected, see Figure 4.5a. On the contrary, for white rot caused by *T. versicolor*, there is a pronounced degradation of lignin and hemicelluloses, while up to 16 weeks cellulose is not degraded, see Figure 4.5b. These results correspond to well known effects of brown rot and white rot degradation (Côté, 1965; Fengel and Wegener, 1984; Schwarze, 2007).

Decreases in EMC of 9.9 % ( $\pm 1.4$  %, n=14) after 16 weeks brown rot, from initially 11.0 % to 9.8 % ( $\pm 0.2$  %, n=14) and of 7.6 % ( $\pm 1.8$  %, n=14) after 28 weeks white rot, from

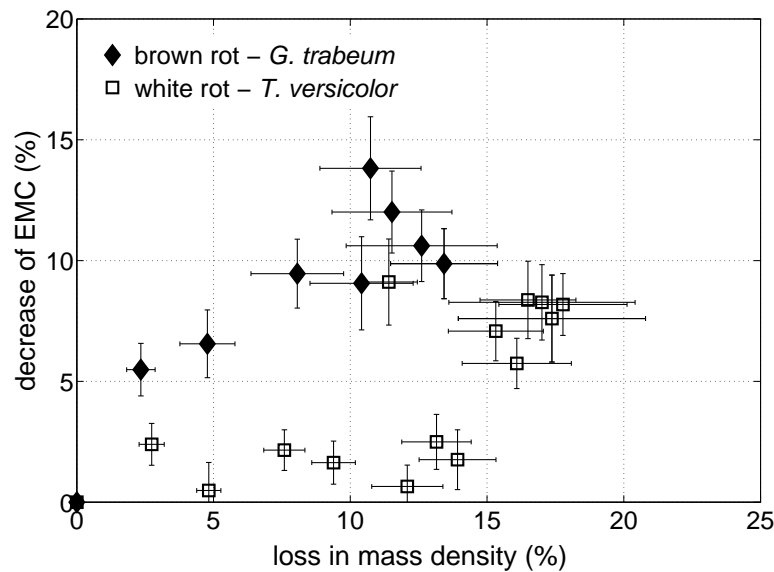


**Figure 4.6:** Relationship between loss in mass density and corresponding decrease of equilibrium moisture content (EMC) for samples degraded by *G. trabeum* and *T. versicolor*. Error bars indicate corresponding standard deviations ( $n=14$  for each degradation stage and fungus).

initially 11.0 % to 10.2 % ( $\pm 0.2$  %,  $n=14$ ), were observed (see Table 6.3). In this test with Scots pine sapwood samples, a higher degradation results in lower EMC (see Figure 4.6), and EMC is more strongly affected by brown rot than by white rot fungi. Apparently, those chemical components of the cell wall responsible for moisture uptake are more strongly degraded by brown rot than by white rot, namely hemicelluloses and cellulose as also obvious from the chemical composition data. This is due to the high hygroscopicity of hemicelluloses and of the amorphous parts of cellulose [see Smith and Langrish (2008) and references therein]. The previously mentioned delayed start of cellulose degradation for white rot samples after 14 weeks is also visible in the course of the EMC change (cf. Figure 4.6).

## 4.4 Conclusions

Aiming finally at relating changes in mechanical behavior of softwood to the underlying physical and chemical alterations, we presented changes of mass, mass density, EMC, and chemical composition of pine sapwood degraded by *G. trabeum* and *T. versicolor* in this first part of a two-part contribution. The stronger degradation by *G. trabeum* leads to a loss in mechanical resistance after 16 weeks degradation, whereas *T. versicolor* degraded Scots pine is less affected and shows lower mass loss. A comparison of mass loss with corresponding loss in mass density elucidates that mass loss comprises two effects: firstly, a decrease in sample size (more pronounced for *G. trabeum*) and secondly, a de-

crease of mass density within the sample (more pronounced for *T. versicolor*). These two concurrent effects result in dependence on sample size of the relationship between mass loss and loss in mass density. Observed changes of chemical composition of the cell wall reveal hemicellulose and cellulose decomposition due to *G. trabeum*, while *T. versicolor* additionally degrades lignin. Particularly, due to the breakdown of hemicelluloses and cellulose, the EMC of degraded samples is lower than that of sound pine.

**Changes in microstructure and stiffness of Scots pine (*Pinus sylvestris*) sapwood degraded by *Gloeophyllum trabeum* and *Trametes versicolor* - Part II: Anisotropic stiffness (Bader et al., 2011d)**

Authored by Thomas K. Bader, Karin Hofstetter, Gry Alfredsen, and  
Susanne Bollmus

Accepted for publication in *Holzforschung*, 2011

Fungal decay considerably affects macroscopic mechanical properties of wood due to modifications and degradations in its microscopic structure. While effects on mechanical properties related to the stem direction are fairly well understood, effects on transversal properties are less investigated. For the purpose of exploring anisotropic stiffness properties, we herein apply tensile and ultrasonic testing for quantification of changes in longitudinal elastic moduli and of radial, tangential, and longitudinal stiffness of Scots pine (*Pinus sylvestris*) sapwood degraded by *Gloeophyllum trabeum* (brown rot) and *Trametes versicolor* (white rot) for up to 28 weeks. Transversal properties are found to be much more strongly degraded and, therefore, more sensitive to degradation than longitudinal properties. This is due to the degradation of the polymer matrix between the cellulose fibers,



which has a strong effect on the transversal stiffness. On the contrary, longitudinal stiffness is mainly governed by cellulose, which is more stable with respect to degradation by the specific fungi considered herein. *Gloeophyllum trabeum* strongly weakens radial stiffness, whereas *T. versicolor* more strongly reduces tangential stiffness, which is concluded to originate from two different degradation strategies of the fungi: *G. trabeum* is more active in earlywood and *T. versicolor* more in latewood. Radial and tangential stiffness, as well as corresponding anisotropy ratios are concluded to constitute suitable durability indicators, which even allow elucidating degradation mechanisms within wood samples.

## 5.1 Introduction

Wood shows a highly anisotropic mechanical behavior in macroscopic mechanical tests. This behavior is governed by the chemical composition and by the morphology of the hierarchically well-organized microstructure of wood. Fungal deterioration alters this microstructure (Côté, 1965; Fengel and Wegener, 1984; Schwarze, 2007) and, thus, results in corresponding changes in mechanical properties (see e.g. Wilcox (1978), Winandy et al. (2000), and Curling et al. (2001, 2002)).

Starting at the smallest length scale, the softwood microstructure can be characterized by four levels of organization: (Ia) a polymer matrix composed of lignin, hemicelluloses, and extractives, where in moist conditions additionally water is incorporated; (Ib) cellulose fibrils with crystalline and amorphous regions; (II) the cell wall material as a fiber-composite assembled of the two aforementioned materials (Ia) and (Ib); (III) the cellular honeycomb structure of softwood cells, which is formed subsequently over a growth period (from earlywood to latewood) with a continuous decrease in radial dimensions of the cells, accompanied by an increase in cell wall thickness; this results in the typical (IV) growth ring structure visible to the naked eye (Kollmann and Côté, 1968).

Degradation and modification of wood constituents at the lowest organizational level are the microstructural origin of loss in (macroscopic) stiffness and strength properties upon fungal decay. They depend on fungal species, wood species, and growth conditions within the wood (Fengel and Wegener, 1984). Traditionally, such a decrease in mechanical properties is related to mass loss in wood durability testing [see e.g. Hartley (1958) in Wilcox (1978)]. However, even under the absence of a measureable mass loss, strength (Curling et al., 2001, 2002; Brischke et al., 2008) and stiffness (Humar et al., 2008) decreases were observed, which reveals the dominant influence of microstructural changes on the overall material behavior.

Relations between microstructural and mechanical effects of fungal decay were previously already investigated by Winandy et al. (2000) and Curling et al. (2001, 2002). They measured stiffness and strength properties in bending tests on Southern pine samples degraded by *G. trabeum* and *Postia placenta* (both brown rot), respectively, for up to 12 weeks and corresponding changes in chemical composition. The experiments indicate hemicelluloses to be degraded from the beginning onwards, before later also the glucan

content starts to decrease. At about 30 % mass loss, the samples comprised no mechanical resistance any more. At this point, the glucan content and also the modulus of elasticity (MOE) in bending start to decrease rapidly, revealing that MOE in longitudinal direction is strongly related to cellulose content. Similar results were found by (Humar et al., 2008) by means of Fourier transform infrared (FT-IR) spectroscopy in combination with dynamic mechanical testing on Norway spruce and Scots pine degraded by *Antrodia vaillantii* and *G. trabeum* (both brown rot), respectively.

To the best knowledge of the authors, all reported investigations of effects of fungal decay on elastic stiffness properties of wood in ambient conditions exclusively concern the behavior in the longitudinal direction. However, the mechanical properties in the transverse directions (radial and tangential) are expected to be much more sensitive to degradation. This is at least known from thermally modified wood [see Korkut (2008) for effect of thermal degradation on tension strength perpendicular to the grain] or from immediate effects of high temperature on the mechanical behavior of wood [see Gerhards (1982) for effect of temperature on MOE perpendicular to the grain]. Recently, it was shown by Przewloka et al. (2008) that radial stiffness and radial compressive strength of water saturated wood samples may constitute suitable indicators to detect incipient decay.

This motivates to investigate experimentally effects of fungal degradation on anisotropic stiffness properties considering also changes of physical and chemical characteristics. In particular, we use samples of Scots pine (*Pinus sylvestris*) sapwood degraded by one fungus causing brown rot (*G. trabeum*) and one fungus causing white rot (*T. versicolor*), respectively. We apply tensile testing and ultrasonic testing for the purpose of quantifying elastic anisotropic stiffness properties of the specimens in initial sound and in degraded states. Ultrasonic testing has a long tradition in wood mechanics and was not only used for measuring stiffness properties of clear wood [see e.g. Bucur (2006) and references therein] but also of decayed wood [see e.g. Ross and Pellerin (1994) and references therein].

The experimental results presented herein are set into relation to changes in physical and chemical properties of the same samples, presented in the first part of this contribution (Bader et al., 2011c). Consequently, conclusions on microstructure/stiffness-relationships can be drawn. Particularly, we want to investigate, if transversal stiffness is more sensitive to degradation than longitudinal stiffness, and how changes of chemical composition and changes in mechanical properties are related.

Finally, the suitability of stiffness properties to become durability indicators is assessed, and possible future research strategies are derived.

## 5.2 Materials and methods

406 specimens of Scots pine (*Pinus sylvestris* L.) sapwood with dimensions of 20 x 15 x 130 mm<sup>3</sup> (radial  $l_R$  x tangential  $l_T$  x longitudinal  $l_L$ ) were characterized in the initial sound condition. For this purpose, the longitudinal elastic modulus of each bar was measured in a tension test and its longitudinal stiffness by means of an ultrasonic method. Both

test procedures are described in more detail below.

Out of the 406 specimens, 14 samples served as reference. They were cut into three cubes with dimensions of  $20 \times 15 \times 20 \text{ mm}^3$  ( $l_R \times l_T \times l_L$ ) and tested for stiffnesses in all three principal material directions by means of ultrasound. The remaining samples were exposed to *Gloephyllum trabeum* [(Pers.) Murrill, strain CTB 863A] and to *Trametes versicolor* [(L.) Lloyd, strain FPRL 280] for up to 28 weeks, 196 bars for each fungus. These decay tests were carried out adapted to EN113 (1996). After every second week, 14 specimens were taken out as representatives of one degradation stage. Additionally, 14 beech samples were used for the virulence test of *T. versicolor*. According to EN113 (1996) the mass loss was determined after 16 weeks degradation time. Brown rot degradation leads to an irregular shape of the specimens. In order to be able to determine mass density and mean stresses in tensile tests, the samples were reshaped (see Bader et al. (2011c)). Brown rot samples were only tested up to 16 weeks degradation, since for longer degradation stages the specimens were considerably cracked and tended to crumble apart. On the contrary, white rot degraded samples could be mechanically characterized for up to 28 weeks degradation time.

After tensile testing of the degraded samples, three cubes with corresponding cross-sections and 20 mm length  $l_L$  were cut out of each bar and used for ultrasonic testing in all three principal material directions - similar to the testing procedure performed on the reference samples.

Additionally to the tests for stiffness properties described herein, physical and chemical properties of the samples in initial sound and degraded states were measured, see Bader et al. (2011c) for the entire test program. In the following, details on the applied experimental techniques for determination of stiffness properties are specified.

### 5.2.1 Tensile tests

Tensile tests were performed on a MTS 858 MiniBionix (MTS Systems corporation, Eden Prairie, MN, USA) with a 15 kN load cell. Longitudinal strain was measured by HBM DD1 clamp-on strain transducers (Hottinger Baldwin Messtechnik GmbH, Wien, Austria) with a zero span of 25 mm (see Figure 5.1a). To ensure elastic conditions during the measurement, tensile specimens were loaded with a cross head speed of 0.3 mm/min up to a maximum displacement of 0.3 mm, which resulted in a maximum stress between 5 and 10 MPa depending on the stiffness of the specimens in initial sound and degraded state, respectively. The elastic modulus  $E_L$  was calculated by fitting regression to the linear part of the recorded curve (10 - 80% of maximum applied stress).

### 5.2.2 Ultrasonic tests

Ultrasonic (US) tests were performed using a pulser-receiver PR 5077 (Panametrics Inc., Waltham, MA, USA), a digital oscilloscope (WaveRunner 62Xi, Lecroy Corporation, Chestnut Ridge, NY, USA), a pair of ultrasonic transducers for longitudinal pulses with a frequency of 100 kHz (Panametrics Inc., Waltham, MA, USA), honey as coupling medium,

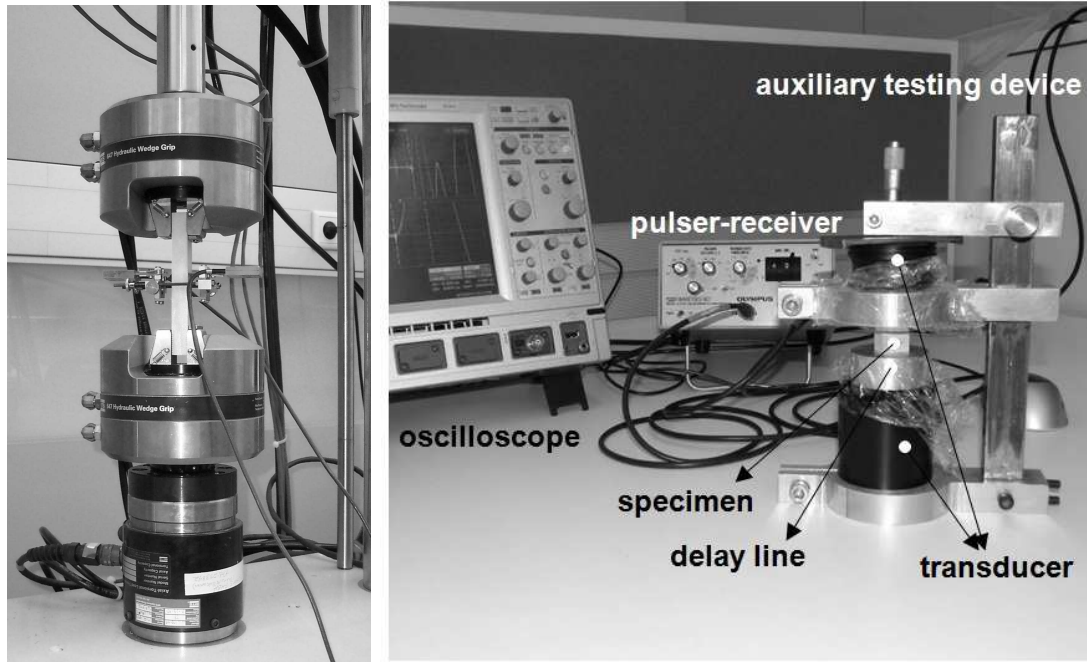


**Figure 5.1:** Experimental set-up for (a) tensile tests and (b) ultrasonic tests.

and an auxiliary testing device to hold the transducers (cf. Figure 5.1b). In addition, a delay line cylinder made of aluminum alloy 5083 with a height of 20 mm, referring to a time delay of  $3.77 \mu\text{s}$ , was used to re-locate the receiver signal out of the time range of receiver disturbances [see Figure 5.1b and Kohlhauser and Hellmich (2010) for further details on method and set-up]. A cellophane film was used to prevent the coupling medium honey from infiltrating the wood microstructure and thus, influencing its stiffness properties. All tests were performed in transmission-through mode in all three principal material directions of wood, namely longitudinal, radial, and tangential direction. The oscilloscope yields the time of flight of the ultrasonic wave through the specimen  $t_i$ , which provides, in combination with the travel distance through the specimen,  $l_i$ , the phase velocity in a specific material direction [ $i = L, R, T$ ] of the wave as  $v_{ii} = l_i/t_i$ . Elastic stiffnesses  $C_{iii}$  related to the corresponding direction are then obtained from

$$C_{iii} = \rho v_{ii}^2 \quad (5.1)$$

where sample-specific mass densities  $\rho$  were employed. Anisotropic stiffnesses of wood are a function of three independent elastic moduli  $E_i$  and three independent Poisson ratios  $\nu_{ij}$ . Thus, it is not possible to derive directly the longitudinal elastic modulus in one material direction from the corresponding stiffnesses.

## 5.3 Results and discussion

### 5.3.1 Mechanical properties of sound samples

The mass densities of the samples at ambient conditions of 20 °C and 65 %RH varied between 0.474 and 0.622 g/cm<sup>3</sup>. Mechanical tests revealed longitudinal elastic moduli ( $E_L$ ) between 8.56 and 20.42 GPa [average 14.41 GPa ( $\pm 2.34$  GPa, n=406) - values in parenthesis refer to corresponding standard deviations, followed by the number of test specimens n] and longitudinal stiffness ( $C_{LLLL}$ ) between 11.17 and 22.03 GPa [average 18.26 GPa ( $\pm 1.88$  GPa, n=406)], see Figure 5.2. As expected, longitudinal stiffnesses are higher than corresponding elastic moduli [see e.g. Bucur (2006)]. In an exemplary manner, the considerable influence of the microstructure on these longitudinal stiffness properties,  $E_L$  and  $C_{LLLL}$ , is pointed out by means of the effect of mass density  $\rho$ , expressed in the following relationships

$$E_L(\rho) = 56.76\rho - 16.91 \text{ [GPa]} \quad (R^2=0.48),$$

$$C_{LLLL}(\rho) = 47.36\rho - 7.92 \text{ [GPa]} \quad (R^2=0.52).$$

These relations are obtained by a linear fit to the results shown in Figure 5.2, with the specified coefficients of determination  $R^2$ , agreeing well with previous reports [see e.g. Eberhardsteiner (2002) for spruce and references therein].

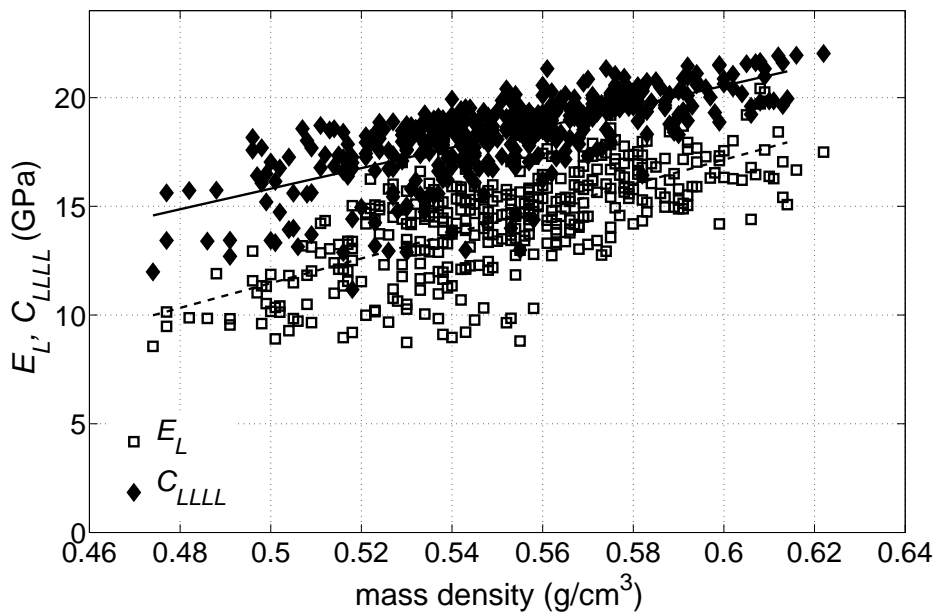


**Figure 5.2:** Initial stiffness properties of sound samples, namely longitudinal elastic modulus in tension  $E_L$ , and longitudinal stiffness  $C_{LLLL}$ , as function of density.

The transversal elastic behavior of the sound samples in radial and tangential directions was investigated by means of 42 reference cubes cut out of the 14 reference specimens. Radial and tangential stiffnesses were found to be between 2.27 and 2.95 GPa [average 2.67 GPa ( $\pm 0.18$  GPa,  $n=42$ )] and between 1.72 and 2.24 GPa [average 1.95 GPa ( $\pm 0.20$  GPa,  $n=42$ )], respectively. Corresponding anisotropy ratios amounted to 1.38 ( $\pm 0.13$ ), 7.18 ( $\pm 0.44$ ), and 9.88 ( $\pm 0.86$ ) for radial to tangential ( $C_{RRRR}/C_{TTTT}$ ), longitudinal to radial ( $C_{LLLL}/C_{RRRR}$ ), and longitudinal to tangential ( $C_{LLLL}/C_{TTTT}$ ) stiffness. From a (micro)mechanical point of view, these ratios depend on intrinsic characteristics of the wooden microstructure [as e.g. shown by Keunecke et al. (2007) for yew and spruce], such as mass density, microfibril angle, or chemical composition. Thus, changes in the microstructure are certainly reflected in these anisotropy ratios, which therefore may even allow drawing conclusions on what is altered within the material from the changing ratios.

### 5.3.2 Mechanical properties of degraded samples

As expected, both the brown rot fungus and the white rot fungus considerably influence mechanical properties of Scots pine sapwood after a durability test adapted to EN113 (1996). The virulence of the fungi was confirmed and met the requirements of the standards (Bader et al., 2011c).

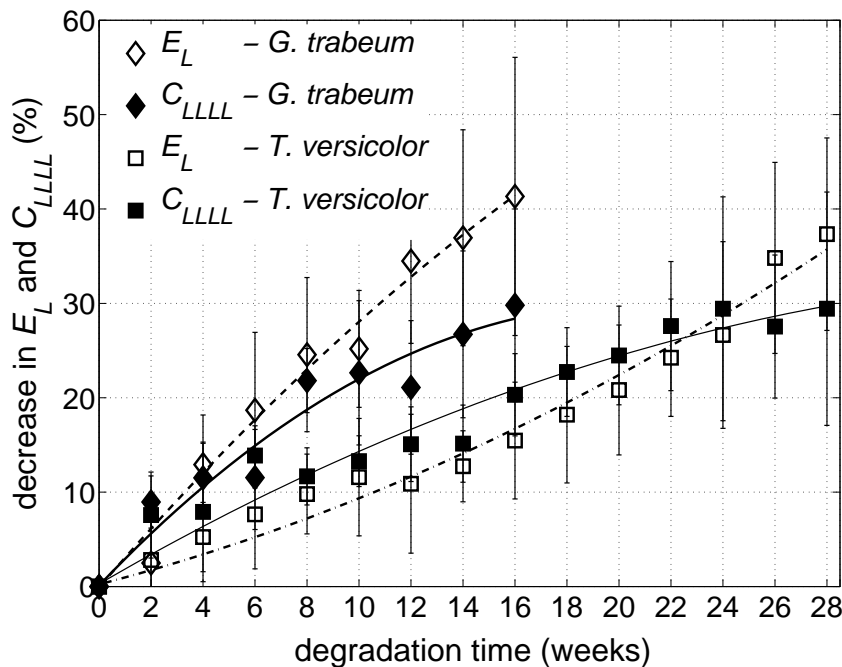


**Figure 5.3:** Decrease of longitudinal elastic modulus  $E_L$  and longitudinal stiffness  $C_{LLLL}$  over degradation time by *G. trabeum* and *T. versicolor*, respectively. Error bars indicate corresponding standard deviations ( $n=14$  for each degradation stage and fungus).

In the course of degradation by *G. trabeum*, all stiffness properties continuously decreased. Longitudinal elastic modulus in tension ( $E_L$ ) and longitudinal stiffness in ultrasonic testing ( $C_{LLLL}$ ) decreased by 41.3 % ( $\pm 14.7$  %) and 29.8 % ( $\pm 10.2$  %), respectively, after 16 weeks degradation, see Table 5.1 and Figure 5.3. The relationship between the longitudinal stiffness and the elastic modulus was found to increase considerably from 1.28 ( $\pm 0.14$ ) to 1.77 ( $\pm 0.40$ ) during the same time, see Figure 5.4. This indicates a reduced resistance to lateral contraction upon degradation, which is more pronounced than the direct reduction of stiffness in longitudinal direction.

After 10 weeks of degradation by *G. trabeum*, samples could no longer bear the gripping pressure applied in tensile tests. Therefore, the edges of the samples were strengthened using a resin [SIKA Biresin G27 (Sika sterreich GmbH, Austria)]. By cutting the samples after testing and visual inspection it was verified that the resin did not penetrate the testing track of the sample, thereby influencing stiffness properties.

Similar trends for the changes in stiffness were observed for samples degraded by *T. versicolor*, however, in reduced intensity and without the aforementioned phenomenon of a pronounced decrease in radial strength. Longitudinal elastic moduli in tension ( $E_L$ ) and longitudinal stiffness in ultrasonic testing ( $C_{LLLL}$ ) decreased by 37.3 % ( $\pm 10.2$  %) and 29.4 % ( $\pm 12.4$  %), respectively, after 28 weeks degradation time, see Table 5.1 and Figure 5.3. The corresponding ratio of stiffness to elastic modulus was found to slightly increase from 1.28 ( $\pm 0.14$ ) to 1.39 ( $\pm 0.17$ ) over the same time, revealing a lower reduction of resistance to lateral contraction than for *G. trabeum* degraded samples, see

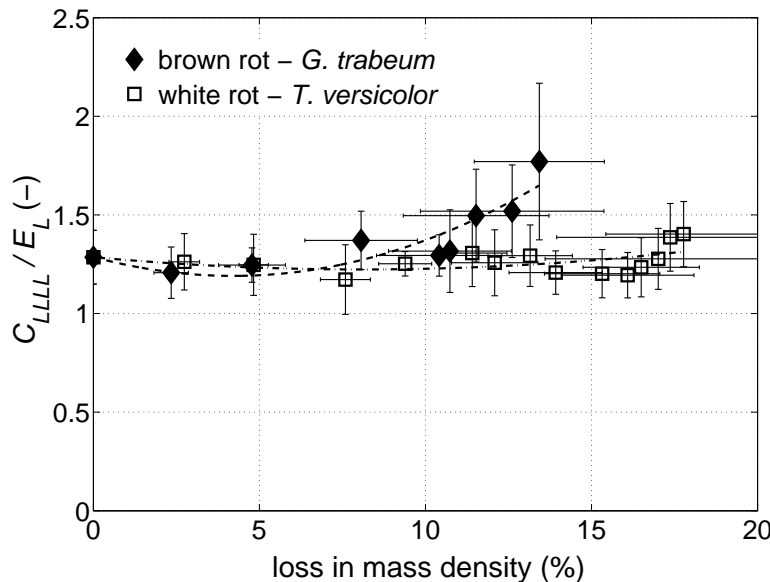


**Figure 5.4:** Ratio of longitudinal stiffness  $C_{LLLL}$  to longitudinal elastic modulus  $E_L$  over loss in mass density for degradation by *G. trabeum* and *T. versicolor*, respectively. Error bars indicate corresponding standard deviations (n=14 for each degradation stage and fungus).

**Table 5.1:** Relative decrease of longitudinal elastic modulus in tension and of stiffness in longitudinal, radial, and tangential direction found in ultrasonic testing, for Scots pine sapwood degradation by *G. trabeum* and to *T. versicolor*, respectively, for 2 to 28 weeks.

weeks of exp.	$E_L$ (tension)		$C_{LLLL}$ (US)		$C_{RRRR}$ (US)		$C_{TTTT}$ (US)	
	mean (%)	std. dev. (%)	mean (%)	std. dev. (%)	mean (%)	std. dev. (%)	mean (%)	std. dev. (%)
<i>G. trabeum</i> (brown rot)								
2	2.5	5.0	9.0	2.8	3.2	5.6	-3.1	7.7
4	12.9	5.3	11.5	3.7	18.3	11.7	1.4	8.6
6	18.7	8.2	11.5	5.5	33.0	15.2	10.5	9.2
8	24.6	8.2	21.8	3.4	40.2	6.9	23.1	10.2
10	25.2	6.2	22.6	7.6	46.4	12.3	25.3	9.5
12	34.5	8.7	21.1	7.1	60.0	16.3	22.5	17.4
14	36.9	11.4	26.7	8.8	71.3	13.9	30.9	13.5
16	41.3	14.7	29.8	10.2	70.0	13.7	38.6	12.7
18								
20								
22			no residual mechanical resistance,					
24			therefore no further testing					
26								
28								
<i>T. versicolor</i> (white rot)								
2	2.8	5.5	7.6	4.6	2.7	8.3	-2.0	8.5
4	5.2	3.7	7.9	7.4	15.0	5.0	14.5	10.1
6	7.7	5.8	13.9	2.8	16.3	6.7	13.7	9.4
8	9.8	4.2	11.7	3.0	11.0	8.8	15.1	11.0
10	11.6	6.2	13.3	2.7	16.1	7.0	19.7	7.5
12	10.9	7.4	15.1	4.0	17.7	10.0	27.2	6.8
14	12.7	3.8	15.1	4.1	24.3	6.9	29.6	7.3
16	15.5	6.2	20.3	4.4	25.5	6.7	34.3	11.3
18	18.2	7.2	22.7	4.7	27.7	7.8	36.1	7.3
20	20.8	6.9	24.5	5.2	26.0	7.6	39.1	10.9
22	24.2	6.2	27.6	6.8	29.0	8.5	40.5	9.8
24	26.7	9.9	29.4	11.9	35.7	8.8	49.2	11.1
26	34.8	10.1	27.5	7.6	36.6	9.0	53.8	11.9
28	37.3	10.2	29.4	12.4	38.8	8.4	52.7	10.9



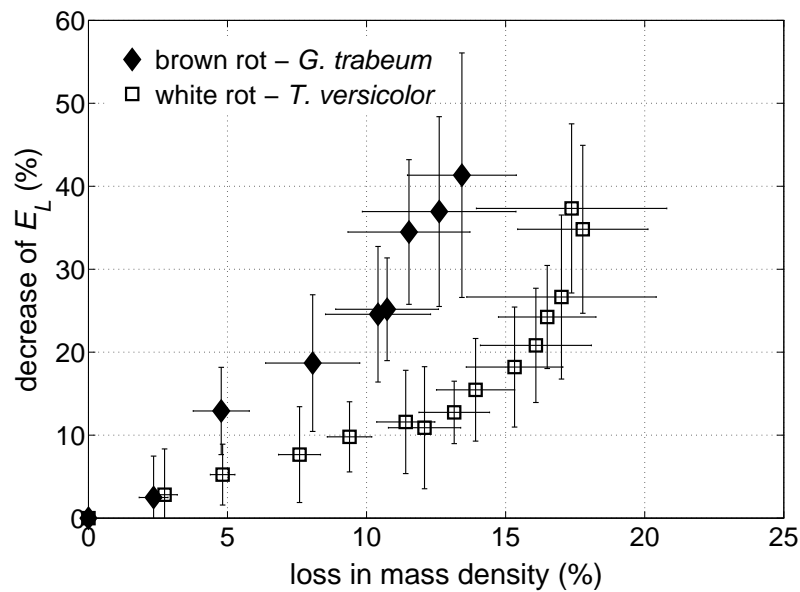


**Figure 5.5:** Relationship between loss in mass density and longitudinal elastic modulus  $E_L$  for degradation by *G. trabeum* and *T. versicolor*, respectively. Error bars indicate corresponding standard deviations (n=14 for each degradation stage and fungus).

Figure 5.4.

Change of mass density and decrease of longitudinal elastic modulus show good correlation over a time of up to 14 weeks degradation by white rot (see Figure 5.5). This indicates more or less uniform degradation of the cell wall material without affecting its overall chemical composition. This is also expressed by the almost constant density-related stiffness, which is an indicator of the stiffness of the cell wall material, during the first weeks (see Figure 5.6). Selective degradation of particular polymers within the walls only starts to be dominant after approximately 14 weeks degradation time. In addition, density-related stiffness is more strongly reduced by *G. trabeum* than by *T. versicolor* as obvious in Figure 5.6.

Compared to the longitudinal properties, transversal stiffness is much more strongly affected by fungal decay, with decreases up to 70.0 % ( $\pm 13.7$  %) and 38.6 % ( $\pm 12.7$  %) for radial and tangential stiffness, respectively, after 16 weeks of brown rot, see Table 5.1 and Figure 5.7. Correspondingly, a continuous decrease in the anisotropy ratio of radial to tangential stiffness ( $C_{RRRR}/C_{TTTT}$ ) from 1.38 ( $\pm 0.13$ ) to 0.69 ( $\pm 0.35$ ) was found for *G. trabeum*, which is shown in Figure 5.8 over the corresponding loss in mass density. The relationship of longitudinal to tangential stiffness ( $C_{LLLL}/C_{TTTT}$ ) hardly changed from 9.88 ( $\pm 0.86$ ) to 10.33 ( $\pm 1.89$ ) for this fungus. However, the ratio of longitudinal to radial stiffness ( $C_{LLLL}/C_{RRRR}$ ) increased considerably from 7.18 ( $\pm 0.44$ ) to 18.23 ( $\pm 8.36$ ), as shown in Figure 5.9 and 5.10 again over the corresponding changes in mass densities. The two latter anisotropy ratios indicate that transversal stiffness properties are more strongly affected than longitudinal ones, and, particularly, the radial direction being finally most strongly weakened. Moreover, as indicated earlier, due to the strong

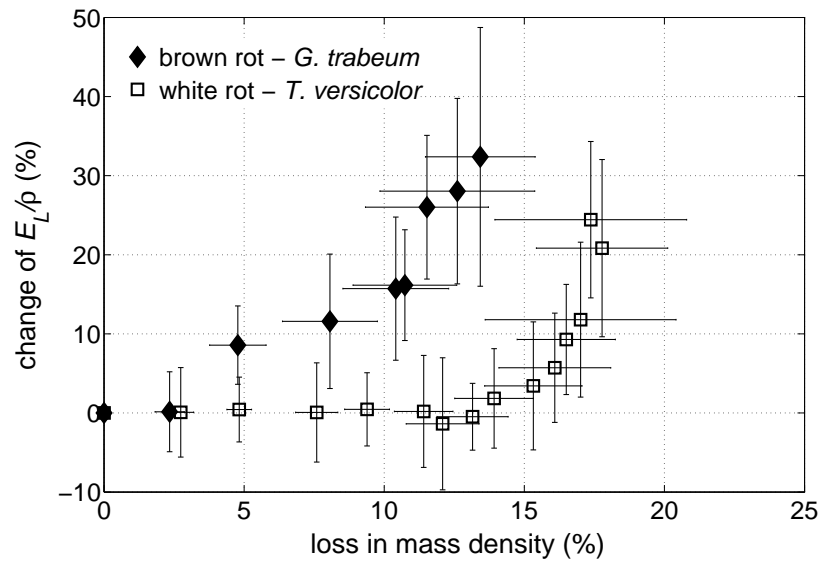


**Figure 5.6:** Relationship between loss in mass density and cell wall stiffness, expressed by the ratio longitudinal elastic modulus  $E_L$  to mass density, for degradation by *G. trabeum* and *T. versicolor*, respectively. Error bars indicate corresponding standard deviations (n=14 for each degradation stage and fungus).

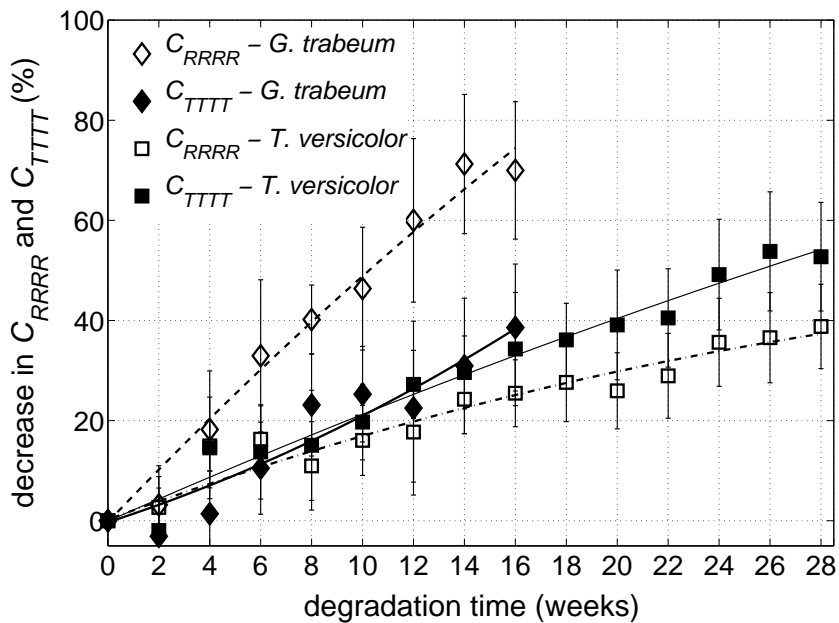


**Figure 5.7:** Decrease of radial and tangential stiffness,  $C_{RRRR}$  and  $C_{TTT}$ , over degradation time by *G. trabeum* and *T. versicolor*, respectively. Error bars indicate corresponding standard deviations (n=42 for each degradation stage and fungus).

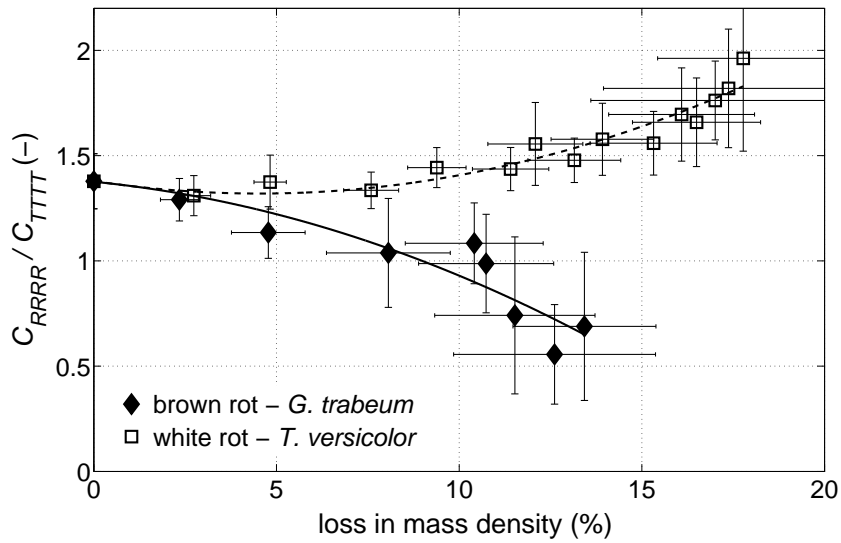


**Figure 5.8:** Change in anisotropy ratio of radial to tangential stiffness,  $C_{RRRR}/C_{TTTT}$ , due to degradation by *G. trabeum* and *T. versicolor* over corresponding loss in mass density. Error bars indicate corresponding standard deviations (n=42 for each degradation stage and fungus).

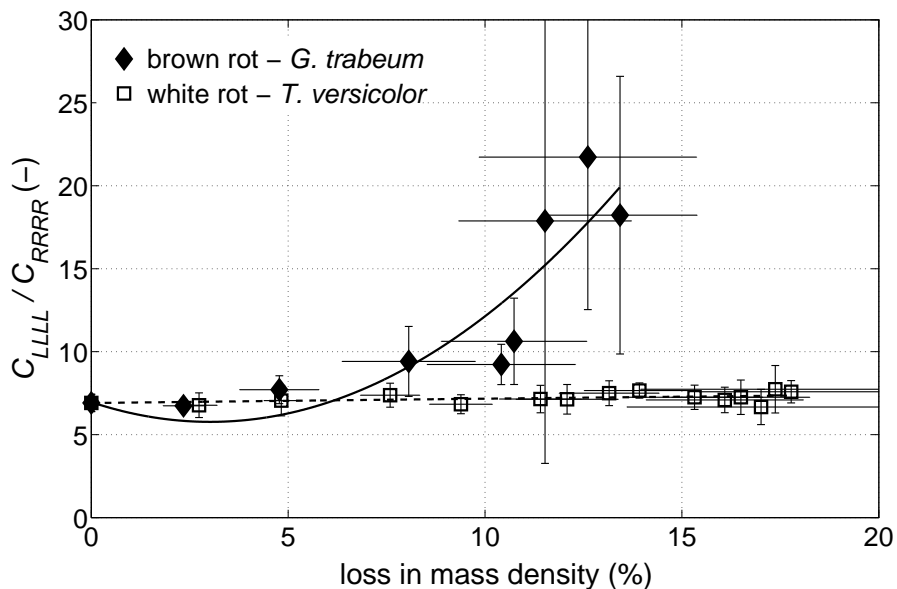


**Figure 5.9:** Change in anisotropy ratio of longitudinal to radial stiffness,  $C_{LLLL}/C_{RRRR}$ , due to degradation by *G. trabeum* and *T. versicolor* over corresponding loss in mass density. Error bars indicate corresponding standard deviations (n=42 for each degradation stage and fungus).

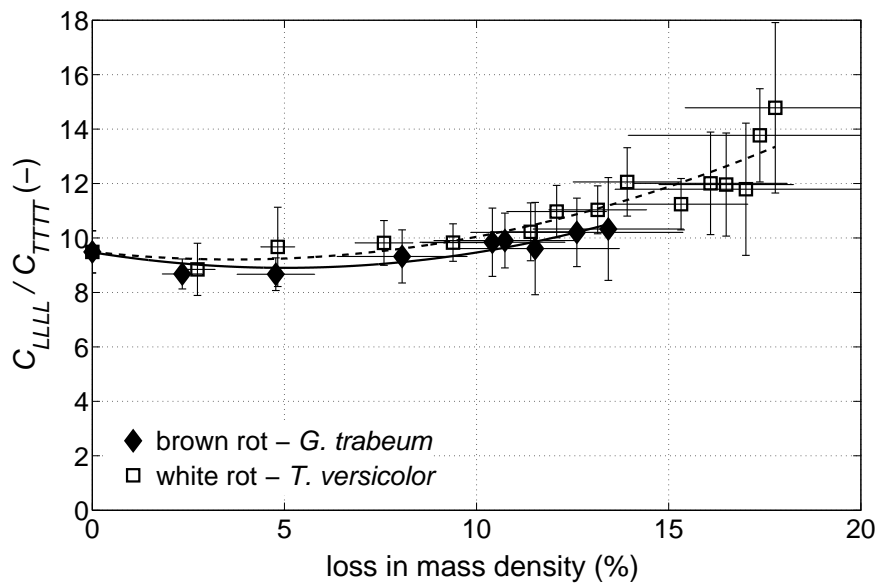


**Figure 5.10:** Change in anisotropy ratio of longitudinal to tangential stiffness,  $C_{LLLL}/C_{TTTT}$ , due to degradation by *G. trabeum* and *T. versicolor* over corresponding loss in mass density. Error bars indicate corresponding standard deviations (n=42 for each degradation stage and fungus).

decrease of transversal mechanical properties, it was no longer possible to perform tensile tests.

Similar trends were observed for *T. versicolor*, where again transversal stiffness is more strongly reduced than the longitudinal one. Decreases amounted up to 38.8 % ( $\pm 8.4$  %) and 52.7 % ( $\pm 10.9$  %) for radial and tangential stiffness after 28 weeks, respectively, see Table 5.1 and Figure 5.7. Correspondingly, a continuous increase in the anisotropy ratio between radial and tangential stiffness from 1.38 ( $\pm 0.13$ ) to 1.82 ( $\pm 0.28$ ) was found, see Figure 5.8. The ratio of longitudinal to radial stiffness just slightly increased from 7.18 ( $\pm 0.44$ ) to 7.74 ( $\pm 1.43$ ), while a considerable increase from 9.88 ( $\pm 0.86$ ) to 13.77 ( $\pm 1.71$ ) was found for the ratio of longitudinal to tangential stiffness, see Figure 5.9 and 5.10. Again, both ratios indicate that transversal properties are much more strongly affected by fungal degradation than longitudinal ones. Particularly, stiffness in tangential direction is considerably reduced and is finally most strongly weakened. Interestingly, this is vice versa to the effects observed for *G. trabeum*.

In order to clarify the reasons for these reverse trends, the growth ring structure is investigated in more detail. In general, transversal stiffness properties of wood are strongly governed by the density variations from early- to latewood and corresponding volume fractions. Recently, it was shown with X-ray microdensitometry that brown rot degradation (*Coniophora puteana*) of Scots pine differently affects early- and latewood regions (Macchioni and Palanti, 2007). Considering the annual ring structure of wood as a laminate composed of earlywood and latewood lamellas and the higher latewood density by

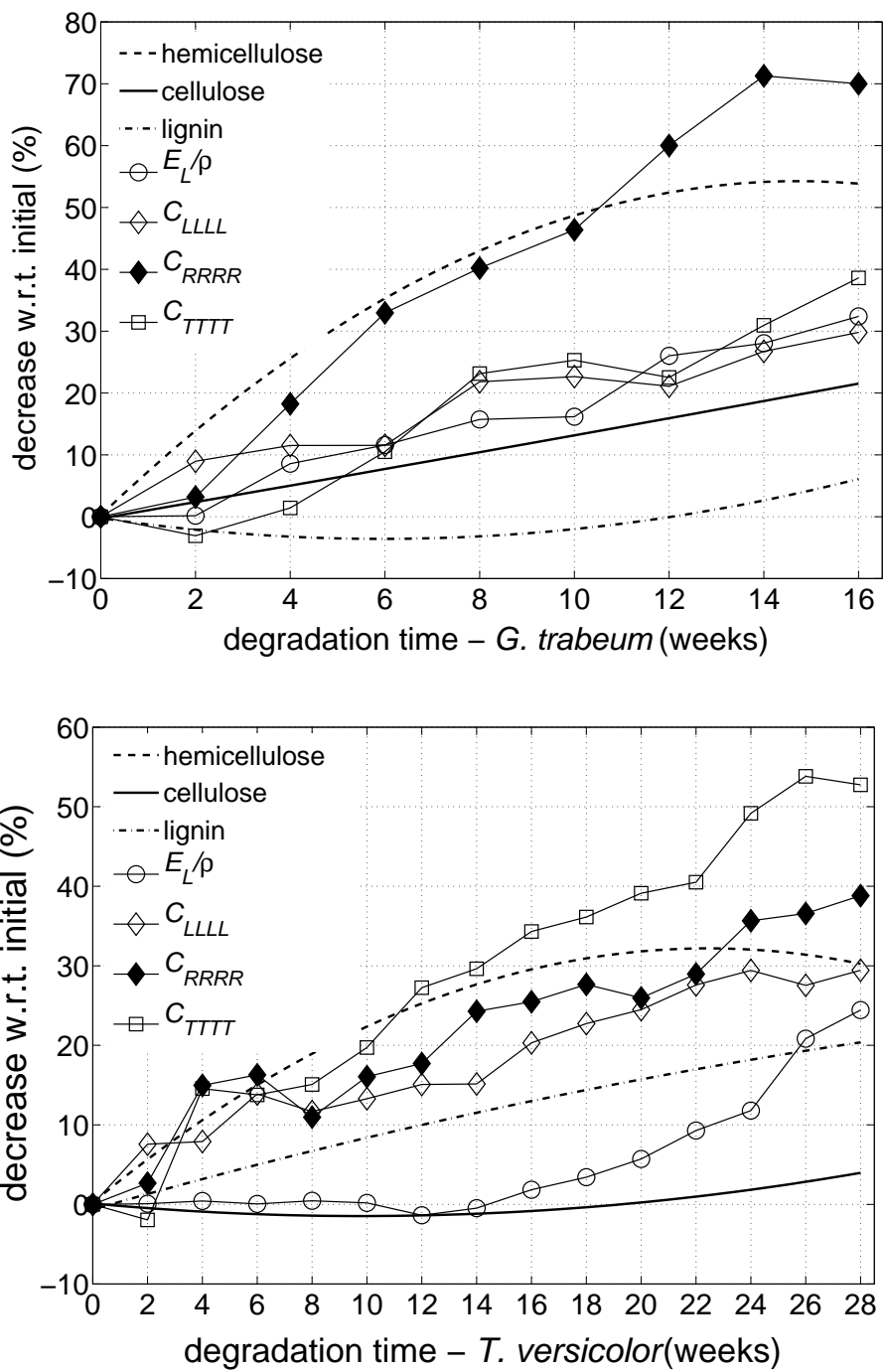


**Figure 5.11:** Change of weight fractions of chemical composition corrected with mass loss (hemicelluloses, lignin, and cellulose), density related elastic modulus ( $E_L/\rho$ ), and stiffness properties ( $C_{LLLL}$ ,  $C_{RRRR}$ ,  $C_{TTTT}$ ) for degradation by (a) *G. trabeum* and (b) *T. versicolor*.

about a factor of 2.5 (Kollmann, 1982), it is obvious that earlywood degradation more strongly affects radial than tangential properties, and vice versa. Considering the experimentally found stiffness anisotropy ratios of radial to tangential stiffness for the two fungi (Figure 5.8), it can be concluded that *G. trabeum* more strongly affects earlywood, while *T. versicolor* more strongly affects latewood.

These different effects on early- and latewood are even visually observable in cross-sections of brown rotted samples, where color differences between early- and latewood regions become more apparent with degradation time, while they are reduced in cross-sections of white rotted samples [see Figure 1 in Bader et al. (2011c)].

When comparing changes in relative longitudinal stiffness (see Figure 5.6) with alterations in the chemical composition [see Figure 5 in Bader et al. (2011c)], the strong relation of longitudinal stiffness to cellulose becomes evident. This is expressed by the same trends of the density related elastic modulus  $E_L/\rho$  and cellulose over degradation time for both decay types, as shown in Figure 5.11. On the contrary, hemicellulose and lignin degradation affect longitudinal stiffness only to a minor degree. However, radial and tangential stiffnesses are very sensitive to degradation of the latter polymer, so that these properties are more strongly reduced than the longitudinal stiffness. This is obvious in initial degradation stages, where particularly for white rot samples, cellulose is not degraded yet and mainly a pronounced decrease of the transversal stiffness properties is observed, see Figure 5.11.

## 5.4 Concluding remarks

In the present study, physical and chemical (Bader et al., 2011c) as well as mechanical properties of Scots pine sapwood in initial sound state and after degradation by brown rot (*G. trabeum*) and white rot (*T. versicolor*) were investigated. We could confirm that transversal stiffness properties are much more affected by degradation than longitudinal properties. Due to *G. trabeum* degradation, radial stiffness is most strongly decreased by up to 70.0 % and due to *T. versicolor* degradation, tangential stiffness is most strongly decreased by up to 52.7 %, while corresponding longitudinal stiffnesses are only decreased by 29.8 % and 29.4 %. Transverse stiffness properties are more sensitive to degradation than longitudinal ones due to being more sensitive to hemicellulose and lignin degradation. On the contrary, longitudinal stiffness is strongly related to cellulose. Consequently, the anisotropy ratios measured by means of ultrasonic testing in consequence of degradation identifies them as suitable indicators for quantification of the extent of degradation. Furthermore, the ultrasonic testing technique comprises the advantages of being simple to apply and non-destructive, which make it a suitable method for practical applications.

Moreover, measured anisotropy ratios can also deliver insight into degradation and allow drawing conclusions on the activity of the fungus within the specimens. This was shown in relation to dominant earlywood or latewood degradation of Scots pine, which is different for *G. trabeum* and *T. versicolor*.

Alternatively to the presented experimental approach, the gap between changes in chem-

ical composition and corresponding mechanical properties can also be bridged by micromechanical modeling of wood (Hofstetter et al., 2005, 2007; Bader et al., 2010, 2011a), which has already been successfully applied to predict mechanical properties of clear wood. These models may even allow verifying or falsifying hypotheses proposed for alterations in the microstructure, since the clear physical origin of the macroscopically observed phenomenon is taken into account. Together with nanoindentation for assessing cell wall stiffness, such a model can help to enhance the current understanding of effects of fungal decay on the microstructure of wood. The suitability of such an approach was recently verified for enzymatically treated wood (Konnerth et al., 2010). For fungal decay, this constitutes current research efforts and will be shown in another publication in the near future.

# Decrease of stiffness properties of degraded wood predicted by means of micromechanical modeling (Bader et al., 2011e)

Authored by Thomas K. Bader, Karin Hofstetter, Gry Alfredsen, and  
Susanne Bollmus

Published in *The International Research Group on Wood Protection*, 42nd annual meeting, Queenstown, New Zealand, IRG/WP 11-40570, 2011.

Wood exhibits a highly anisotropic mechanical behavior due to its heterogeneous microscopic structure and composition. Its microstructure is organized in a strictly hierarchical manner from a length scale of some nanometers, where the elementary constituents cellulose, hemicelluloses, lignin, and extractives are found, up to a length scale of some millimeters, where growth rings composed of earlywood and latewood are observed. To resolve the microscale origin of the mechanical response of the macro-homogeneous but micro-heterogeneous material wood, micromechanical modeling techniques were applied. They allow for prediction of clear wood stiffness from microstructural characteristics.

Fungal decay causes changes in the wood microstructure, expressed by modification or degradation of its components. Consequently, macroscopic mechanical properties are decreasing. Thus, in the same manner as for clear wood, consideration of alterations of wood in a micromechanical model allows predicting changes in the macroscopic mechanical properties.



This contribution covers results from an extensive experimental program, where changes in chemophysical properties and corresponding changes in the mechanical behavior were investigated. For this purpose, Scots pine (*Pinus sylvestris* L.) sapwood samples were measured in the reference condition, as well as degraded by brown rot (*Gloeophyllum trabeum*) or white rot (*Trametes versicolor*). Stiffness properties of the unaffected and the degraded material were not only measured in uniaxial tension tests in the longitudinal direction, but also in the three principal material directions by means of ultrasonic testing. The experiments revealed transversal stiffness properties to be much more sensitive to degradation than longitudinal stiffness properties. This is due to the degradation of the polymer matrix between the cellulose fibers, which has a strong effect on the transversal stiffness. On the contrary, longitudinal stiffness is mainly governed by cellulose, which is more stable with respect to degradation by fungi. Consequently, transversal stiffness properties or ratios of normal stiffness tensor components may constitute suitable durability indicators. Subsequently, simple micromechanical models, as well as a multiscale micromechanical model for wood stiffness, were applied for verification of hypotheses on degradation mechanisms and model validation.

## 6.1 Introduction

Wood is a natural material, optimized for the needs of living trees. Its microstructure is hierarchically well organized and very heterogeneous. This results in a highly anisotropic material behavior on the macroscopic scale. For example, stiffness in different material directions may vary by a factor of up to 20. As a natural material, wood has manifold advantages from ecological and economical points of view. However, one drawback is its susceptibility to deteriorating organisms. Fungal degradation alters the microstructure of wood (Côté, 1965; Fengel and Wegener, 1984) and, consequently, mechanical properties are affected.

Relationships between microstructural alterations and changes in mechanical properties have mainly been expressed in terms of empirical relations, thereby mainly based on mass loss. To overcome the restrictiveness of such relations to the specific considered characteristics, we herein apply micromechanical modeling that allows predicting changes in mechanical properties from physical alterations within the material. The development of such a model for clear wood stiffness and strength (Hofstetter et al., 2005, 2007; Bader et al., 2010, 2011a) motivates to apply a similar approach also for studying changes in stiffness upon wood decay. However, what is missing yet is the input to such a model in terms of a consistent set of parameters that describe the physical and chemical alterations within the wood. Moreover, consistent data on alterations of the mechanical behavior for validation of model predictions cannot be found in literature. Thus, we herein report on results of an extensive experimental program, where these alterations were quantified.

The paper is organized as follows. In the beginning, the hierarchical organization of wood and fundamentals of homogenization theory are reviewed (Section 6.2). Then the micromechanical model for wood stiffness is presented (Section 6.3). Thereon, the ex-

perimental program and corresponding results, serving as input for the micromechanical model and also for model validation, are discussed (Section 6.4). In Section 6.5, the validity of the modeling approach is assessed by comparing model predictions with corresponding experimental results. The paper is concluded and future research efforts are derived in Section 6.6.

## 6.2 Hierarchical organization of wood and fundamentals of homogenization theory

### 6.2.1 Hierarchical organization of wood and alterations due to fungal decay

As mentioned earlier, wood exhibits a well organized hierarchical structure from a length scale of some nanometers up to a length scale of some millimeters (see Figure 6.1). Starting at the macroscopic level, the softwood microstructure can be characterized by four levels of organization. The growth ring structure is visible to the naked eye and evolves from the alternating formation of bright earlywood and dark latewood during each growth season. Under the microscope, the cellular structure of wood, with hexagonally shaped wood cells running in stem direction, becomes evident. The cell wall is composed of different layers, whereby the S2 layer is the most dominant one by volume. The cell wall material

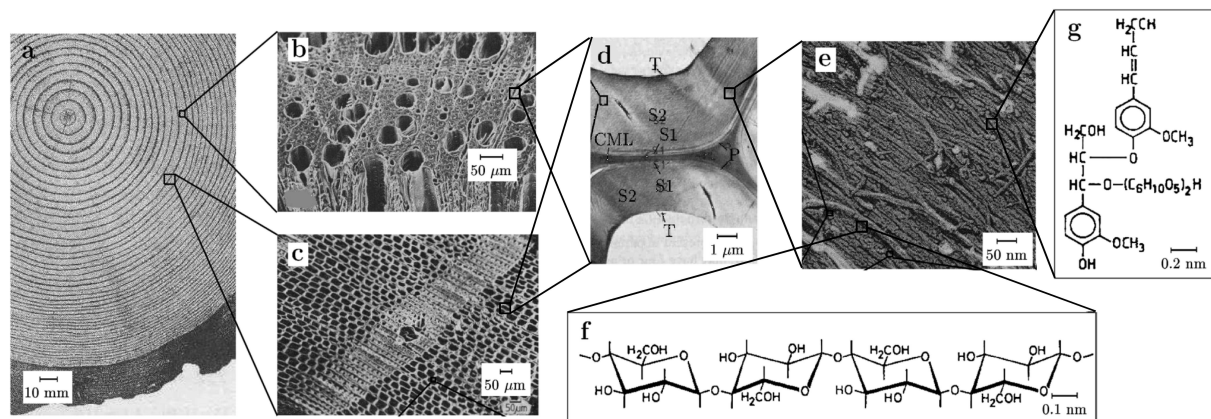


**Figure 6.1:** Hierarchical structure of wood: (a) cross-section of a log (*Ponderosa pine*) (WHB, 1999); (b) Transverse and longitudinal section through a hardwood (*European beech*), SEM (Fengel and Wegener, 1984); (c) Transverse section through a softwood (*Scots pine*), SEM (Fengel and Wegener, 1984); (d) Section through the cell wall, showing the cell wall layers, TEM (Fengel and Wegener, 1984); (e) Fibrillar structure of the S2 wall, RFDE micrograph (Hafren et al., 2000); (f) Chemical structure of cellulose chain (Fengel and Wegener, 1984); (g) Chemical structure of basic unit of lignin-polysaccharide complex (Fengel and Wegener, 1984); reproduced from (Hofstetter et al., 2005).

is a typical fiber composite, composed of partially crystalline cellulose fibrils embedded in a polymer matrix of hemicelluloses, lignin, and extractives. The orientation and the amount of cellulose vary for the different layers. For the S2 layer, the cellulose fibrils are highly orientated and inclined to the cell axis, by the so-called microfibril angle. In moist conditions, water is incorporated in the cell wall.

Wood degradation by fungi is characterized by a breakdown or/and modification of chemical constituents to varying extents, depending on the fungal species, the wood species, and the growth conditions within the wood (Côté, 1965; Fengel and Wegener, 1984). Mainly the polysaccharides and lignin are affected. Related to the degradation strategy of basidiomycetes, there are two wood decay types: brown rot and white rot (Côté, 1965; Fengel and Wegener, 1984; Schwarze, 2007). Fungi related to the first decay type degrade and mineralize wood polysaccharides, leaving behind a modified lignin that gives the decayed wood its characteristic color. On the contrary, white rot fungi are able to degrade and mineralize all major wood constituents using ligninolytic and cellulolytic/hemicellulytic enzymatic systems (Côté, 1965; Fengel and Wegener, 1984; Schwarze, 2007). Due to degradation of the constituents, a mass loss occurs, which is traditionally measured in wood durability tests.

## 6.2.2 Fundamentals of homogenization theory

In the following, fundamentals of homogenization theories, aiming at predicting effective or macro-homogeneous mechanical properties of micro-heterogeneous materials are shortly reviewed. Methods for materials with random microstructures (continuum micromechanics) are presented as well as methods for materials with periodic microstructures (unit cell method).

### 6.2.2.1 Continuum micromechanics – random homogenization theory

In continuum micromechanics (Hill, 1963; Suquet, 1997; Zaoui, 2002), a material is understood as a macro-homogeneous, but micro-heterogeneous body filling a representative volume element (RVE) with characteristic length  $\ell$ ,  $\ell \gg d$ ,  $d$  standing for the characteristic length of inhomogeneities within the RVE, and  $\ell \ll \mathcal{L}$ ,  $\mathcal{L}$  standing for the characteristic lengths of geometry or loading of a structure built up by the material defined on the RVE. In general, the microstructure within one RVE is so complicated that it cannot be described in complete detail. Therefore, quasi-homogeneous subdomains with known physical quantities (such as volume fractions, elastic properties, and eigenstresses) are reasonably chosen. They are called material phases. The homogenized mechanical behavior of the overall material, i.e., the relation between homogeneous deformations acting on the boundary of the RVE and resulting (average) stresses, or the relation between an internal pore pressure and stresses acting on the boundary of the RVE, can then be estimated from the mechanical behavior of the aforementioned homogeneous phases (representing the inhomogeneities within the RVE), their dosages within the RVE, their characteristic shapes, and their interactions. The homogenized material behavior can be derived from suitably

chosen Eshelby-Laws-type matrix-inclusion problems. If a single phase exhibits a heterogeneous microstructure itself, its mechanical behavior can be estimated by introduction of an RVE within this phase, with dimensions  $\ell_2 \leq d$ , comprising again smaller phases with characteristic length  $d_2 \ll \ell_2$ , and so on, leading to a multistep homogenization scheme.

### 6.2.2.2 Unit cell method – periodic homogenization theory

The unit cell method (Suquet, 1987; Böhm, 2004) proposes to approximate the real (micro-) heterogeneous material through one with a periodic (repetitive) microstructure, by means of defining a basic repetitive unit (the unit cell), such that the spatial variations of a physical quantity can be represented as a combination of local fluctuations at the level of the elementary (unit) cell and a drift at the level of the macroscopic structure. Subjecting the unit cell to periodic deformations at its boundaries (whose average is equal to the macroscopic strain) allows for determination of the resulting inhomogeneous microstress and microstrain fields in the microstructure. Depending on the complexity of the microstructure, these fields are determined either analytically or numerically, e.g. by means of the Finite Element method. The homogenized mechanical behavior is estimated from evaluating the average value of the periodic microstress field in the unit cell in relation to the macroscopic strains acting on the boundary of the unit cell.

## 6.3 Micromechanical model for softwood stiffness

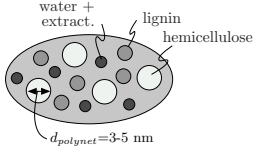
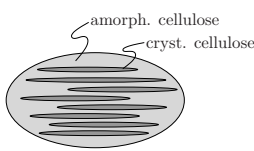
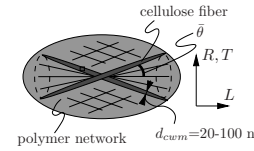
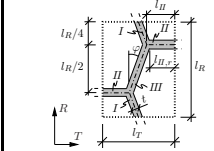
The hierarchical organization of softwood is well represented by a four level homogenization scheme (Hofstetter et al., 2005, 2007; Bader et al., 2010, 2011a), see Figure 6.2:

- Step (Ia): Polymer-network: At a length scale of some nanometers, there is a mixture of hemicelluloses, lignin, and extractives. If also water is incorporated in this matrix in moist states, a poromechanical extension of the described model is applied [see Bader et al. (2011a) for details]. Due to the intimate mixture of the components, a self-consistent scheme is adopted.
- Step (Ib): Cellulose: At the same length scale, effective stiffness properties of cellulose fibrils composed of amorphous and crystalline parts are estimated using the Mori-Tanaka method. The degree of crystallinity is considered in terms of a volume fraction of crystalline cellulose.
- Step (II): Cell wall material: At a length scale of about one micron, the homogenized mechanical behavior of the cell wall material, as a fiber reinforced composite with cellulose fibers embedded in the polymer-network, is determined by using again the Mori-Tanaka method. The inclined orientation of cellulose with respect to the cell axis (microfibril angle) is considered.
- Step (III): Softwood: At a length scale of about one hundred microns, the material softwood is defined, built up by wood cells forming a honeycomb structure of hollow

tubes oriented in stem direction. The stiffness of the honeycomb is estimated by the unit cell method in order to suitably resolve bending and out-of-plane shear deformations at transverse loading [see Hofstetter et al. (2007) for details].

Based on universal elastic properties of the nanoscaled constituents, namely amorphous and crystalline cellulose, hemicelluloses, lignin, and extractives [see Hofstetter et al. (2005) for the values], the multiscale model allows for prediction of wood tissue-specific macroscopic elastic properties from tissue-specific input parameters, namely

- mass density - mainly governing the cell wall thickness,
- moisture content,
- chemical composition, and
- microfibril angle - inclination of cellulose fibers with respect to the cell axis.

step	(Ia)	(Ib)	(II)	(III)
	<i>polymer-network</i>	<i>cellulose</i>	<i>cell wall material</i>	<i>softwood</i>
phase	hemicellulose, lignin, extractives, and water	crystalline and amorphous cellulose	polymer-network and cellulose	cell wall material and lumens
RVE model	 Self-consistent scheme	 Mori-Tanaka method	 Mori-Tanaka method	 Unit Cell method

**Figure 6.2:** Multiscale homogenization procedure for elastic stiffness properties of softwood (Hofstetter et al., 2005, 2007; Bader et al., 2010, 2011a).

Degradation in terms of removal of wood constituents within the cell wall results in generation of a pore space. Consideration of such effects on the cell wall stiffness requires extension of the micromechanical model. Since degradation due to fungal decay mainly affects the polymer-network components, we consider the pore space as an additional phase in the first homogenization step (polymer-network), see Figure 6.3. Applying the homogenization strategies sketched in Bader et al. (2011a), the homogenized poroelastic properties of softwood, namely the drained stiffness  $\mathbb{C}_{SW}^{hom}$ , the tensor of Biot coefficients  $\mathbf{b}_{SW}^{hom}$ , and the Biot modulus  $N_{SW}^{hom}$  in Eqs. (23), (24), and (27) in Bader et al. (2011a) are obtained, with which the poroelastic state equations of softwood can be formulated as

$$\Sigma_{SW} = \mathbb{C}_{SW}^{hom} : \mathbf{E}_{SW} - \mathbf{b}_{SW}^{hom} p, \quad (6.1)$$

$$(\phi - \phi_0)_{SW} = \mathbf{b}_{SW}^{hom} : \mathbf{E}_{SW} + \frac{1}{N_{SW}^{hom}} p. \quad (6.2)$$

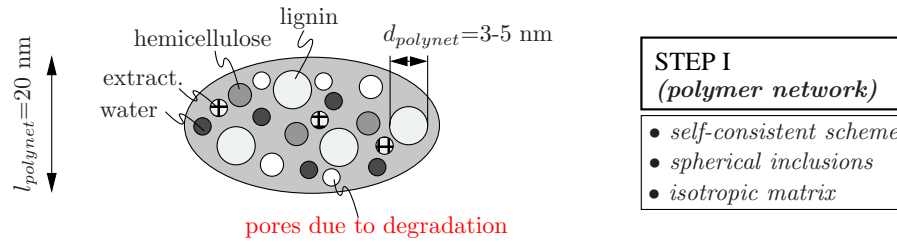


**Figure 6.3:** Representative volume element of polymer-network with pore space.

Equation (6.1) describes the relation between macroscopic stresses  $\Sigma_{SW}$  and the two loading parameters, namely pore pressure  $p$  and macroscopic strain  $\mathbf{E}_{SW}$ . Equation (6.2) gives the change of initial porosity  $\phi_0$ , again as a function of the loading parameters. In wood undrained conditions are prevailing, expressed by constant fluid mass in the RVE under mechanical loading. This allows relating the pore pressure  $p$  to the macroscopic strain  $\mathbf{E}_{SW}$ , which is then the only loading parameter.

## 6.4 Experimental program and results

### 6.4.1 Materials and Methods

For the purpose of investigating consistently on one and the same specimen changes in physical, chemical, and mechanical properties upon fungal degradation, we performed an extensive test series within the WoodWisdom-Net project *WoodExter* (cf. Figure 6.4), for details see Bader et al. (2011c,d). Particularly, 406 sapwood samples of Scots pine (*Pinus sylvestris* L.) were characterized in the initial unaffected condition (see Figure 6.4 for details on shape and dimensions of specimens) in terms of mass, mass density, and equilibrium moisture content. Moreover, the longitudinal elastic modulus in tensile tests and the longitudinal stiffness by means of ultrasonic testing were measured. All tests, except for determination of the oven-dry mass, were performed under constant climatic conditions of 20 °C and 65 % relative humidity (RH).

After quantification of the initial state, specimens were exposed either to *Gloeophyllum trabeum* [(Pers.) Murrill, strain CTB 863A] or to *Trametes versicolor* [(L.) Lloyd, strain FPRL 280] in durability tests adapted to EN113 (1996). 14 samples were included in the decay tests for each degradation stage from two to 28 weeks degradation duration. Due to the severe degradation by *G. trabeum*, the samples could only be tested up to 16 weeks degradation duration.

After determining loss in oven-dry mass and conditioning the samples at 20 °C and 65 %RH, the bars were characterized by measuring mass, mass density, and EMC. As in the reference state, the specimens were again tested in uniaxial tension tests to determine the degraded elastic modulus.

In order to determine anisotropic stiffness properties in the three principal material directions [longitudinal (in stem axis), radial (from pith to bark), and tangential (circum-

ferential) direction], ultrasonic testing was applied. This testing technique was used for measuring 42 reference cubes from undegraded reference bars, as well as for measuring all brown rot and white rot degraded cubes cut out of the corresponding degraded tensile test specimens.

Finally, the chemical composition, in terms of weight fractions of hemicelluloses, cellulose, lignin, and extractives of the dry cell wall, were determined by means of thermogravimetric analysis (TGA) and verified by means of wet chemical analysis techniques.

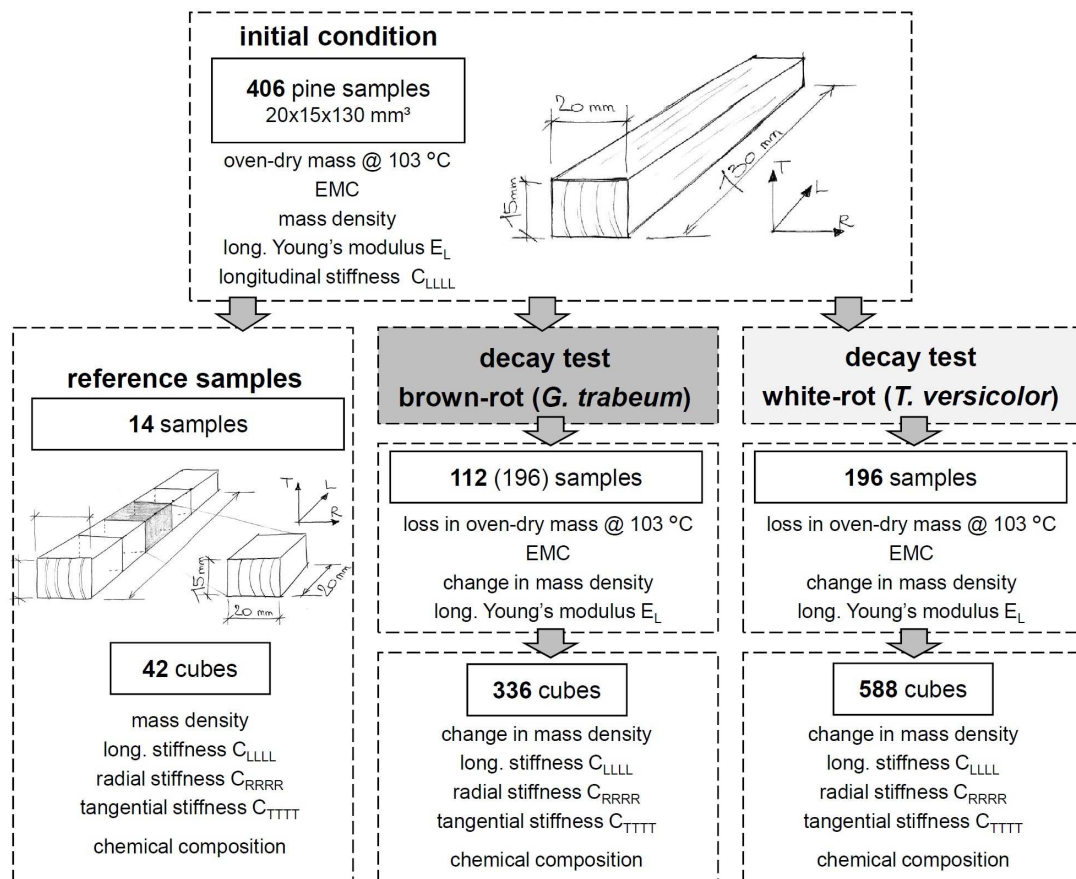


**Figure 6.4:** Experimental program for measuring changes in physical, chemical, and mechanical properties upon fungal degradation.

### 6.4.2 Results and Discussion

In the following, results of the tests for the initial condition, as well as for brown rot and white rot degradation up to 16 weeks degradation duration are discussed.

Physical, chemical, and mechanical properties in the initial unaffected condition were found to be in good agreement with literature data for sapwood of Scots pine. Mass densities varied from 0.474 to 0.622 g/cm<sup>3</sup>, longitudinal elastic moduli from 8.65 to 20.42 GPa, longitudinal stiffnesses from 11.17 to 22.03 GPa, radial stiffnesses from 2.27 to 2.95 GPa, and tangential stiffnesses from 1.72 to 2.24 GPa. The EMC amounted to 11.0 %.

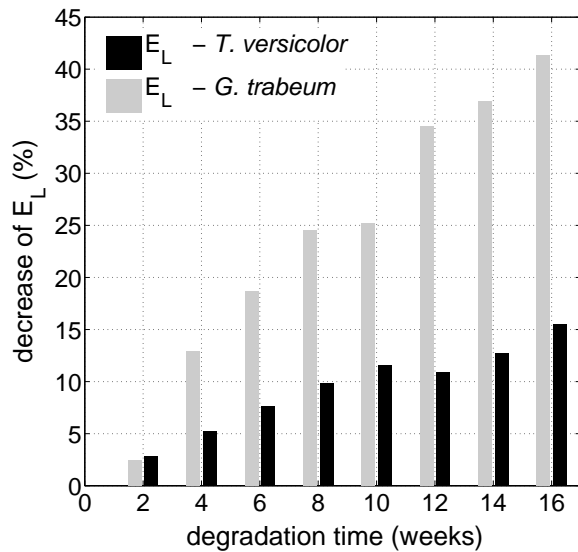


**Figure 6.5:** Decrease of longitudinal elastic modulus over degradation time - *G. trabeum* and *T. versicolor*.

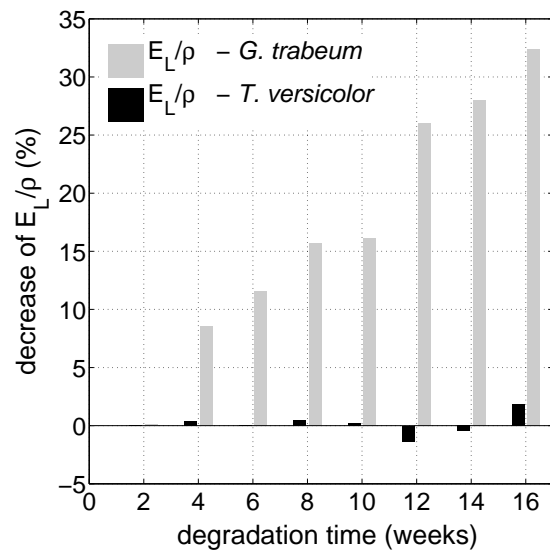


**Figure 6.6:** Decrease of density related stiffness over degradation time - *G. trabeum* and *T. versicolor*.

As expected, both fungi had a considerable influence on physical, chemical, and mechanical properties. For *G. trabeum* degraded specimens, this becomes already obvious by visual inspection. A pronounced decrease in sample size was clearly visible. On the contrary, *T. versicolor* samples did not look much affected and a decrease in sample size was not visible. Two distinctly different effects of the two considered fungi on Scots pine become evident when mass loss (sample size dependent) is compared with mass density (samples size independent). During brown rot, mass is more strongly reduced than mass density, whereas during white rot they decrease by about the same amount. This reveals a high effect of *G. trabeum* on the sample surface.

As expected, chemical composition changes in the course of brown rot and white rot degradation. *Gloeophyllum trabeum* mainly degrades hemicelluloses and cellulose. *Trametes versicolor* additionally was able to degrade lignin, while cellulose was less affected by this fungus. These alterations are reflected in the change of EMC, which is more pronounced for degradation by *G. trabeum* than for degradation by *T. versicolor*.

As expected, mechanical properties decreased as well upon degradation in consequence of the changes in physical and chemical characteristics of Scots pine. The longitudinal elastic modulus decreased by about 41 % and 16 % after 16 weeks brown rot and white rot degradation, respectively (Figure 6.5). According decreases in longitudinal stiffness were found to be about 30 % and 20 % for the two fungi after the same degradation duration. Consequently, the ratio of longitudinal elastic modulus to stiffness considerably increased in the course of brown rot degradation. The density related stiffness, as an indicator of cell wall stiffness, hardly changed up to 16 weeks white rot degradation, whereas it considerably changed during brown rot degradation (Figure 6.6).

Transversal stiffness was found to be more sensitive to degradation than longitudinal



stiffness. Corresponding decreases amount to about 70 % (radial) and 40 % (tangential) for 16 weeks brown rot degradation (Figure 6.7a) and to about 26 % (radial) and 34 % (tangential) for 16 weeks white rot degradation (Figure 6.7b). Consequently, anisotropy ratios of stiffnesses changed upon degradation. The trend of the ratio longitudinal to tangential stiffness was similar for both fungi, while the courses of the change of the ratio longitudinal to radial and the ratio radial to tangential stiffness, respectively, were found to be distinctly different for the two fungi. Considering the annual ring structure of wood, the radial to tangential stiffness ratio allows to conclude that *G. trabeum* more strongly affects earlywood, whereas *T. versicolor* more strongly affects latewood.

When relating changes in mechanical properties to the underlying alterations in chemical composition, it becomes obvious that longitudinal stiffness and elastic modulus are strongly related to cellulose content, whereas radial and tangential stiffness are very sensitive to degradation of the polymers hemicelluloses and lignin (Figure 6.7).

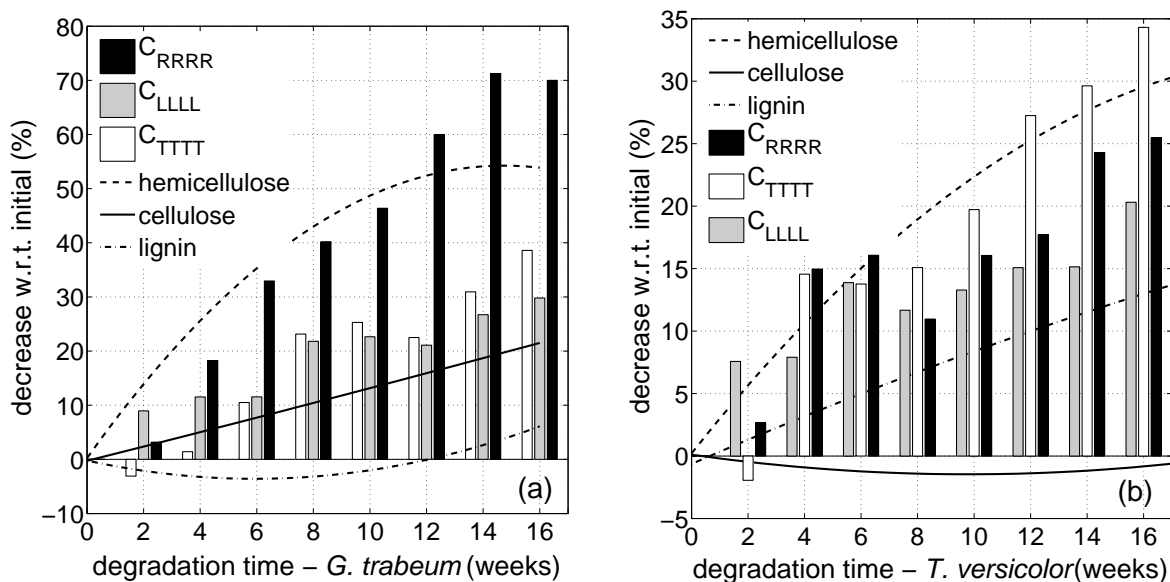


**Figure 6.7:** Decrease of weight fractions of chemical constituents (hemicelluloses, lignin, and cellulose) and stiffness properties ( $C_{LLLL}$ ,  $C_{RRRR}$ ,  $C_{TTTT}$ ) for degradation by (a) *G. trabeum* and (b) *T. versicolor*.

## 6.5 Experimental validation of micromechanical model

In the following, we assess the applicability of the micromechanical model (described in Section 6.3) to predict stiffness properties of Scots pine sapwood, not only in unaffected but also in degraded states, by comparing model predictions with corresponding experimental results discussed in Section 6.4.

### 6.5.1 Modeling of unaffected initial condition

The suitability of the modeling approach to predict clear wood stiffness was already shown in Hofstetter et al. (2005, 2007) by comparing experimental results with model predictions based on wood species-specific chemical composition, average morphological characteristics, but sample-specific mass densities and moisture contents. For the unaffected initial condition of the 14 reference specimens, we adopt the following parameters for the model:

- sample-specific input parameters:
  - mass density at 20 °C and 65 %RH,
  - equilibrium moisture content at 20 °C and 65 %RH,
  - chemical composition (fractions of cellulose, hemicelluloses, lignin, and extractives),
- average input parameters for all samples:
  - density dependent microfibril angle,
  - average crystallinity of cellulose of 0.66,
  - morphological characteristic related to the cellular softwood structure.

The corresponding comparison of model predictions with experiments is shown in a correlation plot in Figure 6.8. Perfect agreement would be given for all points lying on the diagonal of the plot. The predictive capability of the model is underlined by the low mean error  $e$  and the high coefficient of correlation  $R^2$ . Use of sample-specific microfibril angles, which were available for two samples (1.1.1 and 1.1.2), further improved the prediction accuracy.

Consideration of variations of microstructural characteristics in the micromechanical model, allows predicting maximum and minimum longitudinal elastic moduli. This is shown by the horizontal dashed lines in Figure 6.8, where maximum and minimum values of cellulose content (0.49/0.45 w%), microfibril angle (25/15°), and mass density (0.565/0.517 g/cm<sup>3</sup>) of the reference bars are combined such that maximum and minimum elastic moduli are obtained. The comparison with the corresponding test results for maximum and minimum elastic moduli of the reference bars (vertical dashed lines) reveals good agreement.

In Figure 6.9, the comparison of model predicted longitudinal elastic moduli with corresponding experimental test results is shown for all 406 Scots pine sapwood specimens in the initial state. Compared to the reference bars, the chemical composition is considered as an average of the 14 reference bars. Again, there is good agreement between model predictions and experiments.

### 6.5.2 Modeling of brown rot (*G. trabeum*) and white rot (*T. versicolor*) degraded samples

As described in Section 6.4 in detail, physical and chemical characteristics of wood change due to fungal degradation. This can be considered in the micromechanical model described

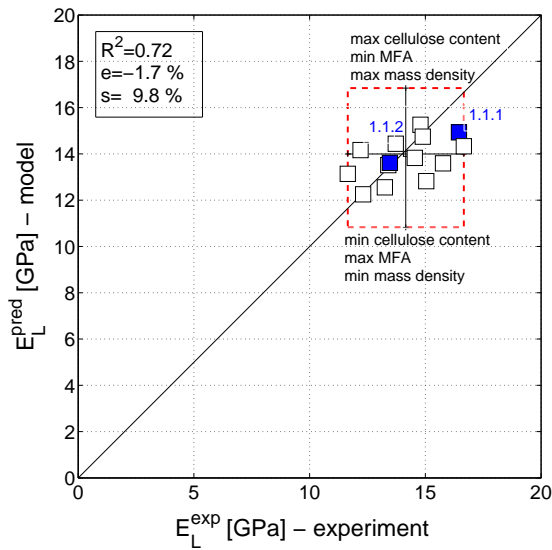


**Figure 6.8:** Comparison between experimental and model predicted elastic moduli for 14 reference specimens.

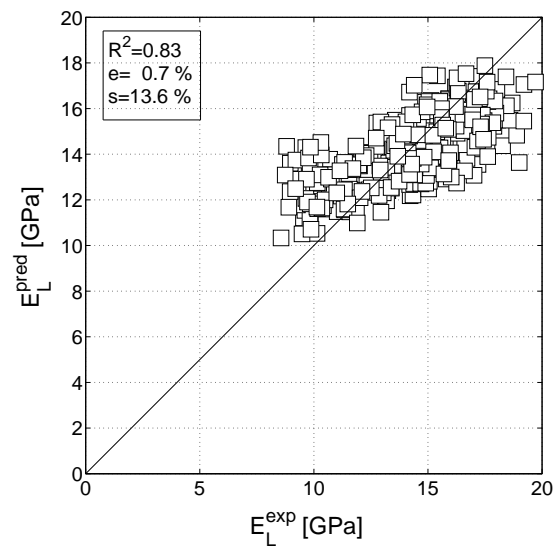


**Figure 6.9:** Comparison between experimental and model predicted elastic moduli for unaffected initial state of all 406 tested specimens.

in Section 6.3. Wood is a porous material and thus, macroscopic mass density is a function of the density of the cell wall material and of lumen porosity (thicker cell walls result in higher mass densities). Consequently, a reduction of mass density can either be ascribed to a reduction of the thickness of the cell walls, or to a decrease in cell wall density. For white rot degradation by *T. versicolor*, experimental results showed rather small changes in cell wall-related stiffness  $E_L/\rho$ , indicating rather a thinning of the cell walls than creation of pores in the cell walls. On the contrary, brown rot degradation by *G. trabeum* resulted in pronounced changes of the density related stiffness, indicating high activity of the fungus within the cell walls. These two different phenomena of cell wall degradation are considered in the following model predictions. Particularly, we apply the following input parameters:

- sample-specific input parameters:
  - mass density at 20 °C and 65 %RH,
  - equilibrium moisture content at 20 °C and 65 %RH,
- average input parameters for all samples:
  - average chemical composition for each degradation state,
  - density dependent microfibril angle,
  - crystallinity of cellulose of 0.66 for white degradation and a linear decrease in crystallinity of cellulose from 0.66 in the initial condition to 0.42 after 16 weeks

- brown rot degradation [it was e.g. shown by Howell et al. (2009), that crystallinity of cellulose considerably decreased upon *G. trabeum* degradation],
- morphological characteristic related to the cellular softwood structure.

Based on the aforementioned characteristics, sample-specific model predictions were determined. For the elastic modulus, this is exemplarily shown in Figure 6.10 for 14 weeks brown rot degraded and 16 weeks white rot degraded specimens. In these two graphs, model predictions agree well with corresponding test results. Furthermore, average decreases of the longitudinal elastic modulus were calculated from experimental results and from the model predictions, see Figure 6.11, showing again a very good agreement. Consequently, comparing the predicted course of decrease of the elastic modulus over degradation time (see Figure 6.12) reveals also good agreement with corresponding experimental observations. The variability in decreases of the elastic modulus found in the experiments (indicated by the horizontal bars in Figure 6.11) cannot be reproduced by the model (indicated by the vertical bars in Figure 6.11). This may indicate a pronounced effect of the variability of changes in chemical composition, which is not considered in the model evaluations.

The micromechanical model was also validated for transversal stiffnesses and shear stiffnesses of various softwood species by Hofstetter et al. (2005, 2007). For the specimens considered herein, model predicted transversal (radial and tangential) stiffnesses are lower than corresponding results. This is due to transversal stiffness properties measured by means of ultrasound being considerably higher than elastic moduli measured in quasistatic tests. Thus, we only consider relative changes in the transversal elastic behavior of wood

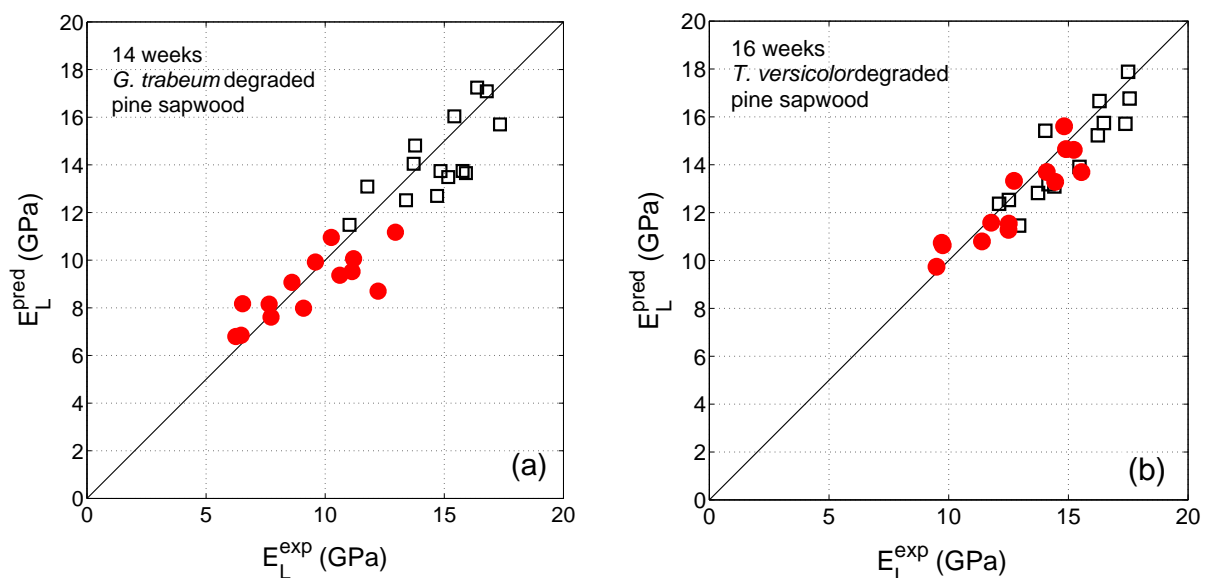


**Figure 6.10:** Sample-specific comparison between experimental and model predicted elastic moduli for (a) 14 weeks degradation by *G. trabeum* and (b) 16 weeks degradation by *T. versicolor* [(o) reference condition and (o) degraded state].

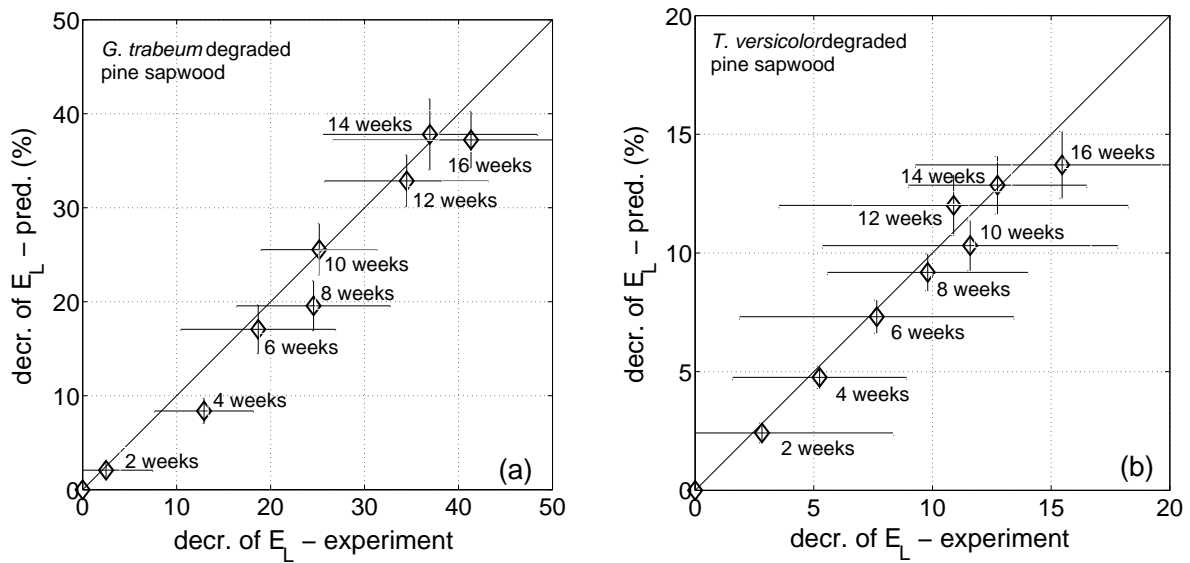


**Figure 6.11:** Comparison between experimental and model predicted decreases of the elastic modulus for 2 to 16 weeks degradation by (a) *G. trabeum* and (b) *T. versicolor*. Error bars indicate corresponding standard deviations.

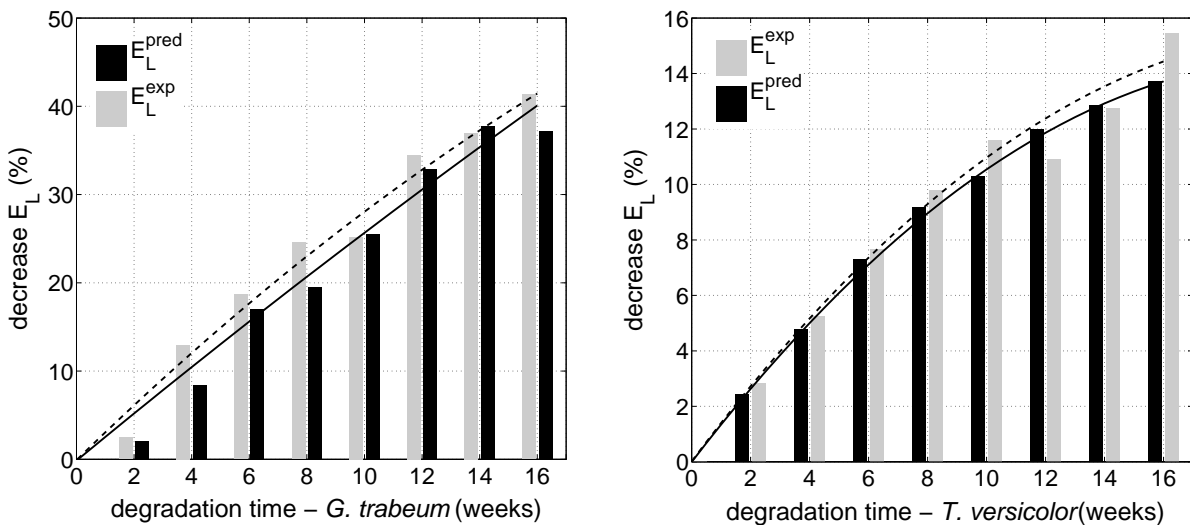


**Figure 6.12:** Comparison between experimental and model predicted decreases of Young's modulus up to 16 weeks degradation by *G. trabeum* and *T. versicolor*.

and compare the model predicted changes with experimental results, as shown in Figure 6.13 for both types of rot. The average decrease of transversal properties is well predicted by the model. However, the model does not show the different effects on radial and tangential stiffnesses, which probably result from different degradation strategies for earlywood and latewood described in Section 6.4. Since the model does not include the growth ring structure, it fails to correctly predict the transversal behavior. This motivates

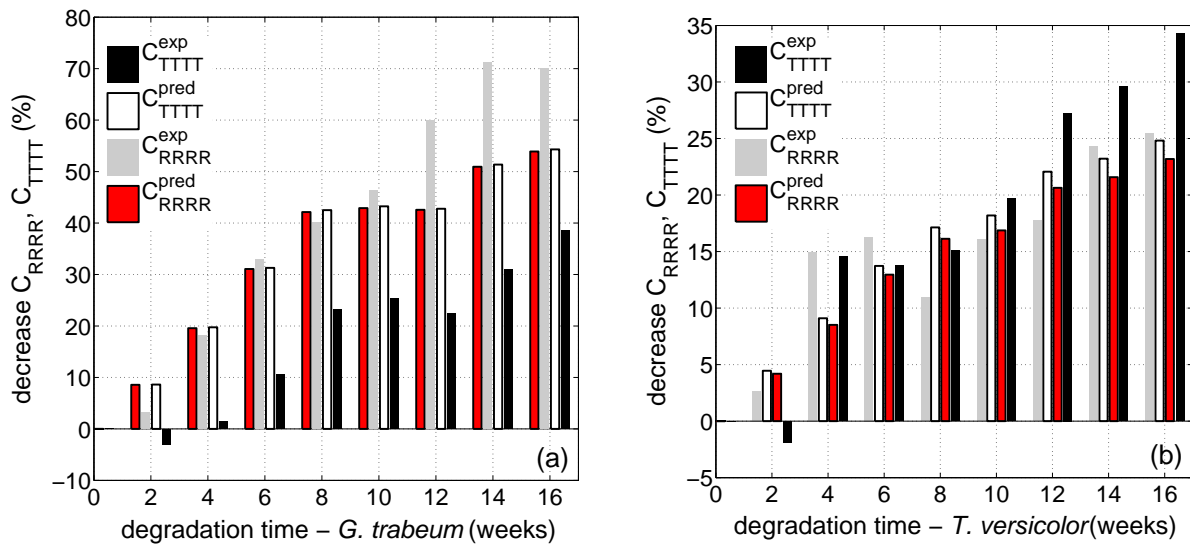


**Figure 6.13:** Comparison between experimental and model predicted decreases of radial and tangential stiffness up to 16 weeks degradation by (a) *G. trabeum* and (b) *T. versicolor*, respectively.

adding another homogenization step based on laminate theory, which constitutes current and future research efforts.

## 6.6 Conclusions and Perspectives

Micromechanical modeling is a suitable technique to quantify the decrease of stiffness properties upon degradation. This was shown herein by comparing model predictions with experimental data from an extensive experimental program. Thereby, Scots pine sapwood samples were characterized in unaffected state and degraded by *G. trabeum* (brown rot) and by *T. versicolor* (white rot), respectively, determining physical and chemical alterations of the wood samples as well as corresponding changes in mechanical properties. The good agreement between model predictions and corresponding experimental results finally underlines the predictive capability of the micromechanical model to estimate changes in anisotropic stiffness properties of wood upon fungal decay.

The applied experimental techniques, particularly ultrasonic testing and chemical analysis, comprise the advantage of being non-destructive or requiring only small-scale specimens. This makes them suitable methods for determining the remaining load bearing capacity of existing timber structures. Micromechanical modeling is not only applicable for the herein considered fungal degradation, but could in the same manner also be applied to predict changes in the mechanical properties due to thermal degradation or chemical modification.

Moreover, micromechanics can also be used to get more insight into the heterogeneity of the degradation and to verify or falsify hypotheses on alterations within the microstructure

of wood. In this particular project, simple micromechanical considerations of the annual ring structure of softwood, allowed to conclude that *G. trabeum* more strongly affects earlywood, whereas *T. versicolor* more strongly affects latewood in Scots pine sapwood specimens.

Together with nanoindentation for assessing cell wall stiffness, the micromechanical model can help to enhance the current understanding of effects of fungal decay on the microstructure of wood. The suitability of such an approach was recently validated for enzymatically treated red oak (Konnerth et al., 2010). For fungal decay, this constitutes current research efforts and will be shown in another publication in the near future.

# Bibliography

- Alfredsen, G., Bader, T.K., Dibdiakova, J., Filbakk, T., Bollmus, S., Hofstetter, K., 2011. Thermogravimetric analysis for wood decay characterisation. *European Journal of Wood and Wood Products*, accepted for publication.
- Ashkenazi, E., 1966. Strength of Anisotropic Wooden and Synthetic Materials. *Lesnaja Promyshlennost*, Moscow, in Russian.
- Auriault, J.L., Sanchez-Palencia, E., 1977. Etude du comportement macroscopique d'un milieu poreux saturé dèformable [study of macroscopic behavior of a saturated deformable medium]. *Journal de Mècanique* 16, 575–603, in French.
- Bader, T.K., Hofstetter, K., Hellmich, Ch., Eberhardsteiner, J., 2010. Poromechanical scale transitions of failure stresses in wood: from the lignin to the spruce level. *ZAMM* 90(10-11), 750–767.
- Bader, T.K., Hofstetter, K., Hellmich, Ch., Eberhardsteiner, J., 2011a. The poroelastic role of water in cell walls of the hierarchical composite "softwood". *Acta Mechanica* 217, 75–100.
- Bader, T.K., Hofstetter, K., Eberhardsteiner, J., Keunecke, D., 2011b. Microstructure-stiffness relationships of Common yew and Norway spruce. *Strain*, accepted for publication.
- Bader, T.K., Hofstetter, K., Alfredsen, G., Bollmus, S., 2011c. Changes in microstructure and stiffness of Scots pine (*Pinus sylvestris*) sapwood degraded by *Gloeophyllum trabeum* and *Trametes versicolor* - Part I: Physicochemical alterations. *Holzforschung*, accepted for publication.
- Bader, T.K., Hofstetter, K., Alfredsen, G., Bollmus, S., 2011d. Changes in microstructure and stiffness of Scots pine (*Pinus sylvestris*) sapwood degraded by *Gloeophyllum trabeum* and *Trametes versicolor* - Part II: Anisotropic stiffness. *Holzforschung*, accepted for publication.
- Bader, T.K., Hofstetter, K., Alfredsen, G., Bollmus, S., 2011e. Decrease of stiffness properties of degraded wood predicted by means of micromechanical modeling. IRG/WP 11-40570, International Research Group on Wood Protection 42nd annual meeting, Queenstown, New Zealand.



- Benveniste, Y., 1987. A new approach to the application of Mori-Tanaka's theory in composite materials. *Mechanics of Materials* 6, 147–157.
- Bodig, J., Jayne, B., 1982. *Mechanics of Wood and Wood Composites*. Van Nostrand Reinhold, New York, USA.
- Böhm, H., 2004. A short introduction to continuum micromechanics. In: *Mechanics of Microstructure Materials*. Ed. Böhm, H. CISM Lecture Notes No. 464. Springer Verlag Wien/New York, 1–40.
- Böhm, H., Han, W., Eckschlager, A., 2004. Multi-Inclusion Unit Cell Studies of Reinforcement Stresses and Particle Failure in Discontinuously Reinforced Ductile Matrix Composites. *Computer Methods in Engineering Science* 5(1), 5–20.
- Brischke, C., Welzbacher, C.R., Huckfeldt, T., 2008. Influence of fungal decay by different basidiomycetes on the structural integrity of Norway spruce wood. *Holz als Roh- und Werkstoff* 66, 433–438.
- Bucur, V., 2006. *Acoustics of Wood*. 2nd Edition. Springer Verlag Berlin Heidelberg New York.
- Burgert, I., 2006. Exploring the micromechanical design of plant cell walls. *American Journal of Botany* 93, 1391–1401.
- Cave, I.D., 1968. The anisotropic elasticity of the plant cell wall. *Wood Science and Technology* 2, 268–278.
- Cecchi, A., Sab, K., 2002. Out of plane model for heterogeneous periodic materials: the case of masonry, *European Journal of Mechanics - A/Solids* 21(5), 715–746.
- Chateau, X., Dormieux, L., 1998. Approche micromécanique du comportement d'un milieu poreux non saturé [Micromechanical approach for the behavior of a non-saturated porous medium]. *Comptes Rendus de l'Académie des Sciences Série IIb* 326, 533–538, in French.
- Chateau, X., Dormieux, L., 2002. Micromechanics of saturated and unsaturated porous media. *International Journal for Numerical and Analytical Methods in Geomechanics* 26, 831–844.
- Cockrell, R.A., 1974. A comparison of latewood pits, fibril orientation and shrinkage of normal and compression wood of Giant Sequoia. *Wood Science and Technology* 8, 197–206.
- Côté, W.A., 1965. *Cellular Ultrastructure of Woody Plants*. Syracuse University Press, New York, USA.
- Cousins, W., 1976. Elastic modulus of lignin as related to moisture content. *Wood Science and Technology* 10, 9–17.

- Cousins, W., 1978. Young's modulus of hemicellulose as related to moisture content. *Wood Science and Technology* 12, 161–167.
- Cousins, W., Armstrong, R., Robinson, W., 1975. Young's modulus of lignin from a continuous indentation test. *Journal of Material Science* 10, 1655–1658.
- Coussy, O., 1995. *Mechanics of porous continua*. Wiley, Chistester, England.
- Coussy, O., 2004. *Poromechanics*. Wiley, Chistester, England.
- Crawford, R.L., 1981. *Lignin biodegradation and transformation*. Wiley, New York.
- Curling, S., Clausen, C.A., Winandy, J.E., 2001. The effect of hemicellulose degradation on the mechanical properties of wood during brown rot decay. IRG/WP 01-20219.
- Curling, S., Cluasen, C.A., Winandy, J.E., 2002. Relationship between mechanical properties, weight loss, and chemical composition of wood during incipient brown-rot decay. *Forest Product Journal* 51, 34–39.
- Da Silva, A., Kyriakides, S., 2007. Compressive response and failure of balsa wood. *International Journal of Solids and Structures* 44, 8685–8717.
- Dormieux, L., Kondo, D., Ulm, F.J., 2006. *Microporomechanics*, Wiley.
- Dormieux, L., Ulm, F.J., 2004. *Applied Micromechanics of Porous Materials (CISM Courses and Lectures No. 480)*, L. Dormieux, F.-J Ulm (Hrg.), Springer Verlag, Wien NewYork.
- Dormieux, L., Molinari, A., Kondo, D., 2004. Micromechanical approach to the behavior of poroelastic materials. *Journal of the Mechanics and Physics of Solids* 50, 2203–2231.
- Dvorak, G.J., Benveniste, Y., 1992. Transformation field analysis of inelastic composite materials. *Proceedings of the Royal Society London A* 437, 291–310.
- Easterling, K., Harryson, R., Gibson, L., Ashby, M., 1982. On the mechanics of balsa and other woods. *Proceedings of the Royal Society London A* 383, 31–41.
- Eberhardsteiner, J., 2002. *Mechanisches Verhalten von Fichtenholz: Experimentelle Bestimmung der biaxialen Festigkeitseigenschaften [Mechanical Behavior of Spruce Wood: Experimental Determination of Biaxial Strength Properties]*. Springer Verlag, Wien, New York, in German.
- Eder, M., 2007. *Structure, properties and function of single wood fibres of Norway spruce (Picea abies [L.] Karst.)*. Doctoral thesis, Universität für Bodenkultur, Wien.
- Eichhorn, S., Young, R., 2001. The Young's modulus of a microcrystalline cellulose. *Cellulose* 8, 197–207.
- El Omri, A., Fennan, A., Sidoroff, F., Hihi, A., 2000. Elastic-plastic homogenization of layered composites. *European Journal of Mechanics A/Solids* 19, 585–601.

- EN113, 1996. Wood preservatives - Test method for determining the protective effectiveness against wood destroying basidiomycetes - Determination of toxic values. Brussels, Belgium, European Committee for Standardization (CEN).
- Enoki, A., Tanaka, H., Fuse, G., 1989. Relationship between degradation of wood and production of H<sub>2</sub>O<sub>2</sub>-producing or one-electron oxidases by brown-rot fungi. *Wood Science and Technology* 23, 1–12.
- Eshelby, J., 1957. The determination of the elastic field of an ellipsoidal inclusion, and related problems. *Proceedings of the Royal Society London A* 241, 376–396.
- Esteves, B., Gominho, J., Rodrigues, J.C., Miranda, I., Pereira H., 2005. Pulping Yield and Delignification Kinetics of Heartwood and Sapwood of Maritime Pine. *Journal of Wood Chemistry and Technology* 25(4), 217–230.
- Fengel, D., 1970. Ultrastructure of Cellulose from Wood. Part 2: Problems of Isolation of Cellulose. *Wood Science and Technology* 4, 15–35.
- Fengel, D., Wegener, G., 1984. *Wood – Chemistry, Ultrastructure, Reactions*, 2nd Edition. De Gruyter, Berlin, New York.
- Fratzl, P., Weinkamer, R., 2007. Nature’s hierarchical materials. *Progress in Material Science* 52, 1263–1334.
- Friebel, C., Doghri, L., Legat, V., 2006. General mean-field homogenization schemes for viscoelastic composites containing multiple phases of coated inclusions. *International Journal of Solids and Structures* 43(9), 2513–2541.
- Fritsch, A., Hellmich, Ch., Dormieux, L., 2009. Ductile sliding between mineral crystals followed by rupture of collagen crosslinks: Experimentally supported micromechanical explanation of bone strength. *Journal of Theoretical Biology* 260, 230–252.
- Gamstedt, K., Bjurhager, I., Berglund, L., Keunecke, D., Niemz, P., 2010. Beam theory modeling of the performance of medieval yew longbows. Joint focused Meeting ”Modelling mechanical behavior of wood cultural objects.” Krakow, Poland. [http://cost-fp0802.tuwien.ac.at/fileadmin/mediapool-cost/Diverse/WS\\_Krakow/Gamstedt.pdf](http://cost-fp0802.tuwien.ac.at/fileadmin/mediapool-cost/Diverse/WS_Krakow/Gamstedt.pdf).
- Garab, J., Keunecke, D., Hering, S., Szalai, J., Niemz, P., 2010. Measurement of standard and off-axis elastic moduli and Poisson’s ratios of spruce and yew wood in the transverse plane. *Wood Science and Technology* 44, 451–464.
- Gerhards, C.C., 1982. Effect of moisture content and temperature on the mechanical properties of wood: An analysis of immediate effects. *Wood and Fiber Science* 14, 4–36.
- Gibson, L., Ashby, M., 1997. *Cellular Solids. Structure and Properties*, 2nd Edition. Cambridge University Press, Cambridge, UK.
- Gillis, P.P., 1972. Orthotropic Elastic Constants of Wood. *Wood Science and Technology* 6, 138–156.

- Gindl, W., Gupta, H.S., Schöberl, T., Lichtenegger, H.C., Fratzl, P., 2004. Mechanical properties of spruce wood cell walls by Nanoindentation. *Applied Physics A* 79, 2069–2073.
- Gindl, W., Schöberl, T., 2004. The significance of the elastic modulus of Wood cell walls obtained from nanoindentation measurements. *Composites: Part A* (11), 1345–1349.
- Grønli, M.G., Varhegyi, G., DiBlasi, C., 2002. Thermogravimetric analysis and devolatilization kinetics of wood. *Industrial and Engineering Chemistry Research* 41, 4201–4208.
- Hackspiel, Ch., 2010. A numerical simulation tool for wood grading. On the effect of knots on the mechanical behavior of wooden boards. Doctoral thesis, Vienna University of Technology.
- Hafren, J., Fujimo, T., Itoh, T., Westermarck, U., Terashima, N., 2000. Ultrastructural changes in the compound middle lamella of *Pinus thunbergii* during lignification and lignin removal. *Holzforschung* 54, 234–240.
- Hankinson, R., 1921. Investigation of crushing strength of spruce at varying angles of grain. Air Service Information Circular III 259, US Air Service.
- Harada, H., 1965. Cellular ultrastructure of woody plants. In: Côté, W. (Ed.), *Ultrastructure and organization of gymnosperm cell walls*. Syracuse University Press, Syracuse, pp. 215–233.
- Hashin, Z., Rosen, B.W., 1964. The Elastic Moduli of Fiber-Reinforced Materials. *Journal of Applied Mechanics* 31, 223–232.
- Hellmich, C., Barthélémy, J.-F., Dormieux, L., 2004a. Mineral-collagen interactions in elasticity of bone ultrastructure – a continuum micromechanics approach. *European Journal of Mechanics A/Solids* 23, 783–810.
- Hellmich, C., Ulm, F.-J., 2005. Drained and undrained poroelastic properties of healthy and pathological bone: A poro-micromechanical investigation. *Transport in Porous Media* 58 (3), 243–268.
- Hellmich, C., Celundova, D., Ulm, F.-J., 2009. Multiporoelasticity of Hierarchically Structured Materials: Micromechanical Foundations and Application to Bone. *Journal of Engineering Mechanics (ASCE)*, 135(5), 382–394.
- Hepworth, D., Vincent, J., 1998. Modelling the mechanical properties of xylem tissues from tobacco plants (*Nicotiana tabacum* 'samsun') by considering the importance of molecular and micromechanics. *Annals of Botany* 81, 761–770.
- Hill, R., 1963. Elastic properties of reinforced solids: some theoretical principles. *Journal of the Mechanics and Physics of Solids* 11, 357–372.
- Hill, R., 1965. A self-consistent mechanics of composite materials. *Journal of the Mechanics and Physics of Solids* 13, 213–222.

- Hofstetter, K., Hellmich, C., Eberhardsteiner, J., 2005. Development and experimental validation of a continuum micromechanics model for the elasticity of wood. *European Journal of Mechanics A/Solids* 24, 1030–1053.
- Hofstetter, K., Hellmich, C., Eberhardsteiner, J., 2006. The influence of the microfibril angle on wood stiffness: a continuum micromechanics approach. *Computer Assisted Mechanics and Engineering Sciences* 13: 523–536.
- Hofstetter, K., Hellmich, C., Eberhardsteiner, J., 2007. Micromechanical modeling of solid-type and plate-type deformation patterns within softwood materials. A review and an improved approach. *Holzforschung* 61, 343–351.
- Hofstetter, K., Hellmich, C., Eberhardsteiner, J., Mang, H.A., 2008. Micromechanical Estimates for Elastic Limit States in Wood Materials, Revealing Nanostructural Failure Mechanisms. *Mechanics of Advanced Materials and Structures* 15, No. 6-7, 474–484.
- Hofstetter, K., Gamstedt, E.K., 2009. Hierarchical modeling of microstructural effects on mechanical properties of wood. A review. *Holzforschung* 63, 130–138.
- Holmberg, S., Persson, K., Peterson, H., 1999. Nonlinear mechanical behavior and analysis of wood and fibre materials. *Computers & Structures* 72, 459–480.
- Howell, C., Steenkjaer Hastrup, A.C., Goodell, B., Jellison, J., 2009. Temporal changes in wood crystalline cellulose during degradation by brown rot fungi. *International Biodeterioration & Biodegradation* 63, 414–419.
- Huang, C.L., Jutscha, N.P., Leaf, G.J., Megraw, R.A., 1997. Comparison of microfibril angle measurement techniques. In: Butterfield BG editors. IAWA-press 177–205.
- Humar, M., Bucar, B., Vek, V., Pohleven, F., 2008. Changes of mechanical and chemical properties of wood after brown-rot decay and blue staining. Joint Meeting of COST Action IE0601 "Wood Science for Conservation of Cultural Heritage", and the European Society for Wood Mechanics. Braga, Portugal.
- Jäger, A., Bader, T.K., Hofstetter, K., Eberhardsteiner, J., 2011. The relation between indentation modulus, microfibril angle, and elastic properties of wood cell walls. *Composites Part A* 42, 677–685.
- Kahle, E., Woodhouse, J., 1994. The influence of cell geometry on the elasticity of softwood. *Journal of Material Science* 29, 1250–1259.
- Kameda, J., Yokoyama, Y., Allen, T.R., 2007. Strain-controlling mechanical behavior in noncrystalline materials I: Onset of plastic deformation. *Materials Science and Engineering A* 448, 235–241
- Kaminski, M.M., 2005. *Computational Mechanics of Composite Materials: Sensitivity, Randomness, and Multiscale Behaviour*. Springer Verlag, Berlin, Heidelberg, New York.

- Kanit, T., Forest, S., Galliet, I., Mounoury, V., Jeulin, D., 2003. Determination of the size of the representative volume element for random composites: statistical and numerical approach. *International Journal of Solids and Structures* 40, 3647–3679.
- Keunecke, D., Sonderegger, W., Pereteanu, K., Lüthi, T., Niemz, P., 2007. Determination of Young's and shear moduli of Common yew and Norway spruce by means of ultrasonic waves. *Wood Science and Technology* 41, 309–327.
- Keunecke, D., Hering, S., Niemz, P., 2008. Three-dimensional elastic behaviour of Common yew and Norway spruce. *Wood Science and Technology* 42(8), 633–647.
- Keunecke, D., Niemz, P., 2008a. Axial stiffness and selected structural properties of yew and spruce microtensile specimens. *Wood Research* 53(1), 1–14.
- Keunecke, D., Evan, R., Niemz, P., 2009. Microstructural properties of Common yew and Norway spruce determined with Silviscan. *IAWA Journal* 30, 165–178.
- Kohlhauser, C., Hellmich, C., 2010. Determination of Poisson's ratios in isotropic, transversely isotropic, and orthotropic materials by means of combined ultrasonic-mechanical testing of normal stiffnesses: Application to metals and wood. *European Journal of Mechanics A Solids*. submitted for publication.
- Kohlhauser, C., Hellmich, C., Vitale-Brovarone, C., Rota, A., Eberhardsteiner, J., 2009. Ultrasonic characterisation of porous biomaterials across different frequencies. *Strain* 45, 34–44.
- Kollmann, F., 1934. Die Abhängigkeit der Festigkeit und der Dehnungszahl der Hölzer vom Faserverlauf [Dependence of wood strength and Poisson's ratio on the fiber orientation]. *Der Bauingenieur* 15, 198–200, in German.
- Kollmann, F., 1982. *Technologie des Holzes und der Holzwerkstoffe* [Technology of Wood and Wood Products], 2nd Edition. Vol. 1. Springer Verlag, Berlin, Heidelberg, New York, in German.
- Kollmann, F., Côté, W., 1968. *Principles of Wood Science and Technology*. Vol. 1. Springer Verlag, Berlin, Heidelberg, New York.
- Konnerth, J., Eiser, M., Jäger, A., Bader, T.K., Hofstetter, K., Follrich, J., Ters, T., Hansmann, C., Wimmer, R., 2010. Macro- and micromechanical properties of red oak wood (*Quercus rubra* L.) treated with hemicellulases. *Holzforschung* 64, 447–453.
- Korkut, S., 2008. The effects of heat treatment on some technological properties in Uludag fir (*Abies bornmuelleriana* Mattf.) wood. *Building and Environment* 43, 422–428.
- Laws, N., 1977. The determination of stress and strain concentrations at an ellipsoidal inclusion in an anisotropic material. *Journal of Elasticity* 7 (1), 91–97.
- Lemarchand, E., Ulm, F.-J., Dormieux, L., 2002. Effect of inclusions on friction coefficient of highly filled composite materials. *ASCE Journal of Engineering Mechanics* 128 (8), 876–884.

- Macchioni, N., Palanti, S., 2007. Measurements of fungal wood decay on Scots pine and beech by means of X-ray microdensitometry. *Wood Science and Technology* 41, 417–426.
- Mackenzie-Helnwein, P., Eberhardsteiner, J., Mang, H., 2003. A multi-surface plasticity model for clear wood and its application to the finite element analysis of structural details. *Computational Mechanics* 31 (1–2), 204–218.
- Mark, R., 1967. *Cell Wall Mechanics of Tracheids*, 2nd Edition. Yale University Press, New Haven, USA.
- Michel, J.C., Moulinec, H., Suquet, P., 1999. Effective properties of composite materials with periodic microstructure: a computational approach. *Computer Methods in Applied Mechanics and Engineering* 172, 109–143.
- Mori, T., Tanaka, K., 1973. Average stress in the matrix and average elastic energy of materials with misfitting inclusions. *Acta Metallurgica* 21, 571–574.
- O’Sullivan, A., 1997. Cellulose: the structure slowly unravels. *Cellulose* 4, 173–207.
- Oeggl, K., 2009. The significance of the Tyrolean Iceman for the archaeobotany of Central Europe. *Vegetation History and Archaeobotany* 18, 1–11.
- Oliver, W.C., Pharr, G.M., 1992. An improved technique for determining hardness and elastic-modulus using load displacement sensing indentation experiments. *Journal of Material Research* 7, 1564–1583.
- Ostoja-Starzewski, M., 2006. Material spatial randomness: From statistical to representative volume element. *Probabilistic Engineering Mechanics* 21, 112–132.
- Papka, S.D., Kyriakides, S., 1999. In-plane biaxial crushing of honeycombs – Part II: Analysis. *International Journal of Solids and Structures* 36, 4397–4423.
- Pedersen, O.B., 1983. Thermoelasticity and Plasticity of Composites - I. Mean Field Theory. *Acta Metall.* 31, 1795–1808.
- Persson, K., 2000. Micromechanical modelling of wood and fibre properties. Doctoral thesis. Lund University.
- Pichler, B., Scheiner, St., Hellmich, Ch., 2008. From Micron-Sized Needle-Shaped Hydrates to Meter-Sized Shotcrete Tunnel Shells: Micromechanical Upscaling of Stiffness and Strength of Shotcrete. *Acta Geotechnica* 3, 273–294.
- Pichler, B., Hellmich, Ch., Eberhardsteiner, J., 2009. Spherical and Acicular Representation of Hydrates in a Micromechanical Model for Cement Paste: Prediction of Early-Age Elasticity and Strength. *Acta Mechanica* 203(3-4), 137–162.
- Pichler, B., Hellmich, Ch., 2010. Estimation of Influence Tensors for Eigenstressed Multi-phase Elastic Media with Non-Aligned Inclusion Phases of Arbitrary Ellipsoidal Shape. *Journal of Engineering Mechanics* 136(8), 1043–1053.

- Przewloka, S.R., Crawford, D.M., Rammer, D.R., Buckner, D.L., Woodward, B.M., Li, G., Nicholas, D.D., 2008. Assessment of biodeterioration for the screening of new wood preservatives: Calculation of stiffness loss in rapid decay testing. *Holzforschung* 62, 270–276.
- Quinson, R., Perez, J., Rink, M., Pavan, A., 1997. Yield criteria for amorphous glassy polymers. *Journal of Materials Science* 32, 1371–1379.
- Ross, R.J., Pellerin, R.F., 1994. Nondestructive testing for assessing wood member in structures - A review. General Technical Report FPL-GTR-70. USDA Forest Service, Forest Products Laboratory, Madison.
- Salmén, L., Burgert, I., 2009. Cell wall features with regard to mechanical performance. A review, COST Action E35 2004-2008: Wood machining micromechanics and fracture. *Holzforschung* 63, 121–129.
- Scheiner, St., Hellmich, C., 2009. Continuum Microviscoelasticity Model for Aging Basic Creep of Early-Age Concrete. *Journal of Engineering Mechanics (ASCE)*, 135(4), 307–323.
- Schwarze, F.W.M.R., 2007. Wood decay under the microscope. *Fungal Biology Reviews* 21, 133–170.
- Senft, J.F., Bendtsen, B.A., 1985. Measuring microfibrillar angles using light microscopy. *Wood and Fiber Science* 17(4), 564–567.
- Smith S.A., Langrish T.A.G., 2008. Multicomponent Solid Modeling of Continuous and Intermittent Drying of *Pinus radiata* Sapwood Below the Fiber Saturation Point. *Drying Technology* 26, 844–854.
- Stamm, A.J., 1964. *Wood and Cellulose Science*. Roland Press, New York.
- Stevanic, J.S., Salmén, L., 2009. Orientation of the wood polymers in the cell wall of spruce wood fibres. *Holzforschung* 63, 497–503.
- Suquet, P., 1987. Elements of homogenization for inelastic solid mechanics. In: *Homogenization Techniques for Composite Media*. Eds. Sanchez-Palencia, E., Zaoui, A. Lecture Notes in Physics, No. 272. Springer Verlag, Wien/New York. 193–278.
- Suquet, P. (Ed.), 1997. *Continuum Micromechanics*. Springer Verlag, Wien, New York.
- Tang, R., 1973. The microfibrillar orientation in cell-wall layers of virginia pine tracheids. *Wood Science and Technology* 5, 181–186.
- Tappi standard, 1983. T 222. Cm-00, Acid in-soluble lignin in wood and pulp.
- Tappi standard, 1998. T 204. Cm-07, Solvent extractives of wood and pulp.
- Tappi standard, 2000. T 249. Cm-00, Carbohydrate composition of extractive-free wood and wood pulp by gas-liquid chromatography.



- Tashiro, K., Kobayashi, M., 1991. Theoretical evaluation of three-dimensional elastic constants of native and regenerated celluloses: role of hydrogen bonds. *Polymer* 32 (8), 1516–1526.
- Thompson, M, Willis, J., 1991. A reformation of the equations of anisotropic poroelasticity. *Journal of Applied Mechanics* 58, 612–616.
- Tjeerdsma, B.F., Boonstra, M., Pizzi, A., Tekely, P., Militz, H., 1998. Characterisation of thermally modified wood: molecular reasons for wood performance improvement. *Holz als Roh- und Werkstoff* 56, 149–153.
- Tsai, S., Wu, E., 1971. A two-dimensional orthotropic model for simulating wood drying processes. *Applied Mathematical Modelling* 20, 60–81.
- Vincent, J., 2003. Biomimetic modelling. *Philosophical Transactions of the Royal Society London B358*, 1597–1603.
- Wilcox, W.W., 1978. Review of literature on the effects of early stages of decay on wood strength. *Wood and Fiber* 9(4), 252–257.
- Wimmer, R., Lucas, B.N., Tsui, T.Y., Oliver, W.C., 1997. Longitudinal hardness and Young's modulus of spruce tracheid secondary walls using nanoindentation technique. *Wood Science and Technology* 31, 131–141.
- WHB, 1999. *Wood Handbook*. Forest Products Society, USA.
- Winandy, J.E., Clausen, C.A., Curling, S.F., 2000. Predicting the effects of decay on wood properties and modeling residual service-life. *Proceedings of the 2nd annual conference on durability and disasters mitigation in wood-frame housing*, 261–263.
- Windeisen, E., Bächle, H., Zimmer, B., Wegener, G., 2009. Relations between chemical changes and mechanical properties of thermally treated wood. *Holzforschung* 63, 773–778.
- Yildiz, S., Gezerb, E.D., Yildiza, U.C., 2006. Mechanical and chemical behavior of spruce wood modified by heat. *Building and Environment* 41, 1762–1766.
- Young, R., Lovell, P., 1991. *Introduction to Polymers*, 2nd Edition. Chapman & Hall, London.
- Yu, Y., Fei, B., Wang, H., Tian, G., 2011. Longitudinal mechanical properties of cell wall of Masson pine (*Pinus massoniana* Lamb) as related to moisture content: A nanoindentation study. *Holzforschung* 65, 121–126.
- Zaoui, A., 2002. Continuum micromechanics: Survey. *ASCE Journal of Engineering Mechanics* 128 (8), 808–816.
- Zhang, K., Duan, H., Karihaloo, B.L., Wang, J., 2010. Hierarchical, multilayered cell walls reinforced by recycled silk cocoons enhance the structural integrity of honeybee combs. *Proceedings of the National Academy of Sciences* 107(21), 9502–9506.

- 
- Zimmermann, T., Sell, J., Eckstein, D., 1994. Rasterelektronenmikroskopische Untersuchungen an Zugbruchflächen von Fichtenholz [Scanning electron microscope investigation of the fracture surface of spruce]. Holz als Roh- und Werkstoff 52, 223–229, in German.

# Publications and conference presentations

## Publications

Konnerth, J., Eiser, M., Jäger, A., Bader, T.K., Hofstetter K., Follich, J., Ters, T., Hannsmann, C., Wimmer, R.:

*Macro- and Micromechanical Properties of Red Oak Wood (Quercus Rubra L.) Treated with Hemicellulases,*

Holzforschung 64 (2010) 447–453.

Jäger, A., Bader, T.K., Hofstetter, K., Eberhardsteiner, J.:

*The relation between nanoindentation modulus, microfibril angle, and elastic properties of wood cell walls,*

Composites Part A 42 (2011) 677–685.

Alfredsen, G., Bader, T.K., Dibdiakova, J., Filbakk, T., Bollmus, S., Hofstetter, K.:

*Thermogravimetric analysis for wood decay characterisation,*

accepted for publication in European Journal of Wood and Wood Products (2011).

## Conference presentations

Bader, T.K., Hofstetter, K., Hellmich, Ch., Eberhardsteiner, J.:

*Multiscale Microporomechanics Model for Estimation of Elastic Limit States of Softwood Materials”,*

COST Action FP0802 Workshop - Experimental and Computational Methods in Wood Micromechanics, Vienna, Austria, 11/05/2009–13/05/2009 (oral presentation).

Bader, T.K., Hofstetter, K., Hellmich, Ch., Eberhardsteiner, J.:

*Homogenization and Localization in a Multiscale Microporomechanical Model for Wood Strength,*

7th EUROMECH Solid Mechanics Conference, Lisbon, Portugal, 07/09/2009–11/09/2009 (oral presentation).

Bader, T.K., Braovac, S., Hofstetter, K.:

*Microstructure-Stiffness Relations of the Ancient Oak Wood from the Oseberg Ship,*

International Workshop on ”Modeling Mechanical Behavior of Wooden Cultural Objects”, Krakow, Poland; 12/04/2010–13/04/2010 (oral presentation).

Bader, T.K., Hofstetter, K., Hellmich, Ch., Eberhardsteiner, J.:

*Multiscale Microporomechanics of Softwood - Applications and Experimental Model Validation,*

IV. European Conference on Computational Mechanics (ECCM 2010), Paris, France, 16/05/2010–21/05/2010 (oral presentation).

Bader, T.K., Wikete, C., Jäger, A., Hofstetter, K., Eberhardsteiner, J.:  
*Mechanical Properties and Microstructural Characteristics of Hardwood*,  
COST Action FP 0802: Wood Structure/Function-Relationships, Hamburg, Germany,  
05/10/2010–08/10/2010 (poster presentation).

Bader, T.K., Hofstetter, K., Hellmich, Ch., Eberhardsteiner, J.:  
*From Lignin to Spruce: Poromechanical Upscaling of Wood Strength*,  
Material Research Symposium Fall Meeting, Boston, Massachusetts, 29/11/2010–03/12/2010  
(conference paper DOI: 10.1557/opl.2011.534).

Bader, T.K., Hofstetter, K.:  
*Pilzabbau von Holz - Quantifizierung des Steifigkeitsverlusts auf Basis von mikromechanischen Überlegungen*,  
"Wiener Holzschutztage 2010", Holzforschung Austria, Vienna, 2010, (in German), ISBN:  
978-3-9503036-1-2, 50–55 (conference paper).

Bader, T.K., Hofstetter, K., Alfredsen, G., Bollmus, S.:  
*Decrease of stiffness properties of degraded wood predicted by means of micromechanical modeling*,  
42nd annual meeting of the International Research Group on Wood Protection (IRG/WP),  
Queenstown, New Zealand, 08/05/2011–12/05/2011 (conference paper and oral presentation).

# Curriculum Vitae

## Personal Data

Name: **Dipl.-Ing. Thomas Karl BADER**  
Date of Birth: 24th April 1980  
Place of Birth: Mistelbach, Austria  
Nationality: Austrian  
Military service: Alternative service (02/2000 – 01/2001)  
Current address: Tullnerbachstraße 9-11/3/71, 3002 Purkersdorf  
Material status: Married (Martina Bader-Rehak)  
Children: 2 children (Maximilian, Konstantin)

## Education

11/2007 – 06/2011 Doctoral studies at Vienna University of Technology, Vienna, Austria  
10/2001 – 10/2007 Diploma studies in Civil Engineering at Vienna University of Technology, Vienna, Austria, graduation with distinction  
09/1994 – 07/1999 High school student in Civil Engineering, Krems, Austria

## Activities abroad

08/2009 University of Oslo, Museum of Cultural History, Oslo, Norway, Short term scientific mission on "Mechanical properties of ancient wood"  
01/2007 – 05/2007 The University of Edinburgh, Edinburgh, UK, Short term scientific mission on "Structural design of stadia"

## Work Experience

11/2007 – present University Assistant at the Institute for Mechanics of Materials and Structures, Vienna University of Technology, Vienna, Austria  
09/2007 – 10/2007 Stipendiary at the Institute for Mechanics of Materials and Structures, Vienna University of Technology, Vienna, Austria  
05/2001 – 06/2007 Engineer, Hans Zöchling GesmbH, Hainfeld, Austria  
02/2001 – 04/2001 Engineer, K&W Dienstleistungsmanagement GmbH, St. Pölten, Austria  
08/1999 – 09/2000 Engineer, Domus Bau GmbH, St. Pölten, Austria  
08/1998 Trainee, Anton Traunfellner GesmbH, Scheibbs, Austria  
07/1997, 07/1998 Trainee, DI Groissmayer, St. Pölten, Austria  
07/1996 Trainee, Josef Lux & Sohn GesmbH, Hainfeld, Austria  
07/1995 Trainee, DI Hanns Schubert, St. Pölten, Austria

## Awards

2011 Ron Cockcroft Award of the International Research Group on Wood Protection  
2005, 2006 Award for excellent performance as a student, granted by the Faculty of Civil Engineering of Vienna University of Technology